HAL open science

Interface modeling within eXtended Finite Element Method for dissipative vibro-acoustic problems

Shaoqi Wu

To cite this version:

Shaoqi Wu. Interface modeling within eXtended Finite Element Method for dissipative vibro-acoustic problems. Acoustics [physics.class-ph]. École centrale de Nantes, 2022. English. NNT : 2022ECDN0041 . tel-03975890

HAL Id: tel-03975890

https://theses.hal.science/tel-03975890v1

Submitted on 6 Feb 2023

HAL is a multi-disciplinary open access archive for the deposit and dissemination of scientific research documents, whether they are published or not. The documents may come from teaching and research institutions in France or abroad, or from public or private research centers.

L'archive ouverte pluridisciplinaire **HAL**, est destinée au dépôt et à la diffusion de documents scientifiques de niveau recherche, publiés ou non, émanant des établissements d'enseignement et de recherche français ou étrangers, des laboratoires publics ou privés.

THESE DE DOCTORAT DE

L'ÉCOLE CENTRALE DE NANTES

ECOLE DOCTORALE N° 602
Sciences pour l'Ingénieur
Spécialité : Mécanique des Solides, des Matériaux, des structures et des surfaces

Par
Shaoqi WU

Eléments finis étendus pour la modélisation des interfaces en vibro-acoustique dissipative

Thèse présentée et soutenue à l'Ecole Centrale de Nantes le 05 Octobre 2022
Unité de recherche : UMR 6183 Institut de recherche en Génie Civil et Mécanique (GEM)

Rapporteurs avant soutenance :

Elke DECKERS Assistant Professor, KU Leuven, Diepenbeek, Belgique
Régis COTTEREAU Chargé de recherche HDR, CNRS, Marseille

Composition du Jury :

Président :	Peter GORANSSON	Professor, Kungliga Teknista högskolan (KTH), Suède
Examinateurs :	Hadrien BERIOT	Senior Research Engineering Manager, Siemens Industry Software N.V., Belgique
	Nicolas MOËS	Professeur des universités, Ecole Centrale de Nantes
Dir. de thèse :	Grégory LEGRAIN	Professeur des universités, Ecole Centrale de Nantes
Co-dir. de thèse :	Olivier DAZEL	Professeur des universités, Le Mans Université

Interface modeling within eXtended Finite Element Method (X-FEM) for dissipative vibro-acoustic problems

Shaoqi WU

November 12, 2022

Version: Final version

Nantes Université

Ecole Centrale de Nantes
Le Mans Université
GeM/LAUM

SPI: Solid mechanics

Interface modeling within eXtended Finite Element Method (X-FEM) for dissipative vibro-acoustic problems

Shaoqi WU

1. Reviewer	Régis COTTEREAU Laboratoire de Mécanique et d'Acoustique Aix-Marseille Université
2. Reviewer	Elke DECKERS Department of Mechanical Engineering KU Leuven
Supervisors	Grégory LEGRAIN and Olivier DAZEL

November 12, 2022

Shaoqi WU

Interface modeling within eXtended Finite Element Method (X-FEM) for dissipative vibro-acoustic problems

SPI: Solid mechanics, November 12, 2022
Reviewers: Régis COTTEREAU and Elke DECKERS
Supervisors: Grégory LEGRAIN and Olivier DAZEL

Nantes Université

GeM/LAUM
Ecole Centrale de Nantes
Le Mans Université
Street address
44321 and Nantes

Abstract

With the advancement of industrialization and urbanization, today's society is inundated with an ever-increasing amount of noise. Long-term noise exposure results in non-negligible impacts on human health, promoting people to pursue a quieter environment in a hurry. The research on high-performance noise control techniques is one of the most demanding topics in the acoustic community for years, from active to passive control, from low to high frequency. With the advantage of design flexibility and lightweight, the use of sound absorbing packages made of porous materials might hold a pivotal position among all approaches to tackle the problem. Our prime interest is in the sound packages, which have multiple layers with significant thickness disparity ranging from several meters to millimetres and potentially complex geometries. This thesis aims at elaborating on more efficient numerical methods to identify and predict the vibro-acoustic behaviour of such packages compared to the conventional Finite Element Method (FEM).

Within the classical FEM, this variety of problems is computationally costly in terms of meshing and solving because meshes must be compatible at material interfaces, and element distortions need to be avoided. Such requirement forces high resolution of elements surrounding the thin layers and complex geometric features, leading to a massive discrete linear system to be solved. The eXtended Finite Element Method (X-FEM) as one of the mesh-independent numerical approaches is adopted here to overcome these computational barriers. Thickness condensation along with diverse interface conditions are employed to cope with thin porous layer modelling in relatively large-scale domains. Variationally consistent *penalty*, *Nitsche* and Transfer Matrix Method (TMM) enhanced formulations are proposed to impose the interface models.

The present methods are verified through typical acoustic benchmarks, exhibiting high accuracy and robustness in the X-FEM framework regardless of geometric, materials and frequency evolution. The proposed approaches are demonstrated to be capable of reducing considerably the time on pre-processing and solution of linear system while maintaining the accuracy level in comparison with classical FEM for a series practical applications. This thesis provides all necessary ideas and tools that can be used for shape/topology optimization or uncertainty propagation in dissipative vibro-acoustic problems within X-FEM.

Keywords: Vibro-acoustic, Porous materials, Interfaces, Fluid-structure interaction, high-order X-FEM, Variational formulation

Résumé

La société d'aujourd'hui est inondée d'un bruit de plus en plus important en raison de l'industrialisation et de l'urbanisation. L'exposition au bruit à long terme a des effets non négligeables sur la santé humaine, ce qui incite à rechercher rapidement un environnement plus calme. La recherche sur les techniques de contrôle du bruit à haute performance est l'un des sujets les plus étudiés dans la communauté acoustique depuis des années, du contrôle actif au contrôle passif, des basses aux hautes fréquences. Grâce à l'avantage de la flexibilité de la conception et de la légèreté, l'utilisation d'ensembles d'absorption acoustique constitués de matériaux poreux pourrait occuper une position centrale parmi toutes les approches visant à résoudre ce problème. Notre intérêt principal se porte sur les systèmes d'absorption qui comportent des couches multiples avec une grande disparité d'épaisseur allant de plusieurs mètres à quelques millimètres, et avec des géométries potentiellement complexes. Cette thèse a pour but d'élaborer des méthodes numériques plus efficaces pour identifier et prédire le comportement vibro-acoustique de tels systèmes par rapport à la méthode conventionnelle des éléments finis (FEM).

Dans le cadre de la FEM classique, cette variété de problèmes est coûteuse en termes de génération de maillage et de résolution, car les mailles doivent être compatibles aux interfaces des matériaux et la distorsion des éléments doit être évitée. Une telle exigence oblige à une haute résolution des éléments entourant les couches minces et les zones géométriques complexes, ce qui conduit à un système linéaire discret très coûteux à résoudre. La méthode des éléments finis étendue (X-FEM), une des approches numériques indépendantes du maillage, est adoptée ici pour surmonter ces obstacles de calcul. Une stratégie d'interface mince avec diverses conditions d'interface est employée pour faire face à la modélisation de couches poreuses minces dans un domaine à relativement grande échelle. Des formulations cohérentes sur le plan variationnel de type *pénalité*, *Nitsche* et la méthode de la matrice de transfert (TMM) sont proposées pour imposer les lois d'interface.

Ces nouvelles stratégies sont vérifiées à travers des benchmarks acoustiques typiques, montrant une grande précision et robustesse dans le cadre X-FEM indépendamment de l'évolution de la géométrie, des matériaux et de la fréquence. Nos approches sont capables de réduire considérablement le temps de prétraitement et de résolution du système linéaire tout en maintenant le niveau de précision par rapport aux éléments finis classiques pour une série d'applications pratiques. Nous pensons que toutes les idées et tous les outils proposés peuvent fournir un aperçu et un potentiel pour des recherches pertinentes.

MotsClés: Vibro-acoustique, Matériaux poreux, Interfaces, Interaction de fluid-structure, high-order X-FEM, Formulation variationelle

Acknowledgement (致谢)

As the last text written in this thesis or also for my three years Ph.D. study, please allow me to do some freestyle. No requirement, no grammar, no standard format, no template, just my sincere thank you from heart!

Of course, two my best supervisors are the first people that I want to thank: Prof. Grégory Legrain (Congratulations for being a professor!) and Prof. Olivier Dazel. Also, Prof. Gwénaël Gabard, I consider you as well my supervisor. After three years, I still clearly remember our first meeting for the application interview. I have to admit that this subject was not my first choice because I had no idea about "acoustic" at that moment. Just because of an unsaid feeling and the first nice conversation with you, I chose this subject. On this aspect, I should also thank myself three years ago. That was definitely a wise choice. During three years, I appreciate every time you explain me some very basic problems, derive the formulations and show me the procedure step by step. The way you "teach" me affects deeply the way I "teach" the students (for the TD, TP and projects). I appreciate a lot your wisdom, patience and humorousness. I appreciate every (over 100) weakly meetings and discussions during past three years.

It is very lucky, profitable, enjoyable to work with you. I am grateful that you bring me into the world of numerical acoustic which might become my whole lifetime career. Your personalities give me deep influence not only on the research but also on the life. There is no doubt that you are the best supervisors over the world!

Then, thanks to Prof. Elke Deckers and Dr. Régis Cottereau for being my thesis's referees. Thank you very well for your appreciation of my work and for all the useful suggestions and questions. I appreciate so much for your careful check. All these remarks make the manuscript more comprehensive. Equally, thanks to all the other jury members: Dr. Hadrien Bériot, Prof. Peter Gorransson and Prof. Nicolas Moës for your time and all the constructive questions. And all your previous scientific works which gives me lots of insight and inspiration along this three years.

Research is never the individual work, besides my supervisor, I gratefully thank to the collaborators: Prof. Anthony Nouy and Dr. Mathieu Gobarit for the help and advice during my PhD.

Three-year is not only about the research, it is more about the life. Therefore, thanks to all the people and friends appearing in these years. Thanks to my two cuties "officemates": Vasu

and pauline. Thanks for your accompany, the conversations and all helps during these years. Thanks to my chinese friends, especially: Dr. Xiaodong Liu, Dr. Huan Wang, Dr. Yuliang Zou, Dr. Zhiping Wang, Dr. Zhen Hong, Ningyue and your relatives... I appreciate as well the time in the "Union des Cheurcheurs et Etudients Chinois à Nantes" and all the members I meet. I will not cite all the names here, but Chunxiao and Jiabing. Lastly, of course, Xueying, I really appreciate every time spending with you, thanks for your understanding and support. Thank you for allowing me to work late in nights :-)

Last by not least, to my parents: Wenjing WU (吴文静) and Ling XIAO (肖玲):
二十年学生生涯落下帷幕，五年留法也进入尾声。感谢爸妈这么多年在各方面的理解和支持。父母在，不远游。游，必有方。

06/10/2022
Nantes, France
Shaoqi WU
吴少奇

昨夜西风凋碧树，独上高楼，望尽天涯路；
衣带渐宽终不悔，为伊消得人憔悴；
众里寻他千百度，蓦然回首，那人却在灯火阑珊处。

Be hungry, be patient, be persistent, be successful
I hope this document could help you

Contents

List of Figures xv

List of Tables xxi

1. Introduction 1
- 1.1. General background . . . 1
- 1.2. Overview of physical models . . . 4
  - 1.2.1. Acoustic wave propagation in porous materials . . . 4
  - 1.2.2. Thin layers modelling . . . 6
- 1.3. Overview of relevant numerical techniques . . . 7
  - 1.3.1. Numerical methods for vibro-acoustical problems . . . 7
  - 1.3.2. Geometry-independent techniques . . . 11
- 1.4. Motivations and objective . . . 13
- 1.5. Organization and contribution of the thesis . . . 14

2. Fundamental preliminaries 17
- 2.1. Physic models: governing equations . . . 17
  - 2.1.1. Helmholtz equation and equivalent fluid . . . 18
  - 2.1.2. Biot's equations . . . 20
- 2.2. Traditional numerical methods . . . 21
  - 2.2.1. Finite Element Method (FEM) . . . 21
  - 2.2.2. Transfer matrix for porous materials . . . 24
- 2.3. eXtended Finite Element Method (X-FEM) for interface problems . . . 27
  - 2.3.1. Level-set function and implicit interface . . . 27
  - 2.3.2. Solution approximation with X-FEM . . . 29
  - 2.3.3. Enrichment . . . 31
  - 2.3.4. Imposition of boundary conditions in X-FEM . . . 33
- 2.4. Conclusion . . . 37

3. X-FEM for dissipative acoustic problem 39
- 3.1. Problem statement and interface conditions . . . 39
  - 3.1.1. Fluid-fluid coupling . . . 40
  - 3.1.2. Fluid-PEM coupling . . . 40
  - 3.1.3. PEM-PEM coupling . . . 41

3.2. Spatial discretization and enrichment . . . 41
3.2.1. Interface between two fluid-like media . . . 42
3.2.2. Interface between two PEMs media . . . 43
3.2.3. Interface between an acoustic fluid and a PEM medium . . . 44
3.3. Numerical verification . . . 46
3.3.1. Plane wave propagating in a double-layered square . . . 48
3.3.2. Sound scattering by a poro-elastic cylinder . . . 53
3.4. Conclusion . . . 55

4. Pressure jump interface **57**
4.1. Fluid-(equivalent) fluid coupling . . . 58
4.1.1. Interface conditions and formulations . . . 58
4.2. Spatial discretization . . . 62
4.2.1. Stability analysis . . . 62
4.2.2. Evaluation of stabilization and weighting parameters . . . 64
4.3. Numerical verification . . . 69
4.3.1. Planar interface . . . 69
4.3.2. Curved interface: cylinder scattering problem . . . 78
4.4. Fluid-PEM (Biot) coupling . . . 79
4.4.1. Interface conditions and formulations . . . 80
4.4.2. Numerical verification . . . 83
4.5. Conclusion . . . 86

5. TMM enhanced interface **89**
5.1. Methodology and Formulations . . . 89
5.2. Application to sound absorbing systems . . . 91
5.2.1. General interface condition enhanced by TMM . . . 91
5.2.2. Variational interface operators . . . 95
5.2.3. Symmetry of the variational systems . . . 97
5.3. Discussion on TMM enhanced interface model . . . 98
5.3.1. Comparison with the pressure jump model . . . 98
5.3.2. Sensitivity analysis for thin films . . . 101
5.4. Verification and validation . . . 103
5.4.1. Implementation . . . 103
5.4.2. Verification with Plane wave . . . 104
5.4.3. Validation of impedance tube . . . 112
5.5. Conclusion . . . 115

6. Numerical application on cavity problems **117**
6.1. Preliminary . . . 117
6.1.1. Problem set-up . . . 117
6.1.2. Placement of one single seat . . . 118

6.2. Double-seat configuration 121
6.2.1. From perfect to imperfect (pressure jump) interface 121
6.2.2. From pressure jump to TMM enhanced interface 124
6.3. Conclusion 127

7. Conclusion **129**
7.1. Summary of the main contributions 129
7.2. Future works and perspectives 131
7.3. Scientific dissemination 132
7.3.1. Peer-review journal paper 132
7.3.2. Conference and oral presentation 133

A. Geometric uncertainty within the proposed models **135**
A.1. Problem set-up 135
A.2. Perturbation method 137
A.2.1. Theory and formulations 137
A.2.2. Numerical results and discussion 139
A.3. Reduced basis method 142
A.3.1. Theory and formulations 142
A.3.2. Results and discussion 145
A.4. Conclusion 150

B. Analytical expressions and solutions **151**
B.1. JCA and Biot coefficients 151
B.2. Analytical solutions 153
B.2.1. Planar interface: transmission problem 153
B.2.2. Scattering problem 156

C. Relevant mathematics proof **159**
C.1. Well-posedness of Helmholtz equation with damping materials 159
C.2. Coercivity of the proposed discrete *Nitsche-type* formulation with high-order X-FEM160

D. Methodology and procedure for obtaining specific matrices **165**
D.1. Obtention of matrix $[\mathbf{T}^{\mathbf{f}-\mathbf{P}-\mathbf{f}}]$ 165
D.2. From transfer matrix to Admittance matrix for Biot's model 167

E. Completed discretized terms in linear systems for TMM enhanced interface **169**

Bibliography **171**

List of Figures

1.1. Thick PEMs usage. 2
1.2. Thin PEMs usage. 3
1.3. PEMs (microscopic scale, Representative Elementary Volume (REV) and Homogenized bi-phase model) 4
1.4. Comparison (Absorption α) of Biot model and equivalent fluid model for the same porous foam. 6
1.5. Example of a targeted resolved problem. 14

2.1. An arbitrary domain and boundaries. 17
2.2. Example of shape function in 1D for (a) Lobatto and (b) Bernstein of order $p = 4$. 23
2.3. General plane wave incident in a lateral infinite domain. 24
2.4. (a) State vectors for fluid-like media (b) state vectors for PEMs. 25
2.5. (a) A circular level-set function of radius $r = 0.1$ defined a structured grid of 0.5×0.5 with its iso-value coutour, (b) level-set of the union of two circles. 28
2.6. 2D representation for X-FEM based computational domain. 30
2.7. (a) Linear Level-set interface; (b) NURBS enhanced interface; (c) Sub-grid Level-set interface. with zoomed elements. 30
2.8. Level set and ridge enrichment function (a) Definition in 1D, (b) Illustration on a 2D triangular element. 32
2.9. 1D example of linear elements for Heaviside X-FEM and Hansbo's Cut-FEM of the strong discontinuity. 32

3.1. Example of a two-media problem domain. 39
3.2. Discretization strategy and node distribution for coupling configuration: fluid-fluid coupling (left), Biot-Biot coupling (middle) and fluid-Biot coupling (right). 42
3.3. Wave properties (variation of wave number as function of frequency) for (a) classical foam, (b) polyurethane, (c) XFM (obtained from appendix B.1). 47
3.4. Test configurations (a)Air-PEM coupling, (b)PEM-PEM coupling. 48
3.5. Example of X-FEM meshes and imposed boundary conditions for (a) Air-PEM coupling,(b) PEM-PEM coupling. 49
3.6. Example of solution (real part) of Air-PEM coupling (top) with incident angle $\pi/4$ at $5,000\,\mathrm{Hz}$ and of PEM-PEM coupling (bottom) with incident angle $\pi/18$ at $2,000\,\mathrm{Hz}$ for fluid pressure (in Pa) (a,c) and solid displacement (in m) (b,d) under fourth interpolation order. 50

3.7. Relative error L^2 in percentage on p^f (left) and $\mathbf{u}^s$ (right) as function of D_λ at $70\,\mathrm{Hz}$ (top) and $5,000\,\mathrm{Hz}$ (bottom) for Air-PEM coupling. 51
3.8. Relative error L^2 in percentage on p^f (left) and $\mathbf{u}^s$ (right) as function of D_λ at $70\,\mathrm{Hz}$ (top) and $5,000\,\mathrm{Hz}$ (bottom) for PEM-PEM coupling. 52
3.9. Cylinder scattering problem with an example of X-FEM mesh. 53
3.10. Example of solution (real part) for (a) pressure (in Pa) and (b) displacement (in m) of cylinder scatter problem in $2,000\,\mathrm{Hz}$ with the fourth order polynomials. . . 54
3.11. Relative error L^2 in percentage on p (left) and $\mathbf{u}^s$ (right) as function of D_λ at $70\,\mathrm{Hz}$ (top) and $2,000\,\mathrm{Hz}$ (bottom). 55

4.1. Two-media problem domain with an imperfect interface. 57
4.2. Inverse inequality constant C_I w.r.t number of elements N and polynomials degree p for (a) two identical media problem and (b) large contrast of media ($\rho_2 = 10^5\rho_1$). 68
4.3. Illustration of impedance tube problem. 69
4.4. Real part of pressure solution (in Pa) for (a) perfect interface problem ($\sigma d = 0$) and imperfect interface $\sigma d = 775\ \mathrm{N\,s\,m^{-3}}$ under $2,000$ Hz. 70
4.5. Sensitivity of the relative error to the stability parameter β_h in function λ for (a) perfect interface and (b) imperfect interface($\sigma d = 775\ \mathrm{N\,s\,m^{-3}}$). 70
4.6. L^2 convergence of Nitsche-type formulation for (a) perfect and (b) imperfect interface ($\sigma d = 775\ \mathrm{N\,s\,m^{-3}}$) condition. 71
4.7. Sensitivity of conditioning number w.r.t the stability parameter β_h ($p = 3$) for different film parameters σd. 72
4.8. (a) L^2 convergence and (b) conditioning of *Nitsche-type* and *penalty-type* formulation for different σd ($p = 3$). 73
4.9. (a) Problem set-up and (b) example of solution for real part pressure (unit in Pa) within X-FEM. 74
4.10. Evaluation of stability parameter β_h by (a) classical strategy ($\gamma = 0.5$) and (b) robust strategy (γ-Nitsche). 74
4.11. Global error on bulk and average interfacial flux for (a) perfect interface; (b) imperfect interface ($\sigma d = 775\mathrm{N\,s\,m^{-3}}$); (c) near-perfect interface ($\sigma d = 1.10^{-15}\mathrm{N\,s\,m^{-3}}$). 75
4.12. (a) Relative error of pressure; (b) relative error of interfacial flux; (c) absolute jump error; (d) condition number of global matrix with respect to the variation of σd under 10 Hz and $1,000$ Hz. 77
4.13. (a) Problem set-up and mesh with refined elements for curved interface; (b) example of real part pressure (in Pa) under excitation of $2,000$ Hz ($p = 4$). 78
4.14. Global error on bulk and average interfacial flux for (a) imperfect interface ($\sigma d = 775\mathrm{N\,s\,m^{-3}}$); (b) near-perfect interface ($\sigma d = 1.10^{-15}\mathrm{N\,s\,m^{-3}}$) for cylinder scatterer problem. 79
4.15. Sensitivity of the relative error in L^2 norm to the stability parameter β_h for (a) pressure and (b) displacement field. 83
4.16. Example of real part (a) pressure (in Pa); (b) solid displacement of x-direction (in m) under excitation of $2,000$ Hz ($p = 10$). 84

4.17. Global error on fluid pressure and solid displacement for (a) imperfect interface ($\sigma d = 775 \mathrm{N\,s\,m^{-3}}$); (b) near-perfect interface ($\sigma d = 1.10^{-15} \mathrm{N\,s\,m^{-3}}$) for planar interface problem. 85
4.18. (a) Example of real part pressure (in Pa); (b) solid displacement of x-direction under excitation of $2,000$ Hz ($p = 5$) 85
4.19. Global error on fluid pressure and solid displacement for (a) imperfect interface ($\sigma d = 775 \mathrm{N\,s\,m^{-3}}$); (b) near-perfect interface ($\sigma d = 1.10^{-15} \mathrm{N\,s\,m^{-3}}$) for cylinder scattering problem. 86

5.1. Four general interface coupling configurations. 92
5.2. Variation of coefficient related to pressure drop (T_{drop} with normal incidence $\theta = 0$ °and thickness of $d = 1$ mm) for different film models as function of frequency: (a) Non-woven film, (b) woven film. 100
5.3. Configuration for testing the sensitivity of the transfer matrix interface model. . . 101
5.4. Global relative error (%) with respect to incidence angle in the TM: (a) air gap, (b) non-woven film, (c) woven film. 102
5.5. Three test configurations with X-FEM meshes and boundary conditions: (a) coupling fluid-fluid; (b) coupling fluid-PEMs with embedded PEM film; (c) cylinder scattering problem with embedded Limp film 105
5.6. Real part of pressure solutions (Pa) within the proposed approach: (a, b) configuration "f-f-f" (45 °, $3,000$ Hz), (c, d) configuration "f-P-P" (30 °, $3,000$ Hz), (e, f) configuration "f-f-P" in cylinder scattering problem (normal incident $2,000$ Hz). . . 106
5.7. Global convergence (left) and local pressure jump convergence (right) for: (a, b) fluid-fluid coupling; (c, d) fluid-PEMs coupling with an embedded PEM film; (e, f) fluid-PEMs coupling in scattering problem with an embedded Limp film. 108
5.8. Evolution of the condition number with respect to D_λ for configuration "`f-f-f`" (top) and "`f-P-P`"(bottom): (a, c) comparison between perfect interface and generalized interface conditions with $d = 10^{-3}$m using interface conforming mesh; (b, d) Influence of values in interface operators by varying thickness of film d using unstructured interface non-conforming mesh. 109
5.9. Evolution of the global L^2 error with respect to thickness d for configuration "`f-f-f`" (a) and "`f-P-P`"(b) using unstructured interface non-conforming mesh . . 111
5.10. Kundt's tube problem in two-dimensions. 112
5.11. Meshes within standard FE model (a) for oblique planar films; (b) for curved boundary films; (c) Meshes within the proposed approach for the above two geometries. 112
5.12. Real part of pressure solution (in Pa) for standard FEM and the proposed approach (XFEM+TMM) for sandwich absorption systems under different geometries and an excitation of $2,000$ Hz. 114
5.13. Absorption coefficients for the sound absorbing system made of a sandwich film coated on a polyurethane. 115

6.1. Car cavity problem description including the geometry and boundary conditions with associated X-FEM mesh. 118
6.2. Geometry and the associated approximation FEM meshes (a) position A and (b) position B. 119
6.3. Solution of the sound pressure (in dB): with classical FEM (top) and X-FEM (bottom) for position A (left) and B (right). The contour and position of seats is indicated by black dashed line. 120
6.4. Clipping of the solutions along the mid horizontal line for single-seat configuration. 120
6.5. Interpolated Level-set function for the two-seat configuration 121
6.6. Geometry and mesh used for two-seats configuration using interface-fitted FEM. . 122
6.7. Solution of the sound pressure (in dB): with classical FEM (top) and X-FEM (bottom) for perfect interface (left) and pressure jump (right): the contour and position of seats is indicated by black dashed line. 122
6.8. Clipping of the solution for (top) perfect interface and (bottom) pressure jump interface for two-seat configuration. 123
6.9. Frequency Response Function (FRF) for (top) perfect interface and (bottom) pressure jump interface for two-seat configuration. 124
6.10. Geometry and mesh used for thin-layer car cavity configuration using interface-fitted FEM (*Full FEM*). 125
6.11. Solution of the sound pressure (in dB): calculated by classical full-FEM (left) and X-FEM+TMM (right) for two-seat thin layers configuration. 126
6.12. Plot of sliced solution of a horizontal clipping for two-seat thin layer configuration. 126
6.13. Frequency Response Function (FRF) of an evaluated point for two-seat thin layers configuration. 127

A.1. Several geometric uncertainty situation in impedance tube problem: (a) variation of thickness, (b) orientation of media, (c) curvature and (d) the flatness which could be a trigonometric function. 136
A.2. Meshing strategies (a) for simple geometry and its variation; (b) for complex geometries and its variation with elastic analogue deformation. 138
A.3. Accuracy sensitivity of $\Delta\xi$ in finite difference scheme for (a)$\delta\xi = 5\%\bar{D}$ and (b)$\delta\xi = 10\%\bar{D}$. 139
A.4. Example of real part solution at $4,000\,\mathrm{Hz}$ by perturbation method with different expansion order. 140
A.5. FRF of absorption coefficient for variation of (a) 5% and 10%. 140
A.6. FRF of perturbation solution for variation of (a) 10% and 5%. 141
A.7. Convergence of the greedy algorithm: norm of residual as a function of N (number of modes). 146
A.8. FRF of absorption coefficient for variation of (a) 5% and 10%. 146
A.9. Relative L^2 error of ROM solution for 10% variation of thickness of whole system. 147
A.10. Absorption coefficients and their envelope (red curves) for thickness variation obtained by (a) FOM and (b) ROM. 148

A.11. Mesh deformation for rotation of the interface. 148
A.12. Absorption envelop under rotation variation for planar interface obtained by (a) FOM and (b) ROM. 149
A.13. Solutions of curved interface with curvature $r = 0.032\,\mathrm{m}$. 149
A.14. Absorption envelops under curvature variation for curved interface obtained by (a) FOM and (b) ROM. 150

List of Tables

2.1. Material parameters presentation 19

5.1. Matrix size of $M \times M$ $(p = 3)$ of impedance tube problem. 114

6.1. Numerical metric comparison for two-seat thin layers car cavity problem. 126

B.1. Porous material properties used in the manuscript. 151
B.2. Film properties used in the manuscript. 152

Introduction

1

> *Last night the west breeze, Blew withered leaves off trees. I mount the tower high, and strain my longing eye.*
> 昨夜西风凋碧树，独上高楼，望尽天涯路
>
> — **YAN Shu**
> (Die Lian Hua)

1.1 General background

As modern urbanization and industry progress, we are inundated with ever-increasing amounts of noise, from neighbours electric devices to air and road transportation [1]. We are facing a world of noise pollution, which is becoming the second leading cause of illness among environmental risks factors in urban environments, behind atmospheric pollution [2, 3]. According to [4], at least about 19.8 million adults in Europe are affected by noise from road traffic, railways, aircraft or industry. WHO reported [5] that over one billion people aged 12 to 35, risk losing their hearing due to excessive exposure to loud music and other high volume recreational noise. Noise exposure has been studied that it causes physical and mental health issues such as hearing loss [6], heart disease [7], annoyance [8] and insomnia [9]. On the other hand, the demand of a more private and quieter daily environment for human society increases [10]. This contradiction between industrial development and human-life needs thus gives rise to the investigation of noise reduction and control technologies. Government agencies and institutions are actively promoting noise reduction policies and researches [11] over years.

In fact, environmental noise is basically generated from various types of vibrational/random interaction between objects (fluid, structures), so-called vibro-acoustic behaviours. In addition, noise sources are typically relatively small compared to the extent of whole area, and noise propagation involves "complex" and unsteady physical "medium", such as buildings and the atmosphere or even moving vehicles. All these factors make sound propagation much more complicated to be predicted and controlled. Up to now, two main strategies are commonly used to reduce the effects of unwanted vibro-acoustic behaviours between objects: active and passive control. Active noise control (ANC) aims to reduce sound emission from source,

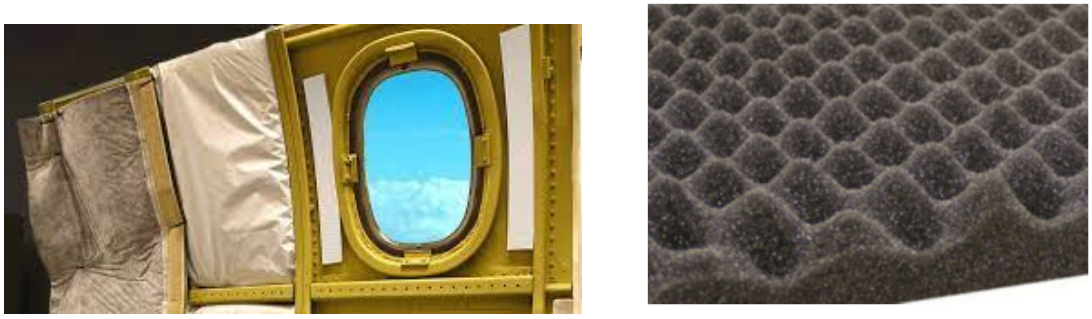

(a) Acoustic Trims (b) Typical foam

Fig. 1.1.: Thick PEMs usage.

which can be realized for instance, by a better design of machinery. While, passive control is more about preventing acoustic propagation and isolating receiver from the source by noise absorbing media or sound mufflers (Chiu, 2010 [12]). Active noise control is best suited for low frequencies and passive treatments a more efficient way for mid-high frequencies (Milosevi and Schaufelberger, 2005 [13]). This thesis focuses on the latter one, where passive sound absorption systems/package will be investigated.

Acoustic absorbing packages are extensively used in various fields in different forms such as sound barriers along high-speed railways (Kitagawa et al., 2015 [14], Ivanov et al., 2017 [15]), sound Trims in vehicles (Fellner et al., 2002 [16], Silva et al., 2014 [17]) and sound panels for room acoustics (Labia et al., 2020 [18]). The most direct and effective design for such systems is to use multi-layered structures (see Lee and Chen, 2001 [19], Dunn and Davern, 1986 [20], Hosseini Fouladi et al., 2010 [21]) where different sound absorption materials are placed sequentially according to specific design requirements. The performance of multi-layer structure is controlled by appropriately selecting the materials and their thickness. In the vehicle industry, for the purpose of NVH (Noise, Vibration and Harshness), we use thick foams (see an example fig. 1.1) that are usually around several to few dozen centimetres varied according to the specific application. They are attached with structural parts everywhere in the compartment, seats as carpet or headliner, which is so-called the Trims component ([22]). Besides of thick layers, thin layers of thickness less than one millimetre broadly exist as well in vehicles, such as sound depressing membranes or films (see fig. 1.2) on the surface of wind-shield, windows or other thick panels. These layers are initially attached for the purpose of protecting the exposed surface from dust, leaks and erosion. Found in the works Chevillotte, 2012 [23], coupling thin acoustic layers with thick foams, could obviously improve the absorbing performance of the whole sound package. This observation has recently been drawn attention and investigated in the works of Gaborit ([24–26]). The present thesis pursues this investigation with a focus on the numerical modelling and simulation in more complex situations.

To better employ and design this sound absorbing systems from selecting appropriate materials and their thickness to shape, topology (Yoon et al., 2020 [27]) or layout optimization (Yu et al., 2021 [28]), it is necessary to identify and characterize the acoustic effects of component

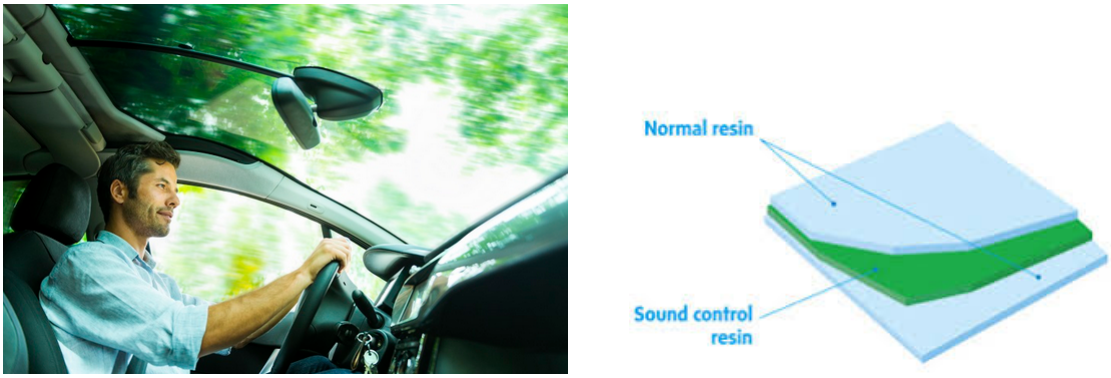

(a) Wind shield (b) Sound resistive film

Fig. 1.2.: Thin PEMs usage.

materials on the whole system. Many researches in the community have been devoted to this aspect. Initially, most of the researches were conducted with the help of real-world experiments. Techniques such as impedance tube method (Dunn and Davern, 1986 [20]) work well for the samples of relative small size under specific conditions and assumptions. Once getting into to more complicated circumstances where the systems have more complex geometries or a statistical study needs to be performed, even in an industrial scale, it becomes even far more costly in terms of duration and material/equipment preparation. As such, physical experiments are mostly used to evaluate the design at the end of the whole manufacturing procedure. The efficiency of the modern manufacturing is greatly restricted by the fact that design cannot be corrected in time.

With the increase in computer power and the gradual maturity of simulation techniques, Computer Aided Engineering (CAE) has grown in popularity due to its efficiency and flexibility compared to traditional experimental methods. One can realize a "real-time" interactive design and manufacturing procedure, leading to a short-cycle production process. In addition, numerical techniques allow an actual "prediction" of the problems. Even though with all these advantages compared to experiments, as the treated problems become larger and more complicated, the computational cost and time of simulations will become huge. The demand for faster simulation techniques is pressing. To this end, efforts are being made from two aspects. The first one is to enhance the computing capabilities, for instance by utilizing High Performance Computing (HPC), which relies on high performance hardware such as clusters or super-computers, sometimes with GPU acceleration and parallel computing architecture such as MPI (Message Passing Interface). The original simulation methods and software should be modified to adapt to the hardware and architectures. The second one aims at simplifying and reducing the size/scale of target problems while maintaining sufficient accuracy. This aspect can be addressed from two directions, either by adopting new physical models and simplified CAD models or by using specific advanced numerical methods.

To better position the work presented in this thesis among the state of the art, this chapter first provides overviews of former key investigation that are mainly related to this thesis. The

review contains physical models of sound propagation in absorbing systems as well as related numerical solution techniques, and mesh-independent numerical techniques with their previous applications. Then, according to the review, the motivations and multiple objectives of this work are presented. Finally, the structure and organization of this thesis are outlined.

1.2 Overview of physical models

This section gives a review of the physical description of the main used materials in sound absorbing systems: porous media. An general introduction of a variety of models for porous materials, followed by a presentation on the physical models for thin layers.

1.2.1 Acoustic wave propagation in porous materials

Porous materials are extensively employed as a main component in sound absorption systems due to their light-weighting and low cost. They consist in elastic skeleton, also called the frame, and poro that is often saturated air. This performance of sound absorption originates from energy dissipation in the material by means of structural, thermal and viscous effects due to the internal interaction between an elastic skeleton and the pore fluid. Because of the complex porous microstructure, it is hard to take the complete geometry of the microstructure into account. The equivalent acoustical response at the macro-scale is typically studied. Homogenization techniques (Allard and Atalla, 2009 [29][chapter 5]) are therefore usually applied to the porous materials in order to obtain an effective physical model. The material is homogenized by a two-phase model that is composed of elastic solid and acoustic fluid phases. Fig. 1.3 depicts a schema of the homogenization process. At the macroscopic scale, one assumes the existence of a Representative Elementary Volume (REV) that is sufficiently small with respect to the wavelength of the phenomena, for which a homogenized description of the superposed solid and fluid coupled phases could be derived.

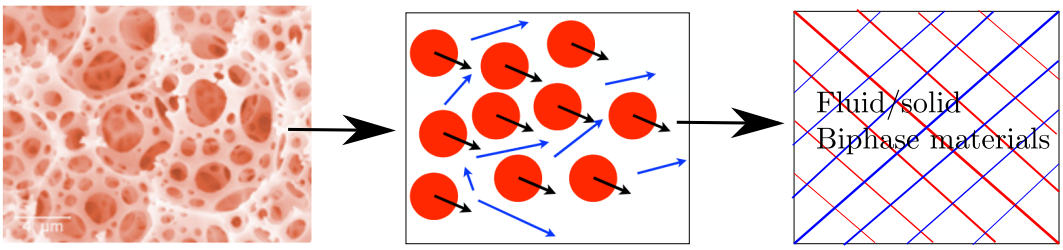

Fig. 1.3.: PEMs (microscopic scale, Representative Elementary Volume (REV) and Homogenized biphase model)

In general, the homogenized models can be classified into two main categories. The first one corresponds to the *equivalent fluid* model where the solid phase is supposed motionless. Under

this assumption, only one fluid compressional wave is allowed to propagate in the material. This model is applicable to the materials which have large skeleton stiffness or when the vibration of solid phase can be ignored compared to the fluid motion in high frequency range. Bruneau and Potel, [30] have proposed a detailed description of the conditions under which an equivalent fluid can be used. The long-wavelength condition is the primary condition that at the microscopic scale, the wavelength is much larger than the characteristic dimension of the pores, and the saturated fluid can behave as an incompressible fluid.

The first work on this model can trace back to Zwikker and Kosten, 1949 [31]. Shortly after, Delany and Bazley, 1970 [32] provided a significantly simplified model for fibrous materials with only two material parameters: the flow resistivity and the density which is able to define the complex-valued characteristic impedance and wave number. Then a set of semi-phenomenological models based on the large scale response were proposed. The key point of this type of models is to define the complex-valued fluid density and bulk modulus accounting for energy damping from viscous and thermal effects with several material parameters. Johnson et al., 1987 [33] first suggested a general model for both effective density and bulk modulus. Effective density then was modified by Pride et al., 1992 [34] to adjust the low-frequency limit and bulk modulus was simplified by Lafarge et al., 1997 [35]. Besides, the model of Wilson, 1993 [36] also contributed to the expressions at medium-frequency. Another special model can be also classified in the equivalent fluid that the inertia of the solid phase is accounted in the effective density. This model is usually called Limp models (Panneton, 2007 [37], Doutres et al., 2007 [38].)

On the other hand, the equivalent fluid model is not generally true that the frame of porous materials cannot be considered rigid. Moreover, in some situations, the mechanical vibration of the frame is inevitable, for instance when the porous material set between two elastic plates. The acoustic response in such cases can be only predicted accurately by considering simultaneously the motion of air and frame, which induces the second class of model for porous materials. The first corresponding model was provided by the *Biot theory* (Biot, 1956 [39], Biot, 1962 [40]) where the frame is considered as elastic solid. Therefore, all the porous materials described by this class of model are specified by poro-elastic materials (PEMs for the following). This model is expressed by two coupled dynamic equations to represent a fluid-structure interaction. Over decades, various formulations based on Biot theory were proposed. The formulation of $(\mathbf{u}^s, \mathbf{u}^f)$ that expressed in terms of the solid and fluid displacement was the original formulation. The formulation $(\mathbf{u}^s, \mathbf{w})$ (Easwaran et al., 1996 [41]) where fluid displacement is replaced by the fluid flow components relative to the solid skeleton measured in terms of volume per unit area of the bulk medium. Atalla et al., 1998 [42] that used the pore fluid pressure instead of its displacement to formulate the Biot theory is known as the mixed $(\mathbf{u}^s, p)$ formulation. Göransson, 1998 [43], added the fluid displacement scalar potential φ^f into mixed formulation, yielding $(\mathbf{u}^s, \mathbf{u}^f, \varphi^f)$. Dazel et al., 2007 [44] proposed an alternative displacement formulation in terms of solid and total displacement $(\mathbf{u}^s, \mathbf{u}^t)$.

From the viewpoint of physic, three waves can appear in the Biot's model, which is the most significant difference compared to the equivalent fluid model. Because of the dynamic description of elastic solid, additional compressional wave and shear wave generated from the solid skeleton propagate in the materials which are so-called frame-borne waves. The circulation of the poro fluid (air) that produces the second compressional wave is called airborne wave. In addition to viscous and thermal effects, the structural effects to the energy dissipation is introduced. The interaction in the Biot's description is much more complicated than in the equivalent fluid. A comparison of absorption coefficients between the two models for a same porous foam is illustrated in fig. 1.4 [1]. A visible difference is observed over the range of frequency. Besides the resonance of poro-fluid around $1,500\,\mathrm{Hz}$, the frame resonance around $1,000\,\mathrm{Hz}$ is also captured by the Biot's model. One can conclude that for this material, equivalent fluid is not suited to model the absorption correctly. That is why it is necessary to consider both models in the thesis.

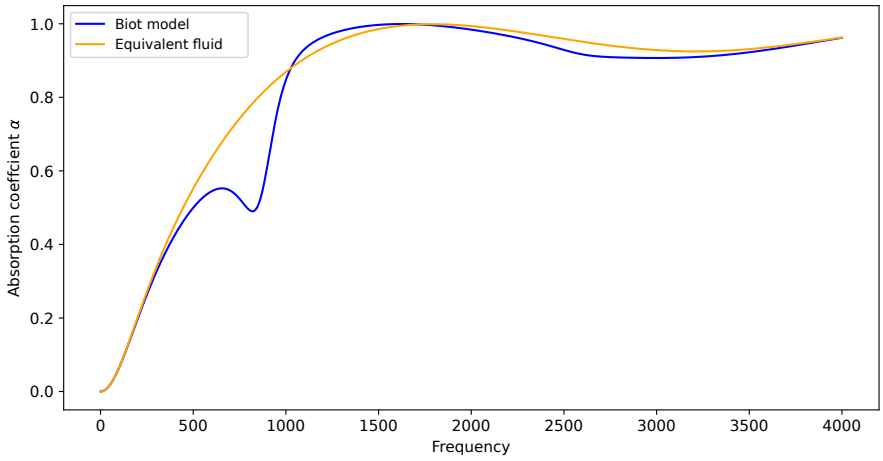

Fig. 1.4.: Comparison (Absorption α) of Biot model and equivalent fluid model for the same porous foam.

1.2.2 Thin layers modelling

For the thin porous layers, from viewpoint of physics, equivalent fluid models and Biot's description presented previously for porous materials can be straightforwardly used. Besides, some analogical and asymptotic models were developed in different fields. Here, we would like to give an overview of thin layers modelling in various fields from literature.

Thin layers are common in various physical problems such as shells, membranes, material coating, inter-phases in heterogeneous composite materials (Bigoni et al., 1998 [45]). Even though the thickness of such layers is excessively small compared to the characteristic dimension of the entire domain, their effects are pronounced and cannot be ignored. Abounding theories and

[1] The curves are calculated analytical for an impedance tube problem

approaches were developed such as shell (Rubin and Benveniste, 2004 [46]), membrane (Mey et al., 2009 [47]), to describe the physical behaviour of thin layers directly or indirectly. Among them, the most employed strategy is to reduce the thickness of the layers to a limiting situation: *non-thickness* interface, and their physical behaviours are described through specific asymptotic models. For thin elastic layers, the investigation began from the works of Aleksandrov, 1969 [48], Meijers, 1968 [49] and Alblas and Kuipers, 1970 [50]. Then, their work was extended to the viscoelastic layers (see Argatov and Mishuris, 2011 [51]. Hashin, 1990 [52], Hashin, 1991 [53], Hashin, 2002 [54], Benveniste, 1985 [55]). Gurtin and Ian Murdoch, 1978 [56] proposed a set of asymptotic models for inter-phase problems considered as a first-order spring-layers. Steigmann and Ogden, 1997 [57] and Gu and He, 2011 [58] developed a more general theory including second-order interface conditions .

In vibro-acoustic problems, there rarely exists systematic investigations on the reduced thin layers models. We cite that pressure jump (drop) is the most commonly used model for fluid thin layers, which was first proposed by Pierce, 1989 [59]. Flow resistivity induces a pressure drop across the media. Then, based on the asymptotic theory, a model for thin elastic and fluid layers in acoustic scattering problems was given by Bövik, 1994 [60]. More recently, Gaborit et al., 2018 [24] proposed a simplified model for thin acoustic screens represented in a matrix form based on the Biot's theory.

1.3 Overview of relevant numerical techniques

1.3.1 Numerical methods for vibro-acoustical problems

To model above sound absorbing systems and predict their acoustic response, numerous methods were proposed in the past decades. Here, these methods are classified into three categories: Matrix based plane wave method, Element based method and wave based method.

Plane wave Transfer Matrix methods (TMM)

When acoustic propagates through homogenous stratified layers whose lateral dimension can be considered infinite, the plane wave assumption can be applied. The thickness is the solely geometric information that is considered. For such problems, the matrix representation could be the most general way to predict acoustic reflection and transmission of the system, where we connect the acoustic state between the two sides of layers by rewriting the wave propagation equations in form of algebraic matrix. Here several pioneering works (see Becker, 1962 [61], Scharnhorst, 1983 [62], Brouard et al., 1995 [63]) are cited here. As it is a reconstruction of governing equations, different nature of materials can be modelled through this method, fluid (Li et al., 2002 [64]), elastic panel (Lee and Xu, 2009 [65]), even for piezoelectric layers

(Pastureaud et al., 2002 [66]) and muffler modelling (Gerges et al., 2005 [67]). The work of Song and Bolton, 2000 [68] is the most cited work in the literature concerned this class of methods for porous materials using Limp and rigid frame model. Then, the matrix description of Biot's equation was given in the work of Khurana et al., 2009 [69]. The work of Dazel et al., 2013 [70] improved the instability of transfer matrix method in high frequencies and for large layer thickness. Based on this work, Gaborit et al., 2018 [24] proposed a simplified matrix representation for thin porous screens. This family of method is greatly favourable for the multi-layer configuration that representation of layers combination is realized readily by matrix algebraic manipulations. Although with less numerical consuming and ease of implementation, this method is mainly restricted to the estimate acoustic response of simple configurations. In order words, it is difficult for this method to handle more practical problems of complex sound excitation and geometries.

Domain discretization methods

To simulate the acoustic field in more complicated situations, one are required to discretize the computational domain/boundaries on which the physical equations are defined into smaller non-overlapping "elements". In the computational acoustic community, Finite Element Method (FEM) and Boundary Element Method (BEM) might be the two most used methods, where BEM is used more often to treat the exterior acoustic problems (Liu, 2019 [71]). Here, only the most relevant works belongs to FEM are reviewed, since the simulation of acoustic field involving porous materials are usually interior problems. In the framework of the FEM, the domain is divided into a finite number of non-overlapping subdomains called elements of size h constructing a mesh. Instead of approximating directly the original partial differential equations (PDE), the equivalent integral formulations namely variational formulations are solved numerically. The solution in the elements is approximated by a linear interpolation with basis functions. Numerous approaches can be classified into the family of FEM. According to the type of basis function, we review this type of method that is applied for vibro-acoustic problems into two major categories.

The first one is referred to the polynomials as the basis functions. The precision of this method can be improved by decreasing the size h of element (h-refinement) or increasing the order p of polynomial basis functions (p-refinement) or to combine the previous two strategies (hp-refinement). We cite the first works of studying h version (Ihlenburg and Babuška, 1995 [72]) and hp-version (Ihlenburg and Babška, 1997 [73]) of FEM for solving Helmholtz equation, in which the analytical H^1 norm error estimation was given as follows:

$$E < C_1 \left(\frac{kh}{2p}\right)^p + C_2 k \left(\frac{kh}{2p}\right)^{2p}, \tag{1.1}$$

where the k is the wave number. The global error of the Helmholtz equation within FEM consists of two parts, the first error can be controlled by using a sufficient number of elements

per wavelength. This leads to the significant "rule of thumb" [2] which are widely used up to now in engineering applications. The second parts in the error corresponds to the pollution effect [3]. The second one will dominate the global error when the frequency continues to increase for which the "rule of thumb" is not sufficient to guarantee a converged solution. The p-refinement was demonstrated to be noticeably efficient to alleviate such numerical issue (Ihlenburg and Babška, 1997 [73] and Bériot et al., 2013 [75]). Followed by that, the high order FEM was extensively investigated for solving Helmholtz equations. The classical Lagrange polynomials that are constructed nodally showed to be computational costly, and the discrete system could become ill-conditioned with high order interpolation (Prinn, [76]). Meanwhile, the polynomials defined with modal contribution was drawn more attention such as Lobatto (Bériot et al., 2013 [75]) and Bernstein shape functions (Farouki, 2012 [77]). Bernstein is found to be more efficient in comparison with Lagrange polynomials when using an iterative solver (Petersen et al., 2006 [78]) and for short wave-number (high frequency) (El Kacimi et al., 2019 [79]) problems. Lobatto shape functions are also called integrated Legendre function, which is hierarchic polynomials, meaning that the basis defined on order p is obtained as a correction to the basis of order $p-1$. This property permits not to construct completely different set of basis when one want to increase the approximation order as the other presented polynomials. This hierarchic property can also facilitate to implement the p-adaptive algorithm that locally determine the optimal interpolation order for each elements. Bériot et al., 2016 [80] proposed an efficient way to select automatically the order of interpolation in each element for large-scale Helmholtz problems. Finally, a common benefit from using modal shape function is that static condensation can be applied to make the computation more efficient while maintaining the accuracy of the solution (Deraemaeker et al., 1999 [74]).

In comparison with numerical solution of Helmholtz equation, the Biot's equations are more difficult to converge not only due to the pollution effects in the dynamic equations but also because of the existence of a huge scale disparity between the two coupled fields. Dauchez et al., 2001 [81] demonstrated the "rule of thumb" is not sufficient to capture a reliably results for the $(\mathbf{u}^s, u^f)$ formulation. Hörlin et al., 2001 [82] and Hörlin, 2005 [83] applied successfully the hierarchic FEM to Biot's equation $(\mathbf{u}^s, u^f)$ and demonstrated that the hierarchical extensions are faster than linear and quadratic Lagrange FEM. Rigobert et al., 2003 [84] conducted a similar research for $(\mathbf{u}^s, p)$ formulation using Legendre hierarchical elements. More lately, the adaptive p hierarchic FEM was developed to solve mixed $(\mathbf{u}^s, p^f)$ Biot's formulation by Jonckheere et al., 2022 [85].

Contrary to the use of polynomials as basis function, an alternative way is to use plane waves as basis functions directly or to enrich the existing basis to capture highly oscillatory solutions. The works of Babuška and Sauter, 1997 [86] constructed a plane wave based within the concept of Generalized FEM (GFEM) to solve the Helmholtz equation. Then, Cessenat and Després,

[2] Eight to ten elements are needed per wavelength

[3] Accumulative local phase shifting dispersion error: discrete error of wave number between FEM and exact solution (see Deraemaeker et al., 1999 [74])

2003 [87] used the similar plane wave basis in the Ultra Weak Variational Formulation (UWVF Huttunen et al., 2002 [88]) for time-harmonic equations. Within the framework of the Partition of Unity FEM (PUFEM) (Melenk and Babuška, 1996 [89]), a series of investigations have been conducted for acoustic problems (see Mohamed et al., 2010 [90], Laghrouche et al., 2003 [91], Laghrouche et al., 2005 [92], Banerjee and Sukumar, 2017 [93]). For modelling porous materials, Chazot et al., 2013 [94] analyzed the performance of wave enriched PUFEM for equivalent fluid JCA model and extended to the $(\mathbf{u}^s, p)$ Biot formulations (Chazot et al., 2014 [95]). Gabard and Dazel, 2015 [96] proposed using plane wave based discontinuous Galerkin methods (DGM Wilcox et al., 2010 [97]) for sound absorbing materials of Biot's $(\mathbf{u}^s, \mathbf{u}^t)$ formulation. Compared to former polynomials FEM basis, more efforts and *a priori* physical knowledge for the implementation are required for this family of methods since local, exact solutions of the governing equations have to be obtained beforehand. This prerequisite complicates the solution procedure, especially for the coupled equations as Biot's equations considered in this thesis.

Wave Based Method (WBM)

Apart from element based method presented above, there exists other numerical methods which have been applied for simulating acoustic behaviour of porous materials such as the method of fundamental solutions (MFS Nennig et al., 2011 [98]) and Wave Based Method (WBM). Here, only the latter one is being reviewed briefly. The group of Wim Desmet developed a series of numerical modelling based on the indirect Trefftz concept (Kita and Kamiya, 1995 [99]), so-called Wave Based Method (WBM) (see Desmet et al., 2002 [100], Pluymers et al., 2004 [101], Pluymers et al., 2007 [102]) for vibro-acoustical problems. Among those, the works of Deckers et al. proposed systematic researches (Deckers et al., 2011 [103], Deckers et al., 2012 [104], Deckers et al., 2012 [105], Deckers et al., 2013 [106]) on using WBM for porous materials with Biot's theory.

Unlike FEM where the whole domain is discretized into many *small* elements to ensure the accuracy of the solution and to describe properly the complex geometry, the WBM partitions problem domain into a limited number of *large* convex subdomains. In each subdomain, the field variables are expanded with wave functions which inherently fulfil the governing equations. This characteristic mitigates the influence of high frequency excitation as in traditional FEM, a satisfactory accuracy of the solution can be obtained within a limited number of dofs, i.e the number of wave functions for high frequency excitation.

Indeed, the typical nature of this method shows some drawbacks. Since the wave functions are complex function and frequency dependence, the discrete matrix system is fully complex and cannot be decomposed into frequency independent submatrices. Moreover, the integration of matrix entities are more computationally involved compared to the polynomial shape functions in FEM. These factors prevent WBM from presenting greater advantages in terms of

computational cost compared to FEM. Moreover, as the use of convex subdomain is required to optimize the computational efficiency, the discretization of a complex geometry would be a challenge and sometimes impossible within the WBM. Although the strategies of multi-level modelling (Van Genechten et al., 2010 [107]) or hybrid FE-WBM (Climent et al., 2022 [108]) were proposed to relieve this issue, the flexibility with respect to the geometry is still limited.

1.3.2 Geometry-independent techniques

It is seen that, except for the FEM, geometric complexity constrains the performance and range of application of these methods. However, in practical applications, complex and irregular structure exists everywhere from micro to macro scale. Furthermore, accompanied by the advance in additive manufacturing (3D printing), more complicated structures involving multiple heterogeneous voids, inclusions and interfaces, etc., can be fabricated. The advanced physical properties of these "products" need to be identified by means of simulation. When handling such geometries, even for the FEM, generation of high-quality mesh is prohibitively time-consuming. This meshing limitation from the traditional FEM is that the elements are required to coincide with the contour of geometries without much distortion, namely interface-fitted mesh. This requirement will make the computation extremely expensive when the geometry evolves, as when shape/topology optimization, is treated. High-resolution of elements is sometimes needed to represent a "continuous" evolution of geometries. In addition, the numerical modelling of the aforementioned thin layers was not yet addressed appropriately. Within the traditional FEM, at least one element is needed in the thickness direction for the thin layer, which demands a high resolution of elements in the vicinity of thin layers. Therefore, finding an effective numerical method to relax this restriction is of prime interest.

The counterpart of the interface-fitted or conforming mesh is the unfitted or non-conforming mesh, the use of which relies on the development of mesh independent techniques. The concept of mesh-independent method can be first raised from the work of Moës et al., 1999 [109], in which the eXtended Finite Element (X-FEM) was proposed to address the crack propagation problem without *re-meshing*. The X-FEM is considered as a special case of the Generalized Finite Element Method (GFEM Melenk and Babuška, 1996 [89]) where the whole or a part of the elements in the computational domain are enriched by additional functions with associated degrees of freedom to represent some complex solution features in the elements such as discontinuity, singularity or other non-smooth behaviour. With the versatility of the enrichment, in the past two decades, the X-FEM has been extensively applied to deal with holes (Sukumar et al., 2001 [110]), inclusions (Sukumar et al., 2001 [110], Moës et al., 2003 [111]), cracks (Stazi et al., 2003 [112]) and fluid structure interaction (FSI Gerstenberger and Wall, 2008 [113]), etc., (for more applications see the review Fries and Belytschko, 2010 [114]). Heaviside enriched X-FEM even becomes the one of most used numerical methods to treat fracture problems (Xiao et al., 2021 [115]).

Meanwhile, Hansbo and Hansbo, 2002 [116] and Hansbo and Hansbo, 2004 [117] proposed an unfitted finite element method to treat discontinuities across interfaces. Without any enrichment, two overlapping elements are defined over the interface through the concept of phantom (Song et al., 2006 [118]) or ghost (Zou et al., 2017 [119]) nodes. This setup allows the construction of discontinuous approximation basis to model the discontinuity. This method, which has been applied, from solid mechanics (Hansbo and Hansbo, 2004 [117]), fluid-structure interaction (Hansbo et al., 2003 [120]) to stokes interface (see Hansbo et al., 2014 [121]) and many other problems (Jiang et al., 2020 [122] and Bernland et al., 2018 [123]), is now being well-known as the class of Cut-FEM methods, (see review Burman et al., 2015 [124]). Compared with X-FEM, Cut-FEM offers more conveniences for representing discontinuities in elements in the sense that the implementation is much easier based on an existing FEM code. On the other hand, the X-FEM provides more flexibilities and possibilities to represent not only discontinuities but also other particular features in elements because of the concept of enrichment.

Now, the geometries are embedded in the elements, continuity of the solution cannot be ensured naturally as in standard FEM with conforming mesh. Therefore, the insurance of continuity or enforcement of discontinuity condition is another key ingredient. Within X-FEM, a weak discontinuity (gradient of the field is discontinuouss) in elements can be recovered by enriching continuous functions (see Sukumar et al., 2001 [110], Belytschko et al., 2003 [125] and Moës et al., 2003 [111]). When a strong discontinuity (the primal variables are discontinuous) is created in elements, it is better to prescribe the boundary/interface conditions weakly by modifying the associated variational formulations. The penalty method (Babuška, 1973 [126]) could be the most straightforward candidate to impose the Dirichlet boundary conditions or to enforce the continuity of solution at interfaces. But, this method is not consistent with the original problems, and it requires a sufficiently large penalty parameter to retain an optimal convergence rate, which destroys the conditioning of the discrete system. Lagrange multipliers (see Babuška, 1973 [127], Ji and Dolbow, 2004 [128], Gerstenberger and Wall, 2008 [113] and Béchet et al., 2009 [129]) is another method that is frequently used, which introduces more unknowns into the formulations, leading to larger algebraic systems to be solved. In addition to this, potential stability issues could be encountered when the multiplier space does not satisfy the inf-sup (or LBB) condition (see Malkus, 1981 [130]).

To overcome these drawbacks, combing the advantages of penalty and Lagrange multipliers, Nitsche's formulation (which can be considered as condensed augmented multiplier method in Hautefeuille et al., 2012 [131]) has been proposed in Nitsche, 1971 [132], and rapidly applied to deal with Dirichlet-type or jump-type conditions. Indeed, Nitsche's formulation also introduces a numerical parameter as in the penalty method, but this parameter is used to ensure coercivity and stability of the solution rather than enforcing boundary conditions, namely stability parameter. The stability parameter is commonly not too large to result in conditioning issue. The definition and choice of the stability parameter need to be treated carefully, and sometimes it is not trivial. Dolbow and Harari, 2009 [133] gave an analytical

expression of the stability parameter for linear triangular elements. Embar et al., 2010 [134] proposed a strategy of evaluating stability parameter using high order spline elements to impose Dirichlet boundary conditions. According to the same idea, the evaluation procedure of the stability parameter to enforce continuous interface conditions was provided by Jiang et al., 2015 [135], and its analytical expression was given recently for general high order elements (Jiang et al., 2022 [136]). However, all these works were mainly applied to the Poisson-type PDEs, the determination of stability in time-harmonic dynamic equation is not trivial. From the author's knowledge, only two relevant works have addressed this aspect. Zou et al., 2017 [119] applied Nitsche's formulation for a classical two-media steady state acoustic problem, where a perfect interface condition was enforced (continuity of the pressure field). The problem was solved using a linear Cut-FEM approach. Yedeg et al., 2016 [137] discussed a Nitsche-type formulation for a complex-valued transmission interface condition, which is attractive because two extreme cases (perfect and imperfect interface) can be recovered by one formulation. In their work, a unique homogeneous media was involved and a conforming finite element mesh was required to discretize the computational domain.

In regard to the numerical solutions involving thin layers/interface, surface element (Nairn, 2007 [138]) is the most common way to account for the additional stiffness of the interface behaviour within standard FEM. Concerning the mesh-independent methods, Burman et al., 2015 [124] discussed the formulations and implementation of Cut-FEM for non-thickness model of first-order discontinuities for various physical problems including heat release, spring-type and surface transport. Han et al., 2019 [139] employed isogeometric cut-cell methods for high-order interface models. Yvonnet et al., 2008 [140], Zhu et al., 2011 [141] and Benvenuti et al., 2013 [142] used X-FEM to implement cohesive interface and spring-layer models in composites. Legay, 2015 [143] coupled thin shell elements within the X-FEM for vibro-acoustic problem. The aforementioned Yedeg et al., 2016 [137], applied Nitsche's method to a transmission wave interface in acoustic problems.

1.4 Motivations and objective

From this brief review, it is found that the numerical methods for classical vibro-acoustic problems have been greatly explored, from fluid-structure interaction to PEMs modelling. Currently, high-order FEM seems to be the most efficient method. In addition, thin layers modelling and its numerical solution were also dived into, exhibiting satisfactory results, where the *non-thickness* asymptotic model were employed. Unfortunately, it is rare to consider thin layers modelling and numerical solution in dissipative acoustic systems simultaneously. Several similar works only addressed part of this aspect (Gaborit, [26] and Yedeg et al., 2016 [137]), but either the problem is solved in "semi-analytical" manner or the considered geometry is relatively simple. The restriction from meshing requirement in conventional domain discretization stills needs to be circumvented.

Therefore, the major objective of this Ph.D thesis is to carry out a systematic investigation for vibro-acoustic problems involving both thick and thin sound absorbing layers in numerical models. And finally, we are able to predict complex acoustic fields accurately in a more efficient way than any mentioned methods. Provided a more concrete instance as seen fig. 1.5, the acoustic response of a cavity (in black) where foam made passenger seat (in blue) coated by a thin porous layer (in red) will be simulated. In standard discretization method, the total degree of freedoms of the numerical model will explode. To ease the establishment of numerical models and solution procedures, all the ideas are build up within an advanced-mesh independent technique: the eXtended Finite Element Method (X-FEM). To the best knowledge of author, this is the first attempt to apply the X-FEM for such problems. Hence, this project offers a set of fundamental insight and wide range of potential and possible applications.

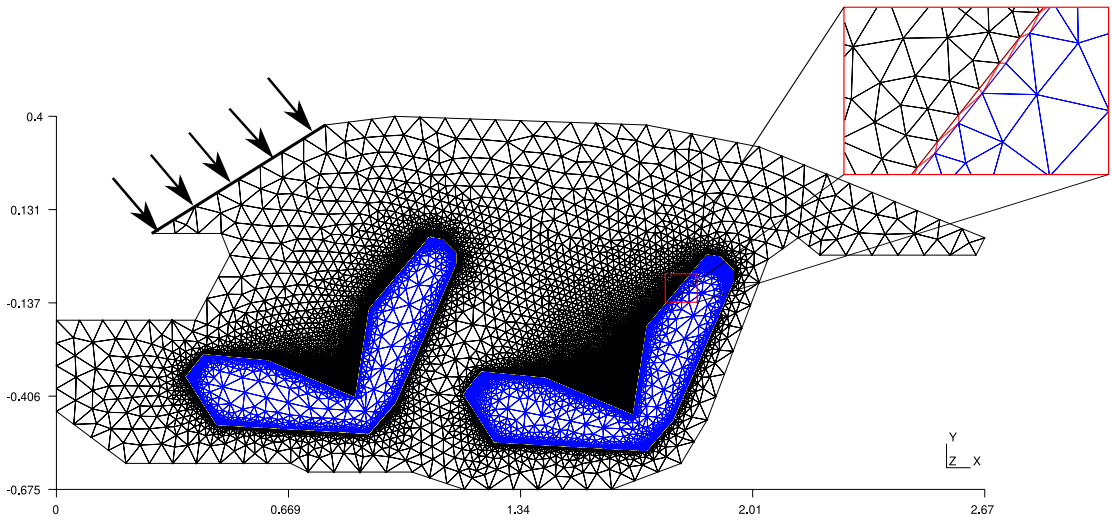

Fig. 1.5.: Example of a targeted resolved problem.

The investigation will be performed step-by-step to approach our final objective. The considered problem in each step will be gradually complicated, in which, the proposed methods will be implemented and verified.

1.5 Organization and contribution of the thesis

Chapter 2 presents the necessary preliminary notions including physical models, equations and associated formulations for acoustic fluids and porous media. The relevant techniques used for the following problems with X-FEM framework is introduced in detail. The well-posedness of the dissipative acoustic equations is given, and the relationship between Heaviside-enriched X-FEM and Cut-FEM is presented.

From chapter 3 to chapter 5, three main problems/models to be treated are discussed sequentially according to their complexity. In chapter 3, thin layers are not considered, leading

to perfect interface: only thick bulk part fills the computational domain. Various coupling conditions with corresponding spatial discretization and enrichment functions are given. These strategies are suitable for all following problems considered in chapter 4 and chapter 5. The performance of methods is examined in detail with classical numerical benchmarks.

In chapter 4, thin layers start to be considered in the domain. The pressure jump model (Pierce, 1989 [59]) is adopted to represent the behaviour of thin porous layers. Two formulations are derived to enforce such interface model weakly. A mathematical proof of the well-posedness for the proposed formulation is given, which can be considered as the major contribution in this chapter. The implementation details of the proposed formulation in the current computational framework are fully presented. For the sake of consistency, similar numerical benchmarks as chapter 3 are conducted to verify and evaluate the proposed methods.

A more general model for thin porous layers based on Transfer Matrix Method (TMM) rather than pressure jump is proposed in chapter 5. Not only for porous layers modelling, a generalized computational framework and formulations are established, which is able to apply for different media. The comparison with the pressure jump model is also discussed. The proposed interface models are assessed analytically and validated numerically.

Chapter 6 presents a series of engineering application situations for a two-dimensional car-like cavity problem. All the methods and formulations are further validated in these more realistic and complex problems. The final objective of this thesis is achieved. The benefits and advantages of the proposed developments are fully demonstrated. The reliably and accuracy of the proposed approaches are illustrated.

In chapter 7, the main contribution of this thesis along with possible future challenges are summarized. The lists of scientific disseminations are provided as well in this chapter. Several appendices followed by the manuscript to complement the main text or for additional information, of which, appendix A provide preliminary results to consider geometric uncertainties in the proposed computational framework.

Fundamental preliminaries

2

Life is just a series of trying to make up your mind

— **T.Fuller**

This chapter is dedicated to present the common and necessary preliminaries used for all following chapters in this manuscript. Two physical models with governing equations for the dissipative vibro-acoustic system is first presented. For solving the prescribed physical models, traditional numerical methods including the standard FEM with associated variational formulations and transfer matrices are formulated. Then, the X-FEM coupled with Level-set for interface problems is introduced with more technical detail on implementation.

2.1 Physic models: governing equations

As aforementioned, equivalent fluid and Biot's theory are both considered in this work to model the acoustic behaviour of porous materials in sound absorption systems. The Helmholtz equation is used to model equivalent fluid and the Biot's mixed formulation is considered to account for poro-elastic media (PEMs). To formulate the equations, a harmonic convention $e^{+\mathrm{j}\omega t}$ is assumed with angular frequency ω, and an arbitrary domain is illustrated as fig. 2.1.

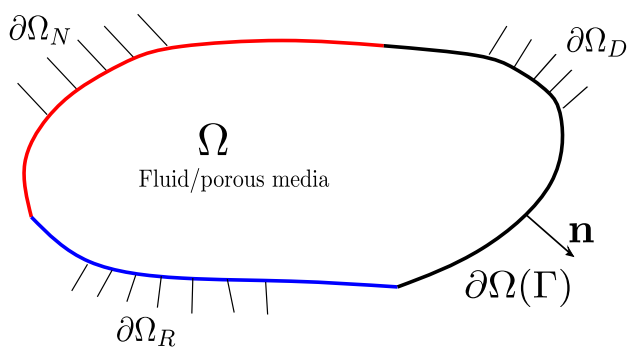

Fig. 2.1.: An arbitrary domain and boundaries.

2.1.1 Helmholtz equation and equivalent fluid

The Helmholtz equation of fluid pressure p^f defined in an arbitrary enclosed domain Ω for a linear wave propagation in a uniform, homogeneous medium reads:

$$\nabla^2 p^f + k^2 p^f = 0, \quad p \in \Omega, \tag{2.1}$$

where k is the wave number expressed by:

$$k = \frac{\omega}{c} = \omega\sqrt{\frac{\rho}{K}}, \tag{2.2}$$

with phase celerity of the wave c, fluid density ρ and compressibility K. All these material constants can be real or complex-valued. Real-valued constants represent common acoustic media such as air, while complex-valued constants are used to consider the energy damping in the material such as for porous materials.

When porous materials are supposed to be frame-rigid, sound propagation can be described as an equivalent fluid governed by the Helmholtz equation with complex-valued material constants. For an equivalent fluid, the wave number k_{eq} in Helmholtz equation is defined as:

$$k_{\text{eq}}(\omega) = \omega\sqrt{\frac{\tilde{\rho}_{\text{eq}}(\omega)}{\tilde{K}_{\text{eq}}(\omega)}}. \tag{2.3}$$

It is seen that the wave number is frequency dependent expressed by the frequency-dependent effective fluid density $\tilde{\rho}_{\text{eq}}$ and bulk modulus $\tilde{K}_{\text{eq}}$. In this thesis, the so-called JCA (Johnson-Champoux-Allard) (Johnson et al., 1987 [33], Champoux and Allard, 1991 [144]) model is employed to provide such complex-valued constants. The energy loss due to viscous effects is taken into account by the effective density defined as following in Johnson et al., 1987 [33], and the damping generated from thermal effects is accounted for within effective modulus $\tilde{K}_{\text{eq}}$ given in Champoux and Allard, 1991 [144]. The five first material properties in table 2.1 that are needed to calculate these two effective parameters are:

- Porosity ϕ: the ratio between the air volume to total volume of porous materials.
- Flow resistivity σ: introducing viscous losses for the sound propagation in the media.
- Tortuosity α_∞: a geometric parameter related to the actual distance the sound pass through a layer.
- Viscous characteristic length Λ: characteristic length providing a correction for the viscous effects.
- Thermal characteristic length Λ': analogy to the viscous characteristic length, in order to better account for the thermal effects.

Tab. 2.1.: Material parameters presentation

Notation	Unit	Description
ϕ	[-]	Porosity
σ	$[\mathrm{N\,s\,m^{-4}}]$	static flow resistivity
α_∞	[-]	Tortuosity
Λ'	$[\mathrm{m}]$	Thermal characteristic length
Λ	$[\mathrm{m}]$	Viscous characteristic length
ρ_1	$[\mathrm{kg.m^{-3}}]$	Frame density
E	$[\mathrm{Pa}]$	Young's modulus
ν	[-]	Poisson ratio
η_s	[-]	Loss factor

The analytical expression to obtain effective density and bulk modulus with these properties are provided in appendix B or can be referred to the detail in handbook Allard and Atalla, 2009 [29].

The Helmholtz equation eq. (2.1) has to be combined with the boundary conditions to obtain the solution. Three types of frequently used boundary conditions to constraint the problem are:

- *Dirichlet boundary condition* specifies acoustic pressure (prescribed constant pressure $\tilde{p}$) on the boundary $\partial\Omega_D$ as:

$$p^f = \tilde{p}, \quad \text{on } \partial\Omega_D. \tag{2.4}$$

- *Neumann boundary condition* specifies the gradient of the field (secondary variable in FEM) as:

$$\frac{\partial p^f}{\partial n} = \tilde{g}, \quad \text{on } \partial\Omega_N, \tag{2.5}$$

  where $\tilde{g}$ is a prescribed value or function. This condition is usually used to impose excitation velocity or displacement, or can define a rigid wall condition when $\tilde{g} = 0$.

- *Robin mixed boundary condition* or called *impedance condition* specifies the relationship between primal and secondary variables on the boundaries, it can be written as:

$$\frac{\partial p^f}{\partial n} + \mathrm{j}kAp = 0, \quad \text{on } \partial\Omega_R, \tag{2.6}$$

  where A represents the relative surface admittance that:

$$A = \frac{\rho c}{Z_n}, \tag{2.7}$$

  with ρ and Z_n are the specific fluid density and acoustic impedance applied on the boundary. This condition is able to approximate non-reflective boundaries.

Remark that for the classical Helmholtz equation with real-valued parameters, the *Robin condition* is necessary to ensure the well-posedness of the problem. Otherwise, the unique solution does not exist on the resonance wave numbers. Detailed proof of this aspect can be found in the textbook of Ihlenburg, 1998 [145]. On the other hand, when energy damping exists in the problem, the existence and uniqueness of the solution can be guaranteed without Robin boundary conditions. The latter would be the arrangement of boundary conditions considered in this manuscript. We give the proof for a one-dimensional problem in appendix C.

2.1.2 Biot's equations

For porous materials of which the frame cannot be assumed motionless, Biot's equations are needed to describe simultaneously the dynamic behaviour of solid frame and poro-fluid by coupling response. As introduced in chapter 1, several formulations of Biot's theory exist with different field variables. In this manuscript, the $(\mathbf{u}^s, p^f)$ mixed formulation proposed by Atalla et al., 1998 [42] is chosen to model the acoustic behaviour of PEMs. One advantage of using this mixed formulation rather than others is that the demanded *dofs* per nodes is reduced to three/four instead of four/six in two/three-dimensional problems when solved using element-based numerical methods.

This formulation is expressed with solid displacement $\mathbf{u}^s$ and poro fluid pressure p^f as:

$$\nabla.\hat{\sigma}(\mathbf{u}^s) = -\omega^2\tilde{\rho}\mathbf{u}^s - \tilde{\gamma}\nabla p^f, \tag{2.8a}$$

$$-\Delta p^f = -\omega^2\tilde{\rho}_{\mathrm{eq}}\tilde{\gamma}\nabla.\mathbf{u}^s + \omega^2\frac{\tilde{\rho}_{\mathrm{eq}}}{\tilde{K}_{\mathrm{eq}}}p^f, \quad \text{on } \partial\Omega \tag{2.8b}$$

with the constitutive equation between fluid pressure and total displacement:

$$p^f = -\tilde{K}_{\mathrm{eq}}.\boldsymbol{\nabla} u^t, \tag{2.9}$$

in which u^t denotes the total displacement of the material. $\hat{\sigma}$ is the in-vacuo stress of the skeleton. The coefficients $\tilde{\rho}$, $\tilde{\rho}_{\mathrm{eq}}$, $\tilde{K}_{\mathrm{eq}}$ and $\tilde{\gamma}$ are the effective density of the solid phase, the effective density and compressibility of the fluid phase and coupling parameter, respectively. The first Biot equation eq. (2.8a) without the coupling term corresponds to a harmonic dynamic equation of elastic displacement (elastodynamics), and the corresponding terms eq. (2.8b) is the Helmholtz equation as eq. (2.1). The interaction between two phases is linked by the coupling term with $\tilde{\gamma}$. Effective coefficients $\tilde{\rho}_{\mathrm{eq}}$ and $\tilde{\gamma}$ are calculated with the last four parameters in table 2.1 (detailed procedure see appendix B).

Note that the physical parameters appearing in equations above are slightly modified compared to the original one in Atalla et al., 1998 [42] and Allard and Atalla, 2009 [29], which leads readily to a natural coupling condition for acoustic fluids and other PEMs.

Regarding boundary conditions, besides of the conditions given in the Helmholtz equation, more other conditions should be imposed because of the existance of solid phase. Dirichlet condition will include as well the imposition of displacement on solid frame $\mathbf{u}^s$. Normal component of total displacement as well as the normal stress in-vacuo will be added for Neumann boundary conditions. A complete description of other boundary and coupling conditions for this Biot's equations can be found in Debergue et al., 1999 [146].

Specifically, in Biot's model, when one assumes the stiffness of the frame is negligible ($\hat{\sigma}^s \approx 0$), it results in a particular model. This model can be considered as a corrected equivalent fluid model where the inertia effects of frame is accounted into the effective density such that:

$$\tilde{\rho}_{\text{Limp}} = \frac{\tilde{\rho}\tilde{\rho}_{\text{eq}}}{\tilde{\rho} + \tilde{\rho}_{\text{eq}}\tilde{\gamma}^2}, \tag{2.10}$$

where $\tilde{\rho}$ takes the density of solid phase into consideration in Biot's theory (detail see appendix B). This is the so-called Limp model (Panneton, 2007 [37]).

2.2 Traditional numerical methods

2.2.1 Finite Element Method (FEM)

Variational formulations

Within finite element method, one searches for the solution of variational formulations rather than original governing equations [1]. Therefore, the weak formulations associated with former presented Helmholtz equation and Biot's mixed equations need to be derived first. These formulations are defined as well in the domain Ω shown fig. 2.1. To distinguish the features of the different boundaries, instead of $\partial\Omega$ for the pure exterior boundaries, Γ is used to represent the boundaries (surfaces) that will potentially be combined with other media.

For the Helmholtz equation, we multiply eq. (2.1) by a test function q^f associated with fluid pressure and apply the Green's formula on the domain, the variational formulation is thus written as follows: find $p^f \in H^1(\Omega)$ such that

$$\underbrace{\frac{1}{\omega^2\rho}\int_\Omega \nabla\bar{q}^f.\nabla p^f \mathrm{d}\Omega - \frac{1}{K}\int_\Omega \bar{q}^f p^f \mathrm{d}\Omega}_{a_B} \underbrace{- \int_\Gamma \bar{q}^f u_n^t \mathrm{d}S}_{a_I} = \underbrace{\int_{\partial\Omega} \bar{q}^f u_n^t \mathrm{d}S}_{\ell}, \quad \forall q^f \in H^1(\Omega), \tag{2.11}$$

with normal component of total displacement u_n^t for the fluid defined as:

$$u_n^t = \frac{1}{\omega^2\rho}\frac{\partial p^f}{\partial n}, \tag{2.12}$$

[1] Strong form

where materials properties ρ and K can be real numbers for classical acoustic fluids or can be complex numbers for energy damping materials such as porous materials. We define $\boldsymbol{a_B}$, $\boldsymbol{a_I}$ and $\boldsymbol{\ell}$ to stand for bulk bilinear form, interface and boundary linear forms, respectively. The interface term $\boldsymbol{a_I}$ and right-hand side term $\boldsymbol{\ell}$ are actually the same linear form defined on different boundaries (surfaces). It is seen that the material constants (ρ and K) are rewritten instead of using wave-number k, which makes the coupling at the interface Γ with Biot mixed formulation easier.

When it comes to the mixed Biot formulation, it concerns two primal variables: poro-fluid pressure and displacement of solid frame, respectively. The variational formulation corresponding to eq. (2.8) therefore involves two test functions $\bar{\mathbf{v}}^s$ and $\bar{q}^f$ as follows: find $\mathbf{u}^s$, $p^f \in H^1(\Omega)$, such that

$$\begin{aligned}\underbrace{\int_\Omega \hat{\sigma}^s_{ij}(\bar{\mathbf{v}}^s)\epsilon^s_{ij}(\mathbf{u}^s)\,\mathrm{d}\Omega - \omega^2\int_\Omega \tilde{\rho}\bar{\mathbf{v}}^s_i\mathbf{u}^s_i\,\mathrm{d}\Omega - \int_\Omega \tilde{\gamma}\bar{\mathbf{v}}^s_i\nabla p^f\,\mathrm{d}\Omega}_{\boldsymbol{a_B}} \underbrace{- \int_\Gamma \bar{\mathbf{v}}^s_i\boldsymbol{n}_j\hat{\sigma}^s_{ij}(\mathbf{u}^s)\,\mathrm{d}S}_{\boldsymbol{a_I}} \\ = \underbrace{\int_{\partial\Omega} \bar{\mathbf{v}}^s_i\boldsymbol{n}_j\hat{\sigma}^s_{ij}(\mathbf{u}^s)\,\mathrm{d}S}_{\boldsymbol{\ell}}\,, \forall\mathbf{v^s} \in H^1(\Omega),\end{aligned} \tag{2.13a}$$

$$\begin{aligned}\underbrace{\int_\Omega \left[\frac{1}{\omega^2\tilde{\rho}_{\mathrm{eq}}}\nabla\bar{q}^f.\nabla p^f - \frac{1}{\tilde{K}_{\mathrm{eq}}}\bar{q}^f p^f\right]\mathrm{d}\Omega - \int_\Omega \tilde{\gamma}\nabla\bar{q}^f\mathbf{u}^s_i\,\mathrm{d}\Omega}_{\boldsymbol{a_B}} \underbrace{- \int_\Gamma \bar{q}^f u^t_n\,\mathrm{d}S}_{\boldsymbol{a_I}} \\ = \underbrace{\int_{\partial\Omega} \bar{q}^f u^t_n \mathrm{d}S}_{\boldsymbol{\ell}}, \quad \forall q^f \in H^1(\Omega),\end{aligned} \tag{2.13b}$$

where the normal component of the total displacement u^t_n stems from the term in Atalla et al., 1998 [42] and Allard and Atalla, 2009 [29], and is defined as:

$$u^t_n = \tilde{\gamma}u^s_n - \frac{1}{\omega^2\tilde{\rho}_{\mathrm{eq}}}\frac{\partial p^f}{\partial n}, \tag{2.14}$$

which represents the relative motion between solid frame and poro-fluid.

It is emphasized that in above given variational formulations eqs. (2.11) and (2.13), symbol $\bar{\bullet}$ denotes complex conjugate. For complex-valued problems, the *sesquilinear* forms are commonly written instead of classical bilinear forms. However, for the formulations appearing in the following manuscript, this conjugate may be removed to simplify slightly the expressions.

High-order FEM approximation

As is customary with the finite element method, the computational domain $\Omega \in \mathbb{R}^{2-3}$ on which the previous variational formulations are defined needs to be discretized into elements Ω_e, constituting a mesh.

The general vector field $\mathbf{u}(\mathbf{x})$ is obtained numerically by a polynomial approximation on each element Ω_e:

$$\mathbf{u}(\mathbf{x})|_{\Omega_e} = \sum_{i=1}^{n} \mathbf{N}_i(\mathbf{x}) u_i \ , \tag{2.15}$$

where n is the number of the degree of freedom on the element, u_i is the ith nodal contribution of this approximation, $\mathbf{N}_i(\mathbf{x})$ represents the ith shape function associated with u_i, which usually is a piecewise polynomial basis.

As aforementioned in chapter 1, one might encounter convergence issues due to the pollution effects for high frequency in dynamic equations and large disparity of scale between two primal variables in Biot's equations. To overcome these problems, *high-order* polynomials are preferred to be used as shape functions $\mathbf{N}$.

Two approaches can be used to increase the order of the shape functions. First one is to introduce more internal nodes in the elements, which corresponds to for example, high-order Lagrange functions. Another is to use a modal expansion of the existing nodes, we call it modal contribution. Considering the computational efficiency and *conditioning* (Prinn, [76]) of the linear system, Lobatto and Bernstein modal polynomials rather than classical Lagrange nodal polynomials are used in this manuscript.

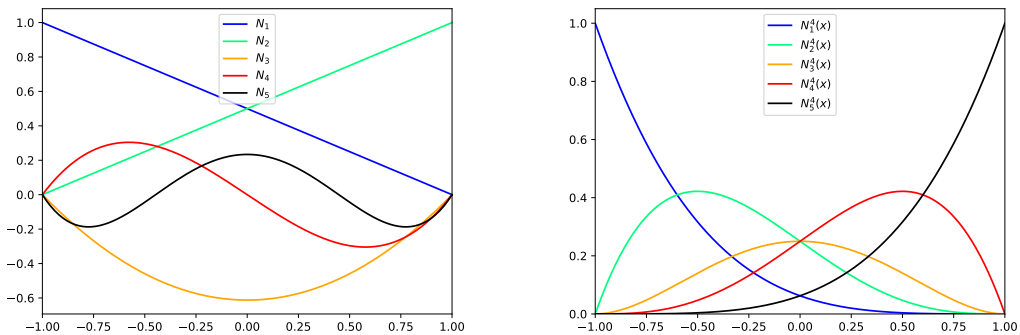

(a) (b)

Fig. 2.2.: Example of shape function in 1D for (a) Lobatto and (b) Bernstein of order $p = 4$.

Fig. 2.2 depicts these two types of shape functions for order $p = 4$ in a one-dimensional reference element $\xi \in [-1, 1]$. One can clearly see that three functions are zero at both external nodes and non-zero inside the element, which are so-called bubble functions. The bubble shape function can be removed from the final linear system using static condensation (Melenk, 2002 [147]) before solution procedure, which reduces considerably the size and improves the conditioning of system while keeping the accuracy.

2.2.2 Transfer matrix for porous materials

Instead of solving the variational formulations, Transfer matrix Method (TMM) provides an algebraic representation of field variables controlled by the governing equations. This method rewrites the solutions on the two sides of a layer satisfying the governing equations under the assumption of plane wave.

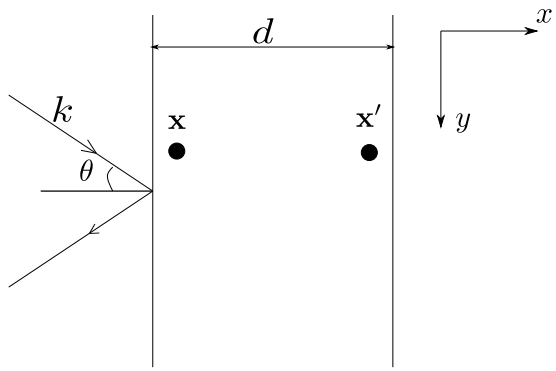

Fig. 2.3.: General plane wave incident in a lateral infinite domain.

A typical plane wave configuration is depicted as fig. 2.3 where a wave impinges upon a medium of thickness d with an incident angle θ. The medium is considered as lateral infinite, therefore the y component of the wave number k_y for each wave propagating in the finite medium is equal to the corresponding component of the incidents wave in the free air:

$$k_y = k\sin(\theta), \tag{2.16}$$

in which k denotes the wave number in free air. A relationship of state vectors $\mathbf{s}(\bullet)$ between the two sides of the layers is established by a so-called transfer matrix $[\mathbf{T}]$ as:

$$\mathbf{s}(\mathbf{x}) = [\mathbf{T}]\mathbf{s}(\mathbf{x}'), \tag{2.17}$$

where $\mathbf{x}$ and $\mathbf{x}'$ are coordinates close to the forward and the backward face of the layers, and the state vector $\mathbf{s}(\bullet)$ includes variables that represent the acoustic field:

$$\mathbf{s}(\mathbf{x}) = \{u(\mathbf{x}), \widetilde{u}(\mathbf{x})\}^T, \tag{2.18}$$

indeed, u and $\widetilde{u}$ correspond to the primal and secondary variables in variational formulations of the media, respectively. In two-dimensional problems, the number of variables in the state vector is equal to *2m* (*m* being the number of waves, that depends on the nature of media).

It is worth noting that, unlike the asymptotic model proposed by Bövik, 1994 [60] or the pressure drop model Pierce, 1989 [59], this relationship fulfils the governing equations, no simplification is made in the method. Coefficients in $[\mathbf{T}]$ are functions of the thickness d,

physical properties and incident angle θ, of which the incident angle is normally known *a priori* for the sound is excited by a plane wave. For a complex sound field where plane wave assumption is not satisfied, the choice of incident angle θ have significant influence if one still want to use TMM to represent acoustic solutions. This aspect will be visited further in chapter 5.

Concerning the TMM for equivalent fluid and PEMs, two state vectors and transfer matrices are specified here for two types of governing equations.

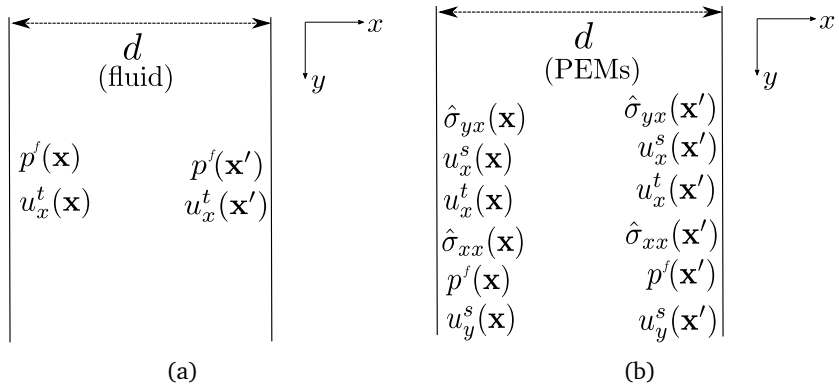

Fig. 2.4.: (a) State vectors for fluid-like media (b) state vectors for PEMs.

The state vector $\mathbf{s}^f$ for materials modelled as fluid is of length two, since only one wave propagates in the media. As shown in fig. 2.4(a), pressure p^f and normal (x-component in our geometric representation) total fluid displacement (velocity) u_n^t of fluid at the interface are primal field and secondary variables (the function of its gradient):

$$\mathbf{s}^f(\mathbf{x}) = \{p^f(\mathbf{x}),\ u_{x(n)}^t(\mathbf{x})\}^T. \tag{2.19}$$

Thus, we have a 2×2 transfer matrix $[\mathbf{T^f}]$ for the layer modelled as a fluid.

For PEMs governed by the mixed Biot's equations, there exists three waves. Six quantities are thus required to represent the solution in the layers, as shown in fig. 2.4(b). The state vector for the considered PEMs $\mathbf{s}^P(\mathbf{x})$ reads:

$$\mathbf{s}^P(\mathbf{x}) = [\hat{\sigma}_{yx}(\mathbf{x}), u_x^s(\mathbf{x}), u_{x(n)}^t(\mathbf{x}), \hat{\sigma}_{xx}(\mathbf{x}), p^f(\mathbf{x}),\ u_y^s(\mathbf{x})]^T, \tag{2.20}$$

where u_x^s and u_y^s are the two components of the displacement of the elastic frame which are the primal field variables, $\hat{\sigma}_{yx}$ and $\hat{\sigma}_{xx}$ correspond to the normal and shear in-vacuo stresses of the solid phase denoting the secondary variables in PEMs. Together with fluid pressure and normal total displacement, three primal and three secondary variables are obtained. With this state vector, the transfer matrix for the PEMs layer is of size 6×6 and denoted as $[\mathbf{T^P}]$.

It is seen that the dimension of the transfer matrices is decided by the nature of the media, while the coefficients and their value in the transfer matrices $[\mathbf{T^f}]$ and $[\mathbf{T^P}]$ depend on the

specific material model. Here, the instance of these two matrices are given, which will also be used directly in the following works.

The transfer matrix $[\mathbf{T^f}]$ for an equivalent fluid JCA layer of thickness d is given as:

$$[\mathbf{T^f}] = \begin{bmatrix} \cos(k_{\mathrm{eq}x}d) & \mathrm{j}\frac{\omega\tilde{\rho}_{\mathrm{eq}}}{k_{\mathrm{eq}}}\sin(k_{\mathrm{eq}x}d) \\ \mathrm{j}\frac{k_{\mathrm{eq}x}}{\omega\tilde{\rho}_{\mathrm{eq}}}\sin(k_{\mathrm{eq}x}d) & \cos(k_{\mathrm{eq}x}d) \end{bmatrix}, \tag{2.21}$$

where $k_{\mathrm{eq}x}$ is the equivalent wave number along x direction (it would be the normal components at the interface). As seen that, the thickness of media d is considered in the matrix. For the Limp model, as mentioned before, only the effective density is changed to eq. (2.10), and the structure of the matrix is retained. Readers keep in mind that the structure and the determinant of these matrices have significant effects for computational models proposed in chapter 5, which will be discussed and refined at that chapter.

The transfer matrix for Biot's model $[\mathbf{T^P}]$ associated with the state vector (2.20) in this manuscript is extracted from the previous work (Dazel et al., 2013 [70]) which gives a complete description for stratified PEMs layers in two dimensions:

$$[\mathbf{T^P}] = \exp(-d\alpha), \tag{2.22}$$

with state matrix α is specified as:

$$\alpha = \begin{bmatrix} 0 & 0 & 0 & \mathrm{j}k_y\frac{\hat{A}}{\hat{P}} & \mathrm{j}k_y\tilde{\gamma} & -\frac{\hat{A}^2-\hat{p}^2}{\hat{p}}k_y^2 - \tilde{\rho}\omega^2 \\ 0 & 0 & 0 & \frac{1}{\hat{P}} & 0 & \mathrm{j}k_y\frac{\hat{A}}{\hat{P}} \\ 0 & 0 & 0 & 0 & -\frac{1}{\tilde{K}_{\mathrm{eq}}} + \frac{k_y^2}{\tilde{\rho}_{\mathrm{eq}}\omega^2} & -\mathrm{j}k_y\tilde{\gamma} \\ \mathrm{j}k_y & -\tilde{\rho}_{\mathrm{s}}\omega^2 & -\tilde{\rho}_{\mathrm{eq}}\tilde{\gamma}\omega^2 & 0 & 0 & 0 \\ 0 & \tilde{\rho}_{\mathrm{eq}}\tilde{\gamma}\omega^2 & \tilde{\rho}_{\mathrm{eq}}\omega^2 & 0 & 0 & 0 \\ 1/\hat{N} & \mathrm{j}k_y & 0 & 0 & 0 & 0 \end{bmatrix}, \tag{2.23}$$

where k_y represents a vertical wave number in the layer under the dependence of $e^{-\mathrm{j}k_y y}$. Other materials' parameters present in the matrix are associated with JCA models and Biot's theory.

All presented formulations and transfer matrices will be employed for the forthcoming chapters to represent the sound behaviours of different types of acoustic media in different problems of interest.

2.3 eXtended Finite Element Method (X-FEM) for interface problems

When there is an interface between two materials, the classical finite-element method requires a mesh that conforms to the interface in order to obtain the optimal rate of the convergence [111]. As mentioned, X-FEM is used in this thesis to alleviate the burden of mesh generation as in the classical FEM, allowing the boundary of geometries to be independent of the elements.

Before presenting the detailed aspects on X-FEM, the representation of geometries is first introduced. In this section, the application of X-FEM is restricted to the interface relevant problems, presenting approximation and enrichments. For other types of problems, different techniques and strategies may be used, but they will not be discussed in this manuscript.

2.3.1 Level-set function and implicit interface

As the interface is no longer described explicitly through the boundary of a conforming mesh, one needs to define the geometry implicitly, independent of the mesh. The most used technique incorporated with X-FEM is the Level-set method, which was initially developed by Osher and Sethian, 1988 [148] to track moving interfaces. It represents the geometry with the help of one dimension higher function $\phi(\mathbf{x})$. Here, we only consider a static interface, which is independent of time t. With the level-set function, the interface Γ is located as the iso-zero curve of ϕ:

$$\Gamma = \{\mathbf{x} \in \mathbb{R}^2 : \phi(\mathbf{x}) = 0\}. \tag{2.24}$$

For example, if the interface corresponds to a circle of radius R, the level-set function reads as:

$$\begin{aligned} \phi(\mathbf{x}) &= x^2 + y^2 - R^2 \\ \Gamma &= \{x, y \in \mathbb{R}^2 | x^2 + y^2 = R^2\}. \end{aligned} \tag{2.25}$$

In practice, such analytical function does not exist for all the geometries, one conventionally construct the level-set function using signed distance function as:

$$\phi_i(\mathbf{x}) = \pm \min_{\mathbf{x}_\Gamma \in \Gamma} \|\mathbf{x}_i - \mathbf{x}_\Gamma\|, \tag{2.26}$$

where $\|\bullet\|$ denotes the Euclidean norm. $\mathbf{x}_i$ are the points in the domain and $\mathbf{x}_\Gamma$ are the set of coordinates on the interface Γ. Still for the circle, one can define a series of circular interfaces with a signed distance function as:

$$\phi_i(\mathbf{x}) = \min_{x_c^i \in \Omega_c^i} \left\{ \left\| \mathbf{x} - \mathbf{x}_c^i \right\| - R_c^i \right\}, \tag{2.27}$$

where Ω_c^i is the domain of the ith circle. $\mathbf{x}_c^i$ and R_c^i are the center and radius of the ith circle, respectively. Boolean operators such as `union` and `intersection`, transformation operator as `translation`, `rotation` and `scaling` can be used for different level-set functions to construct more complicated geometries. In addition, complex geometries can be also obtained by merging the existing images or CAD models by level-set segmentation (Legrain et al., 2011 [149]). We illustrate an example of level-sets with iso-value contour in fig. 2.5, where a single circle and an `union` of two circles are represented.

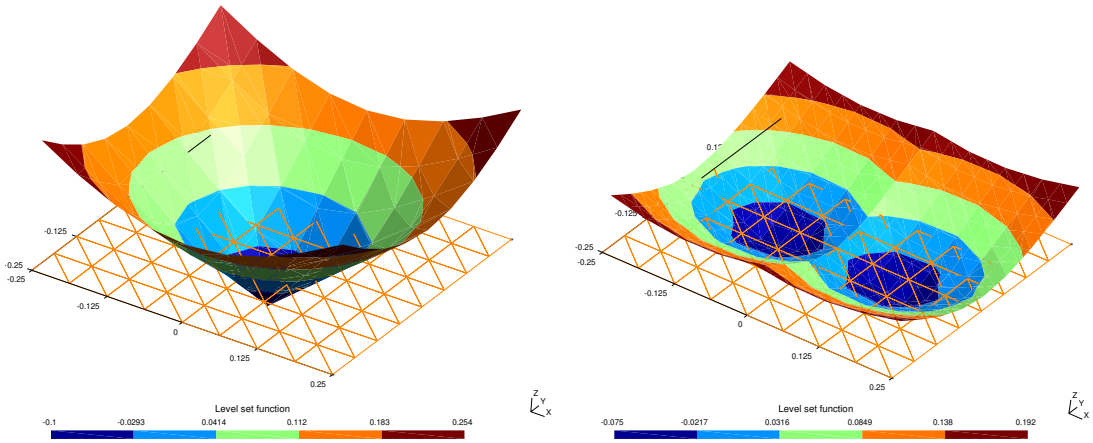

(a) (b)

Fig. 2.5.: (a) A circular level-set function of radius $r = 0.1$ defined a structured grid of 0.5×0.5 with its iso-value coutour, (b) level-set of the union of two circles.

With the help of the sign of the level-set function, the computational domain is then classified that the sign is positive (negative) for all $\mathbf{x}$ inside (outside) $\Omega^{+/-}$ the contour of geometries as:

$$\begin{cases} \mathbf{x} \in \Omega^+ & \phi(\mathbf{x}) > 0 \\ \mathbf{x} =\in \Gamma & \phi(\mathbf{x}) = 0 \\ \mathbf{x} \in \Omega^- & \phi(\mathbf{x}) < 0. \end{cases} \tag{2.28}$$

Intersection of multiple interfaces in the domain, combination of signs can be used to identify the subdomain.

When level-set functions defined on the FE mesh, this smooth function is converted to a discrete functional. The geometrical degrees of freedom at FE nodes are used to determine $\phi(\mathbf{x})$ and the location of interface. The discrete level-set function is interpolated with classical finite element shape functions as:

$$\phi(\mathbf{x}) = \sum_i^n N_i(\mathbf{x})\phi_i, \tag{2.29}$$

where $N_i(\mathbf{x})$ are conventionally the piecewise linear shape functions, and ϕ_i are the signed distances from finite element nodes to the interface. It is noted that such definition of level-set on FE mesh could generate a geometric difference between analytical smooth function and discrete piecewice function. The influence and the proposed solutions for this difference will be discussed soon in next subsection.

2.3.2 Solution approximation with X-FEM

When the material interfaces embedded in the elements, one have potentially kinks (C^0) or jumps (C^{-1}) inside finite elements. In contrast, the classical FEM are generally at least C^1 on the elements and C^0 between elements, which is not able to capture such discontinuous features exactly. Therefore, to represent the solution appropriately, we work on an extended finite element space $\mathcal{U}_h^{XFE}$, enlarging the standard FE space with an additional enriched one such that:

$$\mathcal{U}_h^{XFE} = \mathcal{U}_h^{FE} \oplus \mathcal{U}_h^{ENR}, \tag{2.30}$$

where $\mathcal{U}_h^{FE}$ is classical FE approximation space, and $\mathcal{U}_h^{ENR}$ represents the enriched space. Let us consider a general vector field $\mathbf{u}(\mathbf{x})$, which is approximated in such discrete space as:

$$\mathbf{u}(\mathbf{x})|_{\Omega_e} = \sum_{i=1}^{n} \mathbf{N}_i(\mathbf{x}) u_i + \sum_{j=1}^{n_{\text{enr}}} \mathbf{N}_j(\mathbf{x}) \varphi(\mathbf{x}) a_j \ , \tag{2.31}$$

where n and n_{enr} are the number of standard and enriched finite element nodes. N_i are the classical finite element shape function. a_j is the additional contribution (dofs) for enriched node j, $\mathbf{N}_j(\mathbf{x})$ are shape functions from a basis fulfilling the partition of unity (PU Melenk and Babuška, 1996 [89]), that:

$$\sum_{j=1}^{n_{enr}} \mathbf{N}_j(\mathbf{x}) = 1, \tag{2.32}$$

for which, classical finite element shape functions can be considered. It is noticed that the number of enriched *dofs* $n_{\text{enr}} \ll n$, since the enrichment part is only defined on the entities (nodes) associated to elements intersecting with the interface. The total number of *dofs* of the discretization in X-FEM will not substantially increase compared to interface-fitted mesh.

It is emphasized that, hierarchical Lobatto and Bernstein shape functions lead to different elementary matrices in terms of algebraic property when combined with enrichment functions in X-FEM. It results in a different algebraic treatment when some specific elementary metrics are evaluated. This nuance will be highlighted and discussed in the chapter 4.

The function $\varphi(\mathbf{x})$ represents the enrichment function, which complements the polynomial approximation to represent some complex behaviour such as a discontinuity in the element. The choice of enrichment is to be presented in next subsection.

Based on these notions, the computational domain within X-FEM is typically discretized as shown in fig. 2.6 for a triangular structured mesh, which is divided into standard elements (write elements), fully enriched elements (deep green) and partially enriched elements (light green) called blending elements. It is worth noting that the enriched elements are partitioned into sub-elements, which is to facilitate the modified numerical integration (Sukumar et al., 2001 [110]) in the cut elements.

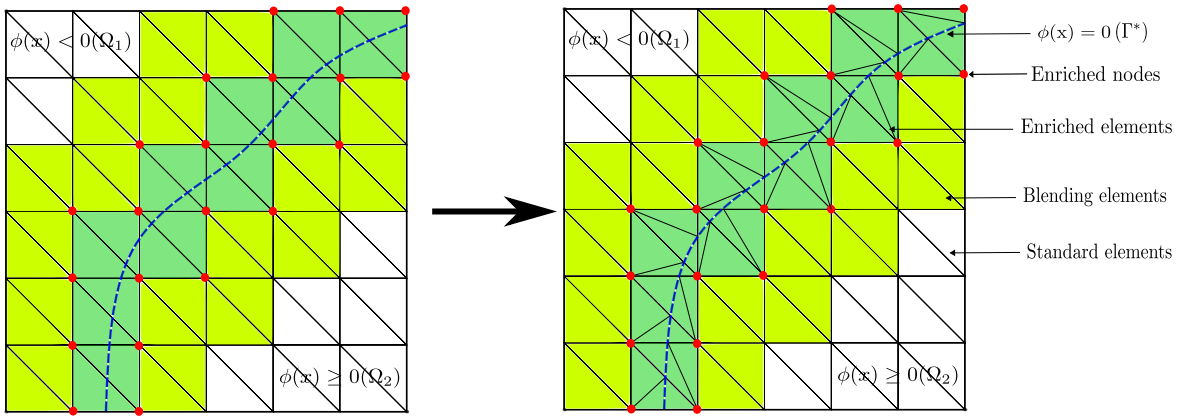

Fig. 2.6.: 2D representation for X-FEM based computational domain.

Geometric errors within high-order X-FEM

The solution is approximated with high order shape functions. However, as mentioned earlier, the interface is interpolated with piecewise linear shape functions, which produces a gap between analytical and discrete level-set for curved geometries (see fig. 2.7(a)). This geometric error will become more important compared to the approximation error when higher order elements are used, which hampers the solution from obtaining optimal rate of convergence (see Dréau et al., [150] and Legrain et al., 2012 [151]). A series of solution have been proposed such as high-order level-sets (Komijani and Gracie, 2019 [152], Legay et al., 2005 [153] and Stazi et al., 2003 [112]), sub-grid level-sets in Dréau et al., [150] (see a resume in Legrain et al., 2012 [151]) and high order isoparametric mapping proposed by Lehrenfeld, 2016 [154].

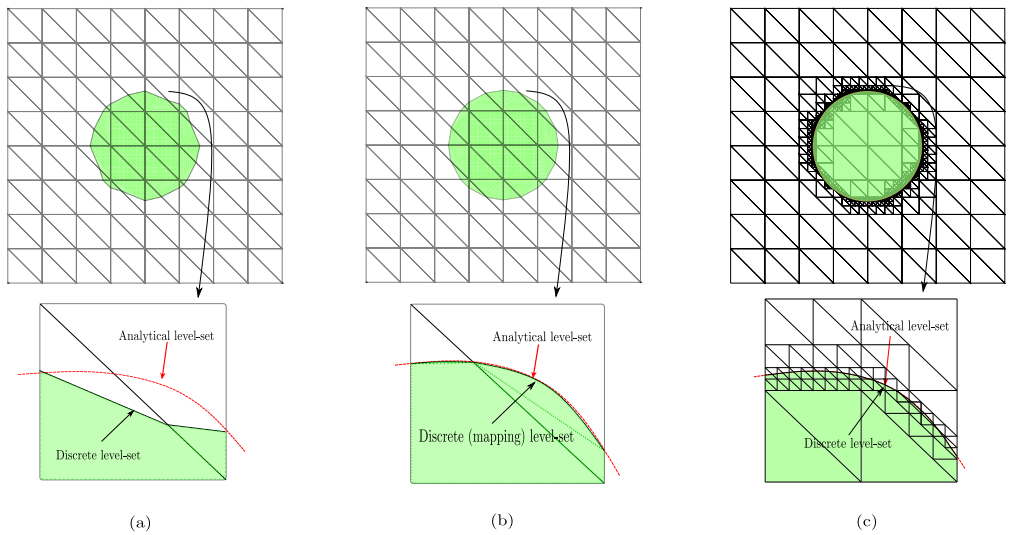

Fig. 2.7.: (a) Linear Level-set interface; (b) NURBS enhanced interface; (c) Sub-grid Level-set interface. with zoomed elements.

In this thesis, the NURBS-enhanced (Legrain, 2013 [155]) interface, and uncoupled sub-grid (Legrain et al., 2012 [151]) strategies are adopted to tackle the geometrics issue. The first one

replaces the interface defined by linear interpolated level-set function by exact CAD NURBS curves defined in sub-elements (see fig. 2.7(b)). The second strategy defines the interface on an adaptively refined (Octree) mesh as in fig. 2.7(c), while the high-order solution is still approximated on a coarse uniform mesh (as shown fig. 2.7(a)). The analytical level-set functions are seen to be much better described with NURBS enhanced and sub-grid strategies using the same coarse background mesh in comparison with linear level-set interface.

2.3.3 Enrichment

The flexibility of the X-FEM benefits majorly from the enrichment function. Different types of enrichment function provide different features of discontinuity as crack (Moës et al., 1999 [109]), hole (Sukumar et al., 2001 [110]) and material interface (Moës et al., 2003 [111]). In our considered problems, the solution at the interface could be strongly/weakly discontinuous [2]. Weak discontinuity represents the natural transition between different materials, and the strong one could represent some pressure jump between acoustic media which will be introduced in section 4.1.

For a perfect materials interface, the weak discontinuity occurs in the elements. A continuous function with a discontinuous derivative should be used. "Ridge" function as the most used enrichment for perfect materials interface is chosen in this manuscript, which was first proposed in Moës et al., 2003 [111]. This enrichment function is constructed with the help of the level-set function ϕ that we defined before:

$$R(\mathbf{x}) = \sum_i |\phi_i| N_i(\mathbf{x}) - \left| \sum_i \phi_i N_i(\mathbf{x}) \right| . \tag{2.33}$$

The different terms involved in the definition of the enrichment function $R(x)$ are depicted in 1D (see fig. 2.8(a)), and a two-dimenstional illustration is given in fig. 2.8(b). One can observe that the ridge function vanishes on the non-enriched elements, which leads to a good conditioning of the matrix system (Moës et al., 2003 [111]), contrary to other enrichment functions proposed in Sukumar et al., 2001 [110], Chessa and Belytschko, 2003 [156]. If the mesh conforms to the interface profile, this X-FEM recovers to the classical FEM since no node is enriched.

Another used enrichment function is the generalized Heaviside functions, such that:

$$H(\mathbf{x}) = \begin{cases} 1 & \phi(\mathbf{x}) \geq 0 \\ -1 & \phi(\mathbf{x}) < 0. \end{cases} \tag{2.34}$$

This enrichment introduces a jump in the field across the interface. As a strong discontinuity is added, one necessitates additional enforcement to regain the weak discontinuity for the perfect

[2] gradient of field is discontinuous

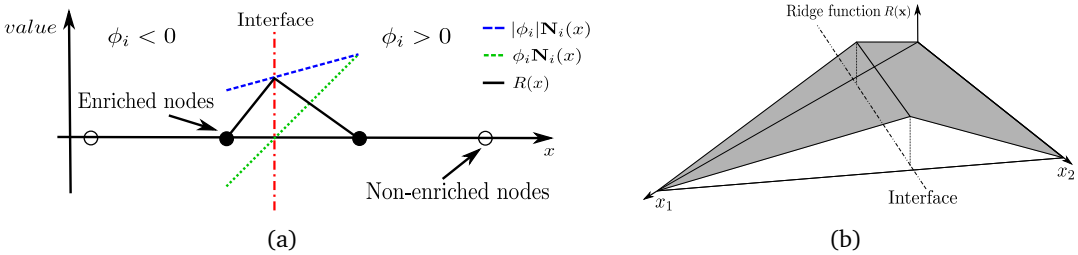

Fig. 2.8.: Level set and ridge enrichment function (a) Definition in 1D, (b) Illustration on a 2D triangular element.

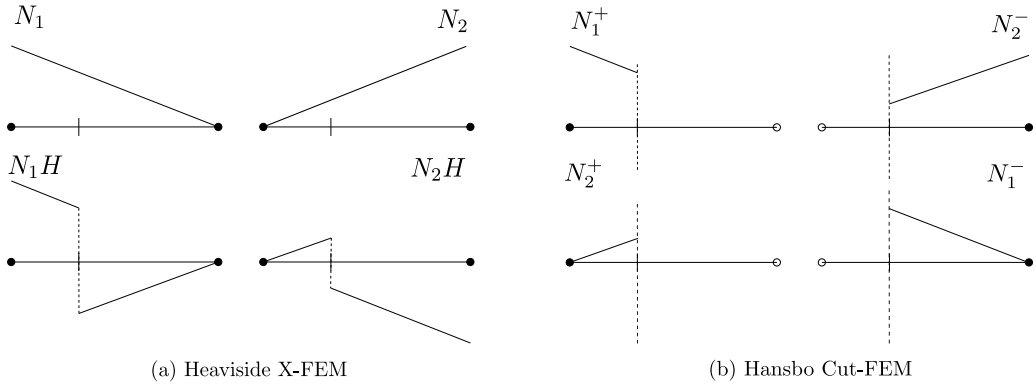

Fig. 2.9.: 1D example of linear elements for Heaviside X-FEM and Hansbo's Cut-FEM of the strong discontinuity.

material interface or to represent specific interface conditions. To this end, various techniques can be used such as Lagrange multiplier (Babuška, 1973 [127]), penalty method (Babuška, 1973 [126]) and Nitsche's approach (Nitsche, 1971 [132])(they will be presented in detail in the following subsection). Note that in the case of a mesh conforming with the interface, the Heaviside enriched X-FEM retrieves an identical approximation as overlapping double nodes in the classical FEM.

X-FEM vs. Cut-FEM

When discussing the Heaviside enriched X-FEM, the Cut-FEM (Burman et al., 2015 [124]) is inevitably brought up at the same time. In fact, the latter one is usually being confused with X-FEM in the literature because of its similarity concerning the resulting approximation space as with X-FEM. The Cut-FEM can be considered as an overlapping of standard finite elements across the interface, which is seen as the reparametrization of the Heaviside enriched X-FEM. Indeed, these two approaches were proven to span the same approximation space in Areias and Belytschko, 2006 [157]. However, the structure of the resulting algebraic matrices are not identical. This distinction will lead to different manipulations to calculate some element-wise quantities, such as the stability parameters in Nitsche's formulation (demonstrated in chapter 4).

We depict the comparison of these two bases in fig. 2.9 for the example of a linear 1D element. It can be seen that functions N_i^+ and N_i^- in Cut-FEM represent the classical shape functions on each side of the interface, which are independent of the one to the other side. However, within X-FEM, all four shape functions (two standard with two enriched) are involved on both sides to approximate the solution.

When the degrees of freedom are arranged in a specific order, the two bases can be linked with each other by an elegant relationship, such that:

$$\begin{Bmatrix} N_1^+ \\ N_2^+ \\ N_1^- \\ N_2^- \end{Bmatrix} = \frac{1}{2} \begin{bmatrix} 1 & 0 & 1 & 0 \\ 0 & 1 & 0 & 1 \\ 1 & 0 & -1 & 0 \\ 0 & 1 & 0 & -1 \end{bmatrix} \begin{Bmatrix} N_1 \\ N_2 \\ N_1 H \\ N_2 H \end{Bmatrix}, \tag{2.35}$$

which can be re-expressed in a general form that allows one to extend to any arbitrary high order basis as:

$$\begin{Bmatrix} \mathbf{N}^+ \\ \mathbf{N}^- \end{Bmatrix} = [\mathbf{T}] \begin{Bmatrix} \mathbf{N} \\ \mathbf{NH} \end{Bmatrix}, \tag{2.36}$$

with a transition matrix $[\mathbf{T}]$:

$$\mathbf{T} = \frac{1}{2} \begin{bmatrix} \mathbf{I} & \mathbf{I} \\ \mathbf{I} & -\mathbf{I} \end{bmatrix}, \tag{2.37}$$

where $\mathbf{I}$ are the identity matrices. This relation allows converting discrete quantities (elementary matrix structure) from one basis to the others, in order to take the most advantage of each basis in different circumstance. Interested readers are recommanded to refer to Areias and Belytschko, 2006 [157] and Menouillard et al., 2008 [158] on other details of equivalence and relationship between two bases. We will use this transition of basis in the chapter 4.

2.3.4 Imposition of boundary conditions in X-FEM

When geometries are embedded inside elements, boundary/interface conditions need to be imposed weakly in the variational formulation. Lagrange multiplier, penalty and Nitsche's method are three mainstream approaches to this aim. This subsection is devoted to explaining basic ideas and providing a first impression of what these methods are like so that readers is able to better understand our methods proposed in the following chapters. The links, benefits and drawbacks between them will also be discussed.

For the sake of simplicity and generality, a Laplacian problem is considered to formulate the problem, The energetic description is used to derive the variational formulation. Let consider a strong form in Ω:

$$\begin{cases} \Delta u + f = 0 \quad \forall u \in \Omega \\ \nabla u.\mathbf{n} = 0 \quad \text{on } \Gamma_N \\ u = u_D \quad \text{on } \Gamma_D, \end{cases} \tag{2.38}$$

where Γ_N is boundary of Neumann condition, Γ_D is boundary of Dirichlet condition. We focus on the enforcement of the Dirichlet boundary condition $u = u_D$ and flux-free is assumed for Neumann boundary. Several spaces of interest are clarified:

$$\mathcal{U}_D = \{u \in H^1(\Omega), u = u_D \text{ on } \Gamma_D\}, \tag{2.39a}$$

$$\mathcal{U}_0 = \{u \in H^1(\Omega), u = 0 \text{ on } \Gamma_D\}, \tag{2.39b}$$

$$\mathcal{U} = \{u \in H^1(\Omega)\}. \tag{2.39c}$$

The energetic functional associated with the problem solved on Ω with the previous mentioned boundary conditions, and a source term f writes:

$$J(u) = \frac{1}{2}\int_\Omega \nabla u \nabla u \, d\Omega - \int_\Omega f u \, d\Omega. \tag{2.40}$$

This problem is a constrained minimization problem (Dirichlet constraints), find $u \in \mathcal{U}_D$:

$$u = \arg\min_{v \in \mathcal{U}_0} J(v). \tag{2.41}$$

Thus, the stationarity of the problem writes:

$$\int_\Omega \nabla v \nabla u d\Omega - \int_\Omega v f \, d\Omega = 0, \quad \forall v \in \mathcal{U}_0. \tag{2.42}$$

Remark: if $v \in \mathcal{U}$ that the test function does not vanish at the Dirichlet boundary, the resulting formulation is written:

$$\int_\Omega \nabla v \nabla u d\Omega - \int_{\Gamma_D} v \nabla u.\mathbf{n} d\Gamma - \int_\Omega v f \, d\Omega = 0, \quad \forall v \in \mathcal{U}. \tag{2.43}$$

Actually, this term make the formulation *consistent* in the space of interest, importance of which will be re-visited very soon.

Lagrange multipliers and penalty method

A standard way to transform a constrained minimization problem such $u \in \mathcal{U}_D$ into an unconstrained one is through the use of Lagrange multipliers or penalty method. For the constraint

to be enforced, the system $\mathcal{L}$ may be built by adding the work of the Lagrange multipliers, $\lambda \in \mathcal{L} = \mathcal{H}^{-1/2}(\Gamma_D)$. The energy functional of this problem writes:

$$J^{Lag}(u, \lambda) = J(u) + \int_{\Gamma_D} \lambda(u - u_D) d\Gamma. \tag{2.44}$$

The solution is to find that:

$$(u, \lambda) = \arg\min_{v \in \mathcal{U}} \max_{\lambda^* \in \mathcal{H}^{-1/2}} J^{Lag}(v, \lambda^*). \tag{2.45}$$

The variational formulation is obtained with:

$$\delta J^{\text{Lag}} = 0, \tag{2.46}$$

thus, we have:

$$\int_\Omega \nabla v \nabla u d\Omega + \int_{\Gamma_D} v\lambda d\Gamma - \int_\Omega v f d\Omega = 0, \quad \forall v \in \mathcal{U}, \tag{2.47a}$$

$$\int_{\Gamma_D} \lambda^*(u - u_D) d\Gamma = 0, \quad \forall \lambda^* \in \mathcal{L}. \tag{2.47b}$$

Remark: When the boundary condition is satisfied $u - u_D = 0$ and the Lagrange multiplier is replaced by $\lambda = -\nabla u.\mathbf{n}$, the formulation returns to eq. (2.43). Therefore, one can conclude that formulations with Lagrange multiplier are *variationally consistent* with original problems. Secondly, physical interpretation of the Lagrange multiplier can be seen as the interfacial flux (traction in a mechanical problem) along the essential boundary.

Meanwhile, this method brings up several inconveniences:

1. The dimension of the resulting systems increases. The $dofs$ of enriched nodes are doubled if in the X-FEM.

2. It results in a saddle point problem which precludes an arbitrary choice of the interpolation space for u and λ. In fact, the interpolation spaces for the Lagrange multiplier λ and for the principal unknown u must verify an inf-sup condition (or LBB condition Malkus, 1981 [130]), in order to ensure the convergence of the approximation.

Penalty method can be derived from the previously described Lagrangian formulation. Firstly, Lagrange multipliers λ is physically interpreted as the flux that should be imposed on Γ_D for the Dirichlet boundary condition. Then, it is assumed that the flux can be approximated in a spring-like form: $\nabla u.\mathbf{n} \approx -\beta(u - u_D)$. The energy functional in eq. (2.44) is recast for the penalty method as:

$$J^{pen}(u) = J(u) + \int_{\Gamma_D} \frac{\beta}{2}(u - u_D)^2 d\Gamma, \tag{2.48}$$

where β is the penalty parameter as the spring stiffness. Therefore, the solution is: find $u \in \mathcal{U}$

$$u = \arg\min_{v \in \mathcal{U}} J^{pen}(v). \tag{2.49}$$

Variational formulation of penalty leads to following:

$$\int_\Omega \nabla v \nabla u d\Omega - \int_\Omega v f d\Omega + \beta \int_{\Gamma_D} v(u - u_D) d\Gamma = 0, \quad \forall v \in \mathcal{U}. \tag{2.50}$$

Comparing with eq. (2.43), as seen in formulation above when $v \in \mathcal{U}$, the term $-\int_{\Gamma_D} v \nabla u.\mathbf{n} d\Gamma$ at Dirichlet boundary disappears. The penalty method is no longer *consistent*, despite that it recovers a one-field formulation from Lagrange multiplier. Moreover, the parameter β needs to be very large so that the boundary condition can be enforced very well, which usually could induce an ill-conditioning linear system.

Augmented Lagrange and Nitsche's formulation

In order to recover the consistency and take the convenience of penalty method, augmented Lagrange multiplier was proposed by Heegaard and Curnier, 1993 [159]. Augmented Lagrange multiplier method can be considered as a numerically stable Lagrange method by adding the "penalty term" for enforcing conditions. The energetic functional reads:

$$J^{Aug}(u, \lambda) = J(u) + \int_{\Gamma_D} \lambda(u - u_D) d\Gamma + \int_{\Gamma_D} \frac{\beta}{2}(u - u_D)^2 d\Gamma. \tag{2.51}$$

And, the Nitsche's energetic functional can be straightforwardly obtained by replacing the Lagrange multiplier λ by its physical interpretation $\lambda = -\nabla u.\mathbf{n}$, the formulation cast:

$$J^{Nit} = J(u) - \int_{\Gamma_D} \nabla u.\mathbf{n}(u - u_D) d\Gamma + \int_{\Gamma_D} \frac{\beta}{2}(u - u_D)^2 d\Gamma. \tag{2.52}$$

then, its variational formulation is cast from minimizing the energetic functional as following:

$$\begin{aligned} \int_\Omega \nabla v \nabla u d\Omega - \int_\Omega v f d\Omega - \int_{\Gamma_D} v(\nabla u.\mathbf{n})\, d\Gamma - \int_{\Gamma_D} (\nabla v.\mathbf{n}) u\, d\Gamma + \int_{\Gamma_D} (\nabla v.\mathbf{n}) u_D\, d\Gamma \\ + \beta \int_{\Gamma_D} v(u - u_D)\, d\Gamma = 0, \quad \forall v \in \mathcal{U}, \end{aligned} \tag{2.53}$$

where β is called stability parameter. Because of the existence of consistent term, this stability parameter is not like penalty method to enforce the boundary condition, which only needs to be selected appropriately to ensure the stability of the whole formulation. In addition, Nitsche's method provides a symmetric formulation [3] with the term $\int_{\Gamma_D} (\nabla v.\mathbf{n}) u\, d\Gamma$, which is also an advantage for solving the discrete system.

In this subsection, we present an energetic functional to derive and explain the Nitsche's formulation. This is not the only approach existing in the literature, we cite the work Schillinger et al., 2016 [160] based on concept of Discontinue Galerkin (DG), and a "direct" construction approach used in Hansbo and Hansbo, 2004 [117] and Yedeg et al., 2016 [137], which will also be adopted in chapter 4.

[3] Non-symmetric Nitsche formulation also exists Schillinger et al., 2016 [160].

2.4 Conclusion

This chapter presented in detail all common notation and techniques that are used in the following chapters. In the first part, the governing equations of the fluid-like and PEMs media with their variational formulations and transfer matrices were formulated. The expressions and parameters of formulations are slightly modified compared to the original ones in the literature to make the following derivation more easily.

Key ingredients in the X-FEM framework were later introduced: construction of level-set functions and implicit interfaces, enrichment space and solution for geometric errors. The readers should keep in mind that there exists differences in terms of algebraic system when using different polynomials and enrichment functions. The difference and transition between high-order Heaviside enriched X-FEM and Cut-FEM were also presented, which can be considered as one minor contribution in this thesis. All these numerical aspects will be addressed and highlighted in the following chapters. Three mainstream numerical approaches to enforce the boundary/interface conditions have been presented and discussed. Compared to the Lagrange multiplier and penalty method, Nitshche's method should be gained more interest because it is a one-field formulation while retaining the numerical stabilization and the physical consistence.

X-FEM for dissipative acoustic problem

3

> *Je pense, donc, je suis.*
>
> — **René Descartes**

In this chapter, the previous presented numerical techniques are firstly applied to solve the dissipative acoustic problems involving the natural material transition or so-called perfect interfaces. This variety of problems is considered as sound absorbing systems introduced in chapter 1 where only thick porous layers is accounted for. This allows to assess the proposed discretization and enrichment strategies, and to show the performance of the X-FEM for solving sound propagation in the porous media.

The general problem is first stated along with diverse interface coupling conditions. Then, the spatial discretization and enrichment strategies adapted to the porous media are presented. Finally, the proposed methodologies are verified through a set of numerical benchmarks.

3.1 Problem statement and interface conditions

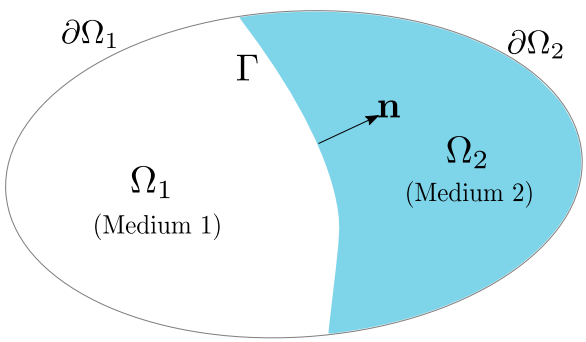

Fig. 3.1.: Example of a two-media problem domain.

For the sake of clarity, a two-media configuration, as shown fig. 3.1, is considered to formulate interface conditions. This configuration permits to model the sound wave propagating from a real acoustic medium such as air to a sound absorption package made of porous materials.

It can be also readily extended to more complex geometries with multiple interfaces in three-dimensional problems.

The physical domain Ω is enclosed by the boundary $\partial\Omega = \partial\Omega_1 \cup \partial\Omega_2$. It is divided into two subdomains $\Omega_1 \cup \Omega_2 = \Omega,\ \Omega_1 \cap \Omega_2 = \emptyset$ representing two different materials (media) by an interface Γ with unit outward normal $\mathbf{n}$ from Ω_1 to Ω_2.

As equivalent fluid and Biot's equations (PEM) are both considered for modelling porous materials, three coupling interfaces are induced: air-equivalent fluid coupling (two fluid), air-PEM coupling and PEM-PEM coupling. The notations associated to the PEM governed by Biot formulation is denoted by superscript $\bullet^b$. The subscripts $(\bullet)_1$ or $(\bullet)_2$ are referred for subdomain number.

3.1.1 Fluid-fluid coupling

When the porous material is considered as an equivalent fluid, two bulk media are of the same physical nature, governed by the Helmholtz equation. The conditions for two fluid-like coupling at the interface Γ reads:

$$\frac{1}{\omega^2\rho_1}\frac{\partial p_1^f}{\partial n} = \frac{1}{\omega^2\rho_2}\frac{\partial p_2^f}{\partial n}, \tag{3.1a}$$

$$p_1^f = p_2^f, \tag{3.1b}$$

where first equation eq. (3.1a) represent the conservation of normal component of the total displacement u^t of fluid [1], and the second one is the continuity of acoustic pressure. In the case of standard FEM or a "ridge" enrichment function for X-FEM presented in the former chapter, the continuity of pressure is satisfied directly. Then, applying the first equality to the combined variational formulations of two media, leads interface integrals $\boldsymbol{a_I}$ to be eliminated mutually.

3.1.2 Fluid-PEM coupling

When the air is attached to the porous materials governed by the Biot's formulations, two different nature of media are involved. Hence, the interface condition reads:

$$\frac{1}{\omega^2\rho_1}\frac{\partial p_1^f}{\partial n} = \mathbf{u}^{t(b)}.\mathbf{n}, \tag{3.2a}$$

$$p_1^f = p_2^{f(b)}, \tag{3.2b}$$

$$\hat{\sigma}^s.\mathbf{n} = 0, \tag{3.2c}$$

where, as previous coupling, eq. (3.2a) represents the conservation of the total normal component of displacement, and eq. (3.2b) represents the equality of the air acoustic pressure

[1] Total displacement can be expressed as the velocity v_n^t that $v_n^t = \mathrm{j}\omega u_n^t = -\frac{1}{\mathrm{j}\omega\rho}\frac{\partial p}{\partial \mathbf{n}}$

and poro-pressure in PEMs. These two conditions will lead the interface integral on fluid part disappeared. Equation (3.2c) represents the free surface condition on the surface of porous material that is no stress applied on it, which make the surface integral in the variational formulation of solid phase disappeared.

3.1.3 PEM-PEM coupling

The interface between two different PEMs media is also considered here. This type of interface is designed to wave propagation in multi-layers porous structures, which reads:

$$\mathbf{u}_1^s\mathbf{n} = \mathbf{u}_2^s\mathbf{n}, \tag{3.3a}$$

$$\mathbf{u}_1^t.\mathbf{n} = -\mathbf{u}_2^t.\mathbf{n}, \tag{3.3b}$$

$$p_1^{f(b)} = p_2^{f(b)}, \tag{3.3c}$$

$$\hat{\sigma}_1^s\mathbf{n} = \hat{\sigma}_2^s.\mathbf{n}. \tag{3.3d}$$

These conditions from eq. (3.3a) to eq. (3.3d) indicates that the continuity of the displacement of solid phase, total displacement, fluid phase pressure and solid stress in-vacuo, respectively. Applying the above conditions to the variational formulations, the surface terms (in-vacuo stress of PEM and the total displacement) in eq. (2.13) and eq. (2.11) vanish at the interface. Same as pressure field, the continuity of the displacement $\mathbf{u}^s$ can be guaranteed in the standard FEM or within the "ridge" enriched X-FEM.

One can summarize that all these types of coupling and interface conditions result in non-interface integral terms defined on Γ for the variational formulations. They are therefore so-called perfect interface or natural couplings, no additional terms needs to be added for the interface quantities.

3.2 Spatial discretization and enrichment

Our computational domain is discretized in the X-FEM space. As the primal variables (pressure of fluid and displacement of solid) will be continuous at the interface, continuity in elements needs to be ensured. One can employ the "Ridge" enrichment function or Heaviside enrichment with a weak enforcement of continuity. The first one is adopted in this chapter and the latter one will be addressed in the forthcoming chapter.

This section offers the specific idea on how to discretize and enrich the entire computational domain for each coupling configuration. The space discretization for above three types of coupling is shown in fig. 3.2 that will be presented in the following. The acoustic fluid medium requires only the scalar pressure field. In contrast, the Biot mixed formulation involves two

different fields: a scalar pressure field p^f and a vector displacement field $\mathbf{u}^s$. For this reason, it is easier to couple two regions with same physical nature since the discretization is the same everywhere in the computational domain. We present fluid-fluid coupling and two PEMs coupling first. The case where a region of acoustic fluid is coupled to a poro-elastic (PEM) region requires more care and is addressed at the last in the following subsection.

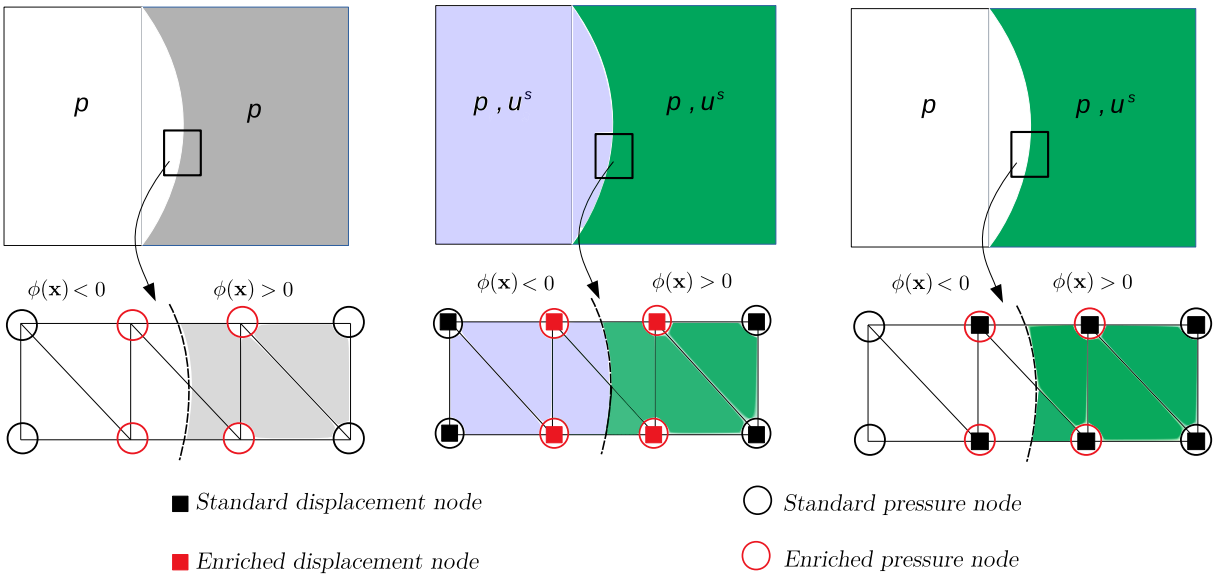

Fig. 3.2.: Discretization strategy and node distribution for coupling configuration: fluid-fluid coupling (left), Biot-Biot coupling (middle) and fluid-Biot coupling (right).

3.2.1 Interface between two fluid-like media

When the porous material governed by the Helmholtz equation couples to other acoustic fluid media, pressure is the sole unknown of finite element discretization (primal variable of variational formulation) in the entire computational domain(see fig. 3.2 (left)). For the elements intersecting with the interface, the pressure field is enriched by the "ridge" function, so the approximation of pressure reads:

$$p^f(\mathbf{x})\Big|_{\Omega_I} = \sum_i^n N_i(\mathbf{x}) p_i^f + \sum_j^{n_{enr}} N_j(\mathbf{x}) R(\mathbf{x}) a_{pj}. \tag{3.4}$$

The whole domain is divided into two subdomains by the interface in order to assign the different material properties in each subdomain. This subdivision is accomplished thanks to the sign of the level-set function. Regarding the rest of pressure in the domain, the standard finite elements are used. Therefore, the discretized linear system can be written as:

$$\left[\begin{array}{c|c} \frac{1}{\omega^2\rho_i}[\mathbf{H}_p] - \frac{1}{K_i}[\mathbf{Q}_p] & \frac{1}{\omega^2\rho_i}[\mathbf{H}_{pa}] - \frac{1}{K_i}[\mathbf{Q}_{pa}] \\ \hline \frac{1}{\omega^2\rho_i}[\mathbf{H}_{pa}] - \frac{1}{K_i}[\mathbf{Q}_{pa}] & \frac{1}{\omega^2\rho_i}[\mathbf{H}_a] - \frac{1}{K_i}[\mathbf{Q}_a] \end{array}\right] \left\{\begin{array}{c} \mathbf{p}_i^f \\ \hline \mathbf{a} \end{array}\right\} = \left\{\begin{array}{c} \mathbf{F}_i \\ \hline \mathbf{F}_a \end{array}\right\}, \tag{3.5}$$

where $[\mathbf{H}_p]$ and $[\mathbf{Q}_p]$ are the kinetic and compression energy matrices of the fluid phases, which are the dot product of derivative of shape functions and shape functions themselves, respectively. $\mathbf{F}_i$ are the external excitation on the acoustic fluid of each subdomain. $\mathbf{F}_a$ represents the external force applied on the enriched elements. The upper-left block of above the system represents the classical linear system in standard FEM for the Helmholtz equation of two-media coupling. It is reminded that each term in the enriched blocks is integrated using a modified Gauss quadrature scheme for partitioned sub-elements with different materials properties, denoted with subscript $(\bullet)_i$.

3.2.2 Interface between two PEMs media

Fig. 3.2 (middle) gives an illustration of the discretization strategy for the coupling of two Biot equations. The pressure and displacement fields are both defined on the entire discretization domain: each node involves three degrees of freedom (for 2D) or four degrees of freedom (for 3D). The displacement of the solid phase $\mathbf{u}^s$ and the pressure p^f defined on an element intersecting the interface both need to be enriched:

$$p^f(\mathbf{x})\Big|_{\Omega_I} = \sum_i^n N_i(\mathbf{x}) p_i^f + \sum_j^{n_{enr}} N_j(\mathbf{x}) R(\mathbf{x}) a_{pj} \ , \tag{3.6a}$$

$$\mathbf{u}^s(\mathbf{x})\Big|_{\Omega_I} = \sum_i^n \mathbf{N}_i(\mathbf{x}) u_i^s + \sum_j^n \mathbf{N}_j(\mathbf{x}) R(\mathbf{x}) b_{uj} \ , \tag{3.6b}$$

where a_j and b_j are the additional enrichment dofs for the pressure and displacement fields associated to the ridge enrichment function. The fields on the elements not containing the interface boundary are expressed by the standard approximation without enrichment terms.

Substituting the prescribed approximations into the variational formulation and the assembly of element contributions result in a linear system of the form:

$$\left[\begin{array}{cc|cc} \mathbf{K_p} & \mathbf{C_{pu}} & \mathbf{K_{pa}} & \mathbf{C_{pb}} \\ \mathbf{C_{up}} & \mathbf{K_u} & \mathbf{C_{ua}} & \mathbf{K_{ub}} \\ \hline \mathbf{K_{ap}} & \mathbf{C_{au}} & \mathbf{K_a} & \mathbf{C_{ab}} \\ \mathbf{C_{bp}} & \mathbf{K_{bu}} & \mathbf{C_{ba}} & \mathbf{K_b} \end{array}\right] \left\{\begin{array}{c} \mathbf{p}_i^{f(b)} \\ \mathbf{u}_i^s \\ \hline \mathbf{a} \\ \mathbf{b} \end{array}\right\} = \left\{\begin{array}{c} \mathbf{F}_p \\ \mathbf{F}_u \\ \hline \mathbf{F}_a \\ \mathbf{F}_b \end{array}\right\}, \tag{3.7}$$

with

$$\mathbf{K_p} = \frac{1}{\omega^2 \tilde{\rho}_{\mathrm{eq}i}}[\mathbf{H}_p] - \frac{1}{\tilde{K}_{\mathrm{eq}i}}[\mathbf{Q}_p], \tag{3.8a}$$

$$\mathbf{K_u} = \hat{P}_i[\mathbf{K}_u] - \omega^2 \tilde{\rho}_i[\mathbf{M}_u], \tag{3.8b}$$

$$\mathbf{K_a} = \frac{1}{\omega^2 \tilde{\rho}_{\mathrm{eq}i}}[\mathbf{H}_a] - \frac{1}{\tilde{K}_{\mathrm{eq}i}}[\mathbf{Q}_a], \tag{3.8c}$$

$$\mathbf{K_b} = \hat{P}_i[\mathbf{K}_b] - \omega^2 \tilde{\rho}_i[\mathbf{M}_b], \tag{3.8d}$$

$$\mathbf{C_{pu}} = \mathbf{C_{up}}^T = -\tilde{\gamma}_i[\mathbf{C}_{pu}], \tag{3.8e}$$

$$\mathbf{K_{pa}} = \mathbf{K_{ap}}^T = \frac{1}{\omega^2 \tilde{\rho}_{\mathrm{eq}i}}[\mathbf{H}_{pa}] - \frac{1}{\tilde{K}_{\mathrm{eq}i}}[\mathbf{Q}_{pa}], \tag{3.8f}$$

$$\mathbf{C_{pb}} = \mathbf{C_{bp}}^T = -\tilde{\gamma}_i[\mathbf{C}_{pb}], \tag{3.8g}$$

$$\mathbf{C_{ua}} = \mathbf{C_{au}}^T = -\tilde{\gamma}_i[\mathbf{C}_{ua}], \tag{3.8h}$$

$$\mathbf{K_{ub}} = \mathbf{K_{bu}}^T = \hat{P}_i[\mathbf{K}_{ub}] - \omega^2 \tilde{\rho}_i[\mathbf{M}_{ub}], \tag{3.8i}$$

$$\mathbf{C_{ab}} = \mathbf{C_{ba}}^T = -\tilde{\gamma}_i[\mathbf{C}_{ab}], \tag{3.8j}$$

where $[\mathbf{K}_u]$ and $[\mathbf{M}_u]$ are the standard global stiffness and mass matrices for the solid phase. The coupling terms $[\mathbf{C}]$ corresponds to the inner products of shape functions and their derivatives between solid and fluid phases. $\mathbf{F}_p$ is the external excitation on the fluid phase and $\mathbf{F}_u$ represents the external forces on the solid phase. $\mathbf{F_b}$ represents the external force applied on enriched solid phase. The upper-left block of above the system represents the classical discretized form of the formulation eq. (2.13) in the standard finite element method as given in Dazel, [161].

3.2.3 Interface between an acoustic fluid and a PEM medium

Contrary to the previous configurations, the number of variables is not equal and the physic nature of media is not compatible at the interface in this coupling. The Biot mixed formulation involves two different fields, but one scalar field is governed by Helmholtz equation. Fig. 3.2 (right) illustrates the porous material governed by Biot equations couples to the acoustic fluid governed by Helmholtz equation.

The discretization strategy in this situation has to include the following features:

- Assignment of different materials properties as in the previous type of coupling;
- Selection of the PEM sub-domain to define the displacement field associated to polynomial spaces;
- Render different governing formulations for acoustic fluid part and porous material part respectively.

The assignment of materials is handled same as the PEM-PEM configuration by the subdivision of the whole computational domain. Thanks to the interface defined by level-set function, the displacement field is being defined only on the elements with level set function $\phi(\mathbf{x}) > 0$ as porous part. The third feature is realized by decomposing the variational formulation into different computational domains. As the pressure of two media is continuous, the Helmholtz bilinear forms in eq. (2.11) and eq. (2.13b) for the pressure terms are defined on the whole domain. The coupling term with $\tilde{\gamma}$ and solid dynamic terms in eq. (2.13a) are defined on PEM subdomain only.

The pressure and the displacement fields are both defined on the elements at the interface to ensure dofs consistency as shown in fig. 3.2 (right), although the displacement is not taken into account on the acoustic fluid side at the numerical integration step. The pressure on the elements crossed by the interface are enriched, whereas the displacement does not need to be enriched, approximated by a standard interpolation:

$$p(\mathbf{x})\Big|_{\Omega_I} = \sum_i^n N_i(\mathbf{x})p_i + \sum_j^{n_{enr}} N_j(\mathbf{x})R(\mathbf{x})a_{pj} \ , \tag{3.9a}$$

$$\mathbf{u}^s(\mathbf{x})\Big|_{\Omega_I} = \sum_i^n \mathbf{N}_i(\mathbf{x})u_i. \tag{3.9b}$$

As before, the fields on the other elements are interpolated by the standard approximation without any enrichment. With these approximations, coupling the eq. (2.11) and eq. (2.13) leads to the following linear system for acoustic fluid-PEM interface problem:

$$\left[\begin{array}{cc|c} \mathbf{K_{pi}} & \mathbf{C_{p_iu}} & \mathbf{K_{p_ia}} \\ \mathbf{C_{up_i}} & \mathbf{K_u} & \mathbf{C_{ua}} \\ \hline \mathbf{K_{ap_i}} & \mathbf{C_{au}} & \mathbf{K_a} \end{array}\right] \left\{\begin{array}{c} \mathbf{p}_i^f \\ \mathbf{u}^s \\ \hline \mathbf{a} \end{array}\right\} = \left\{\begin{array}{c} \mathbf{F}_{pi} \\ \mathbf{F}_u \\ \hline \mathbf{F}_e \end{array}\right\}, \tag{3.10}$$

where $\mathbf{K_{p_i}}$, $\mathbf{K_{p_iu}}$ and $\mathbf{K_{p_ia}}$ are the same types of matrices as previous coupling, only with different material properties. Unknown $\mathbf{p}_i^f$ represents the pressure field in the acoustic fluid and poro-fluid in PEM part. As for the matrix in eq. (3.7), the upper-left block represents the classical FEM system, the same matrix can be found in [70]. The last row and column in the system correspond to the contribution of the enrichment terms associated to the additional degrees of the freedom $\mathbf{a}$ to maintain the continuity of pressure. Again, the numerical quadrature on each enriched term in the matrix is conducted on the sub-elements associated to the corresponding material type.

It is worth emphasizing that the additional degrees of freedom a and b are added locally on the elements containing the interface but not for all the elements. As a consequence, the linear system to be solved does not become much larger than the system obtained from the

classical finite element method. The above discretization strategies based on the X-FEM allow to represent the interface in the elements for different coupling types, but the computation procedure is still based on the idea of the classical FEM. Therefore, some typical characteristics of the solution shall be conserved in the present method as the problem is solved with the classical FEM.

3.3 Numerical verification

In this section, implementation of the proposed discretization and enrichment strategies is verified using several numerical examples. All the algorithms and formulations in this thesis are implemented with own developed `Python` codes for one-dimensional problems, and with `eXlibris` that is an in-house C++ FEM library for two/three-dimensional problems. Without exception, the discrete systems for the following examples are solved by the direct solver `MUMPS` (Amestoy et al., 2019 [162]) which will be used for all computations in the thesis as well.

Since the exact solutions are available for test cases, an analysis of convergence is performed. The convergence is measured through the relative error in the L^2 norm defined for complex-valued fields as follows:

$$\varepsilon_{L^2} = \frac{\|f_{\text{ex}} - f_{\text{FE}}\|_{L^2}}{\|f_{\text{ex}}\|_{L^2}} \times 100\%, \quad \text{with } \|f\|_{L^2} = \left(\int_\Omega |f|^2 d\Omega\right)^{1/2}. \tag{3.11}$$

The errors on the solid phase displacement $\mathbf{u}^s$ and on the fluid phase pressure p^f are calculated separately in order to identify the different convergence behaviour for each field. In acoustic problems, the dispersion error or the pollution effect plays an important role on the convergence behaviour. Dispersion error comes from the difference between the theoretical wave number and numerical wave number represented by the computational scheme. A sufficient amount of dofs per wavelength is needed to control this error. Hence, the number of dofs per wavelength D_λ is defined as:

$$D_\lambda = \frac{2\pi p}{kh}, \tag{3.12}$$

where p is the interpolation degree of shape functions and h represents the element size. The Biot equations for the PEM in 2D supports three distinct complex-valued wave numbers. To provide the upper limit of the convergence condition, the largest absolute value of the three wave numbers is used:

$$k^* = \{|k_i|\}_{\max}, \quad \text{with } i = 1, 2, 3, \tag{3.13}$$

and for two-dimensional problems it is customary to use the total number of degrees of freedom N_{dof} and the area of the computational domain $\text{area}(\Omega)$ instead of p and h to define an average number of dofs per element as in Lieu et al., 2016 [163]. Hence the D_λ can be approximated as:

$$D_\lambda = \frac{2\pi}{k^*}\sqrt{\frac{N_{\text{dofs}}}{\text{area}(\Omega)}}. \tag{3.14}$$

The mesh resolution for the following convergence analysis is measured by D_λ instead of mesh size h as in classical FEM, which allows to compare the quality of the h-extension, polynomial order p-refinement and enriched FEM with the same metric.

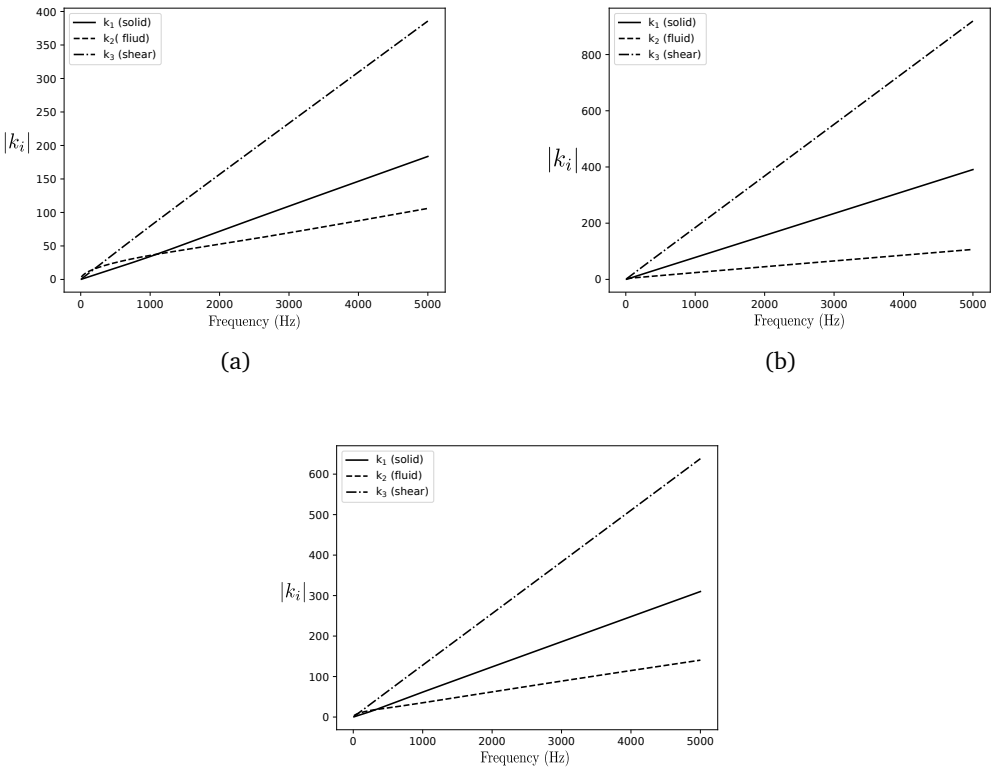

Fig. 3.3.: Wave properties (variation of wave number as function of frequency) for (a) classical foam, (b) polyurethane, (c) XFM (obtained from appendix B.1).

Three typical porous materials are considered in this chapter, which were already used in earlier studies (Hörlin et al., 2001 [82], Hörlin, 2005 [83], Chazot et al., 2013 [94]). The properties of the PEM are contained in table B.1: the first material is a well characterized foam, the second one represents a polyurethane with open cell structure, whose thermal characteristic length is much higher than common foam while the XFM is a material frequently used in the automotive industry.

Before conducting numerical calculations, the properties of wave numbers for each medium is worthy to be discussed, which would help to understand the numerical results. The variation of norm of wave numbers $|k_i|$ as a function of frequency is illustrated in fig. 3.3. Three types of waves are present in a PEM: one compression and one shear wave are generated from the vibration of the solid phase, and the compression wave propagation originates from the fluid phase. For the three materials, there is a range of frequency where the norms of wave numbers are very close to each other and even overlapped. When this occurs, there is a strong coupling between the fluid and solid phases. As frequency increases, the wavenumbers of the solid-borne

waves increase faster than that of the fluid wave. The waves then reach a decoupling region where the gap between the wave numbers is large. The solution and the behaviour of the convergence is directly related to these variations of the wave numbers, which will be discussed in the following numerical tests.

3.3.1 Plane wave propagating in a double-layered square

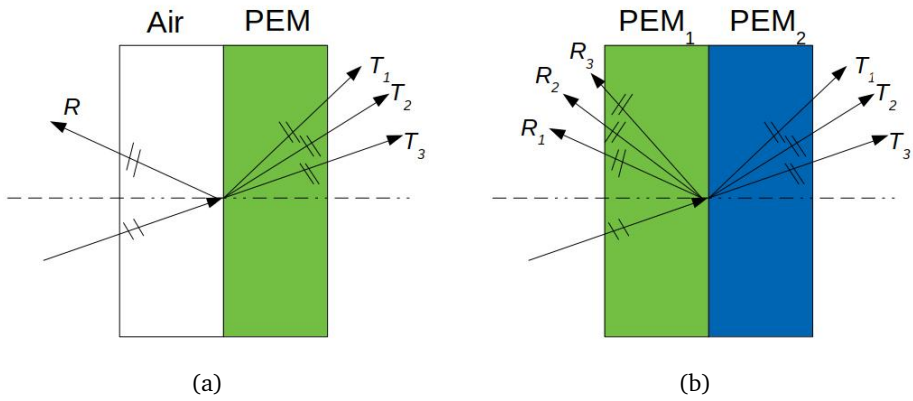

Fig. 3.4.: Test configurations (a)Air-PEM coupling, (b)PEM-PEM coupling.

A standard benchmark is first considered, where an oblique plane wave propagates in a semi-infinite plane filled with an acoustic fluid. This example can be regarded as a simplification of a multi-layer problem (where number of layer is greater than 2) in practical applications. As the implementation of discrete system for fluid-fluid coupling is included within the fluid-PEM coupling, testing the acoustic fluid-PEM and PEM-PEM is sufficient to verify all related discrete operators. Two independent configurations are analysed, as shown in fig. 3.4. In the first type of coupling, air is considered as the acoustic fluid, the polyurethane is used as the material for the poro-elastic region. The chosen foam is attached on the polyurethane as the second layer in the PEM-PEM coupling.

The exact solutions associated to these configurations are obtained by calculating the reflection R_i and transmission T_i coefficients, as shown in fig. 3.4. This involves solving 4×4 or 6×6 linear systems depending on the type of coupling conditions. The analytical solutions are provided in appendix B, the calculation procedure can be also found in handbook Allard and Atalla, 2009 [29].

The computational domain is a square of side L ($0.2\,\mathrm{m}$ for air-PEM and $0.1\,\mathrm{m}$ for the PEM-PEM case) discretized by structured triangular elements. The medium interface defined by a level-set function is placed at $x = 0$ in order to ease the formulation of the exact solutions. Exact Neumann boundary conditions are imposed on the four outer boundaries: For the Air-PEM coupling, fluid velocity in air v_a are imposed on boundaries of the acoustic fluid media (green line), total displacement $\mathbf{u}^t$ and in-vacuo stress $\hat{\boldsymbol{\sigma}}^s$ are imposed on the boundaries of the

poro-elastic media part (blue line) as shown in fig. 3.5(a); for the two PEMs coupling, total displacement $\mathbf{u}^t$ and in-vacuo stress $\hat{\boldsymbol{\sigma}}^s$ are imposed on all outer boundaries (blue line) as in fig. 3.5(b). The simulations are performed from low frequencies in the coupling region to relatively high frequencies in the decoupling region, which allows us to identify different behaviours of solutions and convergence curves depending on the frequency.

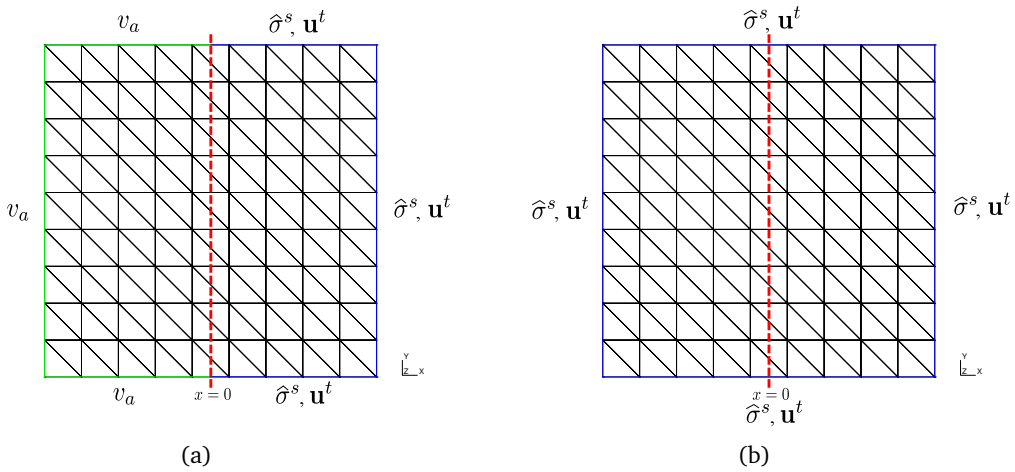

Fig. 3.5.: Example of X-FEM meshes and imposed boundary conditions for (a) Air-PEM coupling,(b) PEM-PEM coupling.

It is recognized firstly from fig. 3.6 that the interface ($x = 0$) is embedded in elements instead of aligning with the boundaries of the elements. A change of propagation angle is observed at $x = 0$ (illustrating the change of material properties) is successfully handled in the elements by the proposed method. Such a complex oscillation of the waves is well captured using such a relatively coarse mesh thanks to the high polynomial orders of the finite-element basis (Fourth order in the example presented in fig. 3.6).

Figs. 3.6(a) and 3.6(b) show the real part of the solution for pressure and the x component of the solid displacement at $5,000\,\mathrm{Hz}$ with incident angle of $\pi/4$ in air-PEM coupling configuration. A dissipation of the pressure wave is observed in the sub-domain $x > 0$. The solution for the displacement is only computed for $x > 0$ as shown in fig. 3.6(b) since it only exists in the porous material. Figs. 3.6(c) and 3.6(d) illustrate the solution of the PEM-PEM coupling configuration at $2,000\,\mathrm{Hz}$ with incident angle $\pi/18$. A rapid attenuation for both pressure and displacement on the whole computational domain and the changes of the wave angle at $x = 0$ are observed. Note that a great disparity of the scale ($> 10^7$) between displacement and pressure is visible at these frequencies, which is one of the reasons that restricts the convergence of the Biot coupled formulation as discussed in Dauchez et al., 2001 [81].

Figs. 3.7 and 3.8 shows the convergence in L^2 norm when refining the element size h and interpolation order p versus D_λ carried out for two coupling types and for two frequencies ($70\,\mathrm{Hz}$ and $5,000\,\mathrm{Hz}$). Again, pressure and displacement errors are calculated separately. The number of elements $N \times N$ in each h-refinement varies from $N = 5$ to $N = 81$, and the p-refinement is performed with the mesh $N = 5$.

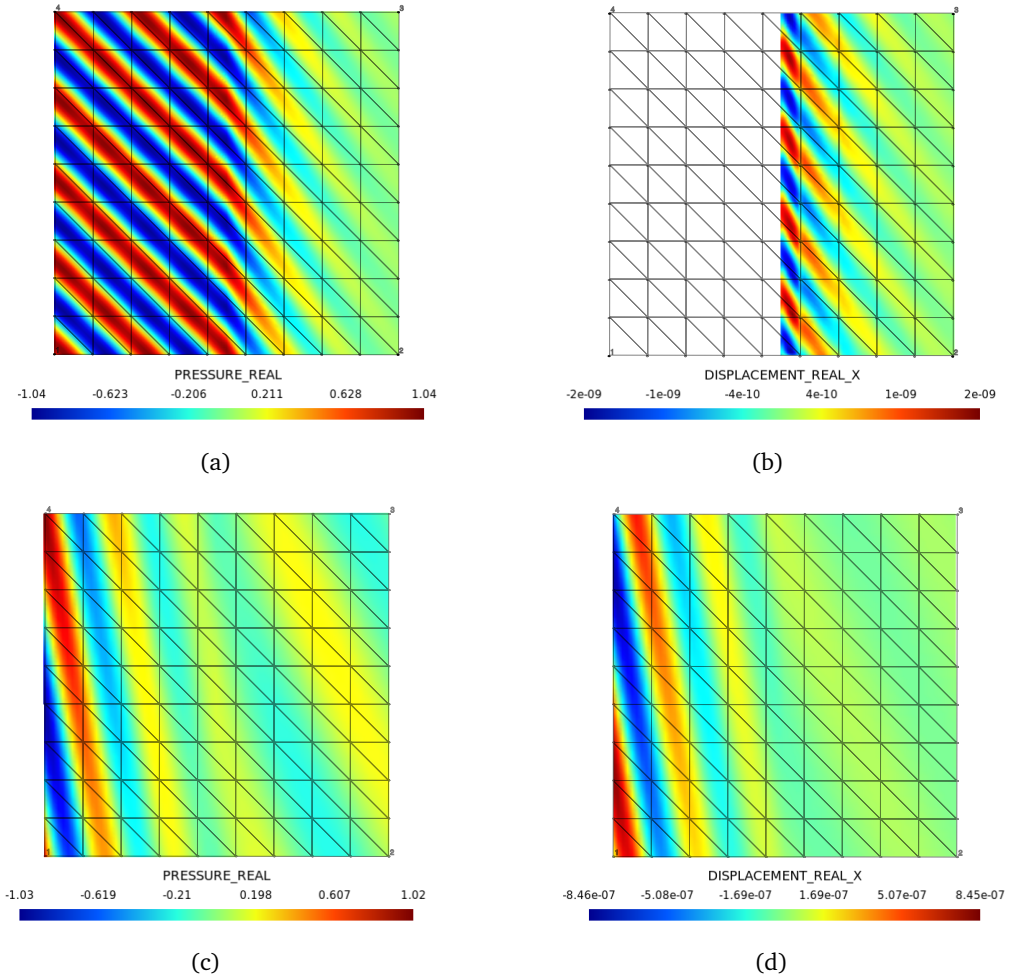

Fig. 3.6.: Example of solution (real part) of Air-PEM coupling (top) with incident angle $\pi/4$ at $5,000\,\mathrm{Hz}$ and of PEM-PEM coupling (bottom) with incident angle $\pi/18$ at $2,000\,\mathrm{Hz}$ for fluid pressure (in Pa) (a,c) and solid displacement (in m) (b,d) under fourth interpolation order.

h-refinement curves in each interpolation degree are close to the so-called 'optimal' rate of convergence ($\mathcal{O}(h^{-(p+1)})$) using the present method for both configurations (Air-PEM fig. 3.7 and PEM-PEM fig. 3.8). p-refinement (in red) shows an exponential rate of convergence compared to h-refinement: (i) keeping the same D_λ, it gives a more accurate solution; (ii) achieving the same magnitude of error, it requires less dofs, meaning less computational effort. These rates of convergence are similar to those reported in Hörlin et al., 2001 [82] and Hörlin, 2005 [83], in which the Biot equations are solved using the classical FEM with hierarchical polynomials.

At $70\,\mathrm{Hz}$, pressure and displacement present a synchronous monotonic convergence, reaching the same error magnitude with the same D_λ as shown in figs. 3.7(a) and 3.7(b). This synchronization corresponds to the fact that we are in a strong coupling frequency range between the fluid and solid phases of the PEM (the wave numbers are close to each other). Differences in the convergence behaviour are obvious at $5,000\,\mathrm{Hz}$ for the Air-PEM configuration in figs. 3.7(c) and 3.7(d). Firstly, the dispersion error for both solutions is observed with linear

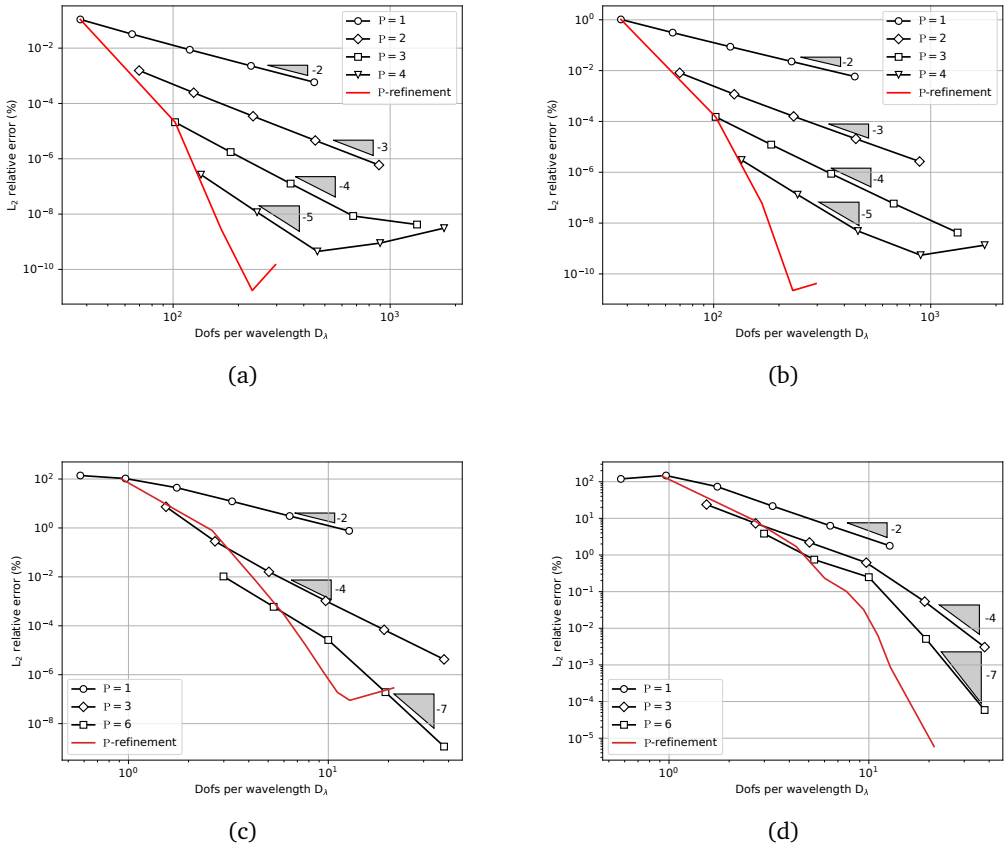

Fig. 3.7.: Relative error L^2 in percentage on p^f (left) and $\mathbf{u}^s$ (right) as function of D_λ at $70\,\mathrm{Hz}$ (top) and $5,000\,\mathrm{Hz}$ (bottom) for Air-PEM coupling.

element and there exists a stage of pre-asymptotic convergence before achieving the 'optimal' rate as D_λ is not sufficiently large (inferiors to ten dofs per wavelength, which agrees to the conclusion in Dauchez et al., 2001 [81]). Secondly, the pressure field converges more quickly than displacement in h-refienement (for the same D_λ, pressure is three orders of magnitude higher than the displacement), which stems from the large difference of wave number at this frequency: the shear solid-borne wave is ten times larger than the compression air-borne wave, as shown in fig. 3.3(b).

Contrary to the Air-PEM coupling, the convergence of the PEM-PEM coupling with chosen materials shows a better concordance between pressure and displacement in fig. 3.8. The error magnitudes are of the same order even in the decoupling region (here $5,000\,\mathrm{Hz}$). This is because the solutions are close to zero in most region of the computational domain with the double-layer absorbing materials at these frequencies. This configuration is much easier to converge for both pressure and displacement.

Note that in figs. 3.7(a) to 3.7(c) and figs. 3.8(a) to 3.8(b), a stagnation or even an increase of the error at the end of convergence curves is observed. This is due to the fact that the conditioning of the global linear system is poor for these high refinements. This observation is

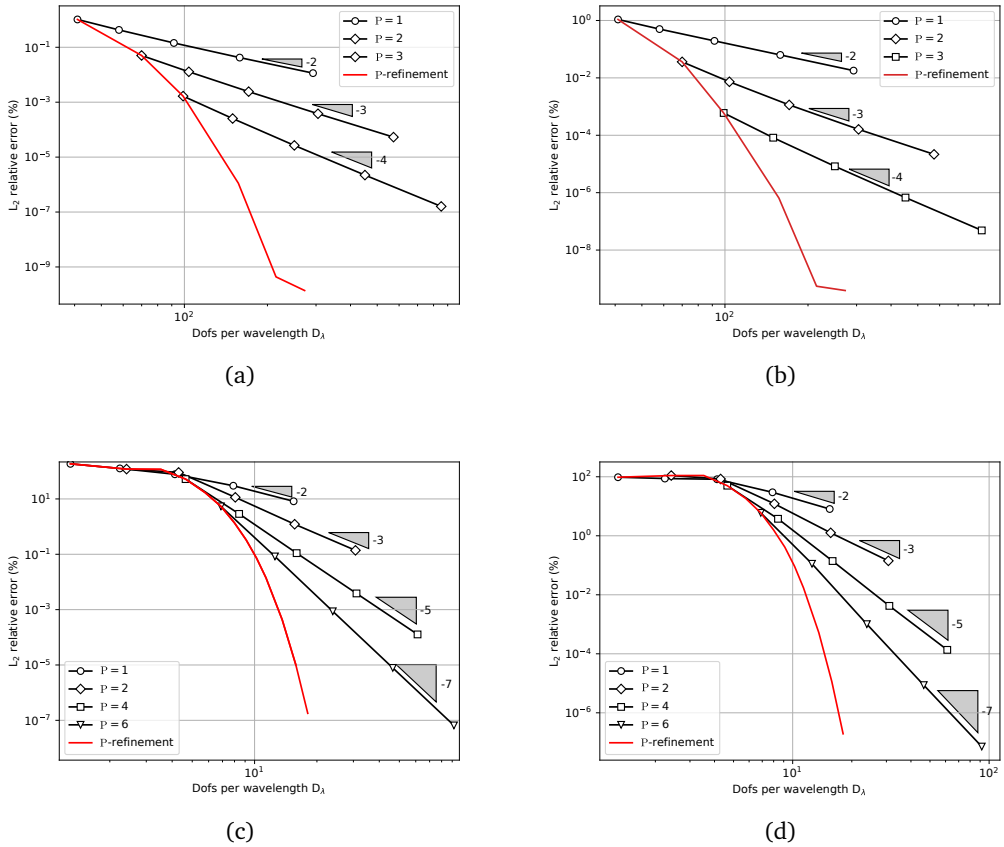

Fig. 3.8.: Relative error L^2 in percentage on p^f (left) and $\mathbf{u}^s$ (right) as function of D_λ at $70\,\mathrm{Hz}$ (top) and $5,000\,\mathrm{Hz}$ (bottom) for PEM-PEM coupling.

also reported when using other numerical methods (Gabard and Dazel, 2015 [96]) to solve the Biot mixed formulation. This ill-conditioning could be improved with a suitable pre-conditioner as in Axelsson et al., 2018 [164] or static condensation as advocated in Lieu et al., 2016 [163]. Nevertheless, a desirable accuracy is obtained with the present method for this problem.

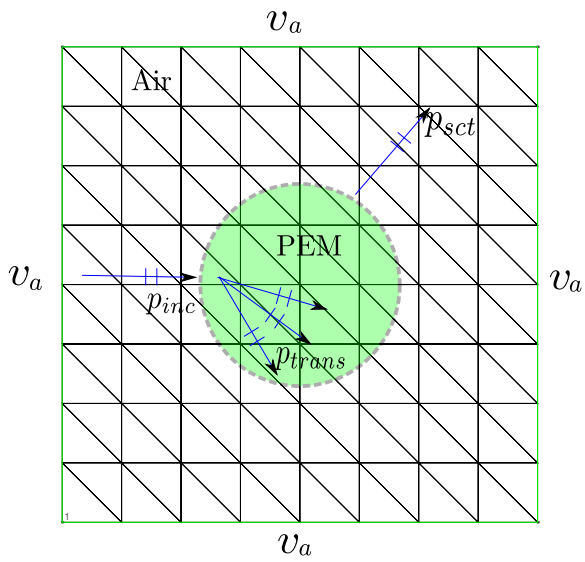

Fig. 3.9.: Cylinder scattering problem with an example of X-FEM mesh.

3.3.2 Sound scattering by a poro-elastic cylinder

The second test case involves a 2D PEM cylindrical scatterer surrounded by air, leading to an acoustic fluid-PEM coupling interface. This case provides an assessment of the proposed method for a more complicated case in both physic and computational aspects. Sound radiation problems in free field involving poro-elastic media result in more complex distributions of the acoustic fields. In addition, the presence of a curved interface may introduce geometrical error in the numerical approximation. The exact solution is also available and provided in appendix B, which allows to calculate the convergence curves.

The computational domain is a square of length of 0.5 m meshed using structured triangular elements. The exact velocity of the fluid in air v_a obtained from the analytical solution is imposed on the outer boundaries (green line) of the domain, as illustrated in section 3.3.2. Within the proposed method, the circular interface with radius $r_0 = 0.1\,\mathrm{m}$ is described implicitly by a level-set function using a linear approximation. The porous sub-domain governed by the Biot equations (2.13) is defined for $r < r_0$. Here, for higher-order approximations ($p \geq 2$), the previous presented NURBS enhanced X-FEM strategy (Legrain, 2013 [155]) is considered to avoid the geometrical error caused by the linear interpolation of the level-set.

Results in fig. 3.10(a) give a good illustration of the pressure distribution for the porous scattering problem. The combination of the incident p_{inc} and the partly reflected waves p_{sct} is observed in outer sub-domain $r > r_0$. The waves are partly absorbed by the porous material in the region $r < r_0$. As seen in the fig. 3.10(b), the displacement of the solid phase is defined and computed in the absorbing region, whose oscillation and dissipation are also well captured. Again, the accuracy of the present method is measured with the relative error compared to the exact solution in L^2 norm. The convergences of h-refinements are conducted using regular triangular $N \times N$ meshes: $N = 4,\ 8,\ 16,\ 32,\ 64$ and p-convergence is performed with the mesh

$N = 4$ with an interpolation order varying between one and fourteen. The convergences at $70\,\mathrm{Hz}$ and $2,000\,\mathrm{Hz}$ are shown in fig. 3.11.

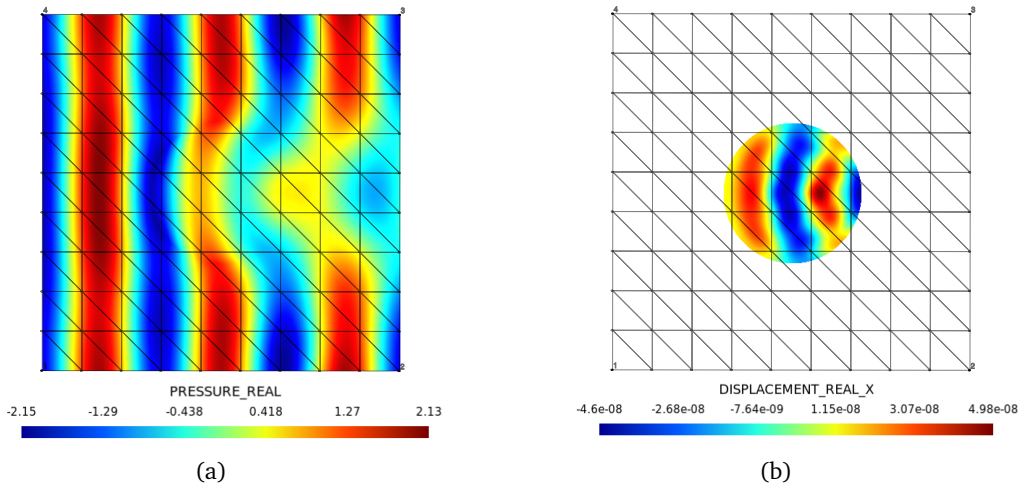

(a) (b)

Fig. 3.10.: Example of solution (real part) for (a) pressure (in Pa) and (b) displacement (in m) of cylinder scatter problem in $2,000\,\mathrm{Hz}$ with the fourth order polynomials.

The h-refinement results are similar to those presented in the first test case: rates close to $\mathcal{O}(h^{-(p+1)})$ are observed for each approximation order when D_λ is sufficient. The convergence of linear element for the displacement field in figs. 3.11(b) and 3.11(d) do not have sufficiently large D_λ. The cut-on phenomenon (explained in Hörlin et al., 2001 [82]) and a pre-asymptotic regime are more apparent in this problem at $2,000\,\mathrm{Hz}$. These high-order convergence rates are in accordance with previous studies reported in Hörlin, 2005 [83]. This agreement confirms that the X-FEM with the proposed discretization strategies is capable of providing an accurate solution for this more complex problem. The p-refinement curves in fig. 3.11 are less efficient than the one in the previous test case. It is due to the fact that with the interface described by NURBS, the enrichment function is defined with Lagrange polynomials instead of the Bernstein basis. It is well-known that the Lagrange polynomials lead to worse conditioning as the interpolation order increases. Even so, a high accuracy of the solutions for this more complex problem is still achieved.

The convergence of the numerical models for the two test cases described so far has been assessed with various porous materials at different frequencies. For brevity, not all these results are shown here, but the same conclusions apply. The convergence behaviour is strictly linked to the materials and frequencies since each term in the finite element matrix is associated to material properties, which are frequency dependent. These differences result in different conditioning of the matrix, leading to different convergence curves and magnitude of error.

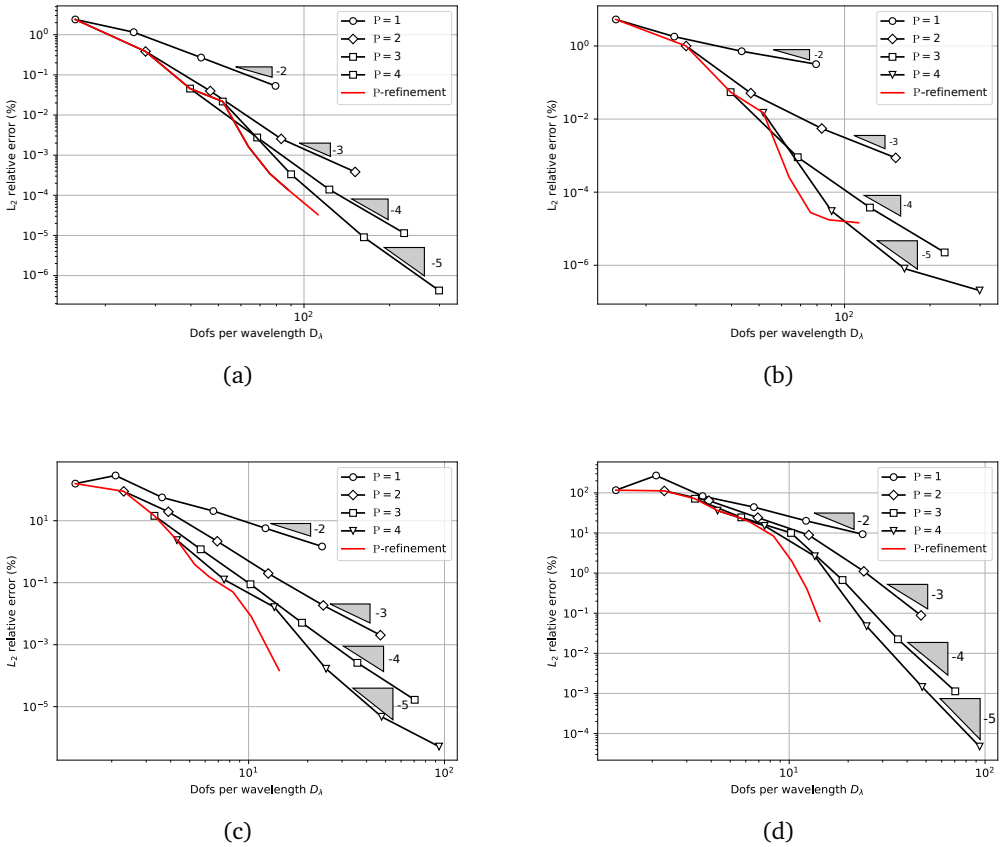

Fig. 3.11.: Relative error L^2 in percentage on p (left) and $\mathbf{u}^s$ (right) as function of D_λ at $70\,\mathrm{Hz}$ (top) and $2,000\,\mathrm{Hz}$ (bottom).

3.4 Conclusion

In this chapter, the space discretization and enrichments designed for the three couplings were provided in detail. They are suited for all models to be presented in following chapters. The discrete linear systems of each variational formulations were given as well. Among them, the coupling involved Biot's equation needs to be treated more carefully.

Two classical numerical benchmarks were tested to verify the implementation of the proposed computational strategies and the variational formulations. They demonstrated that the proposed method is able to recover an optimal rate of convergence regardless of frequency, material, coupling interface, geometry and solution. Concerning the Biot formulations, a higher order of approximation or larger D_λ are recommended for the displacement field in order to achieve a more accurate convergence for the whole solution. The observation of the convergences discretized in the proposed X-FEM framework are similar with the one calculated in the standard FEM, while providing a convenience on meshing.

Pressure jump interface

4

I won't regret, even if the belt on my robe grows looser.
For you, it's worth being wan and haggard.
衣带渐宽终不悔，为伊消得人憔悴

— **LIU Yong**
(Feng Xi WU)

The previous chapter proposed and verified the X-FEM discretization for acoustic problems containing porous media, but thin porous layers were not yet considered. From this chapter, the thin porous layer between two thick bulk media starts to be accounted for. The domain of interest is divided into bulk parts with a characteristic length D and thin layers parts with thickness d, where $d \ll D$. To avoid the discretization of such narrow layers, we condense them into a non-thickness interface and its acoustic effects will be considered with appropriate interface conditions. Therefore, the two-media configuration fig. 3.1 is transferred as shown in fig. 4.1, here Γ is now called the imperfect interface.

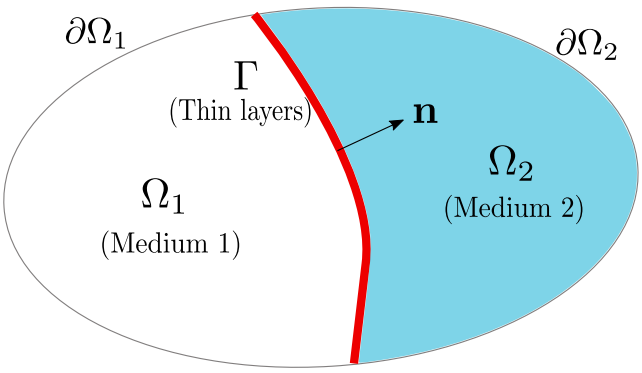

Fig. 4.1.: Two-media problem domain with an imperfect interface.

One focuses on the configuration where sound wave propagating from classical acoustic fluid (air) to typical sound absorbing systems. According to the physical model of thick porous materials, this chapter is divided into two main parts. In the first part, porous media are modelled as equivalent fluids, the fluid-fluid coupling is addressed with all necessary details. Second part, the Biot's mixed formulation is employed to model PEMs, air-PEM coupling is therefore discussed.

The pressure jump (drop) interface condition (Pierce, 1989 [59]) that is a simplified model to account for thin acoustic layers is considered in this chapter. This pressure jump model generates a pressure difference at the interface, which introduces a strong discontinuity. We discuss different approaches (formulations) to enforce such simplified interface condition in the framework of high-order Heaviside enrichment X-FEM.

4.1 Fluid-(equivalent) fluid coupling

4.1.1 Interface conditions and formulations

At the interface, the thin porous layer induces a pressure difference due to its flow resistivity σ (Pierce, 1989 [59], Allard and Atalla, 2009 [29]), so-called pressure jump model. In addition, flow velocity is considered to be conserved at the interface Γ since the thickness of layers d is relatively small. Therefore, the interface conditions are expressed as:

$$p_1^f - p_2^f = \sigma d \bar{v}, \quad \text{on } \Gamma, \tag{4.1a}$$

$$\frac{1}{\rho_1}\frac{\partial p_1^f}{\partial n} = \frac{1}{\rho_2}\frac{\partial p_2^f}{\partial n}, \quad \text{on } \Gamma, \tag{4.1b}$$

which can be written in a compact form as:

$$[\![p^f]\!] - \sigma d \bar{v} = 0, \quad \text{on } \Gamma, \tag{4.2a}$$

$$[\![\frac{1}{\rho}\frac{\partial p^f}{\partial n}]\!] = 0, \quad \text{on } \Gamma, \tag{4.2b}$$

where $[\![\bullet]\!]$ is the jump operator $[\![\bullet]\!] = \bullet_1 - \bullet_2$. $\bar{v}$ represents the mean flow velocity at the interface, which is defined as:

$$\bar{v} = -\frac{1}{\mathrm{j}\omega\rho_1}\frac{\partial p_1^f}{\partial n} = -\frac{1}{\mathrm{j}\omega\rho_2}\frac{\partial p_2^f}{\partial n}, \quad \text{on } \Gamma, \tag{4.3}$$

where the two expressions in eq. (4.3) are identical for the analytical solution due to the continuity condition eq. (4.2b). However, when the problem is solved numerically by means of the X-FEM, the mean flow velocity is related to the numerical solution of interfacial flux (normal gradient) which will depend on the discretization as well. In that case, the definition of this flow quantity becomes more crucial, which is to be addressed in the following part.

This interface condition covers a particular situation where $\sigma d = 0$, the pressure is continuous at the interface. This corresponds exactly to the *perfect interface* discussed in previous chapter 3. Therefore, the methods to be proposed would be able to impose *perfect* and *imperfect* interfaces.

It is worth emphasizing that the pressure discontinuity eq. (4.2a) depends on the pressure gradient, which corresponds to a *generalized Robin interface condition*. This condition is not trivial to be imposed on the interface that is merged in elements. The weak manner of enforcement by modifying the variational formulation is adopted here to impose such conditions.

Penalty-type formulation

In general, the weak solution to the problem at hand can be formulated in a variational form as follows: find $p^f \in \mathcal{P} = H^1(\Omega_1 \cup \Omega_2)$ such that

$$a(q^f, p^f) = \ell(q^f), \quad \forall q^f \in H^1(\Omega_1 \cup \Omega_2), \tag{4.4}$$

where the right-hand linear form $\ell(q^f)$ is the contribution by Neumann boundary conditions. In our case, the bilinear form consists of two parts: the first one denoted as a_B from the two bulk subdomains Ω_1 and Ω_2 and the second one denoted a_I defined on the interface Γ as following:

$$a(q^f, p^f) := a_B(q^f, p^f) + a_I(q^f, p^f). \tag{4.5}$$

The key point for this bilinear form is to consider two interface conditions on Γ. With the test function $q \in \mathcal{P}$ as well, a_B is rewritten as:

$$a_B(q^f, p^f) := \sum_i^2 \left(\int_{\Omega_i} \frac{1}{\rho_i} \boldsymbol{\nabla} q^f \boldsymbol{\nabla} p^f \, \mathrm{d}\Omega - \int_{\Omega_i} \frac{\omega^2}{K_i} q^f p^f \, \mathrm{d}\Omega \right). \tag{4.6}$$

Regarding the interface integrals on Γ, we have:

$$a_I(q^f, p^f) := -\int_\Gamma \frac{q_1^f}{\rho_1} \frac{\partial p_1^f}{\partial n} \mathrm{d}S + \int_\Gamma \frac{q_2^f}{\rho_2} \frac{\partial p_2^f}{\partial n} \mathrm{d}S, \tag{4.7}$$

thanks to the conservation of mean velocity eq. (4.3), a_I can be written as:

$$a_I(q^f, p^f) = \int_\Gamma \mathrm{j}\omega \bar{v} [\![q^f]\!] \mathrm{d}S, \tag{4.8}$$

then, with the pressure jump condition eq. (4.2a), $\bar{v}$ is replaced, and the final interface bilinear form is obtained:

$$a_I(q^f, p^f) = \frac{\mathrm{j}\omega}{\sigma d} \int_\Gamma [\![q^f]\!] [\![p^f]\!] \mathrm{d}S. \tag{4.9}$$

This interface term is similar to spring-like interfaces in solid mechanics, as studied in Hansbo and Hansbo, 2004 [117] or is called "substitution" method as in Ager et al., 2019 [165]. This term has a similar form as penalty method (Babuška, 1973 [126]) to enforce the Dirichlet boundary condition but with real physic constants σ, d and ω instead of a pure numerical

parameter as the role of penalization. That means that once the physical problem is determined, the weak formulation can be readily implemented and solved directly without adding supplementary numerical terms. Moreover, in contrast to conventional penalty methods, such *penalty-type* formulation is variationally consistent with the original problem, so that the interface pressure jump condition is preserved naturally. This type of formulation has been shown to lead to good performances within the X-FEM in Zhu et al., 2011 [141] to treat composite materials. For the following analysis, the results of the *penalty-type* formulation are regarded as a reference.

However, this formulation is not able to model a perfect interface and also cases where $\sigma d \to 0$ for which the corresponding linear system could be potentially ill-conditioned, especially for element embedded interfaces. Therefore, we strive to derive a more general and stable variational formulation in the sense that it can treat seamlessly perfect and imperfect interfaces, while preserving the conditioning of the discrete system regardless of the physical parameters of the interface law.

Nitsche-type formulation

As mentioned in chapters 1 and 2, Nitsche's method is known as a usual approach in the framework of Cut-FEM (Burman et al., 2015 [124]) to impose the boundary/interface conditions. This method should be more stable and could tackle the numerical issues in the afore-derived *penalty-type* formulation. This section is dedicated to construct a variational formulation to above problem based on the Nitsche's concept.

The derivation of a Nitsche-type formulation relied on the idea proposed in Hansbo and Hansbo, 2004 [117] and Yedeg et al., 2016 [137]. To this end, we first rewrite the mean flow velocity at the interface as:

$$\bar{v} := -\frac{1}{\mathrm{j}\omega}\left(\frac{\gamma_1}{\rho_1}\frac{\partial p_1^f}{\partial n} + \frac{\gamma_2}{\rho_2}\frac{\partial p_2^f}{\partial n}\right) = -\frac{1}{\mathrm{j}\omega}\left\langle \frac{1}{\rho}\frac{\partial p^f}{\partial n}\right\rangle_\gamma, \tag{4.10}$$

in which, the $\langle \bullet \rangle_\gamma$ refers to the weighted-average operator with $\gamma_1 + \gamma_2 = 1$. As aforementioned, analytically, any γ_i could be chosen, leading to the same resulting mean flow, since the continuity of the velocity at the interface is always guaranteed. Numerically, the choice of the weighting parameter has a non-negligible influence on the numerical solution, especially here when interface embedded methods such as X-FEM are employed. The detailed discussion for choosing a suitable γ is developed later in the section of discretization.

With such mean flow expression, the pressure jump condition eq. (4.1a) is rewritten as:

$$[\![p^f]\!] + \frac{\sigma d}{\mathrm{j}\omega}\left\langle \frac{1}{\rho}\frac{\partial p^f}{\partial n}\right\rangle_\gamma = 0, \tag{4.11}$$

thus, the interface term a_I eq. (4.7) in the weak formulation becomes:

$$a_I^*(q^f, p^f) = -\int_\Gamma [\![q^f]\!] \left\langle \frac{1}{\rho}\frac{\partial p^f}{\partial n} \right\rangle_\gamma \mathrm{d}S. \tag{4.12}$$

Following by addition and subtraction of the term $\frac{\sigma d}{\mathrm{j}\omega}\left\langle \frac{1}{\rho}\frac{\partial q^f}{\partial n}\right\rangle_\gamma \left\langle \frac{1}{\rho}\frac{\partial p^f}{\partial n}\right\rangle_\gamma$ we obtain:

$$\begin{aligned} a_I^*(q^f, p^f) = &-\int_\Gamma \left\langle \frac{1}{\rho}\frac{\partial p^f}{\partial n} \right\rangle_\gamma \left([\![q^f]\!] + \frac{\sigma d}{j\omega}\left\langle \frac{1}{\rho}\frac{\partial q^f}{\partial n} \right\rangle_\gamma \right) \mathrm{d}S \\ &+ \int_\Gamma \frac{\sigma d}{\mathrm{j}\omega}\left\langle \frac{1}{\rho}\frac{\partial q^f}{\partial n} \right\rangle_\gamma \left\langle \frac{1}{\rho}\frac{\partial p^f}{\partial n} \right\rangle_\gamma \mathrm{d}S, \end{aligned} \tag{4.13}$$

then, we symmetrize the formulation with the interface condition eq. (4.11):

$$\begin{aligned} a_I^*(q^f, p^f) = &-\int_\Gamma \left\langle \frac{1}{\rho}\frac{\partial p^f}{\partial n} \right\rangle_\gamma \left([\![q^f]\!] + \frac{\sigma d}{j\omega}\left\langle \frac{1}{\rho}\frac{\partial q^f}{\partial n} \right\rangle_\gamma \right) \mathrm{d}S \\ -\int_\Gamma \left\langle \frac{1}{\rho}\frac{\partial q^f}{\partial n} \right\rangle_\gamma &\left([\![p^f]\!] + \frac{\sigma d}{\mathrm{j}\omega}\left\langle \frac{1}{\rho}\frac{\partial p^f}{\partial n} \right\rangle_\gamma \right) \mathrm{d}S + \int_\Gamma \frac{\sigma d}{\mathrm{j}\omega}\left\langle \frac{1}{\rho}\frac{\partial q^f}{\partial n} \right\rangle_\gamma \left\langle \frac{1}{\rho}\frac{\partial p^f}{\partial n} \right\rangle_\gamma \mathrm{d}S. \end{aligned} \tag{4.14}$$

Last step, the formulation is stabilized by a term weighted by λ, that:

$$\begin{aligned} a_I^*(q^f, p^f) = &\underbrace{-\int_\Gamma \left\langle \frac{1}{\rho}\frac{\partial p^f}{\partial n} \right\rangle_\gamma \left([\![q^f]\!] + \frac{\sigma d}{\mathrm{j}\omega}\left\langle \frac{1}{\rho}\frac{\partial q^f}{\partial n} \right\rangle_\gamma \right) \mathrm{d}S}_{\text{consistency}} \\ &\underbrace{-\int_\Gamma \left\langle \frac{1}{\rho}\frac{\partial q^f}{\partial n} \right\rangle_\gamma \left([\![p^f]\!] + \frac{\sigma d}{\mathrm{j}\omega}\left\langle \frac{1}{\rho}\frac{\partial p^f}{\partial n} \right\rangle_\gamma \right) \mathrm{d}S}_{\text{symmetry}} + \int_\Gamma \frac{\sigma d}{\mathrm{j}\omega}\left\langle \frac{1}{\rho}\frac{\partial q^f}{\partial n} \right\rangle_\gamma \left\langle \frac{1}{\rho}\frac{\partial p^f}{\partial n} \right\rangle_\gamma \mathrm{d}S \\ &\underbrace{+\lambda \int_\Gamma \left([\![q^f]\!] + \frac{\sigma d}{\mathrm{j}\omega}\left\langle \frac{1}{\rho}\frac{\partial q^f}{\partial n} \right\rangle_\gamma \right) \left([\![p^f]\!] + \frac{\sigma d}{\mathrm{j}\omega}\left\langle \frac{1}{\rho}\frac{\partial p^f}{\partial n} \right\rangle_\gamma \right) \mathrm{d}S}_{\text{stabilization}}. \end{aligned} \tag{4.15}$$

Above is the proposed *Nitsche-type* variational formulation to enforce robin-like pressure jump interface conditions. As seen that when $\sigma d = 0$, the bilinear form becomes the standard Nitsche's formulation that enforces the continuity of pressure at the interface as Zou et al., 2017 [119] with stability parameter λ. On the other hand, when choosing $\lambda = \mathrm{j}\omega/(\sigma d)$, this formulation is reduced to the *penalty-type* one eq. (4.9). In fact, with a clever expression of λ, the *Nitsche-type* formulation can be bounded between these two extreme cases to take advantages of both formulations. In addition, an appropriate choice of λ ensures the stability (coercivity) of the formulation above. All these aspects will be addressed in the discrete set-up.

4.2 Spatial discretization

The space discretization and enrichment is same with the first case presented in the former chapter section 3.2.1. The pressure field is approximated in a same form as eq. (3.4) $p \in \mathcal{P}_h$ but using generalized Heaviside function ($H(\mathbf{x})$) rather than "Ridge" function ($R(\mathbf{x})$) as the enrichment to introduce a strong discontinuity in the elements. The discrete *penalty-type* formulation retains the same properties as in continuous space, no additional discussion is needed. However, for *Nitsche-type* formulation, the average weighting γ_i and λ parameters were not yet determined. These two parameters depend on the mesh configuration and approximation.

We writte the *Nitsche-type* formulation eq. (4.15) in the discrete setting, such that:

$$a_\lambda(q_h^f, p_h^f) := a_B(q_h^f, p_h^f) + a_I^*(q_h^f, p_h^f) = \ell(q_h^f), \quad \forall q_h^f \in \mathcal{P}_h, \tag{4.16}$$

where a clever definition of λ on the interface integral is given as:

$$\lambda = \left(\frac{1}{\beta_h} + \frac{\sigma d}{\mathrm{j}\omega}\right)^{-1}, \tag{4.17}$$

where β_h is a discretization dependent parameters for which both configuration of mesh and approximation order have been taken into account. Unlike the stability analysis presented in Hansbo and Hansbo, 2004 [117] and Yedeg et al., 2016 [137], the element size h is already accounted implicitly in β_h to accommodate the high order approximation and non-matching discretization across the interface. This parameter is required to satisfy a specified condition to ensure the stability (coercivity) of the entire weak formulation a_λ, which is to be explained in the forthcoming subsection.

Such definition of λ provides a natural transition between two extreme cases as well: when the interface parameters vanish ($\sigma d/\omega = 0$), the whole discrete formulation turns into the standard Nitsche's formulation for enforcing continuity, with stability parameter β_h. While for $\beta_h \to \infty$, the formulation tends to approach the *penalty-type* one.

4.2.1 Stability analysis

In this subsection, we analyse the stability (coercivity) of the discrete *Nitsche-type* formulation. During the procedure, the condition needed to be satisfied for β_h in λ is also revealed.

The main ideas of the proof follow the principle described in Yedeg et al., 2016 [137], but with several differences that are the originalities of this part: (i) the effect of complex-valued materials has to be considered in the proof and (ii) a high-order X-FEM approximation is considered.

For the sake of analysis, the bilinear form a_λ is rewritten in the following way:

$$\begin{aligned} a_\lambda(q_h^f, p_h^f) &= a_B(q_h^f, p_h^f) \\ -\int_\Gamma \left(1-\lambda\frac{\sigma d}{\mathrm{j}\omega}\right) [\![q_h^f]\!] \left\langle \frac{1}{\rho}\frac{\partial p_h^f}{\partial n}\right\rangle_\gamma \mathrm{d}S &- \int_\Gamma \left(1-\lambda\frac{\sigma d}{\mathrm{j}\omega}\right) [\![p_h^f]\!] \left\langle \frac{1}{\rho}\frac{\partial q_h^f}{\partial n}\right\rangle_\gamma \mathrm{d}S \\ -\int_\Gamma \frac{\sigma d}{\mathrm{j}\omega}\left(1-\lambda\frac{\sigma d}{\mathrm{j}\omega}\right) \left\langle \frac{1}{\rho}\frac{\partial q_h^f}{\partial n}\right\rangle_\gamma \left\langle \frac{1}{\rho}\frac{\partial p_h^f}{\partial n}\right\rangle_\gamma \mathrm{d}S &+ \int_\Gamma \lambda [\![q_h^f]\!][\![p_h^f]\!]\mathrm{d}S. \end{aligned} \tag{4.18}$$

Two discretization-dependent norms are defined as:

$$\|p_h^f\| = \sum_i^2 \left(\left|\frac{\omega^2}{K_i}\right| \int_{\Omega_i} |p_h^f|^2 \mathrm{d}\Omega \right), \tag{4.19}$$

$$\begin{aligned} |||p_h^f||| = \sum_i^2 &\left(\left|\frac{1}{\rho_i}\right| \int_{\Omega_i} |\boldsymbol{\nabla} p_h^f|^2 \mathrm{d}\Omega + \left|\frac{\omega^2}{K_i}\right| \int_{\Omega_i} |p_h^f|^2 \mathrm{d}\Omega \right) \\ &+ \frac{1}{\beta_h}\int_\Gamma \left| \left\langle \frac{1}{\rho}\frac{\partial p_h^f}{\partial n}\right\rangle_\gamma \right|^2 \mathrm{d}S + \int_\Gamma |\lambda| \left| [\![p_h^f]\!] \right|^2 \mathrm{d}S. \end{aligned} \tag{4.20}$$

The detailed proofs of the following lemmas and theorem are provided in appendix C, we state only the most influential conclusions here.

Lemma 4.2.1. *Let $\beta_h > 0$, the function λ in definition eq.* (4.17) *satisfies:*

$$0 < |\lambda| \leq \beta_h, \tag{4.21a}$$

$$1 - \lambda\frac{\sigma d}{\mathrm{j}\omega} = \frac{\lambda}{\beta_h}, \tag{4.21b}$$

$$\left|\frac{\sigma d}{\mathrm{j}\omega}\left(1-\frac{\sigma d}{\mathrm{j}\omega}\right)\right| \leq \frac{2}{\beta_h}, \tag{4.21c}$$

$$\mathrm{Re}\,(\lambda) + \mathrm{Im}\,(\lambda) - \frac{1}{2}|\lambda| \geq \frac{1}{2}|\lambda|. \tag{4.21d}$$

Lemma 4.2.2. *The imaginary part of the bilinear form a_B in a_λ satisfies* $\mathrm{Im}\,(a_B(\bar{p}_h, p_h)) > 0, \quad \forall p_h \in \mathcal{P}_h$

Proof

$$\mathrm{Im}\left(a_B(\bar{p}_h^f, p_h^f)\right) = \sum_i^2 \mathrm{Im}\left(\frac{1}{\rho_i}\right) \int_{\Omega_i} |\boldsymbol{\nabla} p_h^f|^2 \mathrm{d}\Omega - \sum_i^2 \mathrm{Im}\left(\frac{\omega^2}{K_i}\right) \int_{\Omega_i} |p_h^f|^2 \mathrm{d}\Omega, \tag{4.22}$$

it is known that for porous materials, effective density ρ has a negative imaginary part, and effective compressibility K has a positive imaginary part so that damping due to thermal and viscous effect is introduced. Therefore, we have $\mathrm{Im}\left(\frac{1}{\rho_i}\right) \geq 0$ and $\mathrm{Im}\,(\omega^2/K) \leq 0$, the positivity of the whole term holds. □

Lemma 4.2.3. *There exists a discretization-dependent constant C_I such that (discrete inverse inequality):*

$$\int_\Gamma \left| \left\langle \frac{1}{\rho} \frac{\partial p_h^f}{\partial n} \right\rangle_\gamma \right|^2 \mathrm{d}S \leq C_I \sum_i^2 \int_{\Omega_i} \left| \frac{1}{\rho_i} \right| \left| \boldsymbol{\nabla} p_h^f \right|^2 \mathrm{d}\Omega, \tag{4.23}$$

where C_I depends on the polynomial approximation order and mesh regularity.

This constant can be obtained by solving generalized eigenvalue problems that will be presented in the following section.

With lemmas 4.2.1 to 4.2.3, the stability of the proposed formulation a_λ in the X-FEM discrete space can be proven by the following theorem 4.2.4.

Theorem 4.2.4. *For any $\beta_h \geq 16C_I$, where C_I is the constant in lemma 4.2.3, the bilinear form a_λ satisfies :*

$$|a_\lambda(p_h^f, p_h^f)| + \|p_h^f\|^2 \geq \frac{1}{4} |||p_h^f|||^2, \tag{4.24}$$

which is the Gårding inequality (refer to chapter 2 [145]) that is usually used to prove the coercivity of the variational formulation of the Helmholtz equations.

Up to here, we proved that if we set $\beta_h \geq 16C_I$, the discrete *Nitsche-type* formulation is coercive. The following question is how to evaluate the constant C_I in our discrete setting.

4.2.2 Evaluation of stabilization and weighting parameters

Classical strategy

It is seen that the constant C_I stems from the inverse inequality eq. (4.23). Indeed, this inequality in a discrete space is associated to the eigenvalues of a generalized eigenvalue problem proposed by Annavarapu et al., 2012 [166] as

$$\mathbf{A}\mathbf{x} = \alpha \mathbf{B}\mathbf{x}, \tag{4.25}$$

where matrix $\mathbf{A}$ and $\mathbf{B}$ are given in the scope of our problem as:

$$[\mathbf{A}]_{ij} = \int_{\Gamma_e} \left\langle \left| \frac{1}{\rho} \right| \boldsymbol{\nabla} N_i \right\rangle_\gamma . \mathbf{n} \left\langle \left| \frac{1}{\rho} \right| \boldsymbol{\nabla} N_j \right\rangle_\gamma . \mathbf{n} \, \mathrm{d}\, S, \tag{4.26a}$$

$$[\mathbf{B}]_{ij} = \int_{\Omega_e} \left| \frac{1}{\rho_i} \right| \boldsymbol{\nabla} N_i \boldsymbol{\nabla} N_j \, \mathrm{d}\Omega, \tag{4.26b}$$

where the weighting parameters γ_i need to be fixed a priori, and are chosen as $\gamma_1 = \gamma_2 = 0.5$ in the classical Nitsche's method. Then, the eigenvalue problem could be solved globally as

proposed in Griebel and Schweitzer, 2003 [167] or locally for each element as Dolbow and Harari, 2009 [133]. Herein, the solving procedure at the element-level is presented.

Before proceed the element-wise operation, let stress how the elementary matrix is like for the generalized eigenvalue operators. Here, we note that this matrix system is not identical for Heaviside enriched X-FEM and Cut-FEM. We give an example of the matrices $\mathbf{B}$ for these two bases within a linear element in reference coordinate $x \in [-0.5, 0.5]$[1], where interface is located in the middle of the element and with materials density $2|1/\rho_1| = |1/\rho_2|$:

$$\mathbf{B}_{cut} = \begin{bmatrix} 0.5 & -0.5 & 0 & 0 \\ -0.5 & 0.5 & 0 & 0 \\ 0 & 0 & 1 & -1 \\ 0 & 0 & -1 & 1 \end{bmatrix}, \quad \mathbf{B}_{xfem} = \begin{bmatrix} 1.5 & -1.5 & -0.5 & 0.5 \\ -1.5 & 1.5 & 0.5 & -0.5 \\ -0.5 & 0.5 & 1.5 & -1.5 \\ 0.5 & -0.5 & -1.5 & 1.5 \end{bmatrix}, \tag{4.27}$$

it is seen that unlike with the Cut-FEM basis where $\mathbf{B}_{cut}$ has two diagonal independent blocks by construction, the counterpart of X-FEM $\mathbf{B}_{xfem}$ has a full coupled matrix where no zero entities is found.

In fact, these two matrices are all rank deficient. In the case where a strong discontinuity is introduced into the approximation space, matrix $\mathbf{B}$ is singular with two zero eigenvalues (corresponding to the rigid body motion of two subdomains split by the interface). The associated null spaces are also the null space of $\mathbf{A}$, which leads to indeterminate eigenvalues that can not be used to stabilize the formulation. Therefore, the deflation procedure (Jiang et al., 2015 [135]) needs to be performed at first.

To this end, the null space of $\mathbf{A}$ and $\mathbf{B}$ needs to be found. The null space of $\mathbf{B}$ is known *a priori* in our spatial discretization. We mentioned in chapter 2 that different polynomials used as shape functions multiplied by enrichment function may lead to different elementary null space. The null spaces of Bernstein polynomial and hierarchical Lobatto polynomial need to be identified first. The combination of entities in the null space vector corresponds to the rigid body mode. In two-dimensional domain,the common null space basis of Bernstein shape function for triangular elements are vectors $\tilde{\mathbf{x}}_{\mathbf{B}}$:

$$\tilde{\mathbf{x}}_B = \left[\begin{array}{ccccc|ccccc} 1 & 1 & ... & 1 & 1 & 0 & 0 & ... & 0 & 0 \\ 0 & 0 & ... & 0 & 0 & 1 & 1 & ... & 1 & 1 \end{array}\right]_{2\times 3(p+1)}. \tag{4.28}$$

and for hierarchy Lobatto shape function $\tilde{\mathbf{x}}_{\mathbf{L}}$:

$$\tilde{\mathbf{x}}_L = \left[\begin{array}{ccccc|ccccc} 1 & 0 & ... & 0 & 1 & 0 & 0 & ... & 0 & 0 \\ 0 & 0 & ... & 0 & 0 & 1 & 0 & ... & 0 & 1 \end{array}\right]_{2\times 3(p+1)}. \tag{4.29}$$

[1] In these matrices, the degree of freedom are respectively order as $[N_1^-, N_2^-, N_1^+, N_2^+]$ for Cut-FEM and $[N_1, N_2, N_1H, N_2H]$ for X-FEM

where entries 0 and 1 correspond to the *dofs* associated to enriched and standard shape functions. With this null space, the first and last rows, columns of matrices $\mathbf{A}$ and $\mathbf{B}$ are deleted by calculating:

$$\tilde{\mathbf{A}} = \mathbf{A} - \tilde{\mathbf{x}}^T \mathbf{a}, \tag{4.30a}$$

$$\tilde{\mathbf{B}} = \mathbf{B} - \tilde{\mathbf{x}}^T \mathbf{b}, \tag{4.30b}$$

where $\mathbf{a}$ and $\mathbf{b}$ are the vectors of first and last row of $\mathbf{A}$ and $\mathbf{B}$, respectively. After this operation, the first and last rows of $\mathbf{A}$ and $\mathbf{B}$ becomes zeros so that the first/last rows and columns can be deleted from original matrices to obtain deflated matrix $\hat{\mathbf{A}}$ and $\hat{\mathbf{B}}$. Then, the constant C_I is obtained as the largest eigenvalue of the deflated eigenvalue problem:

$$\tilde{\mathbf{A}}\mathbf{x} = \alpha \tilde{\mathbf{B}}\mathbf{x}. \tag{4.31}$$

Note that the deflated matrix $\tilde{\mathbf{A}}$ may remain singular, but this will not lead to difficulty for solving the determinate eigenvalue problem.

Robust strategy

The choice of weighting average and stabilization parameter presented previously can unfortunately yield to overestimated stabilizations which may sometimes result in large condition number in the cases where large material contrasts are involved, or when elements are cut with very small volume fractions. To alleviate such numerical issues, the so-called γ-Nitsche was proposed by Annavarapu et al., 2012 [166] and was shown to be a robust method for linear triangular and tetrahedral elements. Jiang et al., 2015 [135] further extended the approach to high order elements with help of two one-sided inequalities, such that in our case:

$$\int_{\Gamma_e} \frac{\partial \bar{p}}{\partial n} \frac{\partial p}{\partial n} \, \mathrm{d}S \leq C_1 \int_{\Omega_e^-} \boldsymbol{\nabla} \bar{p} . \boldsymbol{\nabla} p \, \mathrm{d}\Omega, \tag{4.32a}$$

$$\int_{\Gamma_e} \frac{\partial \bar{p}}{\partial n} \frac{\partial p}{\partial n} \mathrm{d}S \leq C_2 \int_{\Omega_e^+} \boldsymbol{\nabla} \bar{p} . \boldsymbol{\nabla} p \, \mathrm{d}\Omega, \tag{4.32b}$$

in which constants C_i are also obtained as the maximum eigenvalues of two generalized eigenvalue problems associated to the above inequalities with two matrices for each side:

$$[\mathbf{A}]^- = \int_{\Gamma_e^{*-}} \boldsymbol{\nabla} N_i . \mathbf{n} . \boldsymbol{\nabla} N_j . \mathbf{n} \, \mathrm{d}S, \qquad [\mathbf{A}]^+ = \int_{\Gamma_e^{*+}} \boldsymbol{\nabla} N_i . \mathbf{n} . \boldsymbol{\nabla} N_j . \mathbf{n} \, \mathrm{d}S \tag{4.33a}$$

$$[\mathbf{B}]^- = \int_{\Omega_e^-} \boldsymbol{\nabla} N_i . \boldsymbol{\nabla} N_j \, \mathrm{d}\Omega, \qquad [\mathbf{B}]^+ = \int_{\Omega_e^+} \boldsymbol{\nabla} N_i . \boldsymbol{\nabla} N_j \, \mathrm{d}\Omega. \tag{4.33b}$$

Let us stress that the procedure proposed in Jiang et al., 2015 [135] was developed using Cut-FEM basis where the matrices originating from negative/positive sides are independent. One can readily extract the non-zero basis in elements, leading to matrices $[\mathbf{A}]^{\pm}$ and $[\mathbf{B}]^{\pm}$ composed of non-zero sub matrix that has only one *a priori* known null eigenvalue. The deflation approach is straightforward.

Here, despite the use of a one-sided quadrature strategy[2], the Heaviside enrichment couples all the *dofs* on the interface (see fig. 2.9 and eq. (4.27)), so that the block nature of the matrices is lost.

The corresponding matrices are of size of $3(p+1) \times 3(p+1)$ for order of p triangular elements. Such matrices have a null space of dimension three, which leads to a worse indeterminate eigenvalue system than before. To remove this type of singularity, a direct deflation could be conducted as with the previous strategy by eliminating three columns and rows of original matrices, respectively.

Alternatively, in order not to find the null space basis for each matrix and to perform the deflation three times, we propose to decouple the matrices and reduce their dimension first. As we know that only half of the *dofs* would be involved in the one-sided matrix if a Cut-FEM basis was considered, the decoupling procedure relies on a conversion of the Heaviside X-FEM basis to the one of Cut-FEM. The relationship between these two bases are revealed by eq. (2.36) with the transition matrix $\mathbf{T}$ eq. (2.37). Matrices $\mathbf{A}$ and $\mathbf{B}$ integrated on each side are multiplied by the transition matrix $\mathbf{T}$:

$$\mathbf{A}^{*\pm} = \mathbf{T}^T \mathbf{A}^{\pm} \mathbf{T}, \tag{4.34a}$$

$$\mathbf{B}^{*\pm} = \mathbf{T}^T \mathbf{B}^{\pm} \mathbf{T}, \tag{4.34b}$$

yielding that the decoupled matrices are in the form of:

$$\mathbf{A}^{*+} = \begin{bmatrix} \mathbf{A}^+ & \mathbf{0} \\ \mathbf{0} & \mathbf{0} \end{bmatrix}, \quad \mathbf{A}^{*-} = \begin{bmatrix} \mathbf{0} & \mathbf{0} \\ \mathbf{0} & \mathbf{A}^- \end{bmatrix} \tag{4.35a}$$

$$\mathbf{B}^{*+} = \begin{bmatrix} \mathbf{B}^+ & \mathbf{0} \\ \mathbf{0} & \mathbf{0} \end{bmatrix}, \quad \mathbf{B}^{*-} = \begin{bmatrix} \mathbf{0} & \mathbf{0} \\ \mathbf{0} & \mathbf{B}^- \end{bmatrix}, \tag{4.35b}$$

now, the dimension reduced matrices are obtained only taking the non-zero block in $\mathbf{A}^{*\pm}$, $\mathbf{B}^{*\pm}$ of size $3p \times 3p$ denoted by $\tilde{\mathbf{A}}^{*\pm}$ and $\tilde{\mathbf{B}}^{*\pm}$. Indeed, they are exactly the same as the ones obtained from Cut-FEM basis for two-sided systems. Then, the same deflation procedure as the one presented in the former section can be applied to obtain the eigenvalue constant C_i. Taking the effects of material's properties into account, we give the weighting parameters:

$$\gamma_i = \frac{1/(C_i|1/\rho_i|)}{(1/(C_1|1/\rho_1|) + 1/(C_2|1/\rho_2|))}, \tag{4.36}$$

with this weighting parameters, the lower bound of constant $C_{I_{min}}$ is derived as:

$$C_{I_{min}} = \frac{1}{1/(C_1|1/\rho_1|) + 1/(C_2|1/\rho_2|))}, \tag{4.37}$$

as seen that, this choice avoids a large stability parameter for the cases where $|1/\rho_1|/|1/\rho_2| \gg 1$ (large contrast) and $C_1/C_2 \gg 1$ (small volume fraction). In fact, substituting weights eq. (4.36)

[2]Matrices $[\mathbf{B}]^{\pm}$($[\mathbf{A}]^{\pm}$) are integrated only on one side of the element.

in the global system with matrices eq. (4.26) and applying the classical strategy, will yield an equivalent minimum value of C_I as eq. (4.37).

It is noted that eq. (4.37) is also equivalent to a more recently proposed analytical expression of the stability parameter [136] for high order Cut-FEM approximation, which can be adapted in our case, such that:

$$C_I = \frac{p(p-1+d^*)\text{meas}(\Gamma)}{d^*} \times \left(\frac{|1/\rho_1|\gamma_1^2}{\text{meas}(\Omega_{e1})} + \frac{|1/\rho_2|\gamma_2^2}{\text{meas}(\Omega_{e2})} \right), \tag{4.38}$$

in which d^* is dimension of simplex.

One can readily verify this equivalence in a 1D case ($d^* = 1$) by setting that interface cut the middle of elements to make $\text{meas}(\Omega_{e1}) = \text{meas}(\Omega_{e2}) = h/2$. Therefore, the constant C_I can be written as the function of elements size h, such that:

$$\frac{C_I}{h} = 2.p^2 \times \left(|1/\rho_1|\gamma_1^2 + |1/\rho_2|\gamma_2^2 \right). \tag{4.39}$$

We calculate the minimum of constants C_I as the function of element size (number of elements) under different polynomials degree in fig. 4.2. Fig. 4.2(a) represents the case with two identical media that $|1/\rho_1| = |1/\rho_2|$ which leads to $\gamma_1 = \gamma_2 = 0.5$. Fig. 4.2(b) plot for the case of large material contrast $\rho_2 = 10^5\rho_1$.

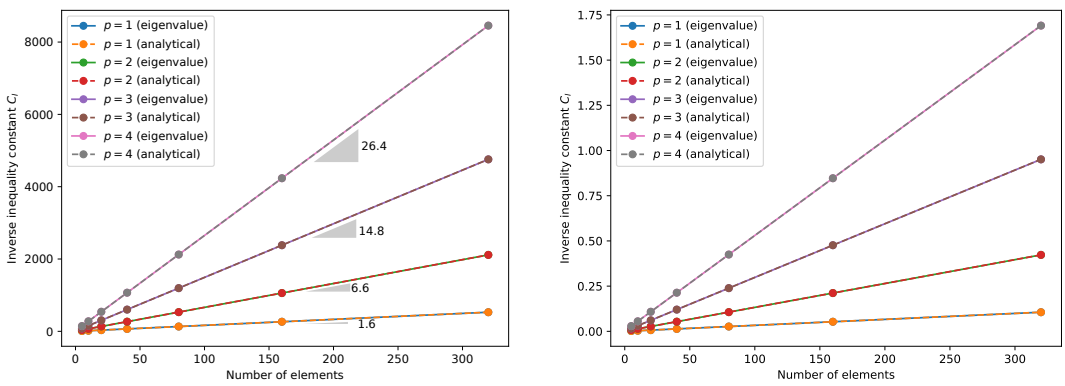

(a) (b)

Fig. 4.2.: Inverse inequality constant C_I w.r.t number of elements N and polynomials degree p for (a) two identical media problem and (b) large contrast of media ($\rho_2 = 10^5\rho_1$).

It is seen that C_I calculated from two approaches provides an identical value, which have a linear relationship with the number of elements N and the slops of each curve is factor to the p^2 from the coefficients in eq. (4.38) as:

$$C_I = \alpha p^2 N, \tag{4.40}$$

where α depends on the material contrast (and weighting parameter γ_i). For the two identical media , the slops are readily computed that $\alpha \approx 2|1/\rho_1|$ as shown in fig. 4.2(a). One can also observe that the stability parameter decreases when the contrast of media increases. In other words, variation of stability parameter is less sensitive to the space approximation (element size and polynomial degree) for large contrast materials problems. This would explain sensitivity curves of stability parameter in fluid-PEM coupling that will be presented in second part section 4.4.

4.3 Numerical verification

To verify the implementation of the proposed formulations and their performance using an X-FEM discretization, we conduct a series of numerical examples. All the porous media used in following problems are modelled as equivalent fluids with JCA parameters (Johnson et al., 1987 [33] and Champoux and Allard, 1991 [144]). A pressure jump model is used as interface law to represent thin acoustic resistive layers with various resistivities σ and thicknesses d. The porous materials used here as well as their properties are same as the ones in previous chapter. In the figures legends, *Nitsche-type* represents formulation eq. (4.15) and *penalty-type* is used for eq. (4.9).

4.3.1 Planar interface

Equivalent 1D problem: impedance tube

We first begin with a simple impedance tube problem, which is a common configuration to characterize porous materials. A normal unit velocity at $2,000$ Hz is prescribed on the left end of the tube and a rigid wall is set at the right end as depicted in fig. 4.3. The air and a plastic foam are set as the two media in the tube, between which a perfect interface or an imperfect interface modelling a resistive film are both to be simulated. As the wave propagates only in the horizontal direction the waveform depends only on x, so that a one-dimensional mesh $\Omega = [-1, 1]$ is sufficient to obtain the solution. The interface is located at $x = 0$ and only cuts the central element of the mesh.

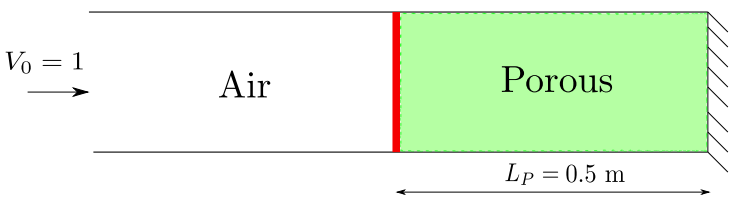

Fig. 4.3.: Illustration of impedance tube problem.

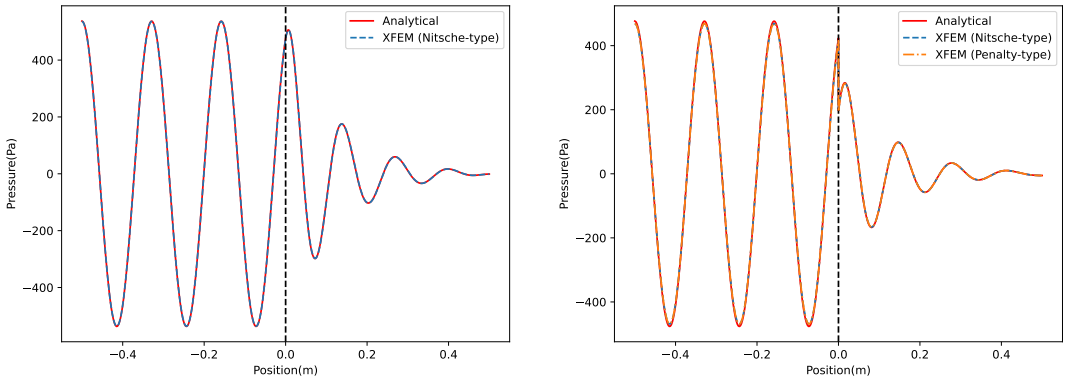

(a) (b)

Fig. 4.4.: Real part of pressure solution (in Pa) for (a) perfect interface problem ($\sigma d = 0$) and imperfect interface $\sigma d = 775\ \mathrm{N\,s\,m^{-3}}$ under $2,000$ Hz.

Fig. 4.4 shows the real part of the solution for the two types of interfaces, numerical solution are obtained with $D_\lambda = 60$. An obvious and progressive attenuation of the pressure is observed for both solutions for $x > 0$ because of the plastic foam. Only the *Nitsche-type* formulation is able to handle the perfect interface condition case ($\sigma d = 0$). When a thin woven film with flow resistivity $\sigma = 775.10^3\ \mathrm{N\,s\,m^{-4}}$ and thickness $d = 1\ \mathrm{mm}$ is inserted at the interface, both *Nitsche* and *penalty-type* formulations can account for the pressure drop caused by this film. All the numerical solutions are in great qualitative agreement with the analytical ones.

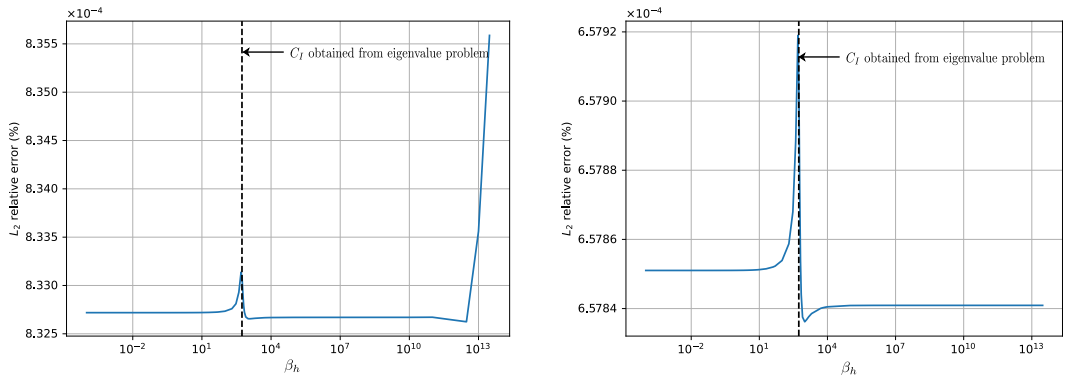

(a) (b)

Fig. 4.5.: Sensitivity of the relative error to the stability parameter β_h in function λ for (a) perfect interface and (b) imperfect interface($\sigma d = 775\ \mathrm{N\,s\,m^{-3}}$).

In order to further quantify the numerical properties of the proposed formulations, the convergence is to be examined. Before that, the sensitivity of the accuracy to variations in the stability parameter β_h needs to be identified for *Nitsche-type* formulation. This allows us to corroborate the stability criterion that was derived from our coercivity proof. We solve the same problems, conducting a set of numerical experiments through sweeping the value of β_h using the same discretization D_λ. Global errors are evaluated in fig. 4.5 for perfect and imperfect interface. For

both types of interface, a 'spike' in the error occurs when β_h is very close to the discretization constant C_I, which confirms our proof of stability that requires $\beta_h \geq 16C_I$. Then, a quite large range of β_h where the error remains to be 'optimal' is observed, which implies that the choice of the stability parameter is less restricted in regard to obtaining an accurate solution. Similar results have also been reported in Embar et al., 2010 [134].

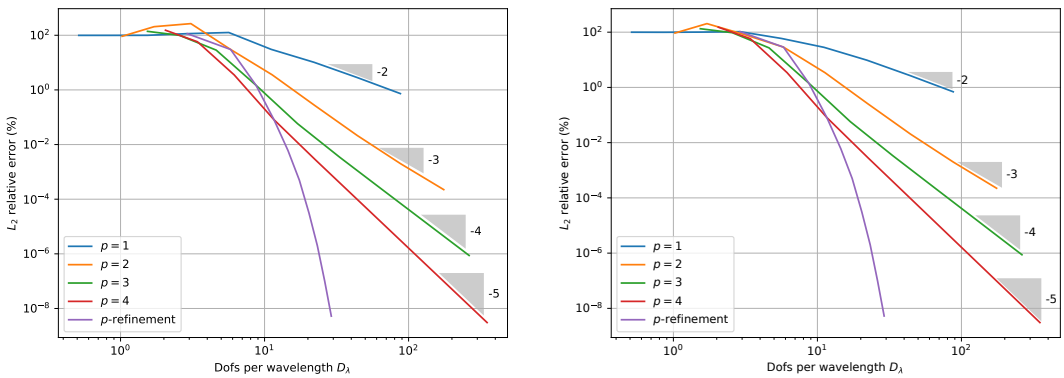

(a) (b)

Fig. 4.6.: L^2 convergence of Nitsche-type formulation for (a) perfect and (b) imperfect interface ($\sigma d = 775\ \mathrm{N\,s\,m^{-3}}$) condition.

Now, we monitor the convergence of the proposed method for the perfect and imperfect interface cases with prescribed physical parameters. h-refinement is conducted with a base discretization about $D_\lambda = 1$ and split the mesh sequentially six times under linear, quadratic, cubic and quartic elements, respectively. p-refinement is also performed by increasing interpolation order until $p = 10$ with the base mesh. The stabilization parameter is chosen as $\beta_h = 16C_I$, with C_I calculated by the robust strategy described in section 4.2.2. Fig. 4.6 shows convergence curves of relative global error for two types of interface. The optimal rates of convergence $\mathcal{O}(h^{-(p+1)})$ are reached for every polynomial degree after a pre-asymptotic stage where the known *rule of thumb* is also verified. Moreover, p-refinement, as expected, exhibits an exponential rate of convergence compared to h-refinement one as reported in Bériot et al., 2013 [75] for Helmholtz equation. To conclude, we showed that the proposed formulation which enforces a discontinuous interface law leads to optimal convergence rates as for the classical Helmholtz equation.

The conditioning of the general global stiffness matrix (stiffness plus mass) is also worth being assessed, as it is associated to the stability and efficiency of the resolution procedure. The plot of the variation of the condition number of the global matrix with respect to β_h for different σd is shown in fig. 4.7. Remind that the frequency affects the pressure drop at the interface as well, since this behaviour depends on the ratio $\sigma d/\omega$. Here, to avoid changing the whole solution, only σd is varied under a fixed frequency. First, little 'spikes' on the conditioning close to the constant C_I are observed as in the global error for all σd. Second, all the condition numbers tend to an asymptotic value when β_h is large enough. In fact, these asymptotic

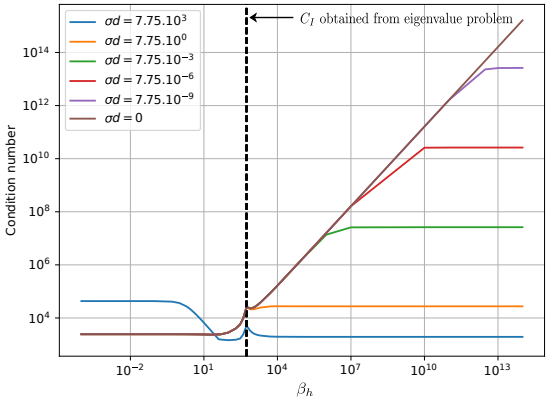

Fig. 4.7.: Sensitivity of conditioning number w.r.t the stability parameter β_h ($p = 3$) for different film parameters σd.

condition numbers correspond exactly to those of the *penalty-type* formulation, implying that the conditioning of the proposed *Nitsche-type* is also bounded for imperfect interfaces because of the definition of the complex-valued λ.

In contrary to the global error shown previously, the condition number is more sensitive to β_h when σd is smaller and for perfect interface. The stability parameter β_h may not be chosen too large to yield a large (ill) conditioned linear systems. We observe that the *Nitsche-type* is able to offer a stable conditioning when stability parameter is chosen about $\beta_h = 16C_I$. Together with the plot of global error fig. 4.5, the lower bound of β_h seems to be the best choice for the stability parameter to obtain the 'optimal' solution in terms of accuracy and conditioning.

Finally, it is known that penalty methods may suffer from ill-conditioning and cannot offer an accurate solution when the penalization parameter becomes very large. This issue drives us to investigate the behaviour of the proposed *Nitsche-type* formulation with the optimal stability parameter for the near-perfect interface case. The convergence and conditioning of the formulation under a h-refinement are examined for three gradual decreasing σd in fig. 4.8. The ones for *penalty-type* formulation are also calculated as a comparison.

The curves corresponding to *Nitsche-type* formulations are all overlapped for both convergence and condition number. Furthermore, optimal convergence rates are observed. In terms of *penalty-type* results, optimal convergence is only maintained for $\sigma d = 1.10^{-5}\ \mathrm{N\,s\,m^{-3}}$, and is completely degraded for $\sigma d = 1.10^{-15}\ \mathrm{N\,s\,m^{-3}}$ beyond certain D_λ. In addition, the *penalty-type* condition numbers are all larger than the ones in *Nitsche-type*. In the literature, these poor convergences are usually attributed to the ill-conditioning (see Ager et al., 2019 [165]). We emphasize that the condition numbers do not increase significantly (even decrease) during the h-refinement. In addition, although these conditioning is much higher, converged solutions should still be obtained when the direct solver is used. Hence, the conditioning should not be the main reason leading to such poor convergence of the solution. It is more probably because under these pressure drop parameters, interface conditions are enforced too strictly

to be able to cope with the other bulk terms in the formulation. We will revisit this aspect in two-dimensional problems to verify this conclusion. Nevertheless, the *Nitsche-type* formulation shows an identically great performance for any pressure jump parameters, whereas the *penalty-type* condition does not for the cases of small σd.

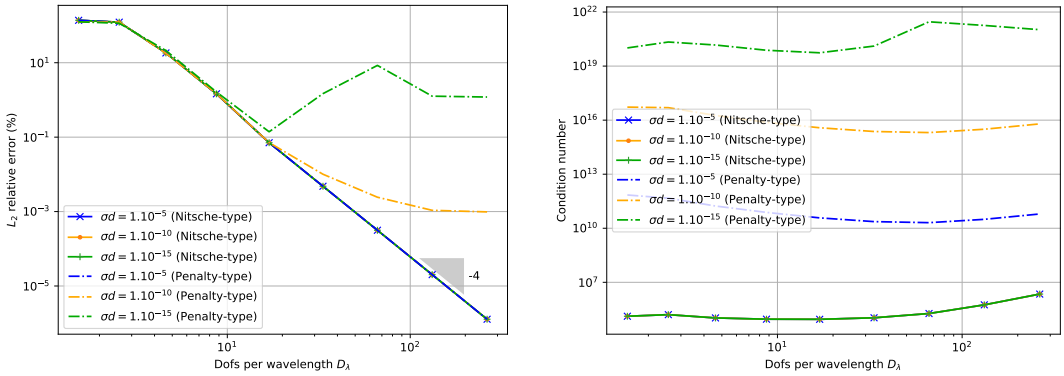

(a) (b)

Fig. 4.8.: (a) L^2 convergence and (b) conditioning of *Nitsche-type* and *penalty-type* formulation for different σd ($p = 3$).

Two-dimensional oblique incident problem

To validate the results obtained in the equivalent one-dimensional problem and to account for the effects of mesh configuration, we consider the same two-dimensional benchmark as in former chapter. The difference is that the computational domain Ω is discretized by unstructured triangular elements, as illustrated in fig. 4.9(a). It is clear that for such mesh, the interface intersects elements in different manner, which allows us to test the robustness of methods with respect to cut elements. Again, the foam medium is modelled by a JCA equivalent fluid and the pressure jump condition is prescribed at the interface to represent the thin layer.

Fig. 4.9(b) gives an example of the corresponding real part of the pressure field using such mesh, solved by the *Nitsche-type* XFEM. An incident plane wave tilted by $\pi/4$ rads under $2,000$ Hz is modelled, and an imperfect interface with $\sigma d = 775.10^3 \times 1.10^{-3}\ \mathrm{N\,s\,m^{-3}}$ is considered. Apart from the attenuation of the pressure field and a change of propagation direction due to the material heterogeneity, pressure drop at the interface is observed as in 1D configuration.

For the proposed *Nitsche-type* formulation, the stability parameter has to be first computed. To highlight the difference between the classical and robust strategies proposed in section 4.2.2 considering the material heterogeneity (density of air and considered foam are $|\rho_a| = 1.213\ \mathrm{kg\,m^3}$, $|\rho_f| = 29.4\ \mathrm{kg\,m^3}$, respectively) and small portion of cut elements, we illustrate in fig. 4.10 the element-wise β_h along the interface obtained by the two strategies under a cubic polynomial approximation ($p = 3$). In general, the classical strategy provides larger β_h than the robust

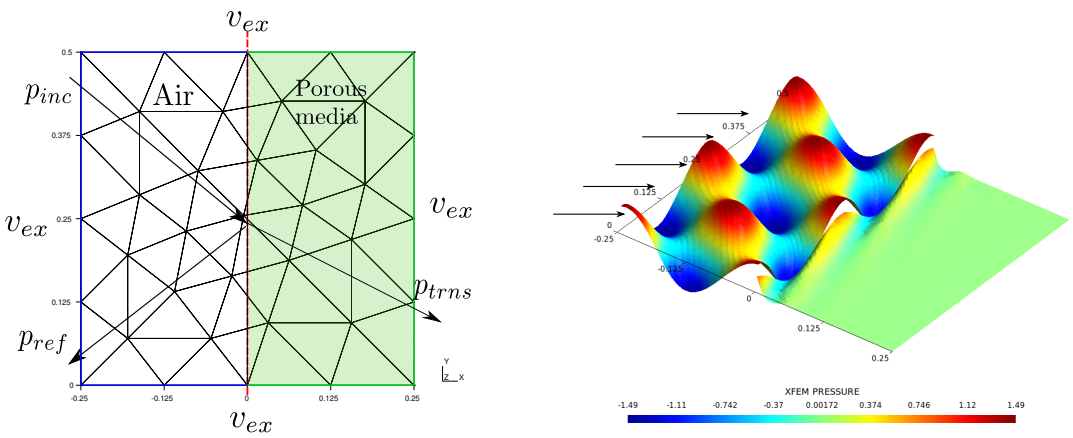

(a) (b)

Fig. 4.9.: (a) Problem set-up and (b) example of solution for real part pressure (unit in Pa) within X-FEM.

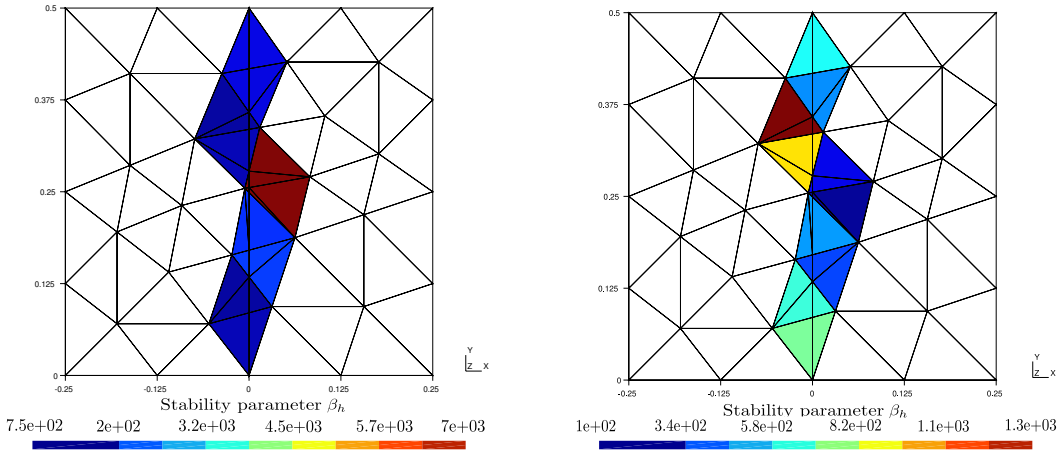

(a) (b)

Fig. 4.10.: Evaluation of stability parameter β_h by (a) classical strategy ($\gamma = 0.5$) and (b) robust strategy (γ-Nitsche).

one. The element with the smallest cut portion lead to the largest stability parameters (deep red in fig. 4.10(a)) which is consistent with what was observed using the classical Nitsche's method. By contrast, the robust strategy averages the two constants C_i on each side with appropriate weightings, yielding a much smaller stability parameters for the same element. It is worth reminding that for Nitsche's method, increasing the stability parameter by one or two orders of magnitude (as observed here) does not lead to any incorrect or non-converged solution as observed in the previous 1D case. Indeed, for problems involving a large contrast in the material properties (for instance a 10^{10} ratio as investigated in Jiang et al., 2015 [135]), classical Nitsche's method will lead to deteriorated results. Although we are not in the case of such large materials contrast, the robust strategy for computing the stability parameter β_h is still employed, without exception, for all the following calculation to obtain the 'optimal' performance of the *Nitsche-type* formulation.

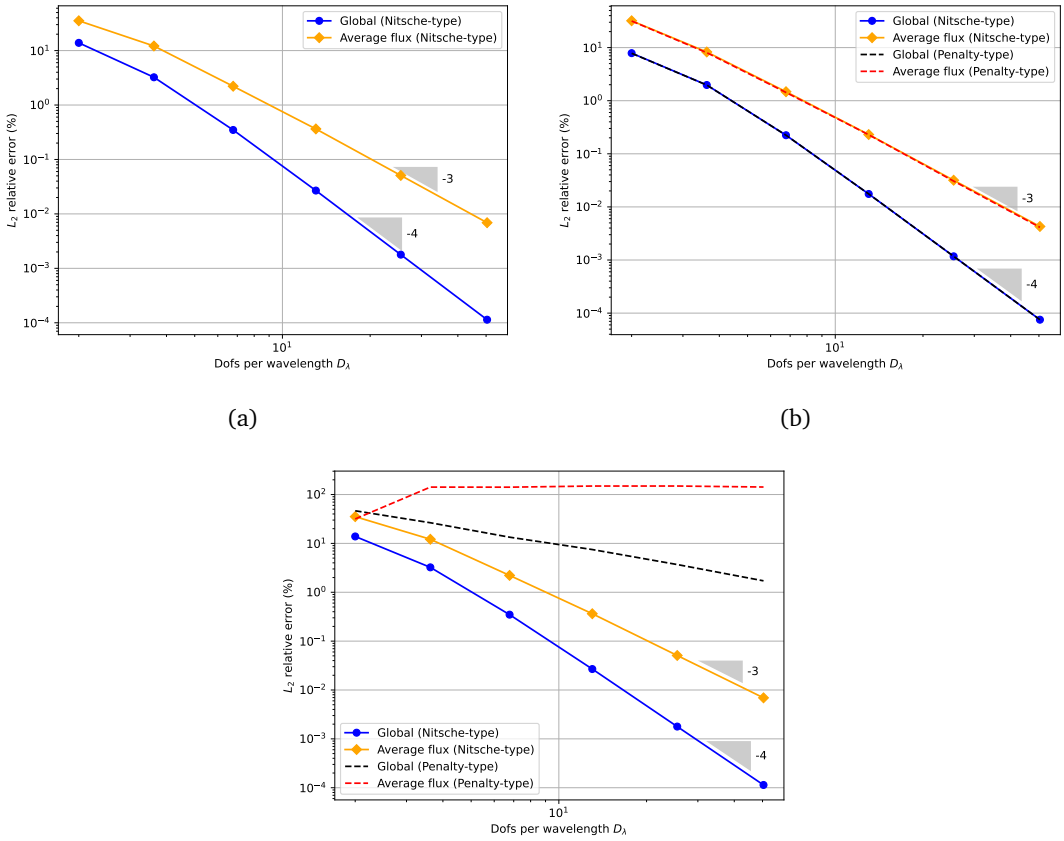

Fig. 4.11.: Global error on bulk and average interfacial flux for (a) perfect interface; (b) imperfect interface ($\sigma d = 775 \mathrm{N\,s\,m^{-3}}$); (c) near-perfect interface ($\sigma d = 1.10^{-15} \mathrm{N\,s\,m^{-3}}$).

The convergence is then analysed, where, in addition to the global error over the domain, the average flux of two sides along the interface is also evaluated to assess the performance of the formulations to capture the local secondary variable. For the sake of brevity, only the results for polynomials degree $p = 3$ are presented. Figs. 4.11(a) and 4.11(b) depict the convergences for perfect and imperfect interfaces with realistic film parameter $\sigma d = 775\ \mathrm{N\,s\,m^{-3}}$. *Nitsche-type* formulation achieves an optimal convergence rate regarding both global solution and average interfacial flux $\mathcal{O}(h^{-p})$ for the two types of interface conditions. *Penalty-type* formulation is not able to impose the perfect interface condition, but exhibits a similar convergence behaviour for imperfect interface. As for the previous numerical example, we compare the convergence behaviour of the two formulations for near-perfect interfaces such when $\sigma d = 1.10^{-15}\ \mathrm{N\,s\,m^{-3}}$, shown in fig. 4.11(c). *Nitsche-type* formulation can still give an optimal convergence with a similar level of error as the two previous interface parameters. However, both global solution and interfacial flux fails to converge for *penalty-type* formulation. These curves confirm the results found within the 1D configuration.

To identify how the *Nitsche-type* formulation behaves, with respect to the value of the interface parameters σd and the divergence of solution within *penalty-type* formulation for small σd. The

variation of solution accuracy and conditioning of the discrete system are evaluated with the decreasing σd.

In order to pay more attention to the solution at the interface, we define two additional error indicators at the interface that are local pressure error along the interface:

$$\varepsilon^{l}_{L^2} = \frac{\left(\int_{\Gamma^*} \left|p^f_{\mathrm{XFE}} - p_{\mathrm{ref}}\right|^2 \mathrm{d}S\right)^{1/2}}{\left(\int_{\Gamma^*} \left|p^f_{\mathrm{ref}}\right|^2 \mathrm{d}S\right)^{1/2}} \times 100\%, \tag{4.41}$$

and local pressure jump (difference) $[\![p]\!]$:

$$\varepsilon^{j}_{L^2} = \left(\int_{\Gamma^*} \left|[\![p^f]\!]_{\mathrm{XFE}} - [\![p^f]\!]_{\mathrm{ref}}\right|^2 \mathrm{d}S\right)^{1/2}. \tag{4.42}$$

The value of $[\![p^f]\!]_{\mathrm{ref}}$ varies (decreases) with respect to σd. Therefore, in order to avoid a large error indicator, the absolute error rather than relative error is calculated for the pressure jump error.

Fig. 4.12 plots the relative average pressure error, average interfacial flux error, absolute pressure jump error and condition number computed in asymptotic stage (forth discretization point in the convergence curves fig. 4.11) as function of $(\sigma d)^{-1}$. The effects of frequency are considered as well in this study by taking a low 10 Hz and a medium $1,000$ Hz frequency excitation. We recall that, the frequency changes the properties of porous media in JCA model, the whole problem and the D_λ under same mesh.

In general, the *Nitsche-type* formulation with the 'optimal' stability parameter, as expected, delivers a stable trend over the entire band of interface parameters for all metrics. Moreover, it exhibits a lower error level in a large range of interface parameter band compared to the *penalty-type* one for local pressure value fig. 4.12(a) and the interfacial flux fig. 4.12(b), especially under the low frequency excitation.

Interestingly, the curves corresponding to the *penalty-type* formulation exhibit two distinct regimes for these metrics. Regarding the local pressure and interfacial flux, it gives a comparable accuracy as the one in *Nitsche-type* at the beginning until about $(\sigma d)^{-1} = 10^{10}$, where the condition numbers are slightly larger. Then, from $(\sigma d)^{-1} = 10^{10}$ to 10^{14}, the error increases brutally, while its conditioning is still in a reasonable range for which the direct linear solver should be able to give an accurate solution. After $(\sigma d)^{-1} = 10^{14}$, even the conditioning keeps increasing with a linear rate, the error remains almost constant. It is seen that there is no strong correlation between convergence loss and conditioning for the *penalty-type* formulation.

When it comes to the error of pressure jump condition, the ones of *penalty-type* continue to decrease with a linear rate after a short range of superimposition with the *Nitsche-type* until around $(\sigma d)^{-1} = 10^6 - 10^{10}$, and after that, the error stays constant. This phenomenon indicates

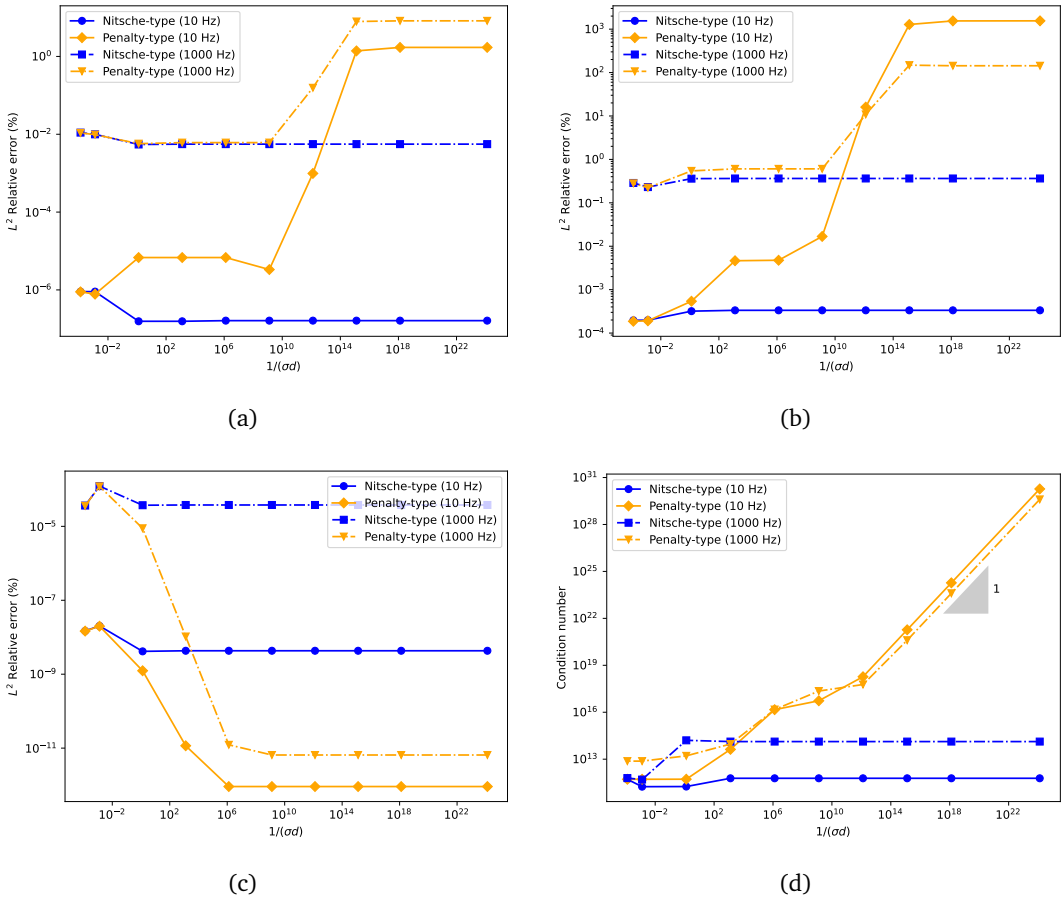

Fig. 4.12.: (a) Relative error of pressure; (b) relative error of interfacial flux; (c) absolute jump error; (d) condition number of global matrix with respect to the variation of σd under 10 Hz and $1,000$ Hz.

that the physical parameters in the interface term of *penalty-type* not only determine the value of pressure jump, but also work as the penalty parameter to penalize the interface condition. The larger the penalty parameter is, the better the interface condition is enforced. That is why we observe a linear slop for the error during the decreasing of σd. However, this 'better' imposition of pressure jump at the interface does not reflect a lower error on the pressure itself and interfacial flux. Contrarily, only the pressure difference $[\![p]\!]$ at the interface is verified, rather than the whole solution. When σd is beyond a certain value, 10^{10} here, the limit of precision for pressure jump is reached, larger σd solely makes the elementary matrices along the interface too stiff to represent the real solution properly. What is more, when $(\sigma d)^{-1}$ become sufficiently large, the interface integral takes control of the whole formulation behaviour. This also explain a linear increasing of the condition number in the range of constant error in pressure jump.

In summary, the proposed *Nitsche-type* formulation within X-FEM presents a stability in terms of accuracy and conditioning with respect to interface parameters. Better prediction of interfacial flux than the *penalty-type* one is observed as well.

4.3.2 Curved interface: cylinder scattering problem

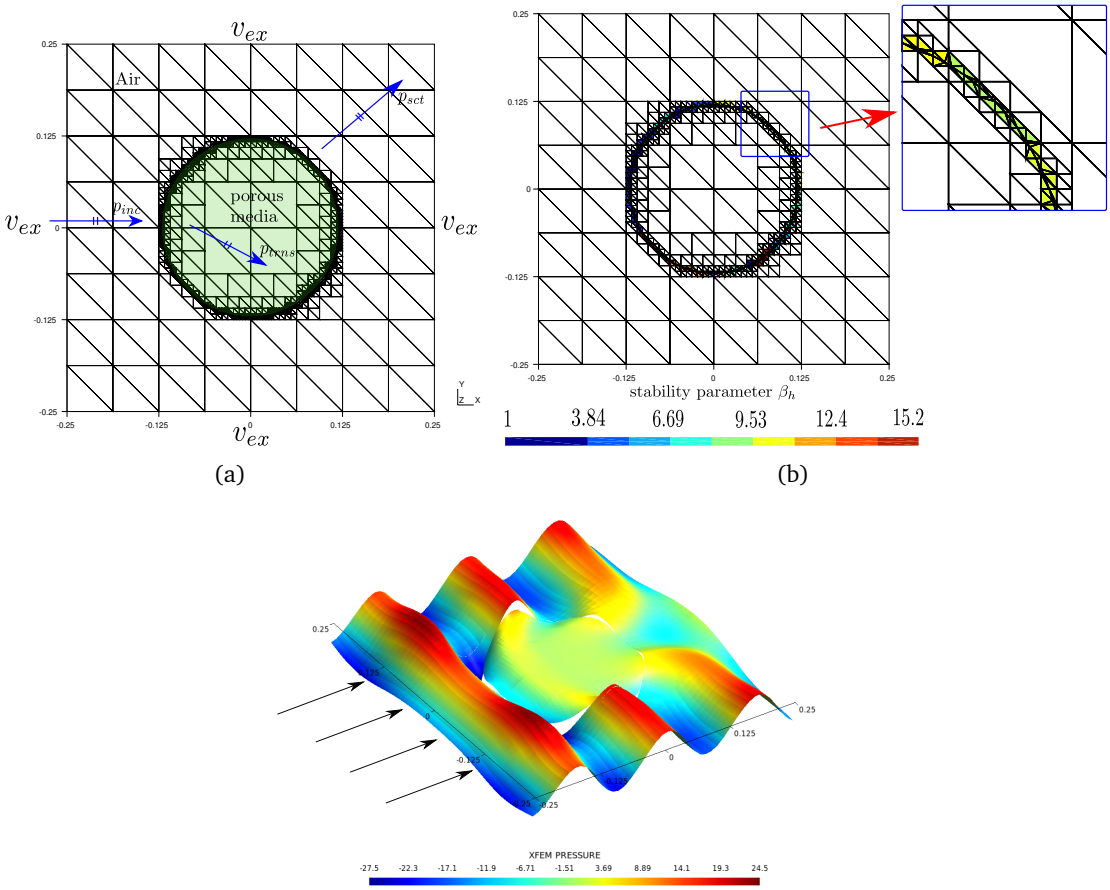

(a) (b)

(c)

Fig. 4.13.: (a) Problem set-up and mesh with refined elements for curved interface; (b) example of real part pressure (in Pa) under excitation of $2,000$ Hz ($p = 4$).

Same as before, a porous scattering problem with curved geometry is tested. Same mesh and boundary conditions are used as in previous chapter. The scatterer profile (circle of radius $r_0 = 0.12$ m origin at $x = 0$) is described by a piecewise linear level-set function. In contrast to the previous chapter, the interface is defined on a refined geometric mesh to recover the optimal rate of convergence. Fig. 4.13(a) illustrates the problem set-up and the three times refined mesh for the geometry of the circle. The element-wise stability parameters β_h computed on this refined mesh are shown in fig. 4.13(b). We recall that although the level-set is defined on the refined mesh, the approximation of the solution is still performed on the uniform coarse mesh. The detailed relationship between approximation and geometric mesh size can be found in Legrain et al., 2012 [151] and Jiang et al., 2015 [135].

Fig. 4.13(c) visualizes an example of solution within *Nitsche-type* X-FEM using the corresponding mesh. The propagation of a plane wave interacts with the porous scatterer attached by a woven film $\sigma d = 775\ \mathrm{N\,s\,m^{-3}}$ under excitation of $2,000$ Hz. The dissipation and discontinuity of

pressure at the interface are simulated properly. Such complex waveform is represented smoothly on this relatively coarse mesh thanks to quartic elements.

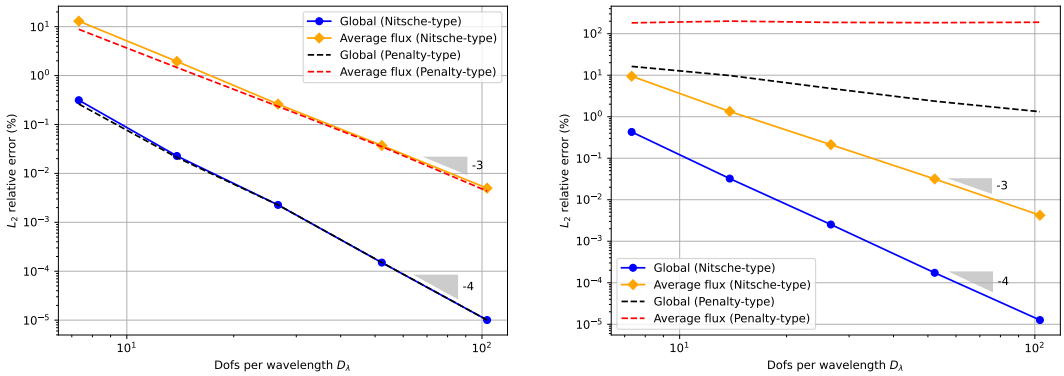

(a) (b)

Fig. 4.14.: Global error on bulk and average interfacial flux for (a) imperfect interface ($\sigma d = 775\mathrm{N\,s\,m^{-3}}$); (b) near-perfect interface ($\sigma d = 1.10^{-15}\mathrm{N\,s\,m^{-3}}$) for cylinder scatterer problem.

Again, the convergence analysis is carried out within the proposed methods. Fig. 4.14 plots the convergence under degree $p = 3$ of relative global error and average interfacial error in L^2 norm. For the parameters corresponding to a woven film at the interface in fig. 4.14(a), the two formulations lead to identically optimal convergence rates for the two error indicators, respectively. These results demonstrate also that optimal convergence rates can be obtained if the geometric error is mastered. As previously, the near-perfect interface condition is tested as shown in fig. 4.14(b). Optimal convergences are still obtained using the *Nitsche-type* formulation and maintain an error level which is similar to the imperfect interface. Like for the planar interface, the *penalty-type* is not able to converge for this problem with these near-perfect interface parameters, where the convergence of interfacial flux is completely degraded.

Up to now, the fluid-fluid coupling coping with pressure jump has been addressed where two variational formulations for enforcing the interface condition are investigated systematically. For the next part, following the same principle, the fluid-PEMs (Biot) coupling is to be explored.

4.4 Fluid-PEM (Biot) coupling

This part extends previous strategy to the fluid-PEM coupling where we have to treat a fluid-solid interface with a pressure jump condition. The porous material is modelled by mixed coupled Biot equations, all the interface and boundary conditions including the displacement of solid phase need to be rewritten.

4.4.1 Interface conditions and formulations

Like in fluid-fluid coupling, at the interface, thin porous layers causes a pressure difference due to its flow resistivity. As the thickness of this layer is relatively small, the conservation of normal component of total velocity/displacement holds as well. Therefore, the interface conditions on Γ reads:

$$p_1^f - p_2^{f(b)} = \sigma d \bar{v}_n^t, \quad \text{on}\,\Gamma, \tag{4.43a}$$

$$\frac{1}{\omega^2 \rho_1}\frac{\partial p_1^f}{\partial n} = \left(\tilde{\gamma}\mathbf{u}_n^s - \frac{1}{\omega^2 \rho_{\text{eq}}}\frac{\partial p_2^{f(b)}}{\partial n}\right), \quad \text{on}\,\Gamma, \tag{4.43b}$$

where the fluid density in PEM subdomain 2 is denoted by $(\bullet)_{\text{eq}}$. The normal velocity v_n^t expressed on the two sides of the interface are:

$$\bar{v}_n^t = \mathrm{j}\omega \bar{u}_n^t = \frac{\mathrm{j}\omega}{\omega^2 \rho_1}\frac{\partial p_1^f}{\partial n} = \mathrm{j}\omega\left(\tilde{\gamma}\mathbf{u}_n^s - \frac{1}{\omega^2 \rho_{\text{eq}}}\frac{\partial p_2^{f(b)}}{\partial n}\right), \quad \text{on}\,\Gamma. \tag{4.44}$$

It is seen that, unlike the two fluids coupling, the expression of the displacement is different at each side in this case. To be consistent with the variational formulation of the Biot mixed formulation, instead of velocity, the displacement is preferred to be used. We rewrite eq. (4.43) in a compact manner in terms of displacement as:

$$[\![p^f]\!] = \mathrm{j}\omega\sigma d u_n^t, \quad \text{on}\,\Gamma, \tag{4.45a}$$

$$[\![u_n^t]\!] = 0, \quad \text{on}\,\Gamma. \tag{4.45b}$$

Always keep in mind that the expression of u_n^t in the jump operator are different on the two sides of the interface, which is different from previous fluid-fluid coupling. Now that the interface conditions are obtained, the following section is devoted to enforce such conditions weakly in the variational formulations.

Penalty-type formulation

As the former two fluid coupling, the left-hand side of the variational formulation of the prescribed problem can be written with bulk and interface integrals. The bulk parts are the combination of bulk terms a_B in eq. (2.11) and eq. (2.13a), which will not be expanded here. In contrast, we focus on the interface terms, that are:

$$a_I := -\int_\Gamma q_1^f u_{n1}^t \mathrm{d}S + \int_\Gamma q_2^f u_{n2}^t \mathrm{d}S, \tag{4.46}$$

thanks to the eq. (4.45), the interface terms can be readily rewritten as

$$a_I := -\int_\Gamma \frac{1}{\mathrm{j}\omega\sigma d}[\![q^f]\!][\![p^f]\!]\mathrm{d}S. \tag{4.47}$$

As fluid-fluid coupling, a penalty-like interface integral is obtained where penalty parameters are resistivity σ, frequency ω and thickness d. In fact, this interface integral is identical with the one introduced in previous part with a factor of ω^2 for all the terms.

This *penalty-type* formulation may also suffer from the numerical issues as demonstrated in the first part, which motivates us to apply Nitsche's method to achieve a stable formulation.

Nitsche-type formulation

Same idea can be applied to derive the *Nitsche-type* formulation as in the fluid coupling case. With the continuity of total displacement u_n^t, we are able to define a numerical average quantity at the interface:

$$\bar{u}_n^t := \frac{\gamma_1}{\omega^2 \rho_1} \frac{\partial p^f}{\partial n} + \gamma_2 \left(\frac{1}{\omega^2 \rho_{eq}} \frac{\partial p^f}{\partial n} - \tilde{\gamma} \mathbf{u}^s . \mathbf{n} \right), \tag{4.48}$$

where the coefficients γ_i are the weighting parameters as in previous case. As mentioned previously, this average quantity plays an important role in controlling the conditioning of the linear system.

To make the expression slightly simpler and clearer, we combine the fluid terms together and rewrite this average quantity as:

$$\bar{u}_n^t := \left(\frac{1}{\omega^2} \left\langle \frac{1}{\rho} \frac{\partial p^f}{\partial n} \right\rangle_\gamma - \gamma_2 \tilde{\gamma} \mathbf{u}_n^s \right), \tag{4.49}$$

as seen that, compared to the fluid-fluid coupling, one more solid displacement quantity is added to the average operator of the gradient of the pressure.

Thus, the pressure drop condition with such numerical displacement is re-written as:

$$[\![p^f]\!] - \sigma d j \omega \left(\frac{1}{\omega^2} \left\langle \frac{1}{\rho} \frac{\partial p^f}{\partial n} \right\rangle_\gamma - \gamma_2 \tilde{\gamma} u_n^s \right) = 0. \tag{4.50}$$

Consequently, the interface term a_I in the variational formulation is rewritten as:

$$a_I^* := - \int_\Gamma [\![q^f]\!] \left(\frac{1}{\omega^2} \left\langle \frac{1}{\rho} \frac{\partial p^f}{\partial n} \right\rangle_\gamma - \gamma_2 \tilde{\gamma} u_n^s \right) \mathrm{d}S. \tag{4.51}$$

The same routine is followed as in former section, which begins by adding and subtracting term:

$$\int_\Gamma \mathrm{j}\omega\sigma d \left(\frac{1}{\omega^2} \left\langle \frac{1}{\rho} \frac{\partial q^f}{\partial n} \right\rangle_\gamma - \gamma_2 \tilde{\gamma} v_n^s \right) \left(\frac{1}{\omega^2} \left\langle \frac{1}{\rho} \frac{\partial p^f}{\partial n} \right\rangle_\gamma - \gamma_2 \tilde{\gamma} u_n^s \right) \mathrm{d}S,$$

where $\mathbf{v}^s$ is the test function of solid displacement $\mathbf{u}^s$. Then, symmetrizing the formulation with the pressure jump condition eq. (4.50) as:

$$-\int_\Gamma \left[[\![p^f]\!] - \sigma d j\omega \left(\frac{1}{\omega^2} \left\langle \frac{1}{\rho} \frac{\partial p^f}{\partial n} \right\rangle_\gamma - (1-\nu)\tilde{\gamma}\mathbf{u}_n^s \right) \right] \left(\frac{1}{\omega^2} \left\langle \frac{1}{\rho} \frac{\partial q_h}{\partial n} \right\rangle_\gamma - \nu_2 \tilde{\gamma} \mathbf{v}_n^s \right) \mathrm{d}S, \tag{4.52}$$

at the end, stabilizing with a λ term, we obtain the final formulation of *Nitsche-type* as:

$$\begin{aligned} a_I^* := & \underbrace{\int_\Gamma \left(\frac{1}{\omega^2} \left\langle \frac{1}{\rho} \frac{\partial p^f}{\partial n} \right\rangle_\gamma - \gamma_2 \tilde{\gamma} v_n^s \right) \left[[\![q^f]\!] - \sigma d j\omega \left(\frac{1}{\omega^2} \left\langle \frac{1}{\rho} \frac{\partial q^f}{\partial n} \right\rangle_\gamma - \gamma_2 \tilde{\gamma} v_n^s \right) \right] \mathrm{d}S}_{\text{consistency}} \\ & - \int_\Gamma \mathrm{j}\omega\sigma d \left(\frac{1}{\omega^2} \left\langle \frac{1}{\rho} \frac{\partial q^f}{\partial n} \right\rangle_\gamma - \gamma_2 \tilde{\gamma} v_n^s \right) \left(\frac{1}{\omega^2} \left\langle \frac{1}{\rho} \frac{\partial p^f}{\partial n} \right\rangle_\gamma - \gamma_2 \tilde{\gamma} u_n^s \right) \mathrm{d}S \\ & \underbrace{- \int_\Gamma \left[[\![p^f]\!] - \sigma d j\omega \left(\frac{1}{\omega^2} \left\langle \frac{1}{\rho} \frac{\partial p^f}{\partial n} \right\rangle_\gamma - \gamma_2 \tilde{\gamma} \mathbf{u}_n^s \right) \right] \left(\frac{1}{\omega^2} \left\langle \frac{1}{\rho} \frac{\partial q^f}{\partial n} \right\rangle_\gamma - \gamma_2 \tilde{\gamma} \mathbf{v}_n^s \right) \mathrm{d}S}_{\text{symmetry}} \\ & \underbrace{+ \lambda \int_\Gamma \left[[\![q^f]\!] - \sigma d j\omega \left(\frac{1}{\omega^2} \left\langle \frac{1}{\rho} \frac{\partial q^f}{\partial n} \right\rangle_\gamma - \gamma_2 \tilde{\gamma} v_n^s \right) \right] \left[[\![p^f]\!] - \sigma d j\omega \left(\frac{1}{\omega^2} \left\langle \frac{1}{\rho} \frac{\partial p^f}{\partial n} \right\rangle_\gamma - \gamma_2 \tilde{\gamma} u_n^s \right) \right] \mathrm{d}S}_{\text{stabilization}}. \end{aligned} \tag{4.53}$$

It can be easily verified that this formulation is consistent with original problem.

This formulation will be solved numerically using X-FEM space. The approximation and enrichment of fields is like eq. (3.9) but with Heaviside enrichment function. The problem in discrete setup reads: Find $p_h^f \in \mathcal{P}^h$, $u_h^s \in \mathcal{U}^h$ such that

$$a_B(q_h, p_h, u_h, v_h) + a_I^*(q_h, p_h, u_h^s, v_h^s) = \ell(q_h, v_h^s), \quad \forall q_h \in \mathcal{P}^h, v_h^s \in \mathcal{U}^h, \tag{4.54}$$

where the coefficient λ needs to be defined. Same idea is applied, we define a complex-valued expression to cover two extreme cases, that:

$$\lambda = \left(\frac{1}{\beta_h} + \sigma d j\omega \right)^{-1}. \tag{4.55}$$

For $\beta_h \to \infty$, the formulation approaches to the *penalty-type*, while, the Nitsche's method for perfect interface is returned when $\sigma d = 0$. β_h is a discretization dependent parameter, which is associated to the local element size and approximation degree. In addition, from the conclusion in the fluid-fluid coupling, this coefficient remains to be selected to recover the "coercivity" of the sesquilinear form in the sense that the solution is stable as function of β_h. We are not able to give any analytical proof for that up to this moment, but this aspect is to be inferred numerically in the following section.

4.4.2 Numerical verification

The numerical examples discussed in this section play two significant roles: (a) identify numerically the range of stability with respect to the stabilization parameter β_h in the proposed *Nitsche-type* formulation due to the lack of a theoretical proof; (b) verify the implementation and accuracy of the formulations.

Planar interface problem

As in fluid-fluid coupling, incident plane wave is calculated in an unstructured meshed domain. Exact Neumann boundary conditions (fluid velocity, in-vacuo stress and total displacement) are imposed on outer contours, respectively, as used for perfect interface in chapter 3. Same set-up for incident wave ($\pi/4$, $2,000\,\mathrm{Hz}$) and same porous media are considered but modelled by Biot's equations.

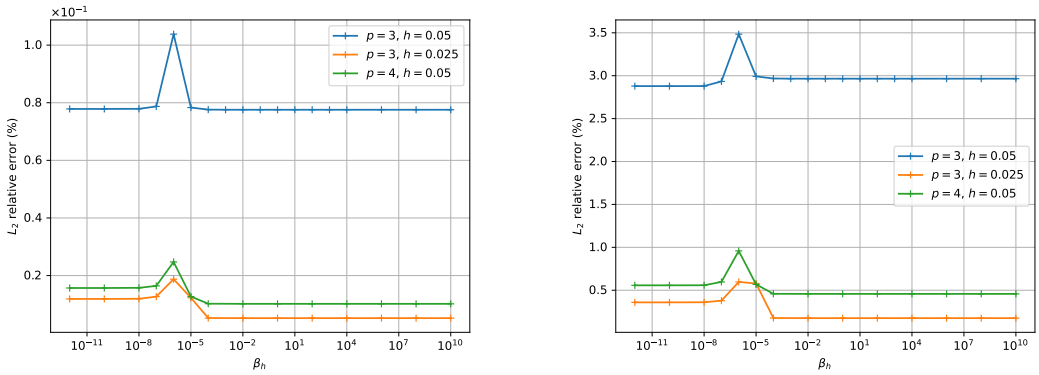

(a) (b)

Fig. 4.15.: Sensitivity of the relative error in L^2 norm to the stability parameter β_h for (a) pressure and (b) displacement field.

A parametric study is first conducted to identify the range of stability parameter β_h in the *Nitsche-type* formulation where the solution is able to stay stable. In order to characterize the influence of the discretization (mesh size h and polynomial order p), three curves of relative error under different h and p are computed for pressure and displacement, respectively (see fig. 4.15). The "spike" of error are monitored as well for both pressure and displacement, which is around 10^{-6}. This value is much smaller and seems not to be changed very much with respect to different discretization compared to the fluid-fluid coupling, leading to a larger stable range for the solution. This insensitivity of the stability parameter to the discretization can be attributed mainly to the large material contrast in the fluid-solid interface as explained previously. This feature greatly eases the choice of a stability parameter in fluid-PEM coupling without *a priori* theoretical analysis. One are permitted to use $\beta_h = 1$ in the following computations.

Fig. 4.16 exhibits a numerical example of real part solution computed by the *Nitsche-type* formulation, where a pressure jump interface is considered with $\sigma d = 775\,\mathrm{N\,s\,m^{-3}}$. The problem is much more difficult to converge due to the existence of large disparity between the two fields, noticing that displacement is nine orders of magnitude fewer than the pressure. A very high interpolation degree of $p = 10$ is necessary to use to obtain smooth solutions for both fields using such coarser mesh. Attenuation of pressure and displacement in porous subdomain is obtained. A strong discontinuity for the pressure at $x = 0$ is also captured very well.

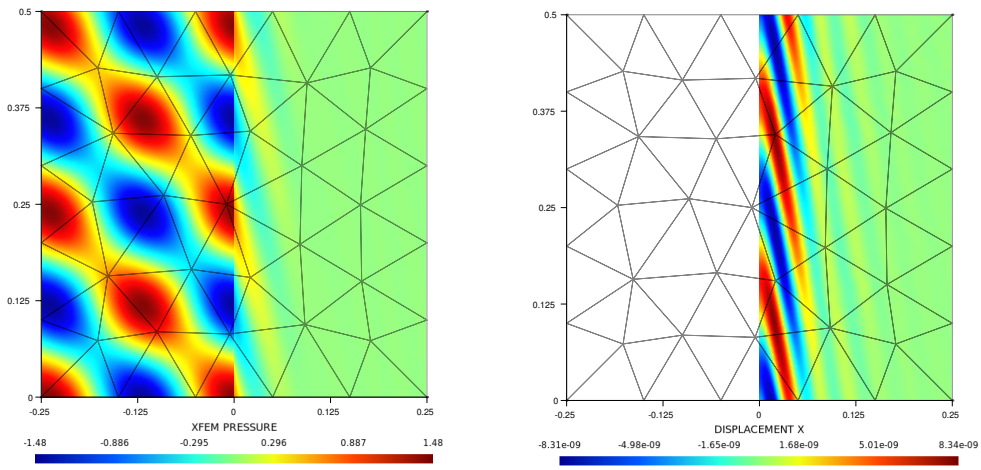

(a) (b)

Fig. 4.16.: Example of real part (a) pressure (in Pa); (b) solid displacement of x-direction (in m) under excitation of $2,000$ Hz ($p = 10$).

Then, h-convergence curves are calculated to quantify the accuracy of the numerical implementation and to verify the choice of stability parameter. *Penalty-type* formulation is also implemented to compare against Nitsche as a reference. As before, both imperfect with typical pressure jump parameter of resistive acoustic screen and near-perfect interfaces are tested. Fig. 4.17 illustrates the global convergences of primal variables (p^f and $\mathbf{u}^s$) with polynomial degree of $p = 4$ and the base mesh shown in fig. 4.16 that is split 5 times sequentially. First, pre-asymptotic ranges are observed for the displacement in both cases, which was already reported in chapter 3. This corresponds to the fact that large disparity exists between the scale of the displacement and pressure fields. Solid displacement is more difficult to be converged than fluid pressure. Secondly, regardless of interface parameter, optimal rate of convergence is obtained when using the *Nitsche-type* formulation with a constant stability parameter β_h. Similar as in fluid-fluid coupling, the *penalty-type* formulation is no longer capable to retain the optimal convergence for a near-imperfect interface.

Cylindrical scattering

The performance of the proposed formulations is then examined with a curved interface. Same mesh and boundary conditions are employed as for previous cases. Again, the two proposed

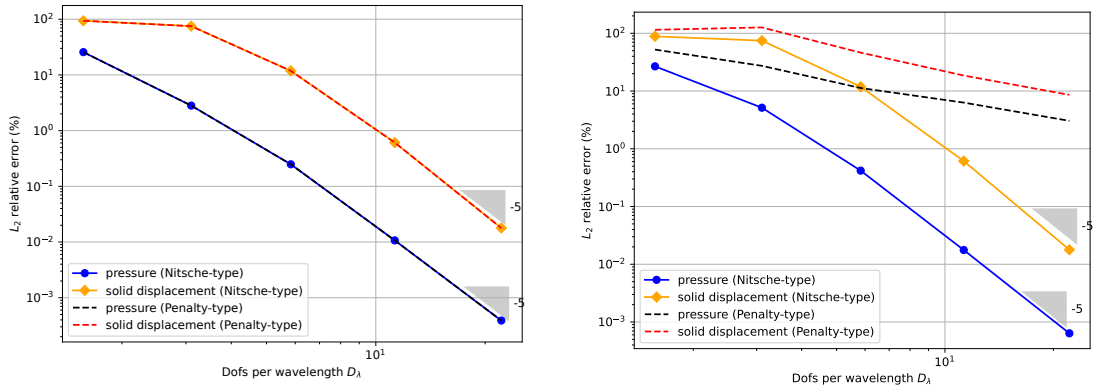

(a) (b)

Fig. 4.17.: Global error on fluid pressure and solid displacement for (a) imperfect interface ($\sigma d = 775\mathrm{N\,s\,m^{-3}}$); (b) near-perfect interface ($\sigma d = 1.10^{-15}\mathrm{N\,s\,m^{-3}}$) for planar interface problem.

formulations are used to enforce the pressure jump condition at the interface. From the observation in the previous planar interface case, the β_h in the *Nitsche-type* formulation is still chosen empirically as $\beta_h = 1$.

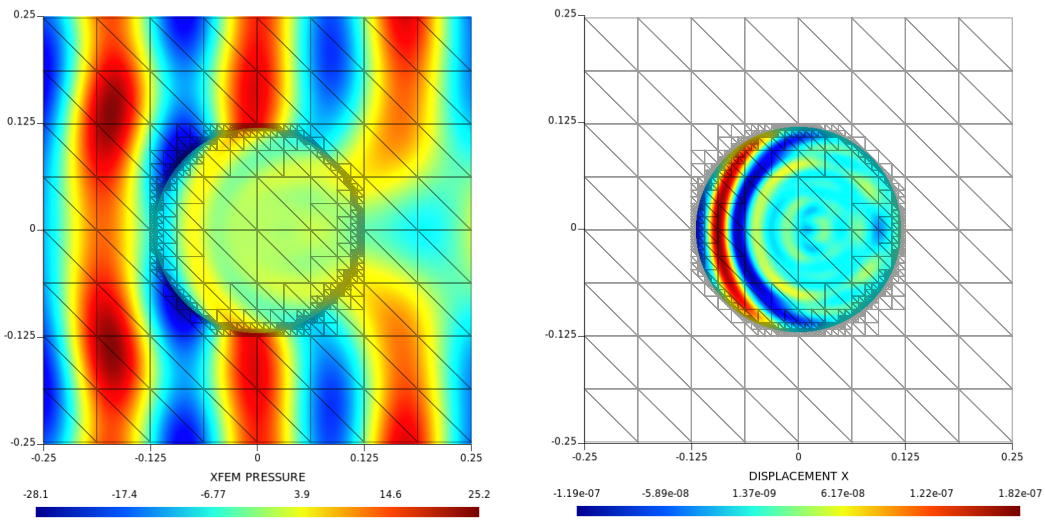

(a) (b)

Fig. 4.18.: (a) Example of real part pressure (in Pa); (b) solid displacement of x-direction under excitation of $2,000$ Hz ($p = 5$)

Fig. 4.18 shows the real part of the solutions under an excitation of $2,000\mathrm{Hz}$. Unlike for planar interface, a multi-refined strategy is used for the elements containing the interface to reduce the geometric error. The attenuation of fields and the discontinuity of the pressure at the interface are captured properly with a relatively coarse mesh, thanks to the high order approximation ($p = 5$ in this case).

The h-convergence of primal variables p^f and $\mathbf{u}^s$ are then analysed to verify the method quantitatively (see fig. 4.19). Same two pairs of interface parameters are tested, $\sigma d = 775\,\mathrm{N\,s\,m^{-3}}$ and $\sigma d = 1.10^{-15}\mathrm{N\,s\,m^{-3}}$ corresponding to a normal woven acoustic film and a near-perfect interface.

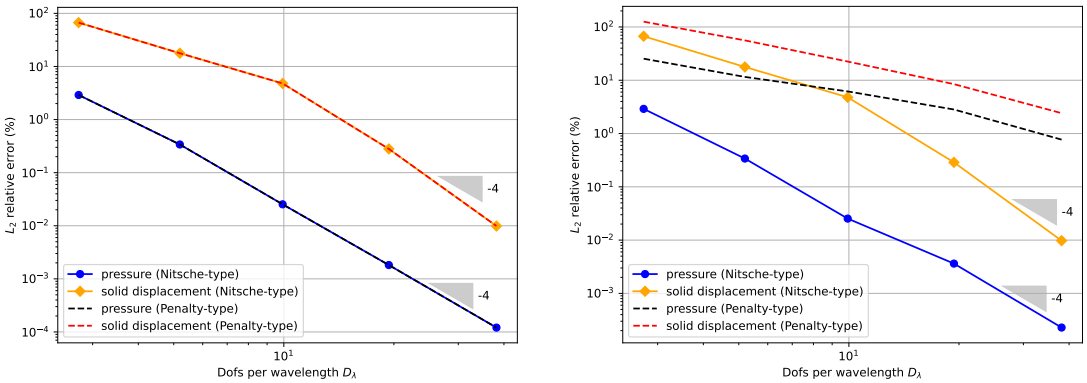

(a) (b)

Fig. 4.19.: Global error on fluid pressure and solid displacement for (a) imperfect interface ($\sigma d = 775\mathrm{N\,s\,m^{-3}}$); (b) near-perfect interface ($\sigma d = 1.10^{-15}\mathrm{N\,s\,m^{-3}}$) for cylinder scattering problem.

In general, the same pre-asymptotic stages are observed for displacement as in the previous case. As expected, for the typical film parameters, the two formulations exhibit a noticeable accordance. In regard with near-perfect interface, *penalty-type* formulation is not able to recover the rate of convergence and accuracy as *Nitsche-type*. It is emphasized that this stability/robustness of the *Nitsche-type* formulation is maintained even under the situation where the stability parameter β_h is chosen empirically as a very moderate constant. This provides more convenience and benefits in the engineering context when using the proposed formulation, meaning that less care needs be paid to select a suitable stability parameter.

4.5 Conclusion

This chapter focused on the enforcement of pressure jump interface condition which corresponds to a simplified model of thin acoustic film. To this end, *penalty* and *Nitsche-type* formulations were proposed for two different couplings: fluid-fluid and fluid-PEM.

In the fluid-fluid coupling, we provided a mathematical proof of the coercivity (stability) for the discrete *Nitsche-type* formulation for which we proposed a clever definition of λ to bound the numerical behaviour. Indeed, the numerical examples verified our proof and demonstrated that the accuracy and conditioning of the *Nitsche-type* formulation is bounded with the proposed complex function λ. The poor convergence of the *penalty-type* formulation was identified as well via a series parametric tests. The *penalty-type* surely leads to a bad conditioning of

the discrete system for small interface parameters. But the divergence behaviour is mainly originated from an over-enforcement of the interface condition rather than other bulk terms in the formulation.

Within the fluid-PEM coupling, same conclusion can be applied for the two formulations. *Nitsche-type* is more robust and stable with respect to the problem parameters. In addition, it was found and verified that because of the large material contrast that exists for fluid-solid coupling, a way larger range of β_h can be selected to retain the advantages of the *Nitsche-type* formulation with this coupling, which would simplify the implementation of the *Nitsche-type* formulation. The theoretical selection of the stability parameter is not clarified up to this moment, a further analytical study may be needed.

In summary, we compared two proposed variational formulation within X-FEM framework. In the range of typical film parameters $\sigma d \in [10^2 \text{ to } 10^4]\ \mathrm{N\,s\,m^{-3}}$, two formulations lead to a similar accuracy. In these cases, the *penalty-type* formulation might be more attractive because of its ease of construction and implementation compared to the *Nitsche-type* formulation using the robust strategy of selecting stability parameter. However, *Nitsche-type* formulation would be always a better choice if one conduct the parametric studies without *a priori* knowledge of physical parameters. In addition, if the interfacial flux is the prime interest, the *Nitsche-type* formulation is also preferred to use. The procedure to determine the stability parameter can be less costly using the analytical expression in Jiang et al., 2022 [136].

TMM enhanced interface

5

> *You can enjoy a grander sight by climbing to a greater height.*
> 欲穷千里目，更上一层楼
>
> — **Wang Zhihuan**
> (Deng Guan Que Lou)

For thin resistive porous layers, the pressure jump condition discussed in chapter 4 is restricted to low wave-number problems. This chapter elaborates a type of more comprehensive interface model enhanced by transfer matrix method (TMM) to represent thin acoustic layers. Before diving into the interface model, a general computational framework to account for thin layers in time-harmonic problems is first provided, which would be applicable for any acoustic media. Then, this approach is applied to typical sound absorbing systems where a series of interface models and general variational operators are proposed. The interface models will first be assessed analytically and compared with pressure jump model. Finally, typical numerical examples further verify the implementation and validate the proposed method.

5.1 Methodology and Formulations

In order to consider a more generalized interface model for various types of porous media, we reformulate our problem in a general manner. The problem is still defined in the same two-media configuration with non-thickness thin layer as fig. 4.1 in chapter 4. Without any loss of generality, for time-harmonic acoustic problems, a variational formulation for each subdomain Ω_i can be written with primal variable u_i with bilinear and linear form. After combining two subdomains, we obtain the final form as following: find $u_i \in \mathcal{U}$ such that:

$$\sum_{i}^{2} [\boldsymbol{a}_{Bi}(\bar{v}_i, u_i) + \boldsymbol{a}_{Ii}(\bar{v}_i, u_i)] = \sum_{i}^{2} \boldsymbol{\ell}_i(\bar{v}_i), \quad \forall v_i \in \mathcal{V}, \tag{5.1}$$

where $\bar{v}_i$ are the test functions of field u_i, which are in a dual Hilbert function space $\mathcal{V}$ of $\mathcal{U}$, $\bar{\bullet}$ denotes the complex conjugation. $\boldsymbol{a}_{Bi}(\bar{v}_i, u_i)$ represent general bilinear forms for bulk parts where stiffness and mass operators are included for steady state dynamic problems. $\boldsymbol{\ell}(\bar{v}_i)$

represent general linear forms for boundary conditions defined on each subdomain $\Omega_i \cup \partial\Omega_i$. Functional $\boldsymbol{a}_{Ii}(\bar{v}_i, u_i)$ are defined on the interface, responsible for the interface conditions.

Here, we focus on these interface terms, which will be connected to our thin layers model. The functionals $\boldsymbol{a}_{Ii}(\bar{v}_i, u_i)$ for two subdomains expanded at the interface are written as:

$$\boldsymbol{a}_{I1}(\bar{v}_1, u_1) + \boldsymbol{a}_{I2}(\bar{v}_2, u_2) = -\mathcal{K}_1 \int_\Gamma \bar{v}_1 \widetilde{u}_1 \mathrm{d}S + \mathcal{K}_2 \int_\Gamma \bar{v}_2 \widetilde{u}_2 \mathrm{d}S, \tag{5.2}$$

with $\widetilde{u}_i$ are given by prescribed interface conditions, and can normally be expressed as a function of the normal gradient of field u_i defined as the dual variable at the interface:

$$\widetilde{u}_i = f(\boldsymbol{\nabla} u_i . \mathbf{n}), \tag{5.3}$$

where the opposite signs in eq. (5.2) come from the outgoing normal which is opposite for the normal vector of the second subdomain at the interface Γ. Coefficients $\mathcal{K}_i$ represent a series of constants related to the media properties. To solve eq. (5.1) within the framework of the finite element method, interface conditions need to be determined first and applied in eq. (5.2).

Similar to the imposition of Neumann boundary conditions, the function of dual variables $\widetilde{\bullet}$ in the interface integral eq. (5.2) is commonly assigned with a prescribed function /expression. Under inspiration of Fluid-Structure Interaction (FSI), the variables on both sides of the interfaces might be expressed one from the others, resulting in coupling terms at the interaction interface. Therefore, we are able to find a linear relationship between primal and dual variables for subdomains in the problems of interest. Here, this relationship is associated with specific interface conditions, which are required to represent properly the acoustic behaviour across thin layers. The function of dual variables in eq. (5.2) expressed by primal ones is written with a relationship in matrix form as:

$$\left\{ \frac{\widetilde{u}_1}{\widetilde{u}_2} \right\} = [\mathbf{A}] \left\{ \frac{u_1}{u_2} \right\}, \tag{5.4}$$

where $[\mathbf{A}]$ is called the generalized admittance matrix in acoustics, since it reveals the ratio of dual and primal variables as admittance of an acoustic media. Then, substituting this equation into eq. (5.2) by replacing dual variables $\widetilde{u}_i$, the variational integrals at the interface are rewritten as following:

$$\boldsymbol{a}_{I1}(\bar{v}_1, u_1) + \boldsymbol{a}_{I2}(\bar{v}_2, u_2) = -\mathcal{K}_1 \int_\Gamma \bar{v}_1 \left(\mathbf{A}_{11} u_1 + \mathbf{A}_{12} u_2\right) \mathrm{d}S + \mathcal{K}_2 \int_\Gamma \bar{v}_2 \left(\mathbf{A}_{21} u_1 + \mathbf{A}_{22} u_2\right) \mathrm{d}S, \tag{5.5}$$

where the terms at the interface remain coupled through primal variables in each subdomain only. Once the coefficients in $[\mathbf{A}]$ are known, the corresponding problem governed by eq. (5.1) can be solved. It is noted that the proposed generalized formulation is inherently consistent to the original problem, as no extra operators such as Lagrange multiplier and supplement conditions are necessary to be added in the original formulation.

The framework presented here can be applied to any acoustical materials such as fluid, solid and even poro-elastic materials through giving specific governing equations. The key point for the following is to determine the matrix $[\mathbf{A}]$, whose dimension and coefficients depend on the specific problem and the adopted interface model. In this chapter, an interface model based on the transfer matrix method and various specific admittance matrices are provided in section 5.2. In addition, the proposed interface operator is suitable for any interface model that can be rewritten in matrix form as eq. (5.4), for instance, the classical pressure drop model that was studied in chapter 4. The adaption of the present framework to this model is discussed in section 5.3.

5.2 Application to sound absorbing systems

In this section, the methodology presented in section 5.1 is applied to deal with waves propagating from an acoustic fluid (air) to a porous absorption system composed of thin films and bulk porous part. Both bulk media and thin films are modelled by two types of governing equations: Helmholtz and Biot's equations, it results in four different coupling configurations and therein four interface conditions.

As shown in fig. 5.1 (a,b,c,d), the interface conditions are described for a bidimensional geometry, in the incident (x, y) plane. To facilitate the derivation of these conditions between sides Γ_1 and Γ_2 (Γ_1^+ and Γ_2^+ in the figures), the arbitrary sides inside the thin layer are denoted by the superscript $\bullet^-$, and the outsides attached with the bulk medium is given by $\bullet^+$.

The thin film layers are represented by transfer matrices that are presented in section 2.2.2. Those relationships allow one to connect the primal and dual variables between Γ_1^- and Γ_2^-. It needs now to be combined with the interface conditions attached to the bulk subdomains to obtain the relationship between faces Γ_1^+ and Γ_2^+. These conditions related to the nature of the media and the coupling configuration will be addressed one by one in the following.

5.2.1 General interface condition enhanced by TMM

This section presents the four considered interface conditions generated from the coupling configurations shown in fig. 5.1. To make all related expressions slightly simpler, a compact notation is used for variables at the interface, for example:

$$
\begin{aligned}
&p^f(\Gamma_1^-) := {p^f}_1^-, \quad p^f(\Gamma_2^+) := {p^f}_2^+,\\
&\hat{\sigma}_{xx}(\Gamma_1^-) := \hat{\sigma}_{xx1}^-, \quad \hat{\sigma}_{yx}(\Gamma_2^+) := \hat{\sigma}_{yx2}^+,\\
&u_n^t(\Gamma_1^-) := {u_n^t}_1^-, \quad u_x^s(\Gamma_2^+) := {u_x^s}_2^+.
\end{aligned}
$$

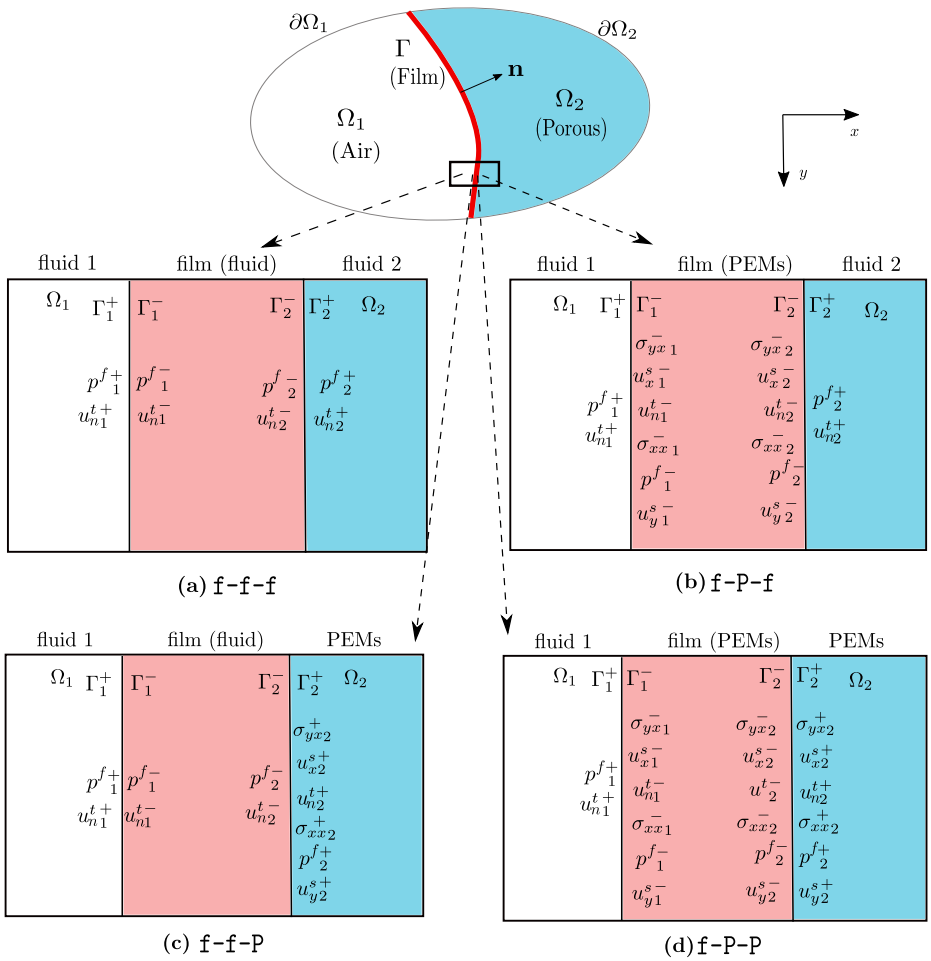

Fig. 5.1.: Four general interface coupling configurations.

Fluid-Fluid coupling with fluid layer (`f-f-f`)

When the film and bulk porous materials are treated as equivalent fluids as fig. 5.1(a), pressure and normal displacement along the interface are the only primal and dual variables. With the conservation of pressure and total fluid displacement across the two faces:

$$\begin{cases} p^{f\,-}_i = p^{f\,+}_i & \text{(5.6a)} \\ u^{t\,-}_{ni} = u^{t\,+}_{ni}, \quad i = 1, 2. & \text{(5.6b)} \end{cases}$$

Thus, the relationship between Γ_1^+ and Γ_2^+ is written as:

$$\begin{Bmatrix} p^{f\,+}_1 \\ u^{t\,+}_{n1} \end{Bmatrix} = \left[\mathbf{T}^{\texttt{f-f-f}}\right]_{2\times 2} \begin{Bmatrix} p^{f\,+}_2 \\ u^{t\,+}_{n2} \end{Bmatrix}, \tag{5.7}$$

where coefficients in $T_{ij}^{\texttt{f-f-f}}$ are the same as in the aforementioned transfer matrix for fluid modelled layer $[\mathbf{T}^{\mathbf{f}}]$ (eq. (2.21) chapter 2).

The relation exposed by eq. (5.7) and following deduced relations eqs. (5.9), (5.11) and (5.14) are the ones we call *generalized interface conditions*. Both pressure and total displacement (function of the gradient of the pressure) are potentially discontinuous through the interfaces. The value of discontinuity (jump) for these variables (primal and dual one) are controlled by every coefficient in the associated transfer matrices.

Fluid-Fluid coupling with PEMs layer (`f-P-f`)

Compared to the previous case, PEMs controlled by the Biot's equations involve 6 variables instead of two due to the solid motion, as illustrated in fig. 5.1(b). The coupling of PEMs with fluid media results in a free surface condition on the in-vacuo elastic frame sides, which is thus added on both sides in the film layer as:

$$\hat{\sigma}^{-}_{yxi} = 0 \quad \text{and} \quad \hat{\sigma}^{-}_{xxi} = 0, \quad i = 1, 2. \tag{5.8}$$

These conditions do not change the structure of the generalized conditions between Γ_1^+ and Γ_2^+, since one still has two variables (p^f and u_n^t) in the state vector of the two bulk media:

$$\begin{Bmatrix} {p^f}_1^+ \\ {u_n^t}_1^+ \end{Bmatrix} = \left[\mathbf{T}^{\texttt{f-P-f}}\right]_{2\times 2} \begin{Bmatrix} {p^f}_2^+ \\ {u_n^t}_2^+ \end{Bmatrix}, \tag{5.9}$$

where the coefficients in the above matrix $\mathbf{T}^{\texttt{f-P-f}}$ are the function of the coefficients in the transfer matrix for Biot's layer $[\mathbf{T}^{\mathbf{P}}]$. Even though the relationship between the two sides of the interface remains similar to the previous case (same state vector with a 2×2 matrix), the coefficients are much more complicated as they are associated with the 6×6 Biot's matrix and free surface conditions (the procedure for obtaining this $\mathbf{T}^{\texttt{f-P-f}}$ matrix is developed in appendix D.1).

Note that it is more common to formulate the transfer matrix condition for fluid-fluid coupling using pressure and total velocity, where total velocity converts to displacement as $v_n^t = \mathrm{j}\omega u_n^t$ under the harmonic convention chosen in this manuscript.

The interface conditions "`f-f-f`" and "`f-P-f`" can be classified as one unique type, since only Helmholtz equation is involved for the bulk media associated by a 2×2 matrix for the interface. However, when the porous bulk media Ω_2 is considered as full PEMs governed by Biot's equations, the number of variables is not compatible between the two sides of the film any more (2 against 6 when coupling with an acoustic fluid). As a result, non-square matrix relationships will be observed for the interface.

Fluid-PEMs coupling with fluid layer (`f-f-P`)

This configuration is described in fig. 5.1(c). Contrary to the previous case, the free surface conditions on the stresses are only applied on the side of the PEM bulk subdomain Γ_2^+:

$$\hat{\sigma}_{yx2}^{+} = 0, \quad \text{and} \quad \hat{\sigma}_{xx2}^{+} = 0. \tag{5.10}$$

As this condition is on the PEMs' side, it is required to be enforced as an interface condition in the equation of solid phase. Then, the generalized conditions in this case are cast as:

$$\begin{Bmatrix} {p^f}_1^+ \\ u_{n1}^{t\,+} \end{Bmatrix} = \left[\mathbf{T}^{\texttt{f-f-P}}\right]_{2\times 4} \begin{Bmatrix} {p^f}_2^+ \\ u_{n2}^{t\,+} \\ \hat{\sigma}_{xx2}^{+} = 0 \\ \hat{\sigma}_{yx2}^{+} = 0 \end{Bmatrix}, \tag{5.11}$$

where the coefficients associated with the ${p^f}_2^+$ and $u_{n2}^{t\,+}$ in the matrix above are the same as in eq. (5.7), which is because these two cases both employ an equivalent fluid model for the embedded thin film.

Fluid-PEMs couling with PEM layer (`f-P-P`)

Replacing the fluid model in the previous case by a Biot's medium for the film, we obtain an interface between two PEMs as shown in fig. 5.1(d). The continuity of all the variables are retained at the interface Γ_2 as:

$$\begin{cases} \hat{\sigma}_{yx2}^{-} = \hat{\sigma}_{yx2}^{+} \quad \text{and} \quad \hat{\sigma}_{yx2}^{-} = \hat{\sigma}_{xx2}^{+}, & (5.12a) \\ u_{x2}^{s\,-} = u_{x2}^{s\,+} \quad \text{and} \quad u_{y2}^{s\,-} = u_{y2}^{s\,+}, & (5.12b) \\ u_{n2}^{t\,-} = u_{n2}^{t\,+}, & (5.12c) \\ {p^f}_2^- = {p^f}_2^+, & (5.12d) \end{cases}$$

and the free surface on Γ_1^-:

$$\hat{\sigma}_{yx1}^{-} = 0 \quad \text{and} \quad \hat{\sigma}_{xx1}^{-} = 0. \tag{5.13}$$

Consequently, the generalized conditions that will be prescribed in the variational formulation are:

$$\begin{Bmatrix} \hat{\sigma}_{yx1}^{-} = 0 \\ \hat{\sigma}_{xx1}^{-} = 0 \\ {p^f}_1^+ \\ {u_{n1}^t}^+ \end{Bmatrix} = \left[\mathbf{T}^{\texttt{f-P-P}}\right]_{4\times 6} \begin{Bmatrix} \hat{\sigma}_{yx2}^{+} \\ {u_{x2}^s}^+ \\ {u_{n2}^t}^+ \\ \hat{\sigma}_{xx2}^{+} \\ {p^f}_2^+ \\ {u_{y2}^s}^+ \end{Bmatrix}, \tag{5.14}$$

where $[\mathbf{T}^{\texttt{f-P-P}}]$ is a 4×6 matrix, the two lines related to the displacement ${u_{x1}^s}^-$ and ${u_{y1}^s}^-$ in the original transfer matrix $[\mathbf{T}^{\mathbf{P}}]$ are eliminated due to the fact that the fluid media does not have a solid phase displacement.

For these four coupling types, we have shown that only three different forms are derived for interface conditions which will be imposed weakly in the variational formulations of bulk subdomains.

5.2.2 Variational interface operators

Now, we impose the generalized interface conditions obtained previously in the coupled variational formulations eq. (2.11) and eq. (2.13). Three interface conditions types are enforced: one interface conditions for two fluid coupling and two for fluid-PEMs coupling. As only the variables on surfaces Γ_i^+ are retained, the superscript $\bullet^+$ is removed to simplify the expression.

Fluid-fluid coupling

Addition to the two formulations eq. (2.11) for media 1 and 2, coupling interface integrals on Γ_1 and Γ_2 are prescribed:

$$\mathscr{I}_{\mathrm{f-f}} = -\int_{\Gamma_1} \bar{q}_1^f u_{n1}^t \mathrm{d}S + \int_{\Gamma_2} \bar{q}_2^f u_{n2}^t \mathrm{d}S, \tag{5.15}$$

where ρ_i are the fluid densities of each subdomain. The generalized interface condition derived from TMM relations cannot be used directly, admittance relationship with matrix $[\mathbf{A}]$ needs first to be obtained. Relationships expressed with transfer matrix in eq. (5.7) and eq. (5.9) are required to be rewritten with a generalized impedance matrix $[\mathbf{A}^{\mathbf{ff}}]$ as:

$$\begin{Bmatrix} u_{n1}^t \\ u_{n2}^t \end{Bmatrix} = \begin{bmatrix} A_{11}^{\mathrm{ff}} & A_{12}^{\mathrm{ff}} \\ A_{21}^{\mathrm{ff}} & A_{22}^{\mathrm{ff}} \end{bmatrix} \begin{Bmatrix} p_1^f \\ p_2^f \end{Bmatrix}, \tag{5.16}$$

where the coefficients in matrix $[\mathbf{A}^{\mathrm{ff}}]$ are expressed by the coefficients in $[\mathbf{T}]$ ($[\mathbf{T}^{\texttt{f-f-f}}]$ and $[\mathbf{T}^{\texttt{f-P-f}}]$):

$$A_{11}^{\mathrm{ff}} = \frac{T_{22}}{T_{12}}, \quad A_{12}^{\mathrm{ff}} = \frac{T_{12}T_{21} - T_{22}T_{11}}{T_{12}}, \quad A_{21}^{\mathrm{ff}} = \frac{1}{T_{12}}, \quad A_{22}^{\mathrm{ff}} = -\frac{T_{11}}{T_{12}}. \tag{5.17}$$

Substituting eq. (5.16) into eq. (5.15) and combining the interface Γ_1 and Γ_2 as Γ, the final interface operator is obtained in a compact form as following:

$$\mathscr{I}_{\mathrm{f-f}} = \sum_{i=1}^{n} (-1)^i A_{ij}^{\mathrm{ff}} \int_{\Gamma} \bar{q}_i^f p_j^f \mathrm{d}S, \quad n = 2. \tag{5.18}$$

Remind that configurations "`f-f-f`" and "`f-P-f`" lead to the same interface operator but only with different coefficients A_{ij}^{ff}.

Fluid-PEMs coupling

Interface terms for fluid-PEMs coupling are obtained by adding eq. (2.11) for media 1 and eq. (2.13) for media 2 together as:

$$\mathscr{I}_{\mathrm{f-P}} = -\int_{\Gamma_1} \bar{q}_1^f u_{n1}^t \mathrm{d}S + \int_{\Gamma_2} \bar{q}_2^f u_{n2}^t \mathrm{d}S + \int_{\Gamma_2} \bar{\mathbf{v}}_i^s \boldsymbol{n}_j \hat{\sigma}_{ij}^s(\mathbf{u}^s)\, \mathrm{d}S. \tag{5.19}$$

Compared to fluid-fluid coupling, a stress surface term appears due to the dynamic equation of the elastic solid phase.

For configuration "`f-f-P`", prescribing interface conditions eq. (5.11) directly conduces the stress terms to vanish. Then, the remaining conditions are the same as fluid-fluid coupling eq. (5.16), resulting in the following form as eq. (5.18).

$$\mathscr{I}_{\mathrm{f-f-P}} = \sum_{i=1}^{n} (-1)^i A_{ij}^{\mathrm{ff}} \int_{\Gamma} \bar{q}_i^f p_j^f \mathrm{d}S, \quad n = 2, \tag{5.20}$$

it can be seen that we obtain the same interface terms as in the previous case. This is because only pressure fields are involved in the interface conditions when the film is modelled by an equivalent fluid.

To impose conditions eq. (5.14) of configuration "`f-P-P`", as previously, we rewrite it with an admittance matrix $[\mathbf{A}^{\mathbf{P}}]$ to express dual variables by means of primal variables as following:

$$\begin{Bmatrix} u_{n1}^t \\ u_{n2}^t \\ \hat{\sigma}_{xx2} \\ \hat{\sigma}_{yx2} \end{Bmatrix} = [\mathbf{A}^{\mathbf{P}}]_{4\times 4} \begin{Bmatrix} p_1^f \\ p_2^f \\ u_{x2}^s \\ u_{y2}^s \end{Bmatrix}, \tag{5.21}$$

where $[\mathbf{A}^{\mathbf{P}}]$ is not easy to obtain from $[\mathbf{T}^{\mathbf{f-P-P}}]$. The procedure for deriving this admittance matrix from $[\mathbf{T}^{\mathbf{f-P-P}}]$ is detailed in appendix D.2. Once matrix $[\mathbf{A}^{\mathbf{P}}]$ is determined, the interface terms in eq. (5.19) are rewritten by substituting eq. (5.21) as the following compact form:

$$\mathscr{I}_{\mathrm{f-P-P}} = \int_{\Gamma} [-\bar{q}_1^f, \bar{q}_2^f, \bar{v}_x^s, \bar{v}_y^s][\mathbf{A}^{\mathbf{P}}][p_1^f, p_2^f, u_x^s, u_y^s]^T \mathrm{d}S. \tag{5.22}$$

It is worth emphasizing that all these interface operators (5.18), (5.20) and (5.22) introduce strong discontinuities for both primal and dual variables.

5.2.3 Symmetry of the variational systems

The variational formulation with generalized interface operator yields a linear system after discretization, to be presented in section 5.4. The structure of the resulting systems is worth being discussed, as it has an impact on the setup of a linear solver that needs to be considered for the following. The symmetry could be identified directly through the variational formulations in continuous space, as stated in this section. The bulk parts render conventionally the symmetry to the system, while the proposed generalized interface operators may bring some non-symmetries.

From variational interface operator (5.18), it can be recognized that the fluid-fluid coupling system is symmetric if $[\mathbf{A}^{\mathbf{ff}}]_{\mathbf{2\times 2}}$ satisfies:

$$A_{ij}^{\mathrm{ff}} = (-1)^i A_{ji}^{\mathrm{ff}} \quad i, j \in 1, 2, \tag{5.23a}$$

which results in an anti-symmetric matrix for fluid-fluid coupling. With the conversion from transfer matrix $[\mathbf{T}]$ to admittance matrix $[\mathbf{A}]$ for this coupling as illustrated in eq. (5.17), the anti-symmetry of $[\mathbf{A}^{\mathbf{ff}}]$ ($A_{12}^{\mathrm{ff}} = -A_{21}^{\mathrm{ff}}$) gives:

$$\frac{T_{12}T_{21} - T_{22}T_{11}}{T_{12}} = -\frac{1}{T_{12}}, \tag{5.24}$$

that leads to the coefficients in $[\mathbf{T}]$ satisfying :

$$T_{22}T_{11} - T_{12}T_{21} = 1, \quad T_{12} \neq 0, \tag{5.25}$$

which means that the resulting linear system will be symmetric when the determinant of the corresponding transfer matrix $[\mathbf{T}]$ is equal to one. The same conclusion is applied to the operator (5.20) for the configuration "`f-f-P`".

When it comes to the configuration "`f-P-P`", symmetry requires that coefficients in matrix $[\mathbf{A^P}]_{4\times4}$ for interface operator (5.22) fulfil:

$$\begin{cases} A^P_{ij} = (-1)A^P_{ji} & \text{when } i = 1, \quad (5.26a) \\ A^P_{ij} = A^P_{ji}, & \text{otherwise}, \quad (5.26b) \end{cases}$$

which results in an anti-symmetry for the terms associated with p^f_1. In this case, the link between transfer matrix in porous film $[\mathbf{T^P}]$ and admittance matrix $[\mathbf{A^P}]$ is not direct, which concerns the reconstruction and inverse of matrices as illustrated in appendix D.2, depending on the specific problem. We cannot give an analytical condition of symmetry for $[\mathbf{T^P}]$ as eq. (5.25). However, $[\mathbf{A^P}]$ can be evaluated numerically a posteriori to verify if the corresponding system is symmetric, in order to choose a suitable linear solver.

In fact, for fluid-fluid coupling with film modelled by equivalent JCA or Limp model, the determinants of transfer matrices eqs. (2.10) and (2.21) satisfy $|\mathbf{T^f}| = 1$. The resulting variational formulations and the linear system are thus symmetric. However, the matrix eq. (2.22) used in configuration "f-P-P" is verified numerically as not fulfilling the symmetry requirement eq. (5.26). Notice that there exists other Biot's transfer matrices, which should be verified case by case when used in the present method. The symmetrization of the Biot's matrices was being tried during this work, unfortunately, it is not realized.

5.3 Discussion on TMM enhanced interface model

This section gives more specific details associated with the proposed interface models for thin porous materials. The TMM enhanced model is compared to the pressure jump model that was used in the previous chapter. Furthermore, to illustrate the aforementioned effects from the assumption of plane wave in TMM, the proposed model is evaluated by a set of sensitivity tests.

5.3.1 Comparison with the pressure jump model

As mentioned, the proposed generalized formulation can be theoretically applied to any media for which an admittance matrix $\mathbf{A}$ can be found. Therefore, before conducting the comparison, we apply our framework to the pressure jump interface conditions. It is straightforward to rewrite the pressure jump conditions eq. (4.1) in algebraic form as:

$$\begin{Bmatrix} p^f_1 \\ v^t_{n1} \end{Bmatrix} = \begin{bmatrix} 1 & \sigma d \\ 0 & 1 \end{bmatrix} \begin{Bmatrix} p^f_2 \\ v^t_{n2} \end{Bmatrix}, \quad (5.27)$$

which can be considered as a transfer matrix equation with $\mathbf{T}^{\mathrm{pj}}$ ($\bullet^{\mathrm{pj}}$ corresponds to pressure jump) and leads to the admittance matrix $\mathbf{A}^{\mathrm{pj}}$:

$$\mathbf{A}^{\mathrm{pj}} = \begin{bmatrix} 1/\sigma d & -1/\sigma d \\ 1/\sigma d & -1/\sigma d \end{bmatrix}. \tag{5.28}$$

Thus, the variational interface operator corresponding to this pressure jump condition as fluid-fluid coupling eq. (5.15) is written as [1]:

$$\boldsymbol{a_I} = \frac{\mathrm{j}\omega}{\sigma d} \int_\Gamma [\![\bar{q}^f]\!][\![p^f]\!] \mathrm{d}S, \tag{5.29}$$

which agrees exactly with the *penalty-type* formulations derived in chapter 4. We refer this model as simplified model for the following, since the matrix of the pressure jump interface is much simpler than for equivalent fluid, Biot and Limp matrices presented in chapter 2.

In fact, the relationship exposed in eq. (5.27) is only suitable for the low frequency limit ($\omega \to 0$). Its flow resistance is frequency independent, which is in contrast with the other proposed models in this chapter. To identify the difference between each thin layer model, we calculate the evolution of the coefficient that corresponds to the pressure drop (T_{12}^f in matrix (2.21) and (2.10) for two equivalent fluid models, $T_{12}^{\mathtt{f\text{-}P\text{-}f}}$ in eq. (5.9) for Biot's model and σd in eq. (5.27)) at the interface with an increasing frequency for the two films presented above. Two representative woven and non-woven films already investigated in a previous work (Gaborit et al., 2018 [24]) are evaluated. Normal incidence ($\theta = 0$) and thickness $d = 1$ mm are selected to evaluate these matrices.

From fig. 5.2, one can see that the coefficients from the pressure jump model stay constant with respect to frequency. The imaginary part is zero for both types of film, which corresponds to the fact that no dissipation due to porous effects is considered in this model. In contrast, the other models lead to a change in the pressure drop coefficient with increasing frequency, especially the imaginary part increases a lot. At low frequencies, the imaginary part of the JCA model tends to zero. When taking the frame into account (that is the Limp and Biot's models), an obvious gap in the imaginary part is noticeable compared with the simplified model, even in the low-frequency range. This behaviour confirms that the simplified pressure drop model is only valid in the limit of low frequency for some materials. On the other hand, the Limp and Biot models exhibit a similar behaviour regarding pressure drop, even in the medium-high frequency range where a superposition of the curves is observed. This is because with the large density of the films considered here, as seen in table B.2, the displacement of the elastic frame considered in Biot's model has minor effects on the poro-fluid behaviour.

To conclude, the proposed general framework presented in section 5.1 can be readily applied to the pressure jump model, yielding the interface operator section 5.3.1 as *penalty-type* formulation. On the other hand, we illustrate that this simplified interface model is not accurate

[1] multiplied by ω^2 for transfer displacement u^t to velocity v^t

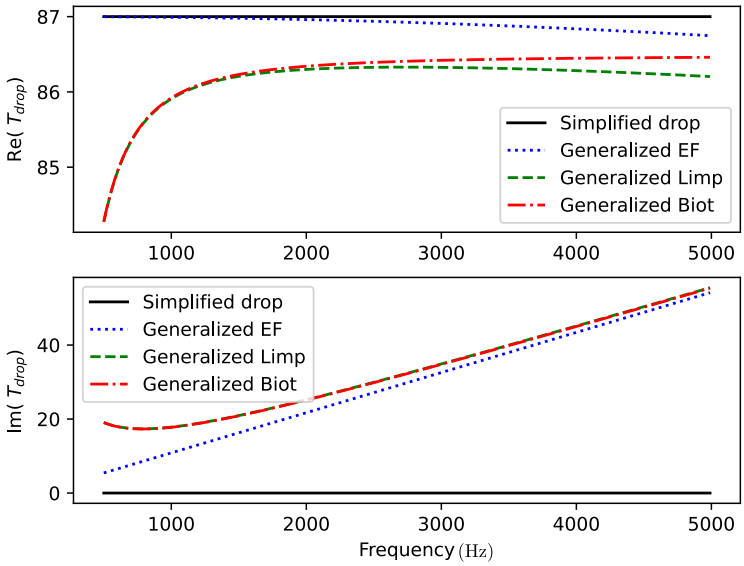

(a)

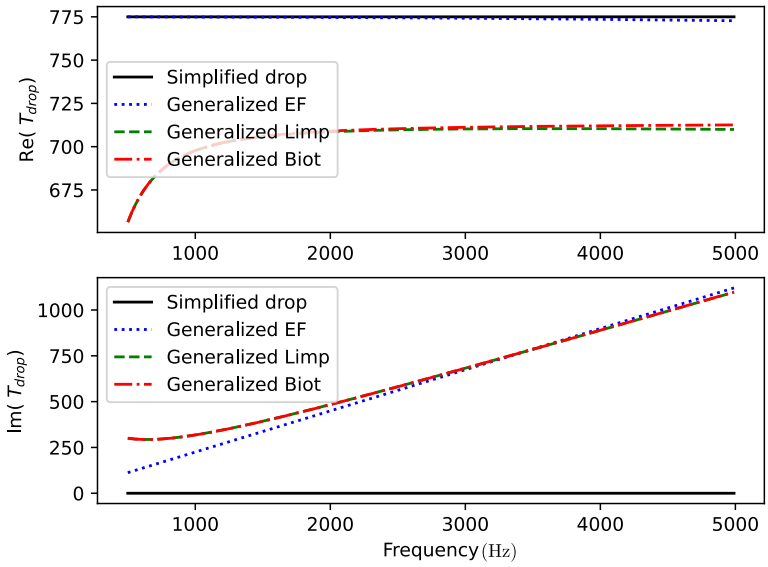

(b)

Fig. 5.2.: Variation of coefficient related to pressure drop (T_{drop} with normal incidence $\theta = 0$ °and thickness of $d = 1$ mm) for different film models as function of frequency: (a) Non-woven film, (b) woven film.

enough to model thin porous films in wide range of frequency. Generalized interface models proposed in this chapter are necessary to account for thin resistive porous films. Furthermore, if we are interested in the pressure field of the solution only, which is the case in most acoustic analysis, the Limp model is preferable to Biot's model. Indeed, the Limp model is able to provide a similar and sufficiently accurate description of Biot's equations to model thin films in TMM. Additionally, it results in a symmetric linear system, which will accelerate the computational procedure.

5.3.2 Sensitivity analysis for thin films

The necessity of using complete transfer matrices as eq. (2.21) and eq. (2.22) rather than the simplified pressure-jump model to represent porous materials has been demonstrated. However, as aforementioned, these transfer matrices are formulated under the assumption of plane wave propagation. This assumption is difficult to be ensured in the general case, especially when the problem is excited by a point source where waves propagate in all directions or if the geometry of the interface is complex. This is due to the fact that a mismatch in the incident angle θ will result in an incorrect wave number and effective propagation distance in layers. Indeed, previous contribution (Jonckheere et al., 2015 [168]) already tried to mitigate the influence of the incident angle in transfer matrices based on WBM where wave function and particular solution dependent angles were proposed.

To address this aspect in our specific case where TMM represents relatively thin porous layers, the solution of a classical transfer matrix without any simplification and modification with respect to incident angle θ is preferred to be evaluated. Here, we carry out a sensitivity study against the incident angle.

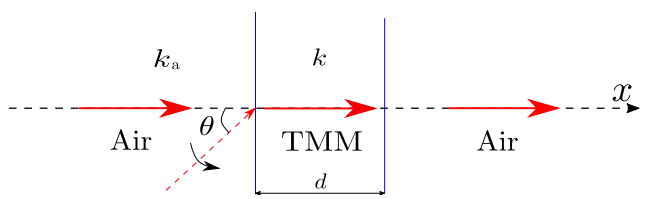

Fig. 5.3.: Configuration for testing the sensitivity of the transfer matrix interface model.

The test cases are performed in a one-dimensional configuration as illustrated in fig. 5.3 where a horizontal incident plane wave propagates in an infinite plane of air (with wave number k_a) in which a layer modelled by TMM is embedded in the middle ($x = 0$). Equivalent fluid model with JCA parameters eq. (2.21) are used for the transfer matrix of the middle layer. To quantify the sensitivity of the interface model with respect to incidence angle, The TMM solution is

compared with varying angle to the exact solution with $\theta = 0$. The varied angle changes the exact wave number k and thickness d of thin layers to k' and d' as:

$$k' = \sqrt{k^2 - k_{\mathrm{a}}^2 \sin(\theta)}, \tag{5.30a}$$

$$d' = d/\cos(\theta). \tag{5.30b}$$

The solution for this problem is expressed with incident p^i and transmission pressure p^t:

$$p^i = \exp(-\mathrm{j}k_{\mathrm{a}}x) + R\exp(\mathrm{j}k_{\mathrm{a}}x) \quad x \leq 0, \tag{5.31a}$$

$$p^t = T\exp(-\mathrm{j}k_{\mathrm{a}}x) \quad x > 0, \tag{5.31b}$$

where the reflection and transmission coefficients R, T are obtained through solving the generalized interface conditions eq. (5.7) associated with the transfer matrix (2.21). The error against the reference solution is calculated numerically in L^2 norm as:

$$\begin{aligned}\epsilon &= \int_{x\leq 0} \left|(R - R_{\theta=0})\exp(\mathrm{j}k_{\mathrm{a}}x)\right|^2 \mathrm{d}x + \int_{x>0} \left|(T - T_{\theta=0})\exp(-\mathrm{j}k_{\mathrm{a}}x)\right|^2 \mathrm{d}x \\ &= \left|R - R_{\theta=0}\right|^2 + \left|T - T_{\theta=0}\right|^2.\end{aligned} \tag{5.32}$$

As can be seen, the error depends on R and T which are functions of incident angle θ in the transfer matrix model for the middle thin layer.

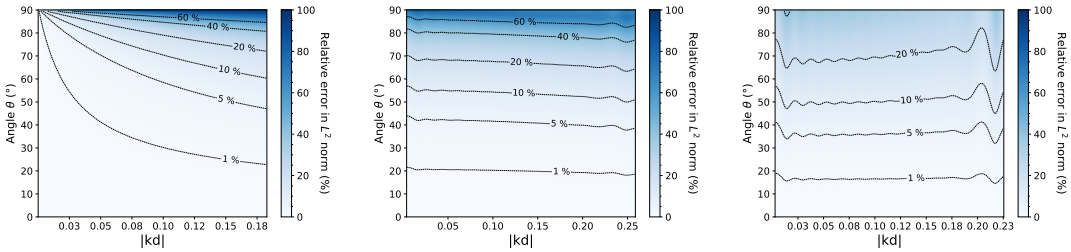

(a) (b) (c)

Fig. 5.4.: Global relative error (%) with respect to incidence angle in the TM: (a) air gap, (b) non-woven film, (c) woven film.

Three TMMs for air gap, non-woven and woven films with different kd are assessed. kd characterizes the number of waves propagating through the layer.

The relative error as a function of θ through sweeping kd are plotted in fig. 5.4. The largest kd in the figure corresponds to a wave propagating in a layer of $2\ \mathrm{mm}$ under an excitation of $5,000\ \mathrm{Hz}$, which could represent an upper bound for thin films in a practical situation.

When the TMM models an air gap (fig. 5.4(a)), the more waves propagate in the layers (larger kd), the more sensitive to the angle mismatch θ of the solution (larger error in same mismatch angle). At $90°$, a drastic increase of the error is observed when kd is small and the maximal error

occurs for the highest kd. These behaviours are consistent with the fact that when the layer is extremely thin, the TMM has an obvious influence only for a grazing incidence. And, when kd becomes larger, more error from the mismatch is accumulated in the TMM layer. Remind that an air gap is a real-valued acoustic media without energy loss.

Fig. 5.4(b) and fig. 5.4(c) exhibit the same assessments for porous films, indicating that the sensitivity against mismatch angle is less dependent of kd. As seen in table B.2, the two porous films have large flow resistivity and solid densities, far more rigid than air. This kind of materials decouples the infinite plane and produces a non-negligible pressure difference at the interface even when kd is small. Moreover, energy damping (complex-valued properties) exists in the porous films. When the layer is resistant enough or when the pressure dissipation in the layer is large enough beyond specific values, the solution tends to be stable. This is why for a fixed kd, the error for the more resistant woven film increases more slowly with respect to change of angle θ than the non-woven one. Nevertheless, for both considered films, the error stays mostly below 20% even until a mismatch of angle $70°$. The angle mismatch for a target error below for instance 1% has a margin of at most $20°$, for both films, which is not a harsh condition to satisfy in general cases. It is admitted that here a quite simple problem is treated to analyse the sensitivity. Conclusions might be different in other cases with different materials, boundary conditions and source excitation, in which a little mismatch may lead to an unacceptable error.

To summarize this part, on the one hand, one should be conscious that approximation exists in our interface model produced from the mismatch of angle θ in TMM. On the other hand, thin porous layers considered in this manuscript are less sensitive to this mismatch, less error produced from inconsistency of angle in most situations. Even in the cases where this angle mismatch cannot be avoided, the proposed approach is still able to provide reliable results for modelling of porous films. This aspect will be demonstrated in the last numerical example of chapter 6.

5.4 Verification and validation

5.4.1 Implementation

As three typologies of interface operator were introduced for coupling the variational formulations, three discrete systems will arise. Substituting the Heaviside enriched approximation into

the previous variational formulations eq. (2.11) together with interface operators (5.15) results in the following discretized algebraic system for fluid-fluid coupling:

$$\left[\begin{array}{cc|c} \mathbf{K}^b_{p1}+\mathbf{K}^I_{p1} & \mathbf{K}^I_{p12} & \mathbf{K}^b_{p1a}+\mathbf{K}^I_{p1a} \\ \mathbf{K}^I_{p21} & \mathbf{K}^b_{p2}+\mathbf{K}^I_{p2} & \mathbf{K}^b_{p2a}+\mathbf{K}^I_{p2a} \\ \hline \mathbf{K}^b_{ap1}+\mathbf{K}^I_{ap1} & \mathbf{K}^b_{ap2}+\mathbf{K}^I_{ap2} & \mathbf{K}^b_{aa}+\mathbf{K}^I_{aa} \end{array}\right] \begin{Bmatrix} \mathbf{p}^f_1 \\ \mathbf{p}^f_2 \\ \mathbf{a} \end{Bmatrix} = \begin{Bmatrix} \mathbf{F}_1 \\ \mathbf{F}_2 \\ \mathbf{F}_a \end{Bmatrix}, \tag{5.33}$$

where $\mathbf{p}^f_i$ are the pressure dofs for each subdomain and $\mathbf{a}$ are the enriched dofs at the interface. $\mathbf{F}_i$ and $\mathbf{F}_a$ represent external forces on the bulk and enriched elements. Terms $\mathbf{K}^b$ and $\mathbf{K}^I$ are the generalized stiffness matrices from bulk and interface contribution respectively.

Configuration "`f-f-P`" has the same interface operator as fluid-fluid coupling, and additional coupling contributions in Biot's bulk part is taken into account in "`f-P-P`" case. Therefore, only the case with embedded PEM film is presented here for fluid-PEM coupling. When enriched pressure and standard displacement approximation are inserted in variational formulations eq. (2.11) and eq. (2.13) with interface terms (5.21), the resulting discretized linear system is written as:

$$\left[\begin{array}{cccc|c} \mathbf{K}^b_{p1}+\mathbf{K}^I_{p1} & \mathbf{K}^I_{p12} & \mathbf{K}^b_{p1ux}+\mathbf{K}^I_{p1ux} & \mathbf{K}^b_{p1uy}+\mathbf{K}^I_{p1uy} & \mathbf{K}^b_{p1a}+\mathbf{K}^I_{p1a} \\ \mathbf{K}^I_{p21} & \mathbf{K}^b_{p2}+\mathbf{K}^I_{p2} & \mathbf{K}^b_{p2ux}+\mathbf{K}^I_{p2ux} & \mathbf{K}^b_{p2uy}+\mathbf{K}^I_{p2uy} & \mathbf{K}^b_{p2a}+\mathbf{K}^I_{p2a} \\ \mathbf{K}^b_{uxp1}+\mathbf{K}^I_{uxp1} & \mathbf{K}^b_{uxp2}+\mathbf{K}^I_{uxp2} & \mathbf{K}^b_{ux}+\mathbf{K}^I_{uxux} & \mathbf{K}^I_{uxuy} & \mathbf{K}^I_{uxa} \\ \mathbf{K}^b_{uyp1}+\mathbf{K}^I_{uyp1} & \mathbf{K}^b_{uyp2}+\mathbf{K}^I_{uyp2} & \mathbf{K}^I_{uyux} & \mathbf{K}^b_{uy}+\mathbf{K}^I_{uxuy} & \mathbf{K}^I_{uya} \\ \hline \mathbf{K}^b_{ap1}+\mathbf{K}^I_{ap1} & \mathbf{K}^b_{ap2}+\mathbf{K}^I_{ap2} & \mathbf{K}^I_{aux} & \mathbf{K}^I_{auy} & \mathbf{K}^b_{aa}+\mathbf{K}^I_{aa} \end{array}\right] \begin{Bmatrix} \mathbf{p}^f_1 \\ \mathbf{p}^f_2 \\ \mathbf{u}^s_x \\ \mathbf{u}^s_y \\ \mathbf{a} \end{Bmatrix} = \begin{Bmatrix} \mathbf{F}_{p1} \\ \mathbf{F}_{p2} \\ \mathbf{F}_{ux} \\ \mathbf{F}_{uy} \\ \mathbf{F}_a \end{Bmatrix}, \tag{5.34}$$

where all the terms including $\mathbf{u}_x$ and $\mathbf{u}_y$ are originated from the displacement field in PEMs and $\mathbf{F}_{ux}$, $\mathbf{F}_{uy}$ are the external forces applied on the elastic phase. Additional bulk contributions $\mathbf{K}^b_{p_iu}$ represent the coupling terms between $\mathbf{p}^f$ and $\mathbf{u}^s$ in Biot's mixed formulations. The detailed expressions of the generalized stiffness matrices $\mathbf{K}$ presented in these discrete systems are provided in appendix E for completeness.

Reminded that every term defined in the enrichment blocks in the system above is integrated using a modified Gauss quadrature on partitioned sub-elements at the interface. In addition, the leading discrete systems being potentially non-symmetric ("`f-P-P`" with the proposed Biot's interface operator), a well-suited assembly graph and algorithm of the direct solver (`MUMPS`) for each system is adapted to improve the solving procedure.

5.4.2 Verification with Plane wave

Typical plane wave benchmarks verify the implementation of the variational formulations for the three interface operators and coupling types within X-FEM. Planar and curved interface

for different acoustic fields such as reflection, transmission and scattering are considered. The analytical solutions associated with each test case are obtained by solving the reflection R, transmission T_i (three transmission coefficients for PEMs subdomains) and scattering coefficients at the interfaces with generalized interface conditions derived before. In this experiment, plastic foam is chosen as porous bulk media whose properties are given in table B.1.

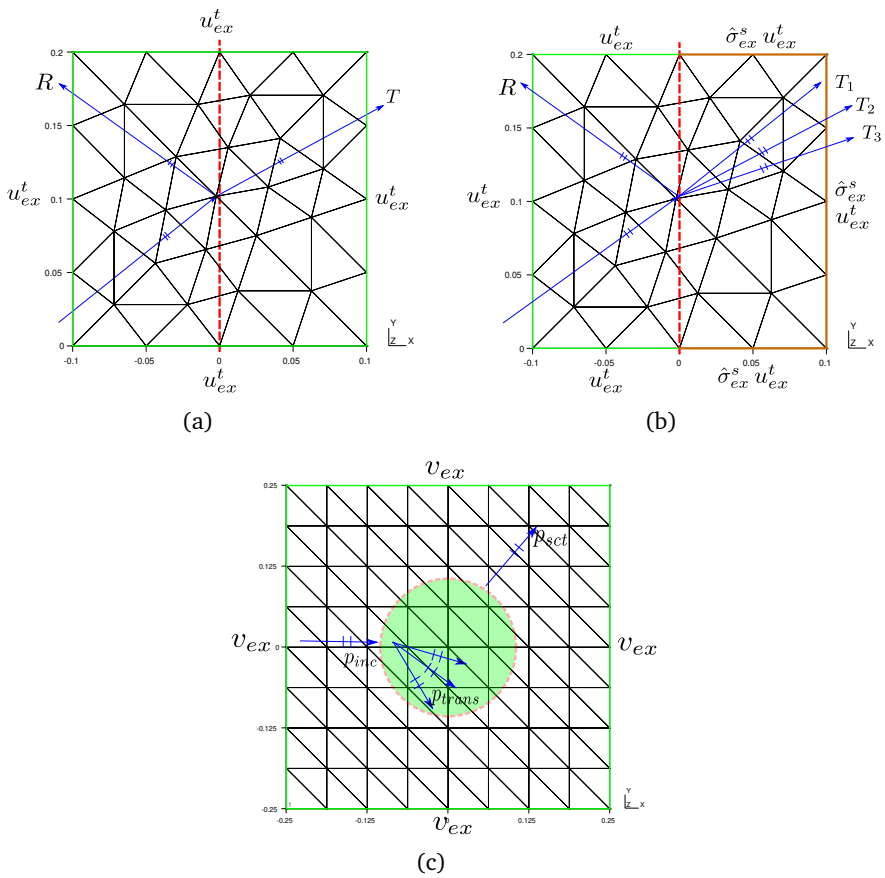

Fig. 5.5.: Three test configurations with X-FEM meshes and boundary conditions: (a) coupling fluid-fluid; (b) coupling fluid-PEMs with embedded PEM film; (c) cylinder scattering problem with embedded Limp film

Fig. 5.5 depicts the three proposed plane wave problems and boundary conditions settings accompanied by representative X-FEM meshes. Operator (5.18) with equivalent fluid matrix (2.21) and operator (5.22) with Biot's matrix given in eq. (2.22) are tested in fig. 5.5(a) and fig. 5.5(b), respectively, while the scattering problem fig. 5.5(c) takes operator (5.20) with Limp model presented in eq. (2.10) into account. The computational domain is a square of length $0.2 \times 0.2\,\mathrm{m}^2$ for the two first cases and $0.5 \times 0.5\,\mathrm{m}^2$ for the scattering problem. The interfaces for the thin film layers are defined by level-set functions ($x = 0$ for planar interface problems and radius $r_0 = 0.1\,\mathrm{m}$ for the scattering problem). The thickness of the thin layer is fixed to $d = 10^{-3}\,\mathrm{m}$ in the transfer matrices in all cases.

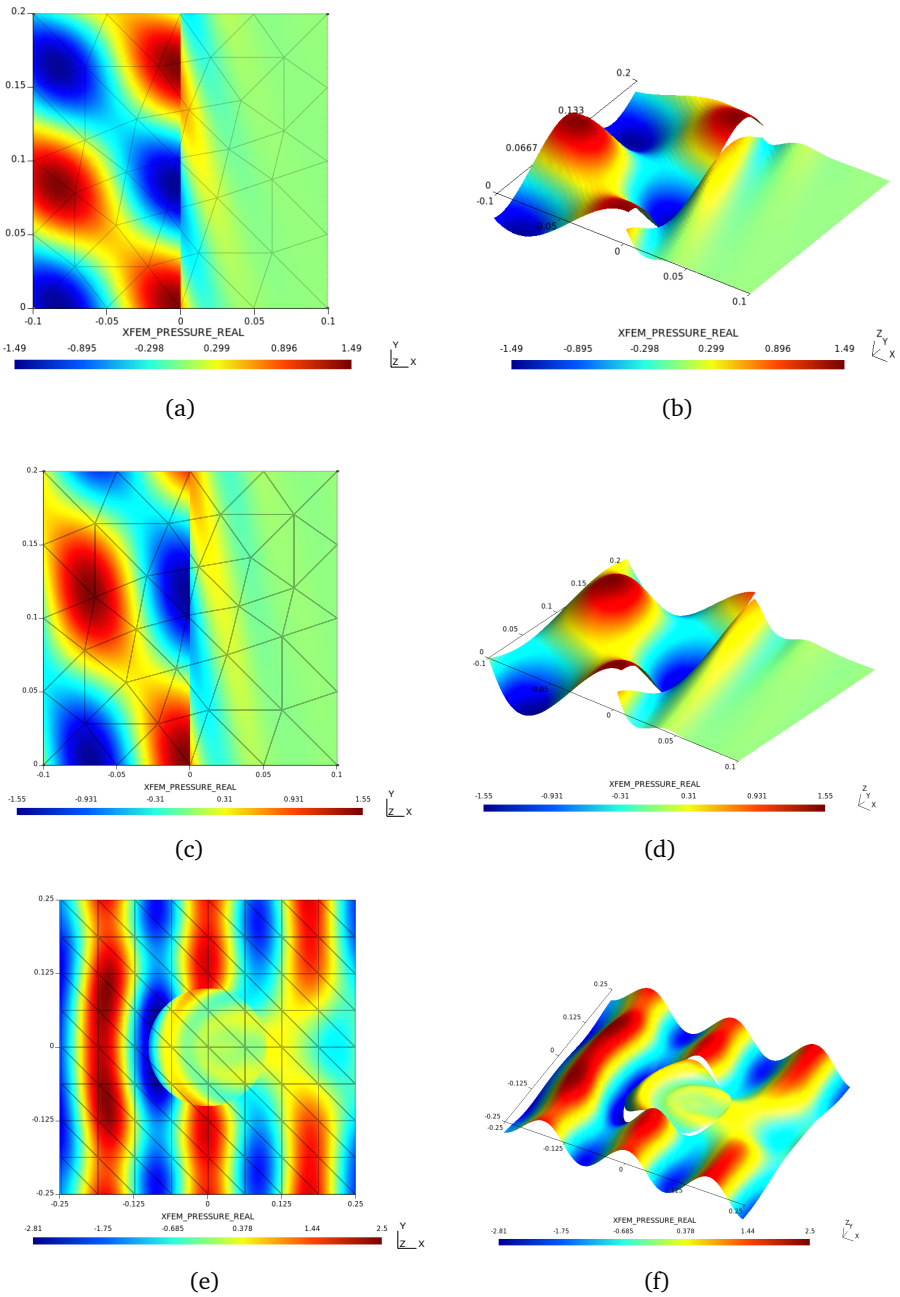

Fig. 5.6.: Real part of pressure solutions (Pa) within the proposed approach: (a, b) configuration "f-f-f" (45 °, 3,000 Hz), (c, d) configuration "f-P-P" (30 °, 3,000 Hz), (e, f) configuration "f-f-P" in cylinder scattering problem (normal incident 2,000 Hz).

For the planar interface problem, the calculation is performed using unstructured meshes to illustrate the robustness of the proposed X-FEM formulations no matter how the elements are cut by the interfaces. On the contrary, a simple structured mesh is used for the curved interface. Exact Neumann boundary conditions are prescribed on the four outer boundaries: acoustic velocity (displacement) v_{ex}/u^t_{ex} for fluid media (green line) and total displacement and in-vacuo stress for poro-elastic media (yellow line).

Fig. 5.6 illustrates numerical solutions of pressure field p^f for plane waves with oblique incidence of $45°$, $30°$ and a normal incidence propagating in each configuration under excitation of $3,000\,\mathrm{Hz}$ and $2,000\,\mathrm{Hz}$. A gradual decrease in pressure amplitude and a change of incidence angle are first observed in the porous bulk domains. Moreover, apparent strong discontinuities are observed across the interfaces: these pressure drops are the effect of accounting for the thin film layer through the interface operators. As exhibited in the results, these discontinuities inside the elements are all well captured at the location of the implicit interfaces, indicating that the X-FEM implementation works properly. Thanks to the high order polynomial approximation ($p = 4$ here), these examples give quite smooth solutions even with such a relatively coarse mesh.

Convergence

To evaluate the accuracy of the implemented formulation, the convergence of the solution needs to be analysed. The problems solved here are the same as shown in examples fig. 5.6. Fig. 5.7 plots the convergence for both h and p refinements: the base meshes shown in fig. 5.5 are split sequentially up to 5 times for h-refinement. Both global and local errors for the pressure are examined by means of global (left column in figures) and local L^2 norms (right column in figures) (eq. (4.41) and relative error of eq. (4.42)) as a function of the number of dofs per wavelength D_λ.

The h-convergence depicted here are performed with linear, quadratic and cubic approximations ($p = 1, 2, 3$). Same observation as in chapter 3, in general, all the curves are close to the so-called "optimal" rate of convergence $\mathcal{O}(h^{-(p+1)})$ in each interpolation degree. The p-refinement (red curves) provides a more efficient convergence rate in the sense that to achieve the same level of accuracy, smaller D_λ are needed. Indeed, this efficiency is not noticeable in certain configurations, which will be explained below. The formulation implemented within X-FEM provides a similar solution accuracy (magnitude of error are in the same order) in terms of the global solution of pressure and the pressure jump at interfaces.

The comparison between fluid-fluid coupling and fluid-PEM coupling can be illustrated from the four first figures (fig. 5.7(a,b,c,d)). As seen that larger D_λ are needed to arrive to the "optimal" convergence stage using the same meshes (pre-asymptotic stage of convergence are more obvious) in figs. 5.7(c) and 5.7(d) than the ones in figs. 5.7(a) and 5.7(b). Same reason as before, the displacement field is involved in fluid-PEMs coupling, leading to a large disparity of scale between pressure and displacement fields in the $\mathbf{u}^s$-p^f mixed Biot's formulation, which prevents the global convergence as reported in Rigobert et al., 2003 [84]. This is also why the efficiency of p-refinement with fluid-PEMs coupling is not obvious as red curves in figs. 5.7(c) to 5.7(f), which was already observed in the previous chapter 3.

The above convergence curves verify the implementation of the proposed formulation within the X-FEM. No matter what types of coupling and how the elements are cut by the interface, a

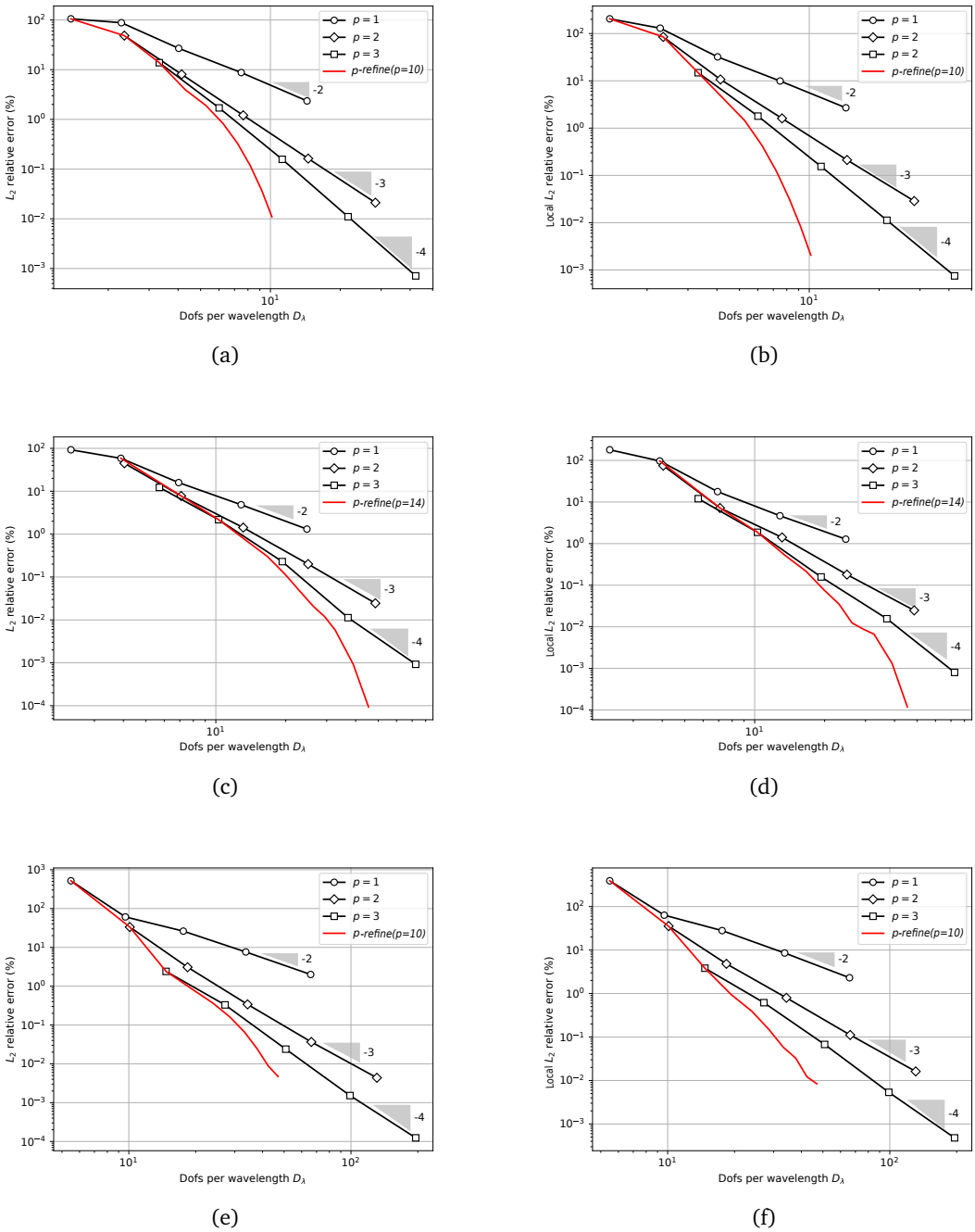

Fig. 5.7.: Global convergence (left) and local pressure jump convergence (right) for: (a, b) fluid-fluid coupling; (c, d) fluid-PEMs coupling with an embedded PEM film; (e, f) fluid-PEMs coupling in scattering problem with an embedded Limp film.

desirable accuracy with a close to optimal convergence is obtained. The convergence has been assessed for other porous systems at different frequencies during this work. For the sake of brevity, only the representative results are provided here, but the same conclusions apply to the others.

Conditioning

The assessment of the conditioning of global stiffness matrices is also important, as it is directly related to the stability and efficiency of the solution, especially when the system is solved through iterative solvers. Configurations "`f-f-f`" and "`f-P-P`" including symmetrical interface operator (5.18) and non-symmetrical one (5.22) are studied. Interpolation degree $p = 3$ is used for all experiments. Fig. 5.8 shows the variations of condition number with respect to D_λ.

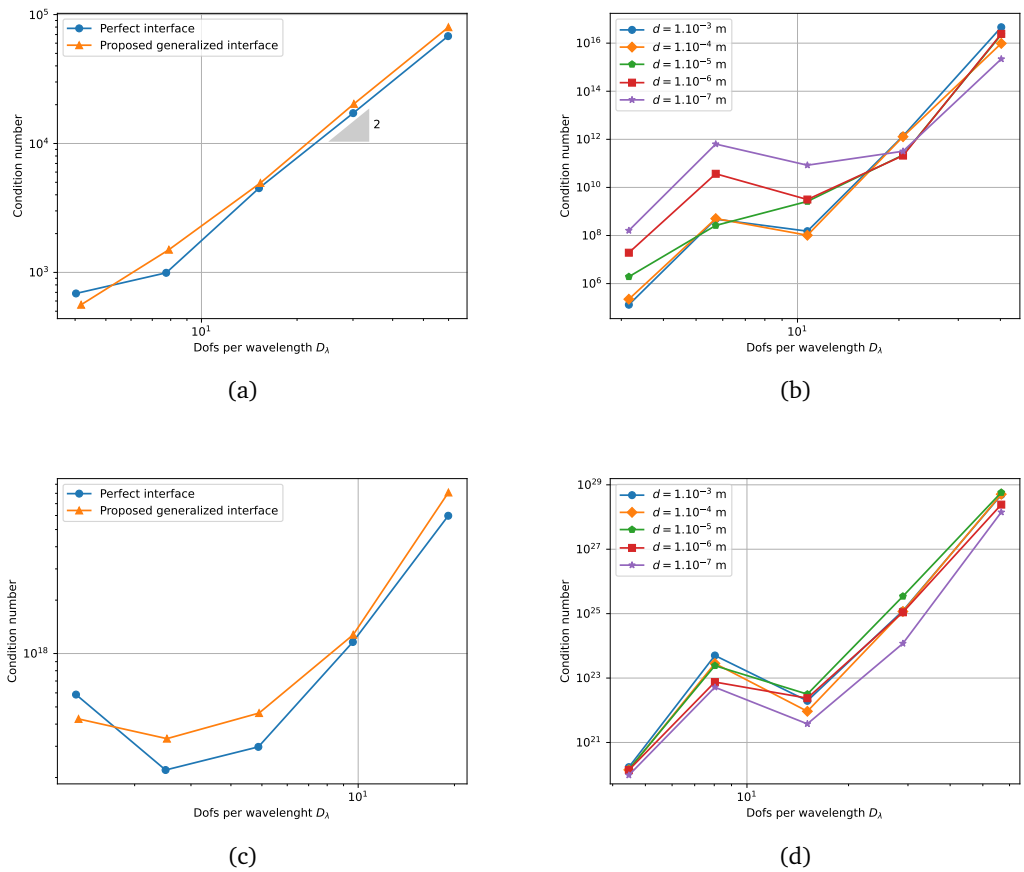

Fig. 5.8.: Evolution of the condition number with respect to D_λ for configuration "`f-f-f`" (top) and "`f-P-P`"(bottom): (a, c) comparison between perfect interface and generalized interface conditions with $d = 10^{-3}\mathrm{m}$ using interface conforming mesh; (b, d) Influence of values in interface operators by varying thickness of film d using unstructured interface non-conforming mesh.

We first examine how the interface operator affects the conditioning of the linear system. Therefore, a perfect interface condition without any discontinuity is first solved within standard FEM as a reference. In order to eliminate the influence of X-FEM on cut elements (as only the influence of the interface operator is characterized here), the implicit interface is defined along the boundaries of elements in a structured mesh. With this mesh, the X-FEM performs like the standard FEM with double nodes along the interface. The parameters for the film used in the interface operators are the same as in the solution figs. 5.6(a) and 5.6(c). Fig. 5.8(a) illustrates that the conditioning for a fluid-fluid coupling involving the proposed interface operator is close to the one from the perfect interface, yielding an increasing rate close to $\mathcal{O}(D_\lambda^2)$. The similarity between these curves indicates that the proposed approach remains relevant, even if implemented within existing commercial FEM codes (the thin layers model for typical porous films does not degrade the conditioning of the original system). For "`f-P-P`" as shown in fig. 5.8(c), the interface operator does not either deteriorate the conditioning compared to a perfect interface, even though we have a non-symmetric linear system in this configuration. It is remarked that the conditioning for this configuration is far larger than the one for "`f-f-f`", which stems from the characteristics of the mixed Biot's formulation: large scale disparity between pressure and displacement. This property also slows down the overall convergence speed, as shown previously in the convergence study. Even with a so large conditioning number of FE systems, a converged solution can be still obtained with the used direct solvers.

Then, the effect of $[\mathbf{A}]$ on the conditioning within X-FEM is examined. The same setup and meshes are used as in figs. 5.6(a) and 5.6(c), but the components of matrix $[\mathbf{A}]$ is varied by changing the thickness d of the layer.

It is first observed in figs. 5.8(b) and 5.8(d) that the magnitude of the condition numbers is at least five orders larger and increases more quickly than the one in figs. 5.8(a) and 5.8(c) under the same D_λ. This worse conditioning stems from the elements cut by the interface, as an unstructured mesh is used. This behaviour can be improved by considering relevant pre-conditioners such as Axelsson et al., 2018 [164]. In practice, we did not encounter any instability issue in enforcing interface conditions under such "irregular" cut elements. Secondly, a noticeable difference is observed for the first points for configuration "`f-f-f`": the smaller the value of the coefficients in the matrix, the larger the condition number of the system. That is because, under coarser meshes, the condition number of the linear system is dominated by the interface terms associated with the value of coefficients A_{ij}. As transformed from matrix $[\mathbf{T}]$ to $[\mathbf{A}]$, smaller thickness in $[\mathbf{T}]$ leads to larger value in $[\mathbf{A}]$. When increasing the mesh resolution, contribution to the global conditioning from the bulk parts' integrals becomes more important than the interface terms. As a consequence, for the last considered mesh points, the condition numbers of different operators approach to each other. In regard to "`f-P-P`" in fig. 5.8(d), no apparent influence is observed with respect to thickness: all the curves are intertwined together. As in our formulations, the final conditioning of the FE system depends on the magnitude of the bulk and interface contributions. The similarity between these conditioning curves is because in the air-PEMs coupling, the contribution for conditioning from generalized interface

terms is much smaller than the one from bulk parts in Biot's equations (it already has a worse conditioning), even with a very small thickness. Conditioning shown in figs. 5.8(b) and 5.8(d) implies that for a converged solution (with sufficiently large D_λ), a subtle influence is produced from the different proposed interface operators within X-FEM to the global conditioning.

From the studies in above subsections, we summarize that for the problems of interest, the variational formulations with the proposed interface operators implemented within the framework of X-FEM are able to give accurate solutions with a limited impact on the conditioning of discrete systems.

It is remarked that the generalized formulations can cover the pressure jump condition as the *penalty-type* formulation, so some characteristics of the *penalty-type* formulation might be inherited, such as the divergence of solutions when σd close to zero.

To verify this point, the same parametric study as previous chapter is performed. For two already considered problems "f-f-f" and "f-P-P", we calculate the global relative L^2 error in function of thickness of film d, shown in fig. 5.9. At the beginning of the curves, errors grow a little and then remain flat over a wide range. Finally, when the thickness is smaller than a specific value, global errors start to increase rapidly. This error behaviour is similar to the ones observed in fig. 4.12(a). The very small d makes the elements on which the interface integrals is defined "over-stiff", causing that other integral terms in the variational formulation cannot be verified properly.

One has to admit that this characteristic is a limitation of our method. To this end, the use of Nitsche's method was investigated during the thesis to stabilize generalized formulations. Unfortunately, it did not work as expected for TMM enhanced interface as for pressure jump conditions. Nevertheless, the TMM enhanced variational formulation is able to provide a stable accurate solution in a large enough range of thickness for typical acoustic films such that $d \in [1.10^{-3}, 1.10^{-5}]\,\mathrm{m}$.

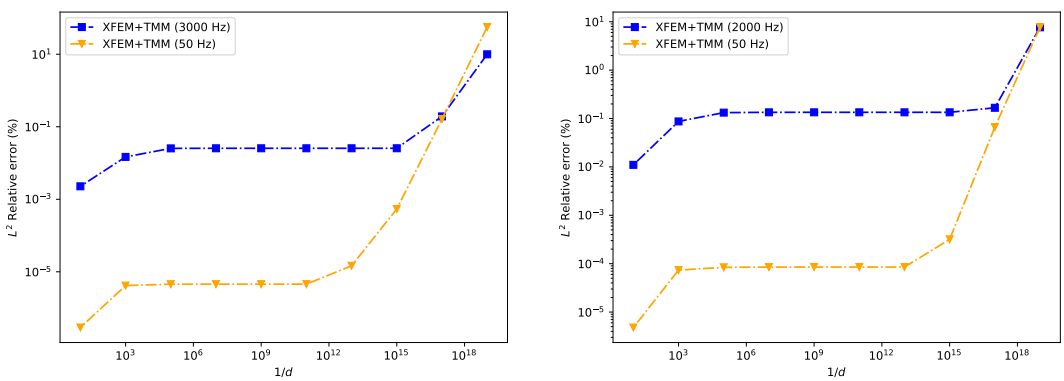

(a) (b)

Fig. 5.9.: Evolution of the global L^2 error with respect to thickness d for configuration "`f-f-f`" (a) and "`f-P-P`"(b) using unstructured interface non-conforming mesh

5.4.3 Validation of impedance tube

The second example aims at validating the proposed model for thin layers systems in a typical application situation through comparison with standard finite elements model where all the material layers are discretized. Here, a sound absorption system composed of a $2\,\mathrm{mm}$ sandwich film layer and a $20\,\mathrm{cm}$ thick polyurethane (properties available in table B.1) is introduced in a rigid, rectangular air cavity tube. The tube has a dimension of $1 \times 0.2\,\mathrm{m}$ subjected to a unit velocity source excitation at the left end, as shown in fig. 5.10.

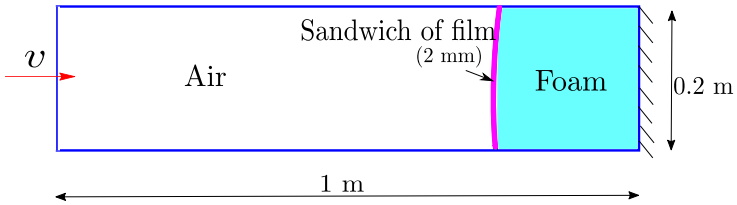

Fig. 5.10.: Kundt's tube problem in two-dimensions.

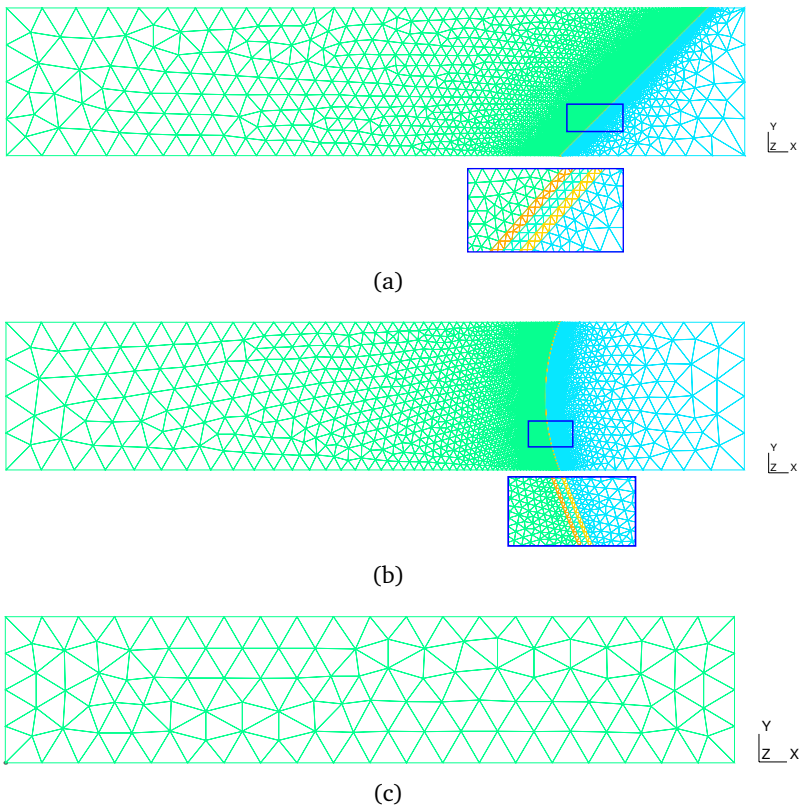

Fig. 5.11.: Meshes within standard FE model (a) for oblique planar films; (b) for curved boundary films; (c) Meshes within the proposed approach for the above two geometries.

Without loss of generality, two geometries of sound absorption systems are considered: an oblique surface at $45°$as well as a curved one with a radius of $0.27\ \mathrm{m}$. For the standard FE models, the meshes for these two geometries have to be refined near the thin layer, as shown in

fig. 5.11(a) and fig. 5.11(b), in order to avoid the distortion of the elements with large aspect ratios and to capture wave propagation in all directions. Additionally, for curved boundaries, such fine meshes are required to describe the curvature of the contour properly, lowering the geometrical error. Note that for certain implementations of p-FEM as the work presented in Bériot et al., 2016 [80], coarser and anisotropic meshes could be used to discretize the planar thin layers while maintaining high accuracy. Here a more conventional mesh is considered for the standard FEM model in order to remain suitable even for low interpolation orders.

In contrast, when the problem is solved within the proposed approach, a unique simple background mesh is sufficient for the different geometries, see fig. 5.11(c), as the thin layers are condensed into interfaces that are implicitly defined by a level-set function. Besides, the number of dofs to be assembled and solved is reduced as using such simple non-conforming mesh compared to the ones used in standard FEM.

Furthermore, the three-layer sandwich of acoustic films used here is composed of two woven films on the two sides and one non-woven film in the centre with thickness of $d_1 = d_3 = 0.6\,\mathrm{mm}$ and $d_2 = 0.8\,\mathrm{mm}$ respectively. This kind of multi-layer system is straightforward to be modelled under our approach thanks to the TMM technique through changing the global transfer matrix. The global transfer matrix for three layers that have the same physical nature is directly written as:

$$[\mathbf{T}]^{\mathrm{sand}} = [\mathbf{T}]_1 \times [\mathbf{T}]_2 \times [\mathbf{T}]_3, \tag{5.35}$$

where $[\mathbf{T}]_i$ are the transfer matrices for each layer. If stratified layers are not of the same nature, the global matrix is obtained by multiplying interface matrices containing the continuity equations at the interfaces (more detail can be found in [section 11]Allard and Atalla, 2009 [29]). Note that in the case of an oblique $45°$ surface, the thickness d_i and $k_{\mathrm{eq}x}$ in each matrix are readily corrected to maintain the angle match between source excitation and orientation of film surface. When standard FEM solves such multiple layers problems, at least one extra dofs per node of each element in two-dimensional problems need to be added to represent each film layer, which introduces far more unknowns to be solved with respect to the proposed method. Therefore, treating multiple layers is another strength of our approach compared to standard FE models.

Fig. 5.12 presents pressure field results for the two sound absorbers of different geometries. We observe that the pressure field computed by the (XFEM+TMM) approach has an excellent agreement with the one computed by full FEM discretization where all three thin films modelled by the Helmholtz Limp models are discretized by finite elements. A significant drop and an obvious pressure "discontinuity" is captured across the thin films in both numerical models. Moreover, it is worth pointing out that p-refinement is used to ensure proper convergence of the solution for both models. It is an efficient approach in acoustics due to its favourable behaviour against pollution, and it also allows for keeping a fixed mesh during the convergence procedure. However, it leads to a large matrix size of the discrete system in the case of the FEM model. Note also that p-adaptative methods such that the work presented in Bériot and Gabard, 2019

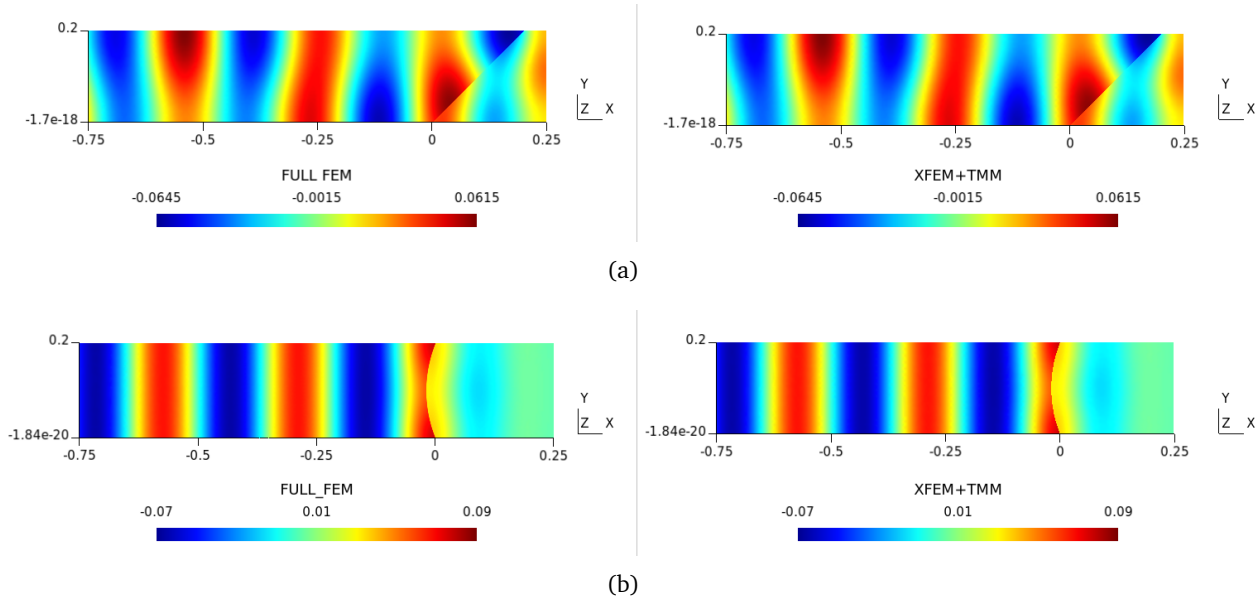

Fig. 5.12.: Real part of pressure solution (in Pa) for standard FEM and the proposed approach (XFEM+TMM) for sandwich absorption systems under different geometries and an excitation of $2,000$ Hz.

[169] could be used to improve the efficiency when using conventional meshes. Nevertheless, our approach is quite direct: one fixed simple background mesh can be used for any geometry and interpolation degree without any adjustment. A brief comparison of matrix size using convential FEM and proposed model for the same considered problems is given in table 5.1. The proposed "XFEM+TMM" economize the size of linear system by a factor of $10 - 20$, which reduces directly the computational resource in terms of memory and computing time when a direct solver is used.

Tab. 5.1.: Matrix size of $M \times M$ $(p = 3)$ of impedance tube problem.

M Geometry / Method	45 ° oblique surface	Curved surface
Classical FEM	184 039	105 535
Proposed approach	1349	1613

To further quantify the accuracy of the proposed approach against standard FEM, the absorption coefficient α of the porous system is estimated. This coefficient is evaluated numerically in the (X)-FE model by calculating the local average pressure and its gradient at the interface for each frequency. Here, an ideal normal incidence (planar interface perpendicular to the incident direction) is considered.

The absorption coefficient with respect to the frequency is plotted in fig. 5.13 for the considered sound absorbing system. The solution calculated by a semi-analytical package "pymls" [170] (based on work of Dazel et al., 2013 [70]) serves as a reference. This absorption exhibits multiple resonances from 1 Hz to $5,000$ Hz. Seventeen points are mostly chosen at the resonance

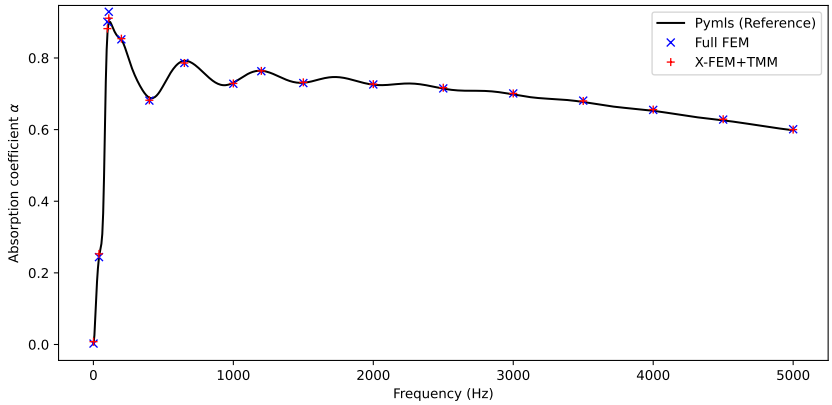

Fig. 5.13.: Absorption coefficients for the sound absorbing system made of a sandwich film coated on a polyurethane.

frequencies, to estimate coefficient α for the full FE model and the proposed approach. The converged solution for each frequency is obtained by increasing the interpolation order while keeping the same mesh. As illustrated, the two numerical models are in good agreement and stay greatly close to the reference in such a wide frequency range.

5.5 Conclusion

This chapter began by establishing a generalized computational approach to account for thin layers in time harmonic acoustic problem. This framework was then applied to typical sound absorbing systems. Four coupling configurations lead to three types of generalized interface condition and two major generalized variational interface operators. The corresponding discrete linear system could be non-symmetric.

The TMM enhanced interface model was demonstrated more fitted and accurate than the pressure jump model presented in chapter 4. The proposed interface model applied for thin acoustic resistive film is completely acceptable with a limit error induced from the angle mismatch in the transfer matrices.

The implementation of the proposed approaches discretized in a X-FEM space passed the verification of numerical benchmarks. Highly accuracy and optimal rates of convergence can be achieved. The conditioning is comparable to the one in conventional FEM.

The impedance validation case revealed threefold benefits of the proposed model: a) Flexibility with respect to the geometry, as the mesh is independent of the surface location. This benefit provides a convenience to test multiple geometries (configurations) of the sound absorption system in Kundt's tube without re-meshing; (b) Economizing computational resources compared to standard FE models; (c) The accuracy of proposed method can be ensured in a wide range of frequency.

6 Numerical application on cavity problems

> *Study extensively, in quire prudently, think carefully, distinguish clearly, and practice earnestly.*
> 博学之，审问之，慎思之，明辨之，笃行之
>
> — **Zhong Yong**
> (Li Ji)

In each previous sections, the implementation of the proposed methods and formulations were verified with analytical benchmarks or validated through simple geometric problems. In this chapter, the afore-proposed approaches are applied for an engineering vibro-acoustic problem concerning a series of practical circumstances. This chapter involves the simulation and prediction of acoustic fields in a two-dimensional car cavity including interior porous seats of complex geometrical profile. Unlike analytical benchmarks where exact solutions exist and some plane wave assumptions are satisfied naturally, the sound field to be simulated is more complex and unpredictable. The objective of this chapter is to eventually illustrate the accuracy and all potential benefits from using the proposed framework/approaches in this thesis.

6.1 Preliminary

6.1.1 Problem set-up

The dimension of a car is approximately $2.67\,\mathrm{m} \times 1.1\,\mathrm{m}$. The cavity is filled with air of which the sound behaviour is modelled by the Helmholtz equation. Passenger seats made of XFM foam (properties given in table appendix B.1) are potentially placed anywhere in the air cavity. The acoustic behaviour of the considered porous material is modelled by the Biot's $(\mathbf{u}^s, p^f)$ mixed formulation. Therefore, in this chapter, all the interface conditions related to the fluid-PEM

coupling are tested. An arbitrary normal velocity ($\partial p/\partial n = 1$) is imposed on the front windshield to generate a sound field excited in the mid frequency range. To assess the acoustic field, the sound pressure levels (SPL in dB) in the cavity will be evaluated:

$$L_p = 20 \log_{10} \left(\frac{P}{P_0} \right), \tag{6.1}$$

where P is the root-mean-square pressure obtained by numerical methods, P_0 is a reference sound pressure for which sound pressure in air are commonly used $P_0 = 20\,\mu\mathrm{Pa}$.

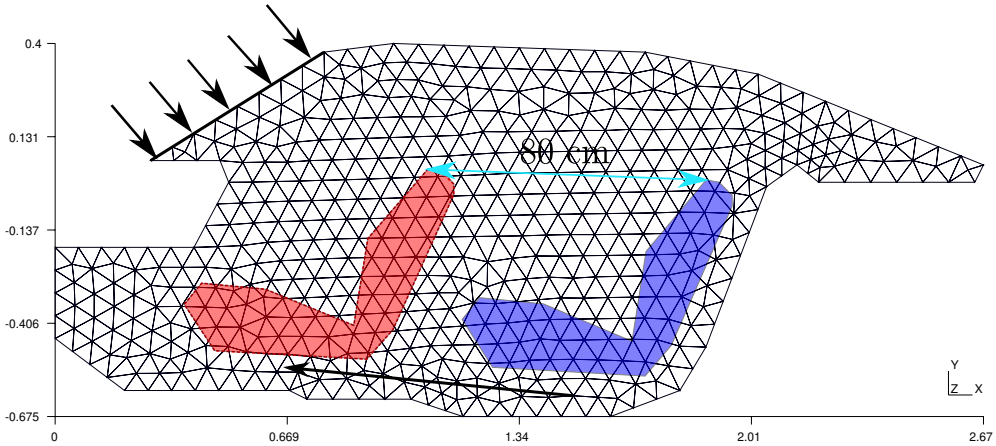

Fig. 6.1.: Car cavity problem description including the geometry and boundary conditions with associated X-FEM mesh.

The computational domain is discretized into unstructured triangular elements with the help of the open source meshing tool `Gmsh` (Geuzaine and Remacle, 2009 [171]). In the proposed computational framework, the profiles of the foam seats are defined by means of linear Level-set functions with sub-grid refinement instead of being meshed explicitly. As a result, one single mesh that is independent of geometries and positions of the interior passenger seats can be used for all following computation scenarii, as shown in fig. 6.1 with element size of about $0.075\mathrm{m}$. In addition, increasing polynomial order (p-refinement) is adopted to obtain a converged solution and to avoid changing the mesh configuration for both X-FEM and interface-fitted FEM.

6.1.2 Placement of one single seat

The perfect coupling when no thin porous layers exists between air and porous seats is firstly examined as a preliminary test. One simulates the change of acoustic field in a common situation where the driver's seat is switched from one position to another position. For this purpose, a sequence of interface-fitted meshes are required in standard FEM. In contrast, such change of position is much more easily realized by translating[1] existing Level-set function without re-meshing.

[1] `Translation` manipulation applied on original level-set

Two conforming meshes used for two extreme positions are depicted in fig. 6.2. It is noticed that the meshes are refined at the top of the seats to describe multiple small geometrical features. Within X-FEM, *Nitsche-type* formulation as proposed in chapter 4 with $\sigma d = 0$ is utilized to ensure the continuity of the pressure inside the elements for the prefect coupling when interface non-conforming mesh is used.

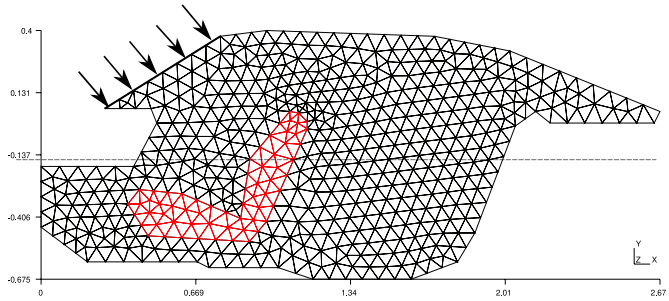

(a)

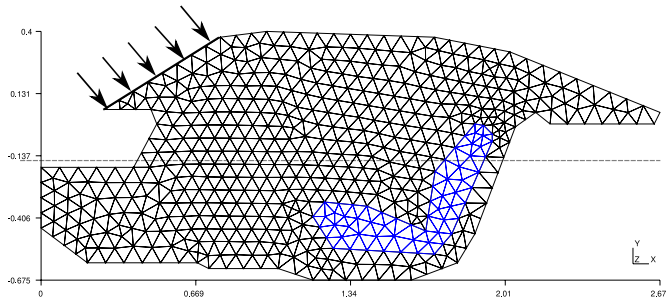

(b)

Fig. 6.2.: Geometry and the associated approximation FEM meshes (a) position A and (b) position B.

The solutions under $2,000$ Hz with the two FE models comparison are illustrated here, in fig. 6.3. It shows a visible agreement between the classical finite element results under approximation order $p = 4$ (see figs. 6.3(a) and 6.3(b)) and X-FEM results with same order (see figs. 6.3(c) and 6.3(d)). Subtle differences can be observed between the two models because the meshes used to post-process the results are not strictly identical. This introduces differences in the graphical interpolation. The evolution of the pressure field is clearly captured as the seat position changes. The attenuation of the pressure level because of the presence of the XFM foam is also described successfully at the location of the passenger seats.

To illustrate the pressure level of the acoustic field and the influence of the porous seat in the car cavity more precisely, a solution along the middle horizontal clipping ($y = 0.5y_{min} + 0.5y_{max}$) for the seat at a specific position is plotted in fig. 6.4. It is observed more clearly that FEM and X-FEM solutions are clearly matching, even no visual difference is observed in this sliced solution. The solution of the empty car cavity (no porous seat) is also calculated and plotted in the figure with orange dashed line as a comparison. It is found that the empty car cavity exhibits a more resonant solution with higher quality factor (excitation mode) and larger variations of pressure level. This demonstrates that the passenger seat is able to lower the average pressure level because of the sound dissipation of porous materials.

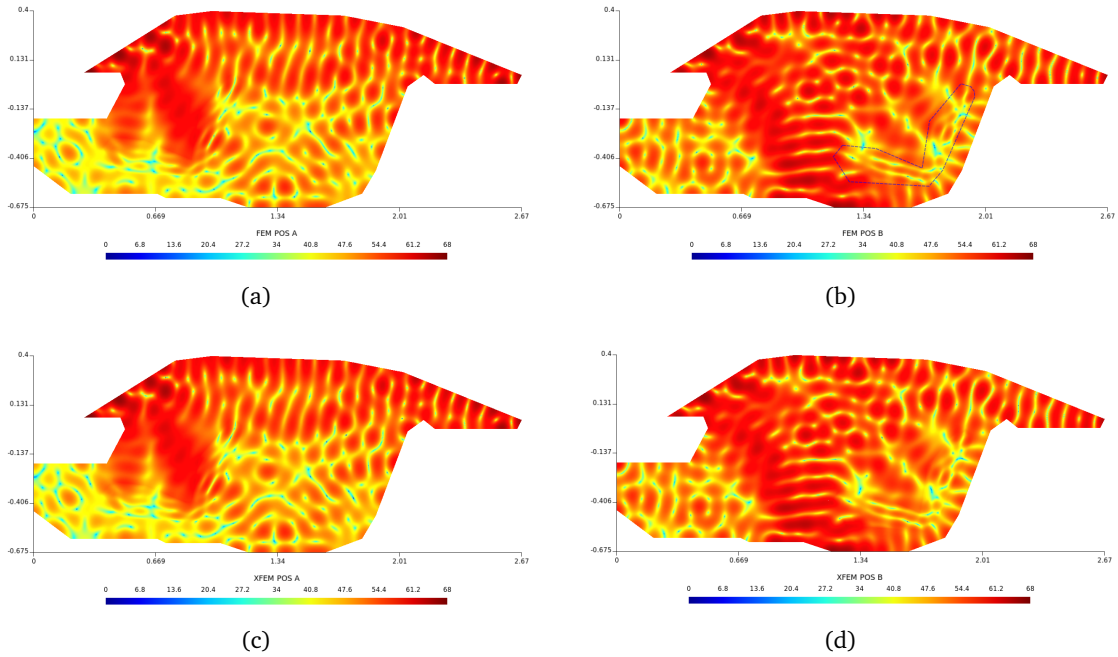

Fig. 6.3.: Solution of the sound pressure (in dB): with classical FEM (top) and X-FEM (bottom) for position A (left) and B (right). The contour and position of seats is indicated by black dashed line.

This case provides as well one representative application where the proposed method is of practical interest. Transformations such as `translation`, `rotation` or `symmetry` of an internal complex geometry (a porous seat in this case) can be handled readily without re-meshing. This can be applied to, for instance, a procedure of parametric or optimization design where a number of simulation for diverse interior geometries need to be tested. X-FEM coupled with Level-set simplifies greatly the pre-processing for CAE engineers.

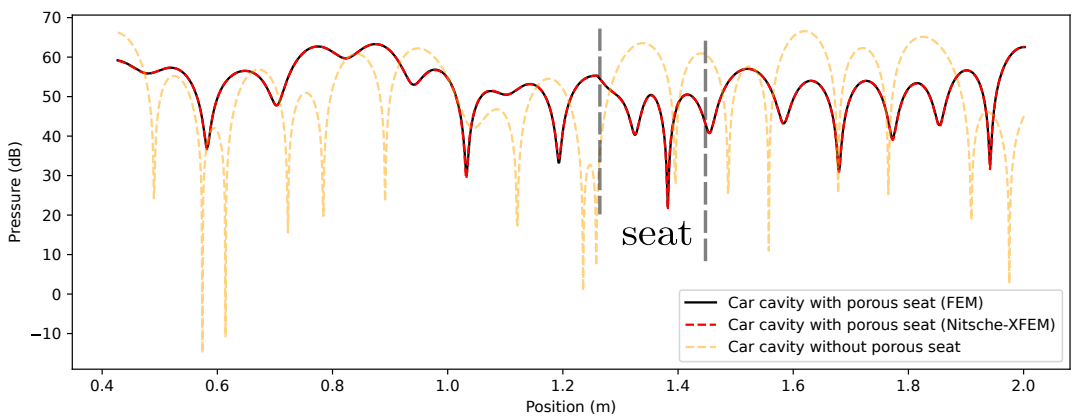

Fig. 6.4.: Clipping of the solutions along the mid horizontal line for single-seat configuration.

6.2 Double-seat configuration

Let us consider a more complicated problem in terms of geometry: two passenger seats made of the same XFM foam are included in the car cavity. For interface-fitted FEM, a re-construction of geometry and re-meshing are needed as shown in fig. 6.6, whereas the same mesh as used in previous case can be utilized directly for X-FEM. The geometry of the two seats is obtained by the **union** operator of the two existing Level-set functions (see fig. 6.5).

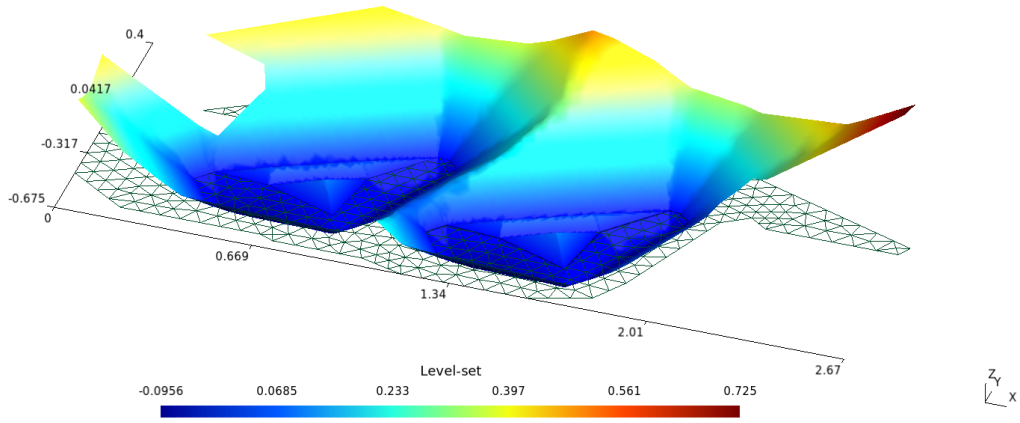

Fig. 6.5.: Interpolated Level-set function for the two-seat configuration

6.2.1 From perfect to imperfect (pressure jump) interface

Here, the sound field involved both perfect coupling and pressure jump interface condition eq. (4.1a) where $\sigma d = 775.10^3 \times 1.10^{-3}\ \mathrm{N\,s\,m^{-3}}$ corresponding a woven film, are to be simulated. One *Nitsche-type* formulations is able to treat these two conditions simultaneously by only changing the value of σd. The stability parameter of this formulation is set $\beta_h = 1$ empirically according to the conclusion in chapter 4. Besides, to demonstrate the stability and robustness of this formulation within the X-FEM, the *penalty-type* formulation is also used to solve the same problem for comparison. It is worth noticing that the *penalty-type* formulation is not able to handle the perfect interface directly, the solution has to be approximated by near-perfect parameters σd. Considering the value of the material coefficients in the variational formulation and the magnitude of discrete matrix terms (they are almost around 0.1 to 1), the $\sigma d = 1.10^{-15}\ \mathrm{N\,s\,m^{-3}}$ is chosen in the variational formulation as a value closed to zero to represent the (near)-perfect interface.

The solution of the interface-fitted FEM serves as the reference. This potential strong discontinuity (pressure jump) is accounted by a double nodes strategy (using Heaviside enrichment function on interface fitted mesh). To verify mutually between the FEM and X-FEM if the choice

of $\sigma d = 1.10^{-15}\ \mathrm{N\,s\,m^{-3}}$ for the interface parameter is able to represent the perfect interface appropriately and can give a converged solution, the same value of σd is employed in the FE reference solution.

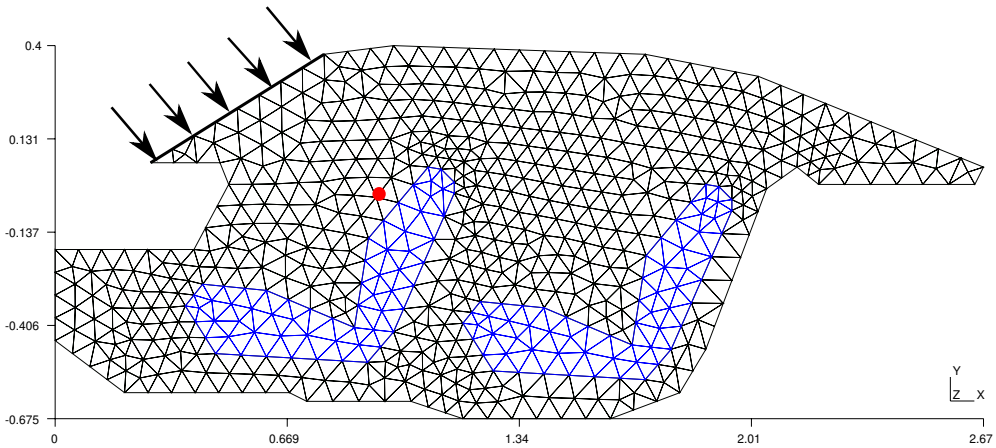

Fig. 6.6.: Geometry and mesh used for two-seats configuration using interface-fitted FEM.

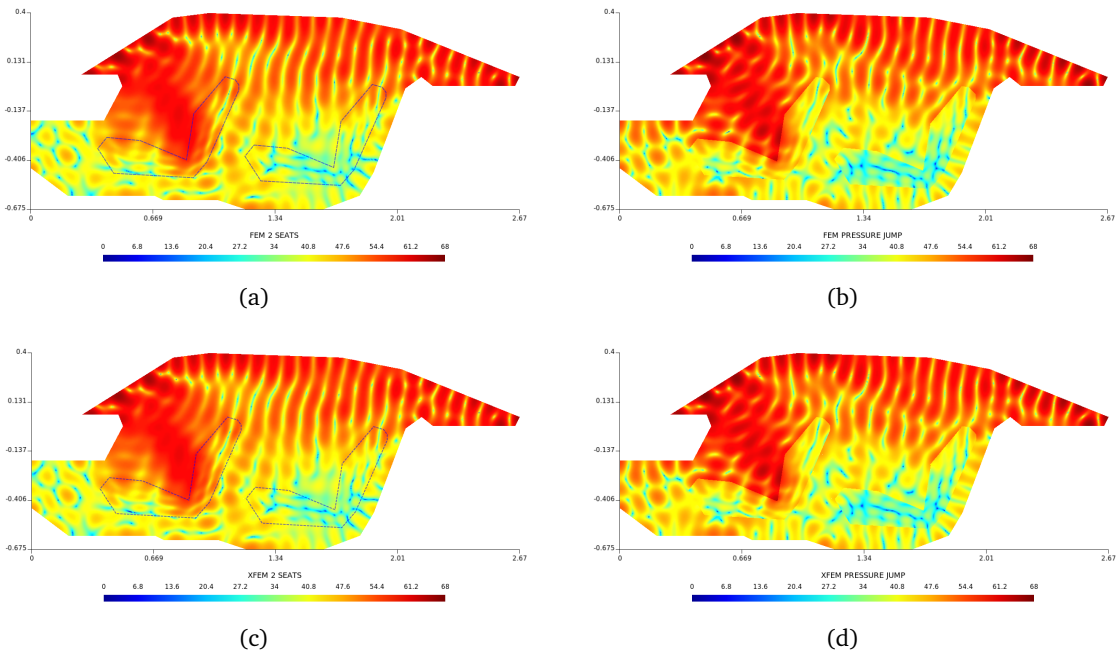

Fig. 6.7.: Solution of the sound pressure (in dB): with classical FEM (top) and X-FEM (bottom) for perfect interface (left) and pressure jump (right): the contour and position of seats is indicated by black dashed line.

Fig. 6.7 shows the sound field under excitation of $2,000\ \mathrm{Hz}$ for the two interface conditions. Again, the two numerical models exhibit great accordance. More sound is observed to be absorbed in the back seats, and the global pressure level decreases in this case compared to the previous single-seat configuration. It is worth highlighting that the contours of the seats are

apparent in figs. 6.7(b) and 6.7(d) compared to figs. 6.7(a) and 6.7(c), which is because of the strong discontinuity which is triggered by the pressure jump condition.

The sliced solution for horizontal clipping is also provided for a detailed comparison, in fig. 6.8. In regard to the perfect interface (see fig. 6.8 top), X-FEM with the *Nitsche-type* formulation gives a more accurate solution than *Penalty-type* referred to the interface-fitted FEM. As the *penalty-type* formulation is also employed in the FEM, this subtle nuances observed in X-FEM, again demonstrates the fact that *penalty-type* formulation within X-FEM suffers from a convergence issue when σd closed to zero, as discussed in chapter 4. Meanwhile, three curves are superposition on each other for pressure jump condition (see fig. 6.8 bottom), presenting an excellent agreement between the two formulations within X-FEM as well as the reference solution, considering there still exists a difference in the post-processing between two non-identical meshes.

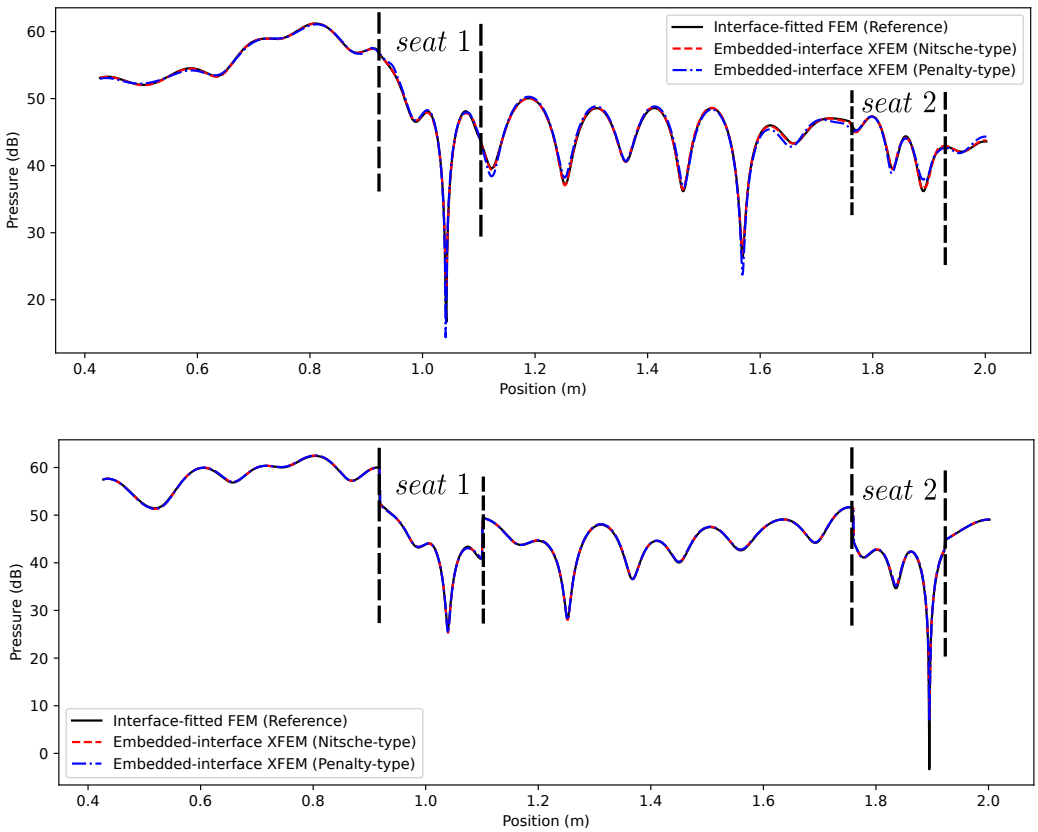

Fig. 6.8.: Clipping of the solution for (top) perfect interface and (bottom) pressure jump interface for two-seat configuration.

In many situations, the frequency response is of primary importance to examine acoustic systems. It is known that the material properties of porous materials (effective density ρ, bulk compressibility K and other Biot's parameters), the interface law ($\sigma d/\omega$) and the global solution are all modified as variation of frequency in our case. Therefore, studying the solution against the frequency allows one to evaluate the robustness of the proposed method with respect to all

these variables. The pressure level at the position of the head of the driver (marked by a red point in fig. 6.6) is assessed in the frequency range of interest $f \in [500, 1200]$ Hz. Similarly, the Frequency Response Function (FRF) is evaluated for both the coated film (pressure jump) and the perfect interface (see fig. 6.9).

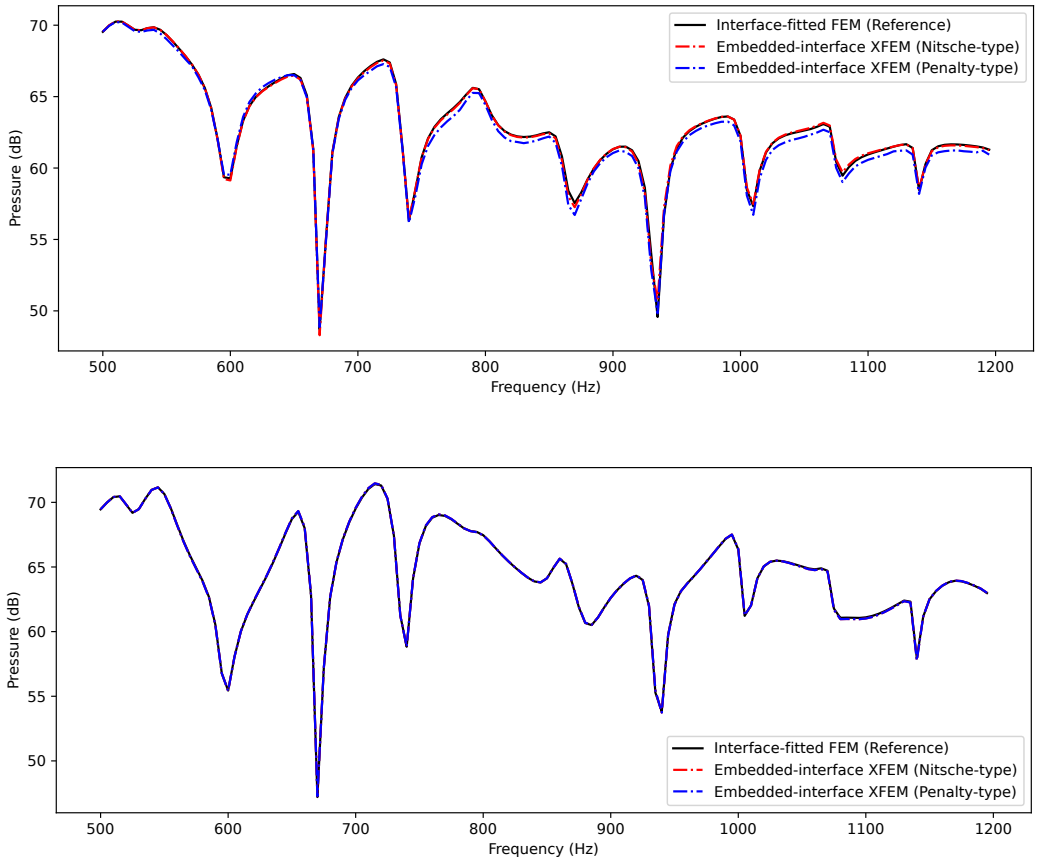

Fig. 6.9.: Frequency Response Function (FRF) for (top) perfect interface and (bottom) pressure jump interface for two-seat configuration.

The three approaches give highly similar solutions for pressure jump interface, while an obvious divergence is observed for the perfect interface case. *Nitsche-type* formulation is able to retain a high accordance with the reference solution over the whole frequency range, whereas *Penalty-type* displays a visible gap with the two other solutions, especially over frequencies $f > 800\,\mathrm{Hz}$.

6.2.2 From pressure jump to TMM enhanced interface

Finally, the transfer matrix enhanced interface condition for representing thin porous materials is tested. The same woven film as previous case with thickness $d = 0.8$ mm is modelled by a transfer matrix (Limp model). As the acoustic field is too complex to correct the incident angle θ in the matrix, the incident angle keeps $\theta = 0$. Therefore, this example also allows us to

account for the error due to the angle mismatch (see section 5.3.2 chapter 5). For the reference solution, a classical interface-fitted FEM model (*Full FEM*) is used. The thin porous layer is discretized with at least one element in the thickness direction. The corresponding mesh is depicted as fig. 6.10, of which the maximum size is same as with the X-FEM ($0.075\,\mathrm{m}$), and is refined gradually in the vicinity of the thin layer to keep a high mesh quality with small aspect ratio. Concerning the X-FEM, compared to last case, the only thing that needs to be changed is the weak formulation where transfer matrix interface condition is imposed.

Here, we stress the meshing time for standard FE model to highlight the benefit of our approach during the pre-precessing stage. The meshing time (CPU time) with `Gmsh` for the mesh shown in fig. 6.10 is $0.84\,\mathrm{s}$ against $0.0088\,\mathrm{s}$ for X-FEM mesh, a difference of almost 100 times. This difference in time can become prohibitive if some repetitive calculation are necessary such as a shape optimization procedure.

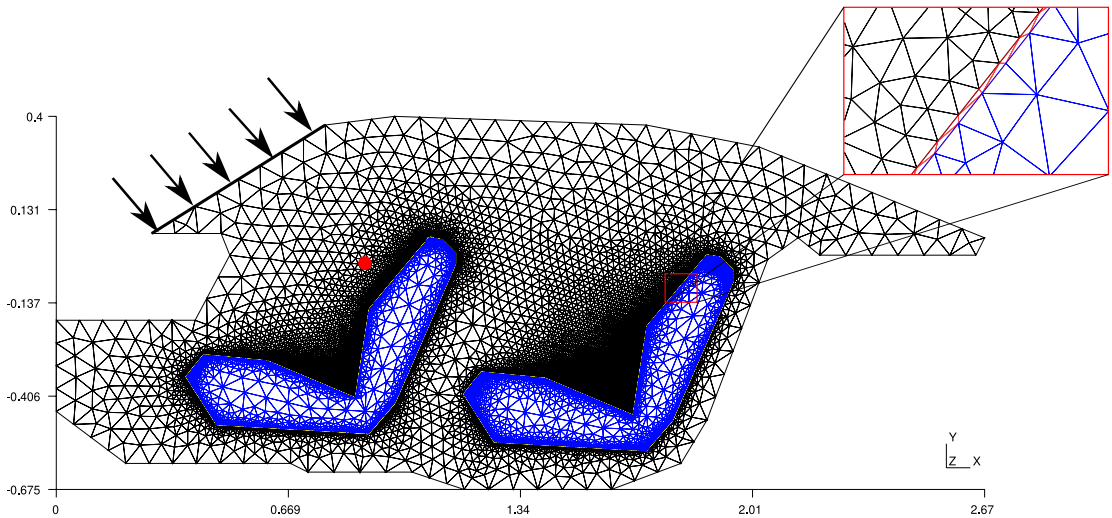

Fig. 6.10.: Geometry and mesh used for thin-layer car cavity configuration using interface-fitted FEM (*Full FEM*).

Moreover, to obtain converged solutions using these meshes, a $247\,167$ (*dofs*) matrix for *Full FEM* model needs to be solved, which is 20 times larger than the one of the proposed method *X-FEM+TMM* ($13\,639$). Consequently, the larger number of unknowns leads to a longer computational time (see table 6.1). The solving time of the linear system using a direct solver is proportional ($\mathcal{O}(N^3)$) to the matrix size, 20 times difference between two models. Whereas the time consumed on assembly for the matrix of *full FEM* model is only about 3 times longer than the one of our method. More time consumed on the assembly stage in X-FEM because of the numerical quadrature on the sub-elements. Nevertheless, we still have an obvious contrast of the consuming-time, which could be accumulated to become extensively huge when a series of simulation need to be done, as the first considered situation where the position of seat changes or for a frequency sweeping.

An example of solutions within *Full FEM* and the proposed approach are compared in fig. 6.11. Again, the two solutions exhibit a perfect visual agreement, where the pressure attenuation in

Tab. 6.1.: Numerical metric comparison for two-seat thin layers car cavity problem.

Method \ Metrics	Assembly time (s)	Solving time (s)
Full discretized FEM	22.928	7.904
X-FEM+TMM	9.458	0.406

the seats and a noticeable pressure discontinuity close to the thin films are observed. The sliced solutions are compared in fig. 6.12 with black solid and red dashed line. The difference between two solutions are below $1\mathrm{dB}(\leq 1\%)$. Considering the angle mismatch exists everywhere in the film model and the re-interpolation of the pressure fields on two such different meshes, this nuance is completely acceptable compared with the full FE model for engineering application, especially when the pre-processing and computational cost (time) is accounted for. The model considering pressure jump as the interface condition is also plotted in the figure. A visible incoherence is observed along the entire curve compared two other models, indicating that pressure jump condition is not sufficient (accurate) to represent the effect of the considered woven film, and corroborating the necessity of using TMM to represent thin porous layers for the problem of interest.

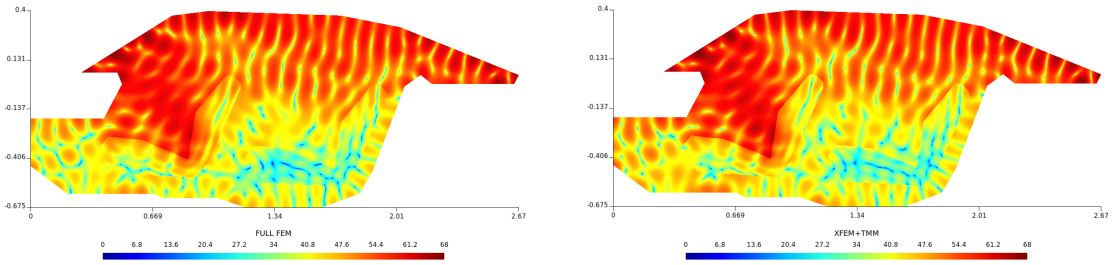

(a) (b)

Fig. 6.11.: Solution of the sound pressure (in dB): calculated by classical full-FEM (left) and X-FEM+TMM (right) for two-seat thin layers configuration.

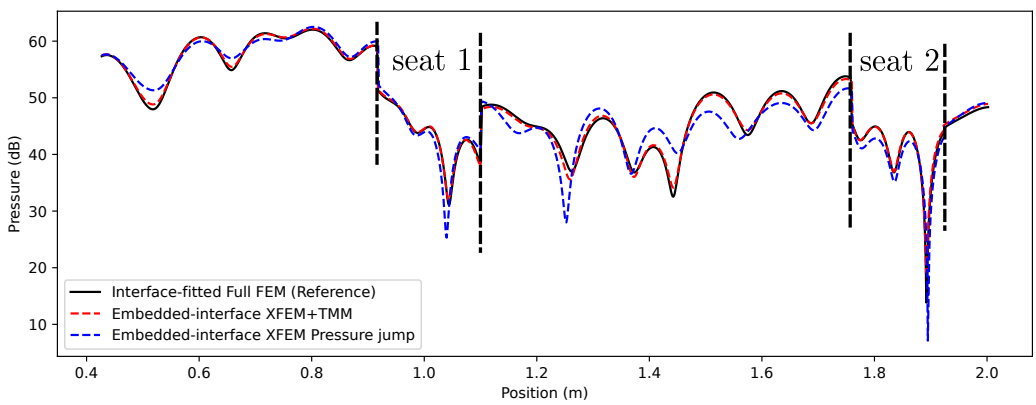

Fig. 6.12.: Plot of sliced solution of a horizontal clipping for two-seat thin layer configuration.

As before, the frequency response of the red marked evaluated point is examined. Besides of the material properties of the porous materials in Biot's equations, the parameters in the transfer matrix of the Limp model will be changed as well, as variation of frequency in this case. The *Full FEM* model is considered as the reference solution. To further highlight the improvement brought by the TMM enhanced model compared to the pressure jump to describe the acoustic behaviour of thin films, the X-FEM solutions for the two interface conditions are both plotted (see fig. 6.13). A similar observation is recognized that TMM enhanced model gives a solution closer to the full discretized FEM over the frequency range than the pressure jump condition, particularly in the range $f \in [600, 750] \cup [1000, 1150]$ Hz.

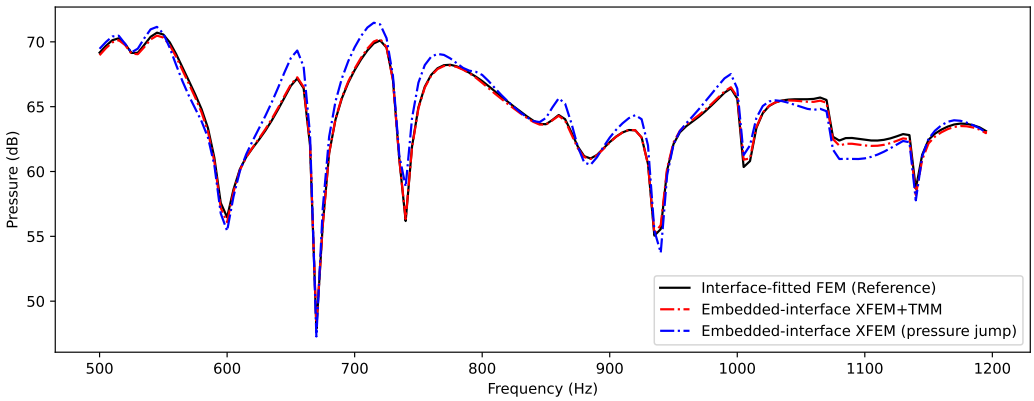

Fig. 6.13.: Frequency Response Function (FRF) of an evaluated point for two-seat thin layers configuration.

6.3 Conclusion

In this chapter, the simulation of sound fields in the car cavity was performed as a summative application of all proposed methods and formulations. In all the tested situations, the proposed approaches exhibited a great accuracy compared to the reference solutions (interface-fitted standard FEM). Thanks to the X-FEM coupled with Level-set functions and the proposed interface conditions, one relative coarse mesh was used in our computational framework regardless of the changes of the passenger seats or the existence of thin films.

The robustness and accuracy of the proposed *Nitsche-type* formulation over a broad range of frequency compared to the *penalty-type* was verified with respect to diverse variations. It was demonstrated, for the TMM enhanced interface model that the error from angle mismatch in the transfer matrix did not deteriorate the solution. The matrix without correction of the incident angle θ can be applied to predict the sound field accurately in such complex situations. Moreover, TMM enhanced interface condition was shown more accurate to represent the thin porous layers in comparison with the pressure jump condition.

Several practical situations where a series of simulations with different geometries or parameters is carried out were provided in this chapter. The proposed approaches displayed the flexibility and efficiency in the sense that it is able to reduce greatly the computing resources during the pre-processing and solving stage without manual intervention.

Conclusion

7

> *A thousand times, I search for her in the crowd. And, suddenly turning my head, discover her where the lantern lights are dim.*
> 众里寻他千百度，蓦然回首，那人却在灯火阑珊处
>
> — **XIN Qiji**
> (Qing Yu An)

This thesis was devoted to the numerical modelling and simulation of sound absorbing systems involving simultaneously thick and thin porous layers. The application of a mesh-independent discretization method (X-FEM) to such problems was investigated to alleviate the meshing restriction due to the existence of thin layers and potentially complex/evolving geometries in the domain. To the author's knowledge, this is the first application of X-FEM for sound dissipation vibro-acoustic problems. The thesis provided all relevant fundamental details to address our problems from modelling, theoretical, numerical aspects. The main contributions of the work is summarized below.

7.1 Summary of the main contributions

From X-FEM discretization for vibro-acoustic problems involving Biot's coupled equations to the thin porous layer modelling and simulation, the contributions of this thesis can be classified as three parts.

First, according to the porous media models and the principle of X-FEM, the enrichments and discretization of the approximation space were provided for three couplings: fluid-fluid, PEM-PEM and fluid-PEM. Specifically, to the author's knowledge, it is the first time in the literature to apply the high-order X-FEM discretization for the $(\mathbf{u}^s, p)$ Biot's coupled equations in acoustic problems. For the perfect interface case, the "ridge" enrichment function was used to enrich the pressure and solid displacement fields. Classical acoustic benchmarks (reflection, transmission and scattering) were performed to verify the implementation. The convergence behaviours of fluid pressure and solid displacement were identified separately. The close-to-optimal convergence rates $\mathcal{O}(h^{p+1})$ were obtained for both primal variables. In general, the

behaviour of h and p-refinement was similar to the observation reported in the literature for classical FEM. High accuracy was achieved for various porous materials which have totally different acoustic properties over a large frequency range.

Secondly, when it comes to the modelling strategy for thin porous layers in the relatively large domain, the reduced non-thickness interface model with appropriate interface conditions (imperfect) was adopted. This work began by the pressure jump interface which is the most used model, considering only the flow resistivity of the medium. This interface condition induces a strong discontinuity of field and depends on the local velocity, which is *robin-type* condition. Heaviside enrichment function was thus used to introduce the jump in the elements. To impose *robin-type* condition in the X-FEM space, the discrete *penalty-type* and *Nitsche-type* variational formulations were derived. The stability (coercivity) of the discrete *Nitsche-type* formulation was proven and the stability condition [1] was given.

A robust approach adapted to the Heaviside enrichment function to calculate the stability parameter at element level was proposed. As such, the difference between Heaviside enriched X-FEM and Cut-FEM was highlighted and the transition procedure between the two bases were given for a general high-order expression. All the approaches were implemented and verified with two-dimensional benchmarks. Two formulations were tested with different acoustic problems for different coupling configurations. Contrary to the *penalty-type* formulation, the pressure jump imposed by the *Nitsche-type* formulation were captured properly in elements without numerical instability regardless of interface parameters (from near-perfect to imperfect). The *Nitsche-type* formulation exhibited a better convergence for evaluating the interface flux compared to *penalty-type* formulation. Moreover, the proposed estimation of the stability parameter was capable of providing an "optimal" solution in terms of accuracy and conditioning.

Then, from the physical viewpoint, the pressure jump condition was found not accurate enough to represent thin porous media over frequencies for a variety of porous materials. A more comprehensive interface law of thin porous layers was needed. Plane wave transfer matrix method (TMM) caught our attention, which is a re-representation of the governing equations of porous media. We demonstrated that it is able to better describe the acoustic behaviour of thin porous layers than the pressure jump conditions over a large range of frequency. According to the coupling configuration, four generalized interface conditions which lead to strong discontinuities in both primal and dual variables were derived.

To account for these more complicated interface conditions, a generalized framework has been formulated where variational formulations were discretized by Heaviside enriched X-FEM. This framework could be applicable to many types of acoustic media and has been applied to sound absorbing systems in the thesis. In addition, because of the properties of TMM, multiple thin layers can be handled readily. This theoretical contribution was validated numerically by classical impedance tube and a set of real size engineering car cavity problems. High accuracy and gain in computational cost (pre-processing and solving time) were demonstrated.

[1] choice of stability parameter β_h

We achieved the initial objective of solving time-harmonic problems including thin porous layers more efficiently than the conventional FEM. Compared to the interface-fitted FEM model, the total number of degrees of freedoms are greatly reduced with the proposed methods. However, there are still some improvements could have been conducted to further reduce the computational cost and speed up the computation procedure. The bubble shape functions in high order approximation could be eliminated for standard elements. The discrete linear systems involved in Biot's equations could be solved with specific pre-conditioners to decrease the conditioning of the system. Because of numerical property of the Biot's equations that displacement of solid is more difficult to converge than the pressure, the variable-p approximation or adaptative-hp schemas could be used for fluid-Biot coupling.

7.2 Future works and perspectives

- In the framework of this thesis, several numerical and technical challenges were encountered, and most of them were fixed in this work. However, there are still several interesting questions raised from the thesis that need to be addressed deeply in short term.

  The *Nitsche-type* formulation proposed in the second part of chapter 4 for pressure jump condition in fluid-PEM coupling lacks a theoretical analysis. The numerical condition of stability (coercivity) for the discrete formulation needs to be clarified.

  For TMM enhanced interface conditions, the linear system yielded from the Biot's matrix enhanced condition is non-symmetric. Searching for a symmetric Biot's matrix or symmetrization of existing interface formulations is worth to be further investigated. In addition, the generalized variational formulation enhanced by TMM suffers also from the divergence of the solutions when the thickness of the film d trends to zero. Construction of a stable formulation regardless of d remains a great interest.

  In this thesis, all the thin layers are reduced into non-thickness interface. Therefore, the real geometric configuration of the problem is more and less simplified. One possible solution that is able to re-represent the geometry without simplification and also make most of the proposed interface models is to use multiple level-set functions or non-matching meshing techniques to create a void across the thin layers.

- On the other hand, besides of the proposed methods, many other techniques have been applied and investigated during this Ph.D project. Relied on all these varieties of methodologies, some future researches can be further developed and dived in for a medium to long-term.

  With the flexibility of the X-FEM and level-set, accounting for the geometry evolution into the proposed methodologies would be first relevant application, such as for shape

optimization and uncertainty propagation of geometric variation in sound absorbing systems. In such cases, in order to avoid numerous repeated large deterministic calculation (even though our models are already smaller than the one of classical FEM) for each geometric parameter where re-meshing, re-assembly and re-solving of linear system are needed, S (stochastic) FEM or the Reduced Order Models (ROM) are desired to be employed. First preliminary results of considering geometric uncertainties in our framework is presented in appendix A.

The proposed generalized framework in chapter 5 can be extended and applied to other physical problems by adapting the governing equations and interface conditions. One can add the complexity of the interface condition to represent specific thin media. The thin periodic meta-materials layers that can be considered with Bloch wave expansion. It is also possible to perform multi-scale analysis where the micro-scale acoustic effects of any arbitrarily manufactured material is considered. An equivalent interface model is obtained firstly at micro-scale. Then, this micro-effects interface model is integrated into macro-scale with our proposed framework.

In vibro-acoustic problems, when thin solid structures are treated as a non-thickness interface in the domain, our method might play a role to connect exterior and interior acoustic field to handle problems like "from exterior to interior". The framework could also be applied in aero-acoustic problems (CAA) to simulate the flow around porous coated objects (Arcondoulis et al., 2021 [172]). Inspired from these two ideas, our method may be extended to connect the aero-acoustics and vibro-acoustics. That can applied, for instance, the interaction between the structural, interior acoustical field and exterior aero-acoustic excitation of a moving vehicle by solving simultaneously the interior vibro-acoustic and exterior air flow equations.

7.3 Scientific dissemination

7.3.1 Peer-review journal paper

- **S.WU**, O.Dazel, G.Gabard, G.Legrain, High-order X-FEM for the simulation of sound absorbing poro-elastic materials with coupling interfaces. Journal of Sound and Vibration. doi:10.1016/j.jsv.2021.116262
- **S.WU**, O.Dazel, G.Legrain, A computational framework based X-FEM for thin porous layers in acoustic problems. International Journal for Numerical Methods in Engineering. doi:10.1002/nme.7006.
- **S.WU**, G.Legrain, O.Dazel, Enforcement of interface laws for dissipative acoustic problems within X-FEM. Computer Methods in Applied Mechanics and Engineering (under review)

7.3.2 Conference and oral presentation

- High-order X-FEM for the simulation of sound absorbing poro-elastic materials with coupling interfaces. SAPEM (Symposium on the Acoustics of Poro-Elastic Materials), Purdue University, USA(Online), 01/04/2021
- Nitsche-XFEM for pressure jump interface condition in vibro-acoustic problems in presence of porous materials. CSMA (French conference on computaional mechanics), Giens, France, 20/05/2022
- A computational framework based on X-FEM for thin porous layers in time-harmonic problems. CFM (Congrès Français Mécanique), Nantes, France, 29/08/2022
- Generalized computational framework based on X-FEM for thin films in time-harmonic problems: Formulation, Validation and Application, ISMA (International Conference on Noise and Vibration Engineering), Leuven Belgium, 15/09/2022

Geometric uncertainty within the proposed models

A

This appendix presents the first preliminary studies to account for the geometrical uncertainty in sound absorbing systems, which shows a part of perspective work to be completed in the near future. The proposed numerical models/methods in the main text of manuscript are extended here. The principle of the methods and the preliminary results are presented.

The shape or geometry of sound absorbing system may have unexpected variations during the manufacturing or experiment stage, such thickness, surface flatness and smoothness of media. These geometric uncertainties might lead to a completely different acoustic response of the entire systems. This type of incertitude is not easy to be controlled and identified in physic experiments. To account for this variability in the simulation, a common method is to use *Monte Carlo* simulation where a large enough amount of deterministic numerical models with different variables needs to be calculated. This method is excessively computationally costly, especially for taking variation of geometry into consideration in conventional FEM, meaning re-meshing is essential for each calculation. Although re-meshing requirement is relaxed in X-FEM, high-fidelity solutions of large number of *dofs* still need to be calculated repetitively. This appendix is devoted to develop more efficient methods for considering geometric uncertainties within the framework proposed in this thesis with as few *re-calculation* and *re-meshing* as possible.

A.1 Problem set-up

The geometric uncertainty of sound absorbing systems in impedance tube is considered as validation problems. The tube has a dimension of $34 \times 3\,\mathrm{cm}$, filled with a porous material of $4\,\mathrm{cm}$ length at the right end of the tube. Two microphones are placed at the left end of the tube to measure the (mean) pressure level in order to calculate the absorption coeffcients.

Despite a simple configuration, many geometric variations can still be considered such as thickness, orientation, curvature and flatness of the media (see fig. A.1). It is worth to investigate effects of these uncertainties in impedance tube, which was rarely studied in the literature such as for the measurement of impedance and absorption coefficients.

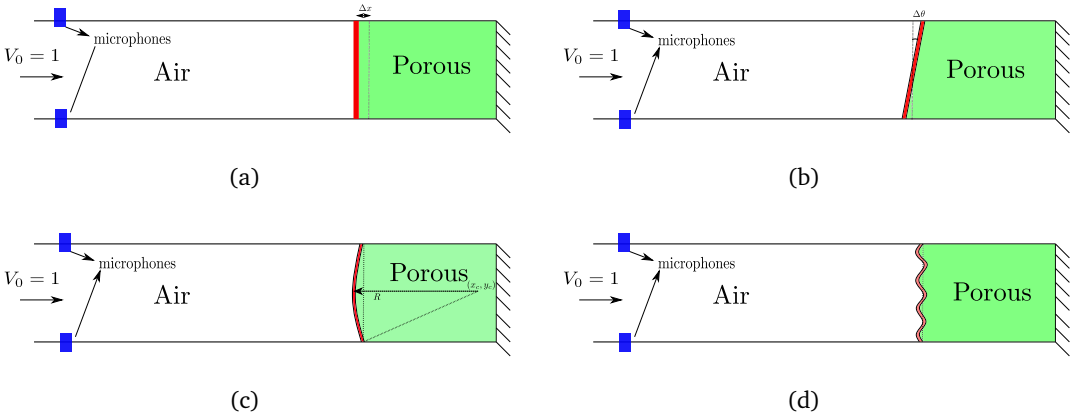

Fig. A.1.: Several geometric uncertainty situation in impedance tube problem: (a) variation of thickness, (b) orientation of media, (c) curvature and (d) the flatness which could be a trigonometric function.

In this appendix, the porous medium is modelled as an equivalent fluid with JCA parameters. Both pressure jump and TMM enhanced interface conditions are considered through a generalized transfer matrix for thin acoustic film coated on the thick porous media. We recall the variational formulation of the considered problem: Find $p_h^f \in \mathcal{P}_h^f$, such that

$$\sum_i^2 \left(\frac{1}{\rho_i} \int_\Omega \nabla \bar{q}^f . \nabla p^f \mathrm{d}\Omega - \frac{\omega^2}{K_i} \int_\Omega \bar{q}^f p^f \mathrm{d}\Omega \right) - \sum_{i,j=1}^2 (-1)^i A_{ij}^{\mathrm{ff}} \int_\Gamma \bar{q}_i{}^f p_j^f \mathrm{d}S = \int_{\partial\Omega} \bar{q}^f u_n^t \mathrm{d}S, \quad \text{(A.1)}$$

with coefficients A^{ff}:

$$A_{11}^{\mathrm{ff}} = \frac{T_{22}}{T_{12}}, \quad A_{12}^{\mathrm{ff}} = \frac{T_{12}T_{21} - T_{22}T_{11}}{T_{12}}, \quad A_{21}^{\mathrm{ff}} = \frac{1}{T_{12}}, \quad A_{22}^{\mathrm{ff}} = -\frac{T_{11}}{T_{12}}, \quad \text{(A.2)}$$

which are the terms in the relationship:

$$\begin{Bmatrix} p_1^{f+} \\ v_{n1}^{t+} \end{Bmatrix} = \left[\mathbf{T}\right]_{2\times 2} \begin{Bmatrix} p_2^{f+} \\ v_{n2}^{t+} \end{Bmatrix}. \quad \text{(A.3)}$$

The above formulation can be re-written in the general discrete form as:

$$\sum_i^2 \left[\mathbf{a_{Bi}}(\bar{q}_{hi}, p_{hi}) + \mathbf{a_{Ii}}(\bar{q}_{hi}, p_{hi})\right] = \sum_i^2 \ell_{\mathbf{i}}(\bar{q}_{hi}), \quad \forall q_i, \quad \text{(A.4)}$$

where $\mathbf{a_{Bi}}$ and $\mathbf{a_{Ii}}$ denotes the general discrete form for bulk parts and interface integrals, respectively. One can write this formulation in a more compact matrix way while considering the uncertainty variables ξ_i:

$$\mathbf{K}(\boldsymbol{\xi})\mathbf{p}^f(\boldsymbol{\xi}) = \mathbf{F}(\boldsymbol{\xi}), \quad \text{(A.5)}$$

where $\mathbf{K}$ is the general global stiffness matrix, $\mathbf{p}^f$ represent the nodal pressure solution and $\mathbf{F}$ denotes the vector of the generalized forces. As seen that all the terms depend on uncertainty

variables, it is thus called parametric discrete PDE. Now, the question is how can we solve this PDE more efficiently rather than through repeated calculation of the full discrete system (High fidelity solution).

A.2 Perturbation method

A.2.1 Theory and formulations

The perturbation method based on the Taylor series expansion is one of the most used stochastic FEM (see review [173]) to account for uncertainty. The basic idea of the method is to express the discrete linear system as the Taylor series. In our case, we re-express our parametric discrete linear system eq. (A.5), as:

$$\mathbf{K}(\boldsymbol{\xi}) = \mathbf{K}_0 + \mathbf{K}^I\boldsymbol{\xi} + \frac{1}{2}\mathbf{K}^{II}\boldsymbol{\xi}^2 + \frac{1}{3\times 2}\mathbf{K}^{III}\boldsymbol{\xi}^3 + \cdots + \frac{1}{N!}\mathbf{K}^N\boldsymbol{\xi}^N, \tag{A.6}$$

where $\mathbf{K}^i$ is the ith sensitivity order of matrix $\mathbf{K}$ to the variable ξ_i as:

$$\mathbf{K}^I = \frac{\partial K}{\partial \xi_i}, \quad \mathbf{K}^{II} = \frac{\partial^2 K}{\partial \xi_i^2}, \quad \mathbf{K}^{III} = \frac{\partial^3 K}{\partial \xi_i^3}, \quad \cdots \tag{A.7}$$

The same expansion is also applied to $\mathbf{p}^f$ and $\mathbf{F}$. In our case, the geometry variation has no effect on the force vector $\mathbf{F}$, hence the derivative of $\mathbf{F}$ is zero for all orders. The nodal solution $\mathbf{p}^f$ is expressed as:

$$\mathbf{p}^f(\boldsymbol{\xi}) = \mathbf{p}_0^f + \mathbf{p}^{fI}\boldsymbol{\xi} + \frac{1}{2}\mathbf{p}^{fII}\boldsymbol{\xi}^2 + \cdots + \frac{1}{N!}\mathbf{p}^{fN}\boldsymbol{\xi}^N, \tag{A.8}$$

and the sensitivity of ith order for solution are:

$$\mathbf{p}_0^f = \mathbf{K}_0^{-1}\mathbf{F}, \tag{A.9a}$$
$$\mathbf{p}^{fI} = \mathbf{K}_0^{-1}(-\mathbf{K}^I\mathbf{p}^{f0}), \tag{A.9b}$$
$$\mathbf{p}^{fII} = \mathbf{K}_0^{-1}(-2\mathbf{K}^I\mathbf{p}^{fI} - \mathbf{K}^{II}\mathbf{p}_0^f) \tag{A.9c}$$
$$\ldots \tag{A.9d}$$

It is seen that the key point to obtain the solution for a specific geometrical configuration is to calculate the ith derivative of stiffness matrix $\mathbf{K}(\xi_i)$. Unlike the materials properties for which an explicit function of $\mathbf{K}$ can be expressed analytically (derivative are hence readily obtained). Here, for geometrical random variation, it is difficult to conduct the differentiation explicitly. For this reason, the sensitivities to the geometric variables are approximated by the

finite difference method. A central scheme is used for the computation such as for the first order:

$$\mathbf{K}^I = \frac{\mathbf{K}(\Delta\xi_i) - \mathbf{K}(-\Delta\xi_i)}{2\Delta\xi_i} + \mathcal{O}(\Delta\xi_i^2), \tag{A.10}$$

where $\Delta\xi_i$ is the small non-zero positive difference of variable ξ_i. It is noted that the accuracy of this approximation is controlled by $\Delta\xi_i$, a pre-parametric study to choose $\Delta\xi_i$ is needed.

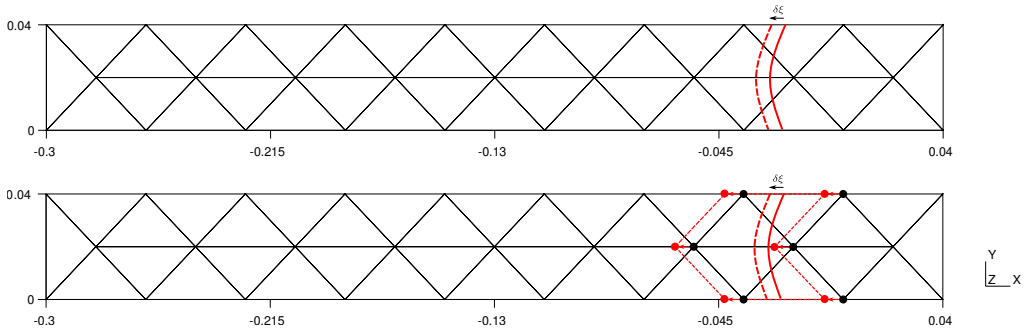

(a)

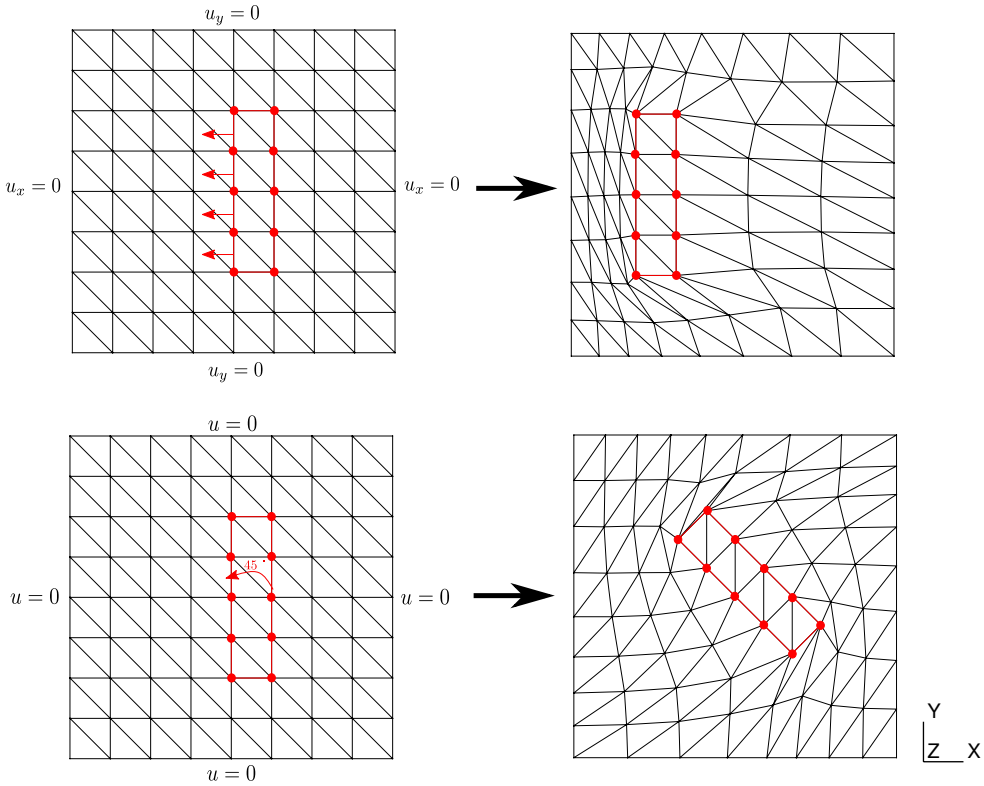

(b)

Fig. A.2.: Meshing strategies (a) for simple geometry and its variation; (b) for complex geometries and its variation with elastic analogue deformation.

Another point should be remarked that the computational domain of X-FEM is composed of standard, blending and enriched elements. When the implicit interface varies, the types of elements and the total degree of freedoms could be changed. This would make the proposed

method fail and give some unexpected results. To avoid such issue, we offer three strategies. First, for some simple and small variation of geometry, one can use coarse mesh where we keep the perturbed interface always remaining in the same elements (see fig. A.2(a) top). Otherwise, one can move manually the layer of elements that contain the interface (see fig. A.2(a) bottom). In practical, when treating complex geometries or variations, manual moving of elements (nodes) is not feasible. The elastic analogy Stein et al., 2004 [174] could be used to deform the associated mesh in a more automatic way, as shown examples in fig. A.2(b) where the displacement solution of a specific elastic problem is imposed to the initial position of the nodes of the mesh. Without exception, two first strategies will be adopted for the following cases.

A.2.2 Numerical results and discussion

Let us consider the variation of material thickness for which the level-set defined interface will be translated along x axis to verify and validate the method at place. As the limitation of perturbation method that it cannot handle a large variation of input random variables, we restrict the maximal variation as $\max(\delta\xi) = 10\%\bar{D}$ ($\bar{D} = 4$ cm).

We first identify the choice of $\Delta\xi$ in the finite difference formulation to calculate the matrix derivative. The global L^2 errors between initial "XFEM+TMM" model that solves the full dimensional linear system eq. (A.5) and perturbation solution that is obtained from Taylor's expansion eq. (A.8) are evaluated for two $\delta\xi = 10\%\bar{D}$ and $\delta\xi = 5\%\bar{D}$ under frequency $1,000$ Hz. In fig. A.3, we plot the relative error against the ratio of finite difference $\Delta\xi$ in FDM with the variation $\delta\xi$ on each order of expansion. $\Delta\xi$ is divided sequentially 5 times relative to $\delta\xi$.

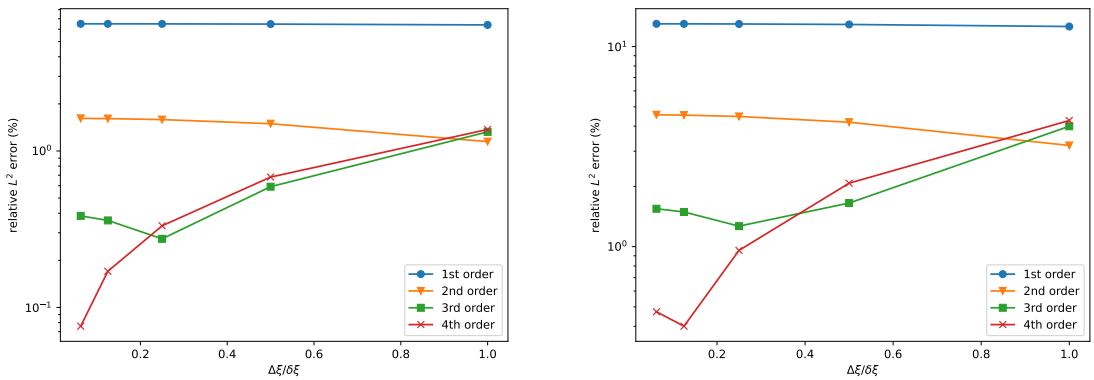

(a) (b)

Fig. A.3.: Accuracy sensitivity of $\Delta\xi$ in finite difference scheme for (a)$\delta\xi = 5\%\bar{D}$ and (b)$\delta\xi = 10\%\bar{D}$.

In general, one can conclude that the solution is more sensitive to $\Delta\xi$ in finite difference scheme with the increasing perturbation expansion order. It is better to use a small enough $\Delta\xi$ for higher order perturbation formulations in order to ensure an optimally accurate solution. In

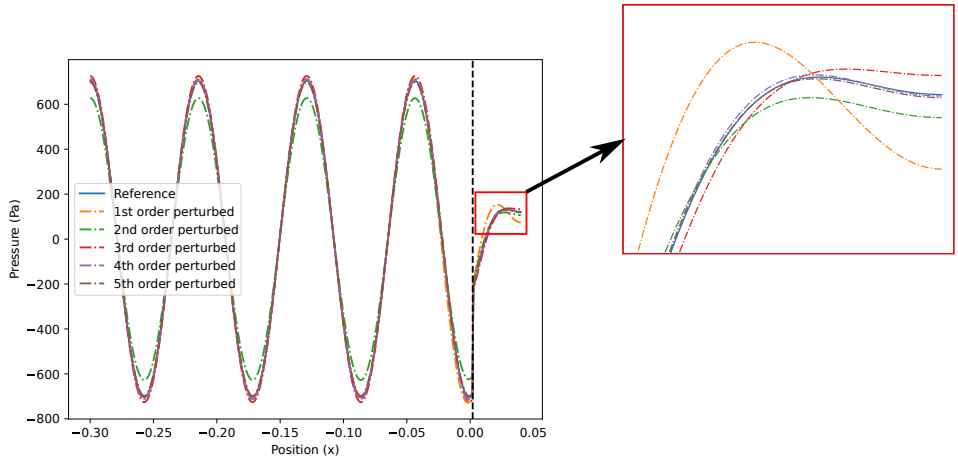

Fig. A.4.: Example of real part solution at $4,000\,\mathrm{Hz}$ by perturbation method with different expansion order.

addition, we observed that higher order perturbation provides an obvious improvement on the accuracy of the solution in our case. This is contrary to the common cases of the perturbation method where first order expansion is enough (for variation of material properties).

Here, for the variation of geometry in a mid-high frequency dynamic problem, higher order is necessary. We illustrate this necessity of using high order expansion qualitatively through the wave solution at $4,000$ Hz (see fig. A.4). It is seen that the solution computed from first order perturbation is far away from the reference solution. The perturbed solutions get closer to the reference one when higher order expansion is used.

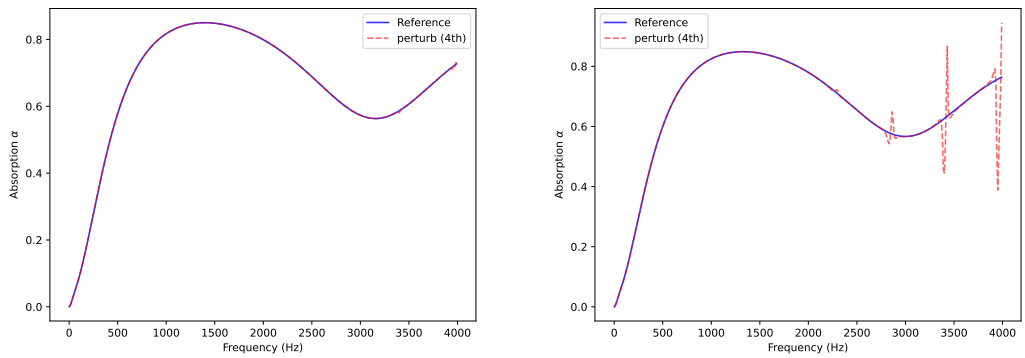

(a) (b)

Fig. A.5.: FRF of absorption coefficient for variation of (a) 5% and 10%.

Up to now, the method is only evaluated at a specific frequency and its performance over a large range of frequency needs to be assessed as well. Hence, Frequency Response Functions (FRF) are then evaluated. The absorption coefficients α of the considered sound system under two variation of geometry are first computed, as shown in fig. A.5. For a 5% variation of thickness, the perturbed solution of 4th order expansion gives a visually excellent accordance to the reference full dimensional solution over the frequencies (see fig. A.6(a)). Once we pass

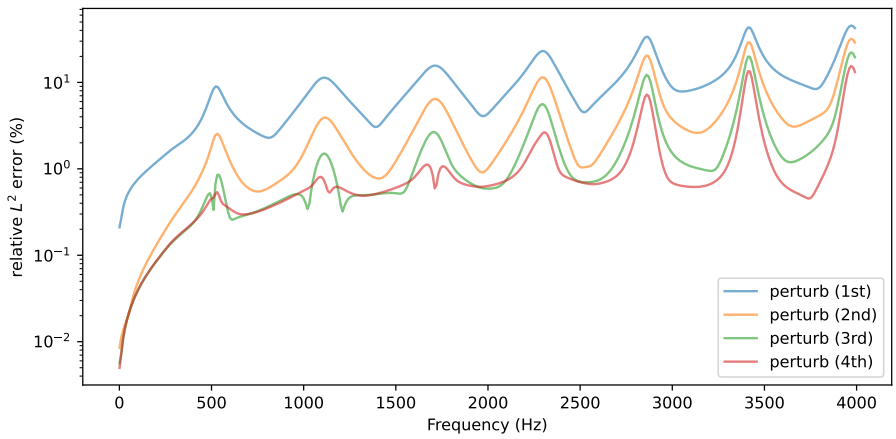

(a)

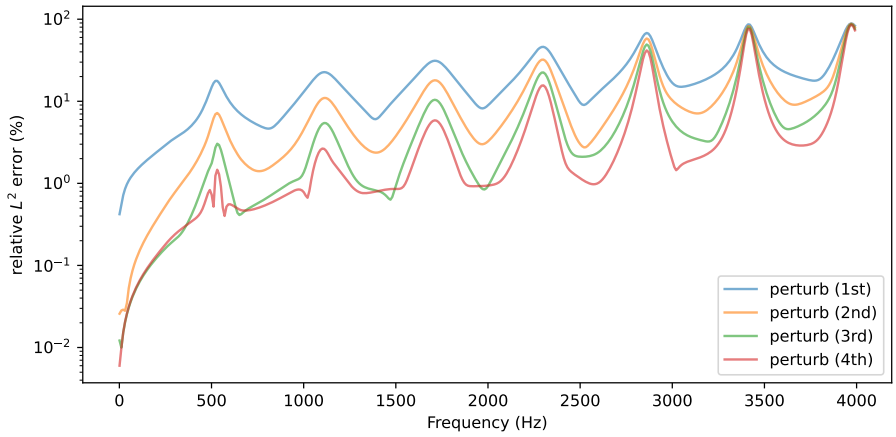

(b)

Fig. A.6.: FRF of perturbation solution for variation of (a) 10% and 5%.

to 10% variation (see fig. A.6(b)), the proposed method fits, on the overall, to the reference one. However, for certain frequencies, noticeable oscillations appear. In fact, the solutions at these frequencies obtained by the perturbed method are completely wrong. In order to further investigate such unexpected oscillation, the global error in L^2 norm for the same configurations under four orders of expansions are calculated (see fig. A.6).

Indeed, the curves in two variations under four expansions all exhibits a synchronized regular oscillation. Moreover, at high oscillation frequencies ("peaks" in the figure), the reduction of error with higher order expansion is not apparent. After a further analytical research, we found out that all frequencies where the "peaks" sited are closed to the resonance (natural) frequencies of the air cavity in the considered impedance tube. This is related to the fact that the evaluated system is highly sensitive to a small variation around the eigenfrequencies. The perturbation method is not able to cope with such strong variations in the solution. Note that the same observation of "peaks" has been reported in Van den Nieuwenhof and Coyette, 2003 [175]. In that work, authors proposed to use mixed perturbation/Monte-Carlo simulations to tackle

this issue. The full dimensional linear systems are solved around the resonance frequencies. That means for each configuration, the eigenfrequencies need to be evaluated *a priori* before launching the mixed perturbation method, which demands more computational efforts for complex geometrical problems.

Additionally, our full dimension linear system eq. (A.5) is frequency (ω) dependent as JCA parameters varies as function of ω. This implies that at each frequency, all related quantities such as initial stiffness matrix and its sensitivity need to be re-assembled and calculated, which is not practical and time-consuming for FRF analysis which is the most common type of analysis in time-harmonic problems. Therefore, a more efficient method is desired to treat the frequency sweeping with the least computational efforts and to be able to avoid the resonance issue highlighted with the perturbation method.

A.3 Reduced basis method

A.3.1 Theory and formulations

Another family of methods that can reduce the computational cost for parametric PDE is Model Order Reduction (MOR). Among them, the Reduced Basis Method (RBMQuarteroni et al., 2016 [176]) will be adopted in our problem to consider seamlessly frequency ω and geometric variation ξ_i as input parameters of full dimensional "XFEM+TMM" linear system.

Given μ belongs to the parameter space $\mathscr{P}$ as a vector:

$$\mu = [\omega, \xi_i] \in \mathscr{P}, i = 1 \cdots . \tag{A.11}$$

To differ from the previous full dimensional parametric system, the new discrete linear system with parameter vector μ is expressed as:

$$\mathbf{A}_h(\mu)\mathbf{p}_h^f(\mu) = \mathbf{F}_h(\mu), \tag{A.12}$$

where $\mathbf{A}_h(\mu) \in \mathbb{R}^{N_h \times N_h}$ and $\mathbf{F}_h \in \mathbb{R}^{N_h}$ with number of degree of freedoms N_h are discrete operators and vectors, respectively. Instead of solving directly the high dimensional linear system, the basic idea of RBM is to seek an approximated solution of a reduced dimensional discrete system. To do so, one first re-expresses the high fidelity solution $p_h^f(\mu)$ as a linear combination of coefficients and basis function as:

$$\mathbf{p}_h^f(\mu) = \mathbf{\Phi}\mathbf{p}_n^f(\mu), \tag{A.13}$$

where $\mathbf{p}_n^f(\mu)$ denotes the RB coefficients, also called the generalized coordinates, of $\mathbf{p}_h^f(\mu)$ in the reduced basis, and $\mathbf{\Phi}$ is the reduced basis. The dimension of $\mathbf{p}_n^f$ (n) is much smaller than

the degree of freedoms of the original high fidelity problem, $n \ll N^h$. This expression can be regarded as a projection of the high fidelity solution on a reduced basis. Substituting eq. (A.13) into eq. (A.12) and applying the Galerkin projection on the two sides of the linear system, we get:

$$\mathbf{\Phi}^T \mathbf{A}_h(\mu) \mathbf{\Phi} \mathbf{p}_n^f(\mu) = \mathbf{\Phi}^T \mathbf{F}_h(\mu), \tag{A.14}$$

that is:

$$\tilde{\mathbf{A}}_n(\mu) \mathbf{p}_n^f(\mu) = \tilde{\mathbf{F}}_n(\mu), \tag{A.15}$$

with:

$$\tilde{\mathbf{A}}_n(\mu) = \mathbf{\Phi}^T \mathbf{A}_h(\mu) \mathbf{\Phi}, \quad \tilde{\mathbf{F}}_n(\mu) = \mathbf{\Phi}^T \mathbf{F}_h(\mu). \tag{A.16}$$

The solution of the problem can be obtained by solving the low-dimensional linear system eq. (A.15) and re-expanding with reduced basis as eq. (A.13).

Now, the key step for the following is to seek an appropriate reduced basis $\mathbf{\Phi}$, which is constructed from a set of snapshots from high fidelity solution as:

$$\mathbf{\Phi} := \mathrm{span}\{\mathbf{p}_h^f(\mu_1), \cdots, \mathbf{p}_h^f(\mu_n)\}, \tag{A.17}$$

where the question is, which sample (parameter) should be selected into the reduced space. Several approaches exits such as POD (Proper Orthogonal Decomposition) and greedy algorithm.

Here a typical greedy algorithm is addressed. This algorithm provides a way to select the sample iteratively thanks to an *a posteriori* error indicator: the residual. At each iteration, the residual for every sample in the parameter space $\mathscr{P}$ is evaluated from current reduced basis:

$$\mu^{(i+1)} = \arg\max_{\mu \in \mathscr{P}} \left\| \mathbf{A}_h(\mu) \Phi_i p_n^f(\mu) - \mathbf{F}_h \right\|, \tag{A.18}$$

then, the sample with the worst (largest) residuals selected to update the basis by solving the underling linear system:

$$\mathbf{A}_h(\mu^{(i+1)}) \mathbf{p}_h^f(\mu^{(i+1)}) = \mathbf{F}_h(\mu^{(i+1)}). \tag{A.19}$$

Remark that the reduced basis needs to be orthonormalized in order to avoid large conditioning of the basis due to linear dependencies between snapshots. In the greedy algorithm, this orthonormalization is performed in each iteration by Gram-Schmidt procedure. The criterion of stopping the algorithm is defined according to a given maximum number of iteration or the residual tolerance. Such procedure is resumed below algorithm 1.

Once the reduced basis is obtained, the dimension of considered high-fidelity linear system is reduced by applying the Galerkin projection. One can decompose the whole procedure into two stages: offline and online. The objective of the offline stage is to construct the reduced basis. While in the online stage, the reduced linear system is solved for any $\mu \in \mathscr{P}$ efficiently.

Algorithm 1 Greedy algorithm for Reduced Basis (RB) construction

Input:
Maximum number of iteration N_{max}
Stopping tolerance ϵ_g
Training set in parameters space $[\mu] \in \mathscr{P}$
system matrices $\mathbf{A}_h(\mu_i)$ and right-hand side $\mathbf{F}_h(\mu_i)$ for all $\mu_i \in [\mu]$
Output: Reduced Basis $\mathbf{\Phi} \in \mathbb{R}^{N_h \times n}$
Initialization $\mathbf{\Phi} = [\,]$, $N = 0$, $\xi = 1$
while $N < N_{max}$ and $\epsilon > \epsilon_g$ **do**
    $N := N + 1$
    compute $\mathbf{p}^f(\mu^N)$
    if $\mathbf{\Phi} = [\,]$ **then** ▷ This is Gram-Schmidt
        $\mathbf{p}_N^f = \mathbf{p}^f$
    else
        $\mathbf{p}_N^f = \mathbf{p}^f - \mathbf{\Phi}\mathbf{\Phi}^T\mathbf{p}^f$
    end if
    $\mathbf{p}_N^f = \mathbf{p}_N^f / \left\|\mathbf{p}_N^f\right\|$
    $\mathbf{\Phi}_i := [\mathbf{\Phi}, \mathbf{p}_N^f]$
    compute maximum residual $\xi = \max_{\mu \in \mathscr{P}} \left\|\mathbf{A}_h(\mu_i)\Phi_i p_n^f(\mu) - \mathbf{F}_h(\mu_i)\right\|$
end while

Although the dimension of the linear system has been significantly reduced in online stage, the left-hand side matrix $\mathbf{A}_h$ and right-hand side vector $\mathbf{F}_h$ all depend on the parameters μ. It means that high dimensional matrices and vectors still need to be calculated and assembled for a great amount of parameters, whose computational cost is also massive for large problems. This restricts the efficiency of the method offline-online splitting.

Typically, the discrete operators (matrix and vector) are written in form of an affine-dependency as:

$$\begin{aligned} \mathbf{A}_h(\mu) &= \sum_{q=1}^{Q_a} \theta_a^q(\mu)\mathbf{A}_h^q, \\ \mathbf{F}_h(\mu) &= \sum_{q=1}^{Q_f} \theta_f^q(\mu)\mathbf{F}_h^q, \end{aligned} \tag{A.20}$$

where $\theta_a^q(\mu)$ and $\theta_f^q(\mu)$ are two sets of parameters dependence functions, $\mathbf{A}_h^q$ and $\mathbf{F}_h^q$ are two sets of μ-independent matrices (vectors). Therefore, the reduced linear system can be rewritten as:

$$\theta_a(\mu)\underbrace{\Phi^T\mathbf{A}_h\Phi}_{\tilde{\mathbf{A}}_\mathbf{k}} u_n(\mu) = \theta_f(\mu)\underbrace{\Phi^T\mathbf{F}_h}_{\tilde{\mathbf{F}}_\mathbf{k}}, \tag{A.21}$$

where $\tilde{\mathbf{A}}_\mathbf{k}$ and $\tilde{\mathbf{F}}_\mathbf{k}$ are the affine reduced matrices and vectors, which can be computed and stored once during the offline stage, enabling a more efficient online assembly of parametric linear system.

The parameters ω and its related fluid density $\rho(\omega)$ and bulk modulus $K(\omega)$ can be taken out directly from the integral in our variational formulation eq. (A.1), leading affine operators. However, the geometric deformation $\Omega(\mu_i)$ and $\Gamma(\mu_i)$ must also be considered, which cannot be easily decomposed from the initial variational operators. Two approaches can be adopted to alleviate this issue. One can find a mapping $\mathcal{M}(\mu_i)$ from reference geometry $\tilde{\Omega}$ which is independent of uncertainty parameter to the deformed geometry $\Omega(\mu_i)$. The operator therefore can be decomposed with a parameter dependent Jacobian function of this mapping. Such mapping can be easily obtained for simple geometrical deformations such as translation, scaling and rotation. Once the variation becomes complex, it is no longer possible to find a mapping analytically.

The second approach relies on numerical interpolation that can approximate the non-affine operators to affine ones, for example the matrix $\mathbf{A}_h$ can be approximated by:

$$\mathbf{A}_h(\mu_i) = \mathbf{A}_M(\mu) + e_{INTP}(\mu) = \sum_{m=1}^{M} \gamma_m(\mu)\rho_m + e_{interp}(\mu), \tag{A.22}$$

with the approximation error $e_{INTP}(\mu)$ under a given tolerance:

$$\epsilon_M(\mu) = \|e_{INTP}(\mu)\|_{L^\infty(\Omega)} \leq \epsilon, \quad \mu \in \mathscr{P}. \tag{A.23}$$

We have:

$$\mathbf{A}_h \approx \sum_{m=1}^{M} \gamma_m(\mu)\rho_m, \tag{A.24}$$

which is exactly what we are looking for, the non-affine operator is approximated by affine operator. In this appendix, the Empirical Interpolation Method (EIM) is used to perform such interpolation.

A.3.2 Results and discussion

The proposed reduced basis method is first validated by the same test case as in previous section, the translation of an interface which is defined implicitly by level-set function is considered, which changes the thickness of whole absorption system. The reduced order model (ROM for the following) is constructed from high fidelity "XFEM+TMM" model (FOM for the following) by considering a training set μ of 1000 pairs of frequency and position of interface $\mu = [\omega_i, \xi]$ with $f \in [1, 4,000]$ Hz and $\xi \in [-10\%\bar{D}, 10\%\bar{D}]$.

The convergence of the greedy algorithm for constructing the reduced basis is first analysed (see fig. A.7). We end up with a reduced space made by $N = 31$ modes, by prescribing a stopping tolerance $\epsilon_g = 1.10^{-4}$ on the residual. Note that the smaller the tolerance set, the more modes are needed, and of course, the more accurate the reduced-order model is compared to the high

fidelity solution. The size of modes correspond to the numbers of degree of freedom in the original FOM.

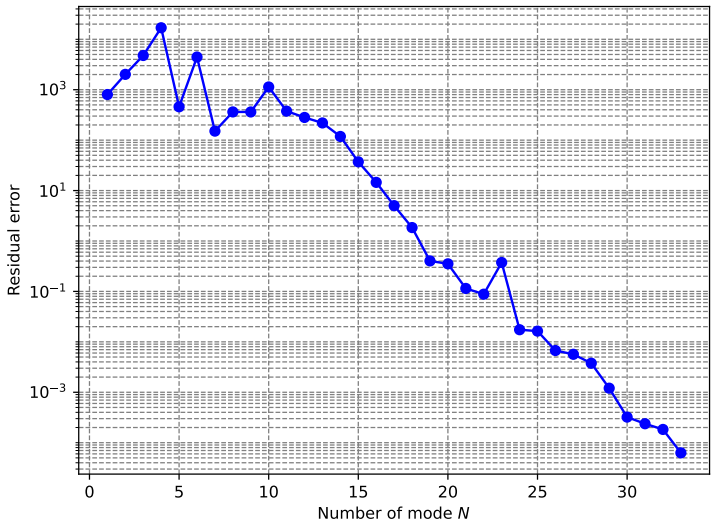

Fig. A.7.: Convergence of the greedy algorithm: norm of residual as a function of N (number of modes).

Once the reduced-order model is established, we can apply it to our uncertainty analysis over frequencies. As the frequency ω is also one variable parameter considered in the reduced model, the computation cost of frequency sweep is very cheap. It is reminded that the perturbation method cannot predict the solution correctly around the resonance frequencies. The same frequency response function absorption coefficients is evaluated by ROM over frequency $f \in [1, 4000]$ Hz, where two geometric variation 5% and 10% are tested. The FOM serves as reference in comparison in fig. A.8.

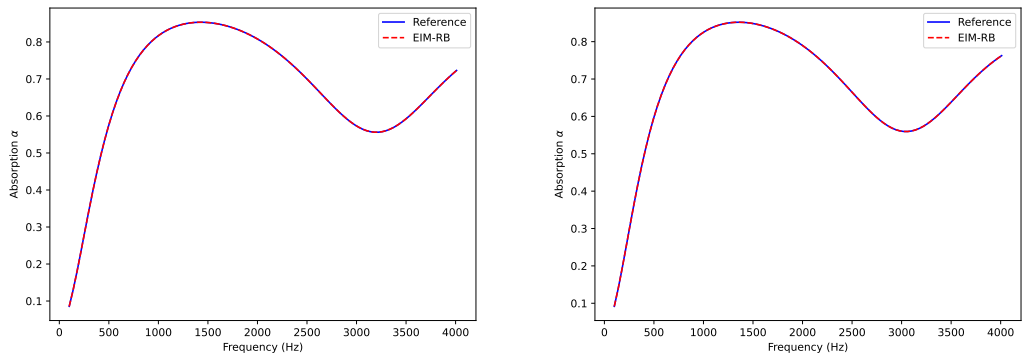

(a) (b)

Fig. A.8.: FRF of absorption coefficient for variation of (a) 5% and 10%.

The ROMs by Empirical Interpolation Reduced Basis Method (EIM-RB) lead to a great agreement over frequencies with the reference solutions. In contrast to the perturbation method, no apparent "spike" is observed here. We then perform a further quantitative study for 10% variation. The relative error in L^2 norm with the reference solution is calculated under three

tolerances of the greedy algorithm, shown in fig. A.9. As previously mentioned, ROM accuracy is positively associated to the tolerance. When the tolerance is set as $\epsilon_g = 1.10^{-4}$, the relative errors are in general less than to 10^{-2} over frequencies.

Some "valleys" are noticed in the curves with similar frequencies. In fact, these frequencies correspond exactly to the resonance frequencies of the problem. Recall that error "spikes" are obtained for these frequencies when using the perturbation method. In contrast, the error is minimized at these frequencies due to the greedy algorithm, where snapshots for the solutions with the maximum residual (which should be around resonance frequencies) are added in the reduced basis.

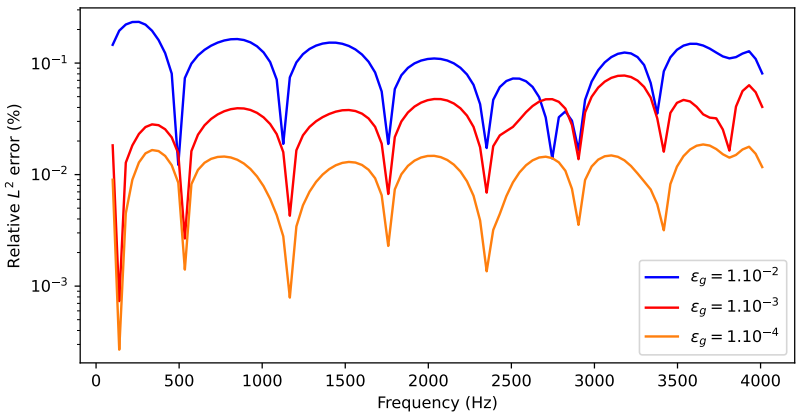

Fig. A.9.: Relative L^2 error of ROM solution for 10% variation of thickness of whole system.

The ROM based on the EIM-RB method is validated and demonstrated to be able to tackle the numerical issue highlighted in the perturbation method and provide accurate solutions over frequencies. Therefore, one can easily generate uncertainty envelop of absorption coefficients with random geometric variation by this model. We evaluate 30 samples of the varied thickness of the porous medium D satisfying an uniform distribution in interval $[-10\%\bar{D}, 10\%\bar{D}]$. The solutions are compared with the one calculated by a FOM Monte Carlo simulation.

Fig. A.10 shows the absorption coefficients where the red curves are calculated by maximal and minimal value of all absorptions at one frequency. ROM offers a visibly identical envelop to the reference obtained from ROM. We can see that 10% thickness variation (about $4\,\mathrm{mm}$) of the considered absorbing system leads to obvious effects for the absorption coefficients, especially in the frequency range from $1,500\,\mathrm{Hz}$ to $4,000\,\mathrm{Hz}$. The largest difference of α is almost 0.2, for which the surface absorption properties of the system is completely changed.

Then, the influence of interface orientation that represents the inclination of the sample surface is studied as shown in fig. A.11. For this geometric configuration, the displacement of the x-component calculated from rotation angle is imposed on the associated enriched nodes to keep the enriched elements unchanged during the interface evolution. We train the ROM with a residual tolerance $\epsilon_g = 1.10^{-2}$, which demands 34 modes in offline stage ($\epsilon_g = 1.10^{-4}$, number

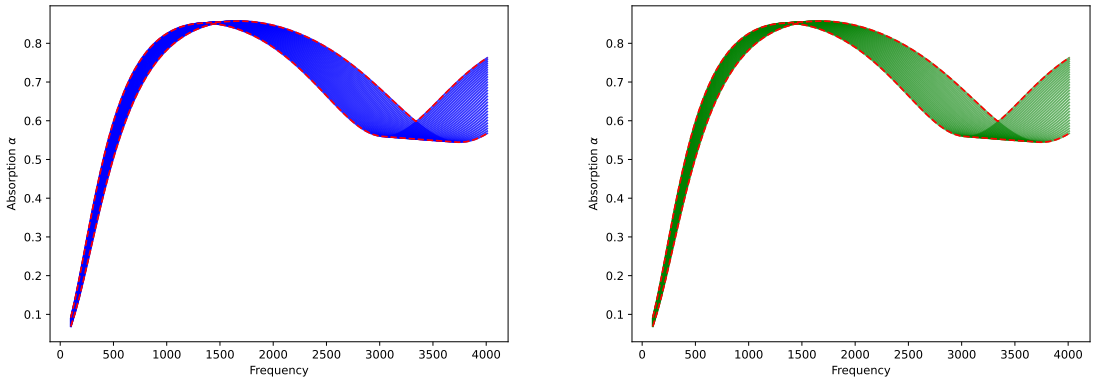

(a) (b)

Fig. A.10.: Absorption coefficients and their envelope (red curves) for thickness variation obtained by (a) FOM and (b) ROM.

of modes is $N = 48$). Obviously, for the geometric rotation, more modes are needed to achieve the same level of tolerance compared to the translation case.

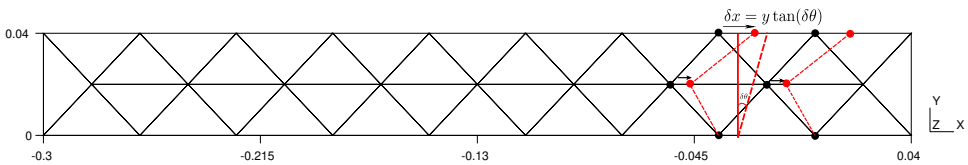

Fig. A.11.: Mesh deformation for rotation of the interface.

The absorption coefficients of 30 samples with a variation of angle $\delta\theta \in [-10°, 10°]$ are calculated online by the trained ROM and FOM references (see fig. A.12). It is seen that even with this larger tolerance, the ROM is able to provide a highly similar absorption curves compared to the FOM solutions. No apparent difference is observed between two figures. The profile of the absorption here is different from the one obtained in thickness variation.

To highlight the advantage of the proposed method, the sound absorbing systems with curved interfaces are studied as well, for which classical FEM needs more elements to describe the geometries. Here, the curved interfaces are defined by level-set functions along with iso-parametric mapping of elements (Lehrenfeld, 2016 [154]) to capture the curved feature with limited element numbers.

The effects of the curvature for the cylinder surface is studied. The interface is defined by level-set function:

$$\phi(\mathbf{x}) = -(\sqrt{((x - r_0)^2 + (y - wp/2)^2}) - r_0), \tag{A.25}$$

where r_0 is the radius and wp the width of the tube. The curvature of the sample is varied by changing r_0. For training reduced model for this configuration, 34 modes are needed at the offline stage for a tolerance $\epsilon = 1.10^{-2}$. We illustrate a comparison between ROM and FOM solutions for $R_0 = 3.8$ cm in fig. A.13. It is noticed firstly that the element containing

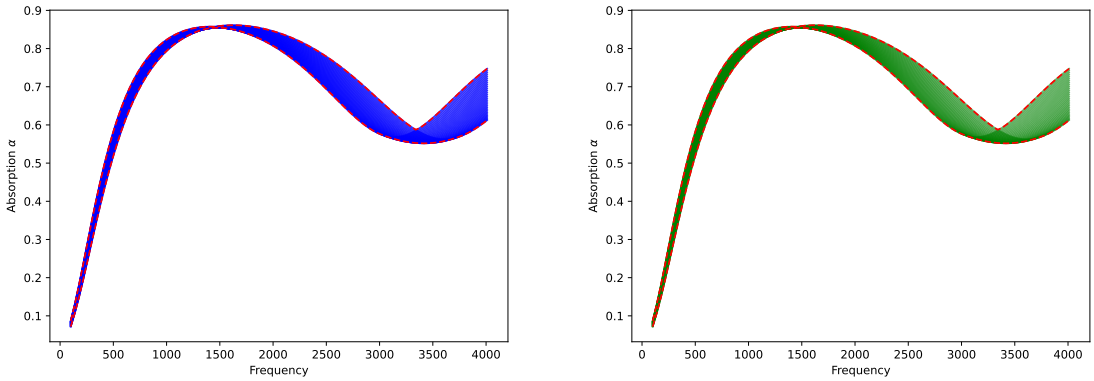

(a) (b)

Fig. A.12.: Absorption envelop under rotation variation for planar interface obtained by (a) FOM and (b) ROM.

the curved interface deforms, which stems from the iso-parametric mapping to better describe curves. EIM-RB ROM exhibits highly accordance to the FOM (XFEM+TMM), where the obvious pressure jump is captured at the interface in the tube.

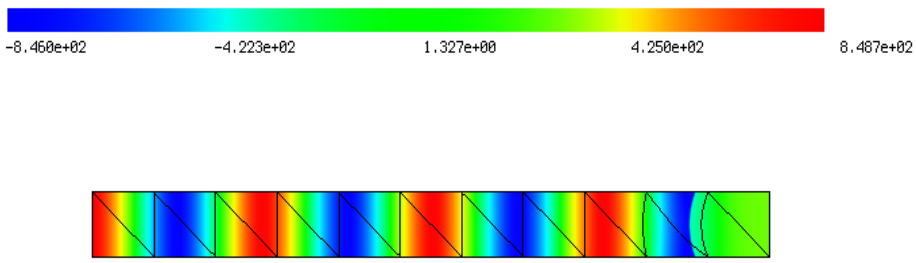

(a) Reference FOM sol

(b) EIM-RB ROM sol

Fig. A.13.: Solutions of curved interface with curvature $r = 0.032\,\mathrm{m}$.

The absorption envelops are calculated as well for a variation of radius $r \in [3.5, 50]$ cm (see fig. A.14). The interface with maximal radius is approach to a planar surface. Two methods offer visibly identical absorptions. We can conclude that the effects of surface curvature on the absorption are not significant compared to previous two variations. About a difference of 0.03 is observed from $1,200$ Hz to $3,000$ Hz and $3,500$ Hz to $4,000$ Hz.

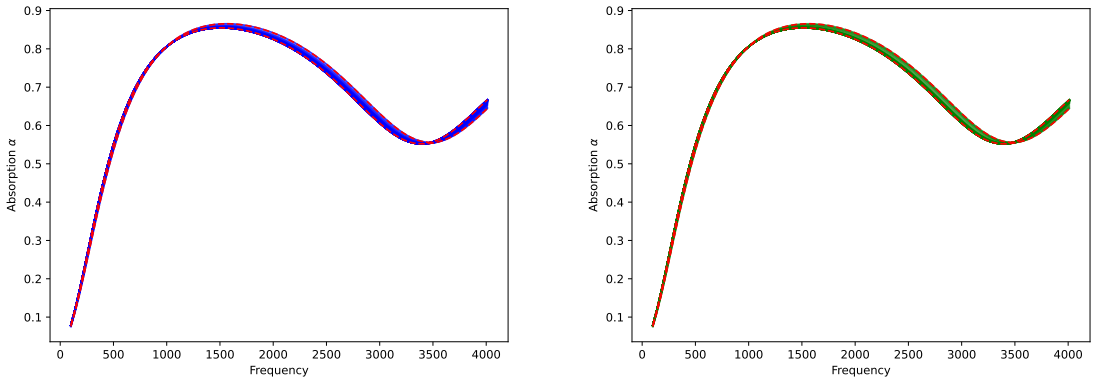

(a) (b)

Fig. A.14.: Absorption envelops under curvature variation for curved interface obtained by (a) FOM and (b) ROM.

A.4 Conclusion

This appendix presented two approaches to efficiently consider the acoustic effects of the geometric variation based on the proposed framework in the manuscript. The idea is to reduce the global computational cost when *Monte Carlo* simulation is performed. The high-order perturbation method was firstly implemented, which can give satisfactory results except for the solution around resonance frequencies. The reduced basis method was then adopted to recover the solutions at the resonance frequencies. Within this method, besides the geometric variable, frequency can be also considered in the parameter space. The greedy algorithm was employed to construct the reduced basis, which eventually minimize the error at the resonance frequencies. The inherent issue in the perturbation method was thus fixed. In addition, as the frequency is also the parameter in the reduced basis, the frequency sweeping is far more efficient. The Empirical Interpolation Method (EIM) was used to decompose the operators that contain the variable geometries to have an efficient offline-online splitting.

With the reduced model from EIM-RB, the absorption envelope of the considered absorbing system can be calculated efficiently for any geometric configurations. The effects of thickness, surface inclination and curvature were investigated and illustrated in this appendix. For more complicated geometrical variation, the mesh deformation and curved geometries need to be treated more carefully.

Analytical expressions and solutions

B

This appendix provides all necessary expressions that were used in the manuscript. The analytical formulas for calculating the JCA and Biot parameters are first provided. The second part offers all the analytical expressions and solutions for the academic benchmarks which were used for the implementation verification.

B.1 JCA and Biot coefficients

Tab. B.1.: Porous material properties used in the manuscript.

Parameters	Classical foam	Classical foam 2	XFM
Porosity ϕ	0.98	0.98	0.98
static flow resistivity σ $(\mathrm{N\,m^{-4}s})$	45×10^3	15.5×10^3	13.5×10^3
Tortuosity α	1.0	1.01	1.7
thermal characteristic length Λ' (m)	250×10^{-6}	200×10^{-6}	160×10^{-6}
Viscous characteristic length Λ (m)	100×10^{-6}	100×10^{-6}	80×10^{-6}
frame density ρ_1 $(\mathrm{kg.m^{-3}})$	23	11	30
Young's modulus E (Pa)	140×10^3	200×10^3	200×10^3
Poisson ratio ν	0.24	0.35	0.35
Loss factor η_s	0.05	0.1	0.05

Parameters	Plastic foam	Polyurethane
Porosity ϕ	0.97	0.98
static flow resistivity σ $(\mathrm{N\,m^{-4}\,s})$	57.3×10^3	57×10^3
Tortuosity α	1.54	1.17
thermal characteristic length Λ' (m)	73.8×10^{-6}	742×10^{-6}
Viscous characteristic length Λ (m)	24.6×10^{-6}	110×10^{-6}
frame density ρ_1 $(\mathrm{kg.m^{-3}})$	46	22.1
Young's modulus E (Pa)	210×10^3	70×10^3
Poisson ratio ν	0.3	0.39
Loss factor η_s	0.1	0.265

One can obtain the coefficients with the provided material's parameters in table B.1 and table B.2. All the definition presented here can be found in other literature as well.

Tab. B.2.: Film properties used in the manuscript.

Parameters	Woven	Non-woven
Porosity $\phi\,(-)$	0.04	0.72
static flow resistivity $\sigma\,(\mathrm{N.m^{-4}})$	775×10^3	87×10^3
Tortuosity $\alpha\,(-)$	1.15	1.02
thermal characteristic length $\Lambda'\,(\mathrm{m})$	230×10^{-6}	480×10^{-6}
Viscous characteristic length $\Lambda\,(\mathrm{m})$	230×10^{-6}	480×10^{-6}
frame density $\rho_1\,(\mathrm{kg.m^{-3}})$	809	171
Young's modulus $E\,(\mathrm{Pa})$	260×10^6	50×10^3
Poisson ratio $\nu\,(-)$	0.3	0.3
Loss factor $\eta_s\,(-)$	0.5	0.5

The effective density of an equivalent fluid $\tilde{\rho}_{\mathrm{eq}}$ is written as:

$$\tilde{\rho}_{\mathrm{eq}} = \frac{\rho_{\mathrm{a}}\alpha}{\phi}\left(1 + \frac{\omega_0}{\mathrm{j}\omega}\sqrt{1 + \frac{\mathrm{j}\omega}{\omega_\infty}}\right), \tag{B.1}$$

with unit imaginary number j. ω_0 and ω_∞ are expressed as:

$$\omega_0 = \frac{\sigma\phi}{\rho_{\mathrm{a}}\alpha}, \tag{B.2a}$$

$$\omega_\infty = \frac{(\sigma\phi\Lambda)^2}{4\eta_{\mathrm{a}}\rho_{\mathrm{a}}\alpha^2}, \tag{B.2b}$$

where ρ_{a}, η_{a} are the density of air and dynamic viscosity of the fluid. The coupling coefficient $\tilde{\gamma}$ in Biot's equations eq. (2.13) and solid equivalent density are expressed as:

$$\tilde{\gamma} = \phi\left(\frac{\tilde{\rho}_{12}}{\tilde{\rho}_{22}} - \frac{1-\phi}{\phi}\right), \tag{B.3}$$

$$\tilde{\rho} = \tilde{\rho}_{11} - \left(\frac{\tilde{\rho}_{12}^2}{\tilde{\rho}_{22}}\right), \tag{B.4}$$

where $\tilde{\rho}_{11}$, $\tilde{\rho}_{12}$ and $\tilde{\rho}_{22}$ are the coefficients related to the geometry of the frame, the detailed relationship between ρ_{a} and density of solid phase ρ_1 are given:

$$\tilde{\rho}_{22} = \phi^2\tilde{\rho}_{\mathrm{eq}}, \quad \tilde{\rho}_{12} = \phi\rho_{\mathrm{a}} - \tilde{\rho}_{22}, \quad \tilde{\rho}_{11} = \rho_1 - \tilde{\rho}_{12}. \tag{B.5}$$

The dynamic effective fluid compressibility $\tilde{K}_{\mathrm{eq}}$ is expressed as:

$$\tilde{K}_{\mathrm{eq}} = \gamma p_0 / \left[\gamma - (\gamma - 1)/\left(1 + \frac{8\eta_{\mathrm{a}}}{\mathrm{j}\omega\rho_{\mathrm{a}}P_r\Lambda'}\sqrt{1 + \frac{\mathrm{j}\omega\rho_{\mathrm{a}}P_r\Lambda'^2}{16\eta_{\mathrm{a}}}}\right)\right], \tag{B.6}$$

where γ represents the ratio of specific heats of air, p_0 is the referred ambient pressure, P_r denotes the Prandtl number.

Concerning the solid phase in the porous materials, the constitutive relationship between stress in vacuum and strain in solid frame is defined classically as:

$$\sigma_{ij}^s = 2Ne_{ij} + \hat{A}(e_{kk})\delta_{ij}, \tag{B.7}$$

where strain e_{ij} is related to the gradient of the solid displacement as:

$$e_{ij} = \frac{1}{2}\left(\frac{\partial u_i^s}{\partial x_j} + \frac{\partial u_j^s}{\partial x_i}\right), \tag{B.8}$$

and the structural Lamé coefficient N and shear coefficient read:

$$N = \frac{E(1+\mathrm{j}\eta_s)}{2(1+\nu)}, \quad \hat{A} = \frac{E\nu(1+\mathrm{j}\eta_s)}{(1+\nu)(1-2\nu)}, \tag{B.9}$$

and we define:

$$\hat{P} = \hat{A} + 2N, \tag{B.10}$$

where E and ν are the Young's modulus and Poisson's coefficient of the elastic solid in vacuum, η_s is the loss factor of the elastic solid phase.

B.2 Analytical solutions

The analytical solutions that were used in the verification benchmarks as reference are presented including wave propagation through planar and cylindrical interfaces for different media configurations.

B.2.1 Planar interface: transmission problem

Fluid-Fluid coupling

The interface is always considered at $x = 0$, the analytical expressions of sound wave in each subdomain are written as:

$$\begin{aligned}
p_1^f &= \exp(-\mathrm{j}k_{1x}x - \mathrm{j}k_{1y}y) + R\exp(+\mathrm{j}k_{1x}x - \mathrm{j}k_{1y}y),\\
p_2^f &= T_1\exp(-\mathrm{j}k_{2x}x - \mathrm{j}k_{2y}y),\\
v_1^f &= -\frac{1}{\mathrm{j}\omega\rho_1}\frac{\partial p_1}{\partial n},\\
v_2^f &= -\frac{1}{\mathrm{j}\omega\rho_2}\frac{\partial p_2}{\partial n},
\end{aligned} \tag{B.11}$$

with

$$
\begin{aligned}
k_{1y} &= k_{2y} = k_y = k_1 \sin(\theta), \\
k_{1x} &= k_1 \cos(\theta), \\
k_{2x} &= \sqrt{k_2^2 - k_y^2},
\end{aligned}
\tag{B.12}
$$

where θ is the incidence angle in the infinite plane and $R\&T$ are the reflection and transmission coefficients. With the interface condition at $x = 0$, the exact solution can be solved numerically by a linear system or expressed the coefficient explicitly. Generalized interface conditions are used here because it can cover perfect interface, pressure jump and TMM enhanced conditions within one formulation by only changing the coefficients:

$$
\begin{Bmatrix} p_1^f \\ u_{n1} \end{Bmatrix} = \begin{bmatrix} T_{11} & T_{12} \\ T_{21} & T_{22} \end{bmatrix} \begin{Bmatrix} p_2^f \\ u_{n2} \end{Bmatrix}. \tag{B.13}
$$

When $T_{11} = 1$, $T_{12} = 0$, $T_{21} = 0$ and $T_{22} = 1$, it represents perfect interface. When $T_{11} = 1$, $T_{12} = \sigma d$, $T_{21} = 0$ and $T_{22} = 1$, it represents pressure jump interface.

Here the matrix expressions are provided to solve the reflection and transmission coefficients.

$$
[\mathbf{M}]_{2\times 2} \begin{Bmatrix} R \\ T \end{Bmatrix} = [\mathbf{V}]_{2\times 1}. \tag{B.14}
$$

Each term in the left-hand side matrix are:

$$
\begin{aligned}
M_{11} &= 1, \\
M_{12} &= -T_{11} - T_{12} k_{2x}/(\omega \rho_2), \\
M_{21} &= -k_{1x}/(\omega \rho_1), \\
M_{22} &= -T_{21} - T_{22} k_{2x}/(\omega \rho_2),
\end{aligned}
$$

and the right-hand side of the vector are:

$$
\begin{aligned}
V_1 &= -1, \\
V_2 &= k_{1x}/(\omega \rho_1).
\end{aligned}
$$

Fluid-Biot coupling

Three waves propagates in PEMs, so three transmission coefficients will appear in the analytical expressions. Besides the pressure and displacement in fluid part. The analytical expression for solid displacement $\mathbf{u}^s$, total displacement $\mathbf{u}^t$, pressure in PEM subdomain are:

$$
\begin{aligned}
&p^b = T_1 \exp(-\mathrm{j}k_{2x}x - \mathrm{j}k_y y) + T_2 \exp(-\mathrm{j}k_{3x}x - \mathrm{j}k_y y),\\
&u_x^s = (-\mathrm{j}k_{2x}A_1 \exp(-\mathrm{j}k_{2x}x - \mathrm{j}k_y y) - \mathrm{j}k_{3x}A_2 \exp(-\mathrm{j}k_{3x}x - \mathrm{j}k_y y) - \mathrm{j}k_y T_3 \exp(-\mathrm{j}k_{4x}x - \mathrm{j}k_y y)),\\
&u_y^s = (-\mathrm{j}k_y A_1 \exp(-\mathrm{j}k_{2x}x - \mathrm{j}k_y y) - \mathrm{j}k_y A_2 \exp(-\mathrm{j}k_{3x}x - \mathrm{j}k_y y) + \mathrm{j}k_{4x} T_3 \exp(-\mathrm{j}k_{4x}x - \mathrm{j}k_y y)),\\
&\mathbf{u}^t = \mu_i \mathbf{u}^s, \quad \text{with } i = 1, 2, 3,
\end{aligned}
\tag{B.15}
$$

with coefficients

$$
A_1 = \frac{T_1}{\tilde{K}_{\mathrm{eq}}\mu_1\delta_1^2}, \quad A_2 = \frac{T_2}{\tilde{K}_{\mathrm{eq}}\mu_2\delta_2^2} \tag{B.16}
$$

with the interface conditions eq. (5.14) at $x = 0$, the analytical coefficients are obtained by solving a 4×4 linear system as:

$$
[\mathbf{M}]_{4\times4} \begin{Bmatrix} R \\ T_1 \\ T_2 \\ T_3 \end{Bmatrix} = [\mathbf{V}]_{4\times1}, \tag{B.17}
$$

where left-hand side coefficients are:

$$
\begin{aligned}
&M_{11} = 1,\\
&M_{12} = -T_{52}(-\mathrm{j}k_{2x})/(\tilde{K}_{\mathrm{eq}}\mu_1\delta_1^2) - T_{53}(-\mathrm{j}k_{2x}/(\tilde{K}_{\mathrm{eq}}\delta_1^2)) - T_{55},\\
&M_{24} = -T_{52}(-\mathrm{j}k_{3x}/(\tilde{K}_{\mathrm{eq}}\mu_2\delta_2^2)) - T_{53}(-\mathrm{j}k_{3x}/(\tilde{K}_{\mathrm{eq}}\delta_2^2)) - T_{55},\\
&M_{14} = -T_{52}(-\mathrm{j}k_y) - T_{53}(-\mathrm{j}\mu_3 k_y),\\
&M_{21} = \mathrm{j}k_{1x}/(\rho_1\omega^2),\\
&M_{22} = -T_{33}(-\mathrm{j}k_{2x}/(\tilde{K}_{\mathrm{eq}}\delta_1^2)) - T_{35} - T_{36}(-\mathrm{j}k_y)/(\tilde{K}_{\mathrm{eq}}\mu_1\delta_1^2),\\
&M_{23} = -T_{33}(-\mathrm{j}k_{3x}/(\tilde{K}_{\mathrm{eq}}\delta_2^2)) - T_{35} - T_{36}(-\mathrm{j}k_y)/(\tilde{K}_{\mathrm{eq}}\mu_2\delta_2^2),\\
&M_{24} = -T_{33}(-\mathrm{j}\mu_3 k_y) - T_{36}(\mathrm{j}k_{4x}),\\
&M_{31} = 0,\\
&M_{32} = -T_{41}(-2.Nk_{2x}k_y/(\tilde{K}_{\mathrm{eq}}\mu_1\delta_1^2)) - T_{42}(-\mathrm{j}k_{2x})/(\tilde{K}_{\mathrm{eq}}\mu_1\delta_1^2),\\
&- T_{43}(-\mathrm{j}k_{2x}/(\tilde{K}_{\mathrm{eq}}\delta_1^2)) - T_{44}(((2.N + \hat{A}) - k_{2x}^2/(\tilde{K}_{\mathrm{eq}}\mu_1\delta_1^2))) - \hat{A}k_y^2/(\tilde{K}_{\mathrm{eq}}\mu_1\delta_1^2),\\
&M_{33} = -T_{41}(-2.Nk_{3x}k_y/(\tilde{K}_{\mathrm{eq}}\mu_2\delta_2^2)) - T_{42}(-\mathrm{j}k_{3x}/(\tilde{K}_{\mathrm{eq}}\mu_2\delta_2^2)),\\
&- T_{43}(-\mathrm{j}k_{3x}/(\tilde{K}_{\mathrm{eq}}\delta_2^2)) - T_{44}((2.N - \hat{A})k_{3x}^2/(\tilde{K}_{\mathrm{eq}}\mu_2\delta_2^2) - \hat{A}k_y^2/(\tilde{K}_{\mathrm{eq}}\mu_2\delta_2^2)),
\end{aligned}
$$

$$
\begin{aligned}
&- T_{44}((2.N - \hat{A})k_{4x}k_y + \hat{A}k_{4x}k_y),\\
&M_{41} = 0,\\
&M_{42} = -T_{11}(-2Nk_{2x}k_y/(\tilde{K}_{\mathrm{eq}}\mu_1\delta_1^2)) - T_{14}(((2.N + \hat{A}) - k_{2x}^2/(\tilde{K}_{\mathrm{eq}}\mu_1\delta_1^2)),\\
&- \hat{A}k_y^2/(\tilde{K}_{\mathrm{eq}}\mu_1\delta_1^2)) - T_{15} - T16)(-\mathrm{j}k_y)/(\tilde{K}_{\mathrm{eq}}\mu_1\delta_1^2),\\
&M_{43} = -T_{11}(-2N.k_{3x}k_y/(\tilde{K}_{\mathrm{eq}}\mu_2\delta_2^2)) + T_{14}((2.N + \hat{A})k_{3x}^2/(\tilde{K}_{\mathrm{eq}}\mu_2\delta_2^2),\\
&- \hat{A}k_y^2/(\tilde{K}_{\mathrm{eq}}\mu_2\delta_2^2)) - T_{15} + T_{16}(\mathrm{j}k_y)/(\tilde{K}_{\mathrm{eq}}\mu_2\delta_2^2),\\
&M_{44} = -T_{11}(Nk_{4x}^2 - k_y^2)) - T_{14}((2.N + \hat{A}) - k_{4x}k_y + \hat{A}k_{4x}k_y) - T_{16}(\mathrm{j}k_{4x}).
\end{aligned}
$$

The right-hand side are:

$$
\begin{aligned}
V_1 &= -1,\\
V_2 &= \mathrm{j}k_{1x}/(\rho_1\omega^2),\\
V_3 &= 0,\\
V_4 &= 0.
\end{aligned}
$$

B.2.2 Scattering problem

For the cylinder scattering problem, the fields are expressed with Hankel and Bessel functions. Here, the particular case where air propagates to a porous cylindrical scatterer of radius $r = r_0$ is presented.

Fluid-fluid coupling with pressure jump interface

Regarding the cylinder scattering problem for two fluid coupling where the porous material is modelled by equivalent fluid. The pressure in the two media are written in polar coordinate (r, θ) as follows:

$$
p_{\mathrm{a}} = \rho_{\mathrm{a}}\omega^2 \left(\mathrm{J}_0(k_{\mathrm{a}}r) + 2\sum_{m=1}^{\infty}(-\mathrm{j})^m \mathrm{J}_m(k_{\mathrm{a}}r)\cos(m\theta) + \sum_{m=0}^{\infty} R_m \mathrm{H}_m(k_{\mathrm{a}}r)\cos(m\theta) \right), \tag{B.18a}
$$

$$
p^{\mathrm{eq}} = \rho_{\mathrm{eq}}\omega^2 \sum_{m=0}^{\infty} T_m(-\mathrm{j})^m \mathrm{J}_m(k_{\mathrm{eq}}r)\cos(m\theta), \tag{B.18b}
$$

where J_m and H_m represent the Bessel and Hankel functions and $\bullet'$ denotes the derivative.

Applying the interface condition at radius $r = r_0$ to obtain coeffcients R_m and T_m, we have a 2×2 linear system with left-hand side matrix:

$$
\begin{aligned}
M_{1,1} &= \rho_{\mathrm{a}}\mathrm{H}_m(k_{\mathrm{a}}r_0),\\
M_{1,2} &= -\rho_{\mathrm{eq}}\mathrm{J}_m(k_{\mathrm{eq}}r_0) - \frac{\sigma d}{\mathrm{j}\omega}k_{\mathrm{eq}}\mathrm{J}'_m(k_{\mathrm{eq}}r_0),\\
M_{2,1} &= k_{\mathrm{a}}\mathrm{H}'_m(k_{\mathrm{a}}r_0),\\
M_{2,2} &= -k_{\mathrm{eq}}\mathrm{J}'_m(k_{\mathrm{eq}}r_0),
\end{aligned}
$$

and with right-hand side vector:

$$V_1 = -2\rho_{\mathrm{a}}(-\mathrm{j})^m \mathrm{J}_m(k_a r_0), \tag{B.19a}$$

$$V_2 = -2k_a(-\mathrm{j})^m \mathrm{J}'_m(k_a r_0). \tag{B.19b}$$

Fluid-PEMs coupling with Limp interface

This solution corresponds to the cylindrical scatter test case used for chapter 5, where the interface was modelled by the Limp model of 2×2 matrix $[\mathbf{T}]$.

Plane waves of the scattering problem in this case are written in potential form. Potential of wave field in acoustic domain with amplitude A_{inc} is represented in polar coordinate (r, θ) as:

$$\varphi = \varphi_{inc} + \sum_{m=0}^{\infty} \hat{A}_{0,m} \mathrm{H}_m(k_a r) \cos(m\theta), \tag{B.20}$$

where φ_{inc} is incident wave potential which is propagating along horizontal direction x:

$$\varphi_{inc} = A_{inc} \exp(-\mathrm{j}k_a x) = A_{inc} \left[\mathrm{J}_0(k_0 r) + 2 \sum_{m=1}^{\infty} (-\mathrm{j})^m \mathrm{J}_m(k_a r) \cos(m\theta) \right], \tag{B.21}$$

where $\mathrm{H}_m(x)$ is the Hankel function of the second kind, $\mathrm{J}_m(x)$ is the Bessel function of the first kind. k_a represents wave number of air fluid.

Potentials of the two compressional waves with amplitude A_i in porous material are given:

$$\varphi_i = \sum_{m=0}^{\infty} \hat{A}_{i,m} \mathrm{J}_m(k_i r) \cos(m\theta), \quad \text{with } i = 1, 2, \tag{B.22}$$

and the one of shear wave in solid phase:

$$\varphi_3 = \sum_{m=0}^{\infty} \hat{A}_{3,m} \mathrm{J}_m(k_3 r) \sin(m\theta), \tag{B.23}$$

where k_1, k_2 and k_3 are compressional and shear wave numbers in fluid and solid phase respectively in Biot modeled porous material. Pressure in acoustic domain is $p = \rho\omega^2\varphi$, while solid displacement in porous material is cast with Helmholtz decomposition as:

$$\mathbf{u}^s = \nabla\varphi + \nabla \wedge \varphi_3, \tag{B.24}$$

where $\varphi = \varphi_1 + \varphi_2$. The other fields such as total displacement $\mathbf{u}^t$ and fluid pressure p are obtained by polarization relationship:

$$\mathbf{u}^t = \mu_i \mathbf{u}^s, \quad \text{with } i = 1, 2, \tag{B.25a}$$

$$p = -\tilde{K}_{eq} \nabla . \mathbf{u}^t, \tag{B.25b}$$

where μ_i are the wave amplitude ratios between solid and total displacement. Once the expression of all the fields are known, the analytical solution is available by solving a 4×4 linear system with the interface conditions eq. (3.2) at $r = r_0$.

The left-hand side of the linear system are:

$$
\begin{aligned}
M_{1,1} &= m\mathrm{H}_m(k_a r_0)/r_0 - k_a \mathrm{H}_{m+1}(k_a r_0),\\
M_{1,2} &= T_{2,2}\left(\mu_1(-m\mathrm{J}_m(k_1 r_0)) + k_1\mu_1 r_0 \mathrm{J}_{m+1}(k_1 r_0)\right)/a - T_{2,1}\tilde{K}_{\mathrm{eq}}\mu_1 k_1^2 \mathrm{J}_m(k_1 r_0),\\
M_{1,3} &= T_{2,2}\left(\mu_2(-m\mathrm{J}_m(k_2 r_0)) + k_1\mu_2 r_0 \mathrm{J}_{m+1}(k_2 r_0)\right)/a - T_{2,1}\tilde{K}_{\mathrm{eq}}\mu_2 k_2^2 \mathrm{J}_m(k_2 r_0),\\
M_{1,4} &= -T_{2,2}\mu_3 m\mathrm{J}_m(k_3 r_0)/r_0,\\
M_{2,1} &= \rho_a\omega^2 \mathrm{H}_m(k_a r_0),\\
M_{2,2} &= -T_{1,1}\tilde{K}\mu_1 k_1^2 \mathrm{J}_m(k_1 r_0) + T_{1,2}\left(\mu_1(-m\mathrm{J}_m(k_1 r_0)) + k_1\mu_1 r_0 \mathrm{J}_{m+1}(k_1 r_0)\right)/r_0,\\
M_{2,3} &= -T_{1,1}\tilde{K}\mu_2 k_2^2 \mathrm{J}_m(k_2 r_0) + T_{1,2}\left(\mu_2(-m\mathrm{J}_m(k_2 r_0)) + k_2\mu_2 r_0 \mathrm{J}_{m+1}(k_2 r_0)\right)/r_0,\\
M_{2,4} &= -T_{1,2}\mu_3 m\mathrm{J}_m(k_3 r_0)/r_0,\\
M_{3,1} &= 0,\\
M_{3,2} &= 2N/r_0^2\left(m(m-1)\mathrm{J}_m(k_1 r_0) - k_1^2 r_0^2 \mathrm{J}_m(k_1 r_0) + k_1 r_0 \mathrm{J}_{m+1}(k_1 r_0)\right) - \hat{A}k_1^2 \mathrm{J}_m(k_1 r_0),\\
M_{3,3} &= 2N/r_0^2\left(m(m-1)\mathrm{J}_m(k_2 r_0) - k_2^2 r_0^2 \mathrm{J}_m(k_2 r_0) + k_2 r_0 \mathrm{J}_{m+1}(k_2 r_0)\right) - \hat{A}k_2^2 \mathrm{J}_m(k_2 r_0),\\
M_{3,4} &= 2N\left(m(m-1)\mathrm{J}_m(k_3 r_0) - k_3 r_0 m\mathrm{J}_{m+1}(k_3 r_0)\right)/r_0^2,\\
M_{4,1} &= 0,\\
M_{4,2} &= \left(2Nk_1 r_0 m\mathrm{J}_{m+1}(k_1 r_0) - 2Nm(m-1)\mathrm{J}_m(k_1 r_0)\right)/r_0^2,\\
M_{4,3} &= \left(2Nk_2 r_0 m\mathrm{J}_{m+1}(k_2 r_0) - 2Nm(m-1)\mathrm{J}_m(k_2 r_0)\right)/r_0^2,\\
M_{4,4} &= N\left((-2m^2 + 2m + k_3^2)r_0^2 \mathrm{J}_m(k_3 r_0) - 2k_3 \mathrm{J}_{m+1}(k_3 r_0) r_0\right)/r_0^2,
\end{aligned}
$$

and the right-hand side terms are:

$$
\begin{aligned}
V_1 &= 2A_{inc}k_a(-\mathrm{j})^m \mathrm{J}_{m+1}(k_a r_0) - 2A_{inc}/r_0(-\mathrm{j})^m m\mathrm{J}_m(k_a r_0),\\
V_2 &= -2A_{inc}\rho_a\omega^2(-\mathrm{j})^2 \mathrm{J}_m(k_a r_0),\\
V_3 &= 0,\\
V_4 &= 0.
\end{aligned}
$$

Relevant mathematics proof

C

Two analytical proof that were used in the manuscript are provided. The first one proves the well-posedness of the Helmholtz equation prescribed by only Neumann boundary conditions with energy dissipative media. The second one is about the stability of the proposed discrete *Nitsche-type* formulation for pressure jump interface in high-order X-FEM space.

C.1 Well-posedness of Helmholtz equation with damping materials

The Helmholtz equation with a complex wave number k (absorbing system without resonance) is well-posed, of which, to our knowledge the proof is not available in the literature. The idea relies on a preliminary proof for the Helmholtz equation with impedance boundary condition given in Ihlenburg, 1998 [145]. We recommand interested readers to refer that textbook in order to better understand our proof.

Existence:
Let $\Omega =]0, 1[$ and let $f \in L^2(\Omega)$ be given. Consider the following boundary value problem (with k complex):

$$u'' - k^2 u = f \tag{C.1a}$$

$$u'(0) = g \tag{C.1b}$$

$$u'(1) = 0. \tag{C.1c}$$

The corresponding weak form is:

$$\int_0^1 u'v'dx - k^2 \int_0^1 uvdx = 0, \quad \forall v \in V. \tag{C.2}$$

As k^2 is complex valued, we express it as $\mathrm{Re}(k^2) + i\,\mathrm{Im}\,k^2$, and the sesquilinear form is rewritten:

$$b(u, v) := \int_0^1 u'\bar{v}'dx - \mathrm{Re}(k^2) \int_0^1 u\bar{v}dx - i\,\mathrm{Im}(k^2) \int_0^1 u\bar{v}dx. \tag{C.3}$$

The test and trial spaces are $V_1 = V_2 = H_0^1(\Omega)$. Let $v = u$, then $b(u, u)$ leads to:

$$\mathrm{Re}(b(u, u)) = \int_0^1 |u'|^2 dx - \mathrm{Re}(k^2) \int_0^1 |u|^2 dx, \tag{C.4}$$

which has the same structure same as in the proof of impedance condition in [145]: the Gårding inequality is thus satisfied for $C \geq \mathrm{Re}(k^2)$.

Uniqueness:

Now, its uniqueness is proved here. Supposing that there are two solutions u_1 , u_2 . Then their difference $w = u_1 - u_2$ satisfies the homogeneous equality $b(w, v) = 0$, and we get:

$$\int_0^1 |w'|^2 dx - \mathrm{Re}(k^2) \int_0^1 |w|^2 dx = i\,\mathrm{Im}(k^2) \int_0^1 |w|^2 dx, \tag{C.5}$$

where left-hand side of this equation is real, and the right-hand side is imaginary. Hence for $\mathrm{Im}(k^2) \neq 0$, equality can hold only if $\int_0^1 |w|^2 = 0$. The w have to be $w \equiv 0$, $u_1 = u_2$.

We proved that the problem has an unique solution whenever the wave number is complex. Following the above theorems, the problem is **well-posed**.

Conclusion: Helmholtz equation is well-posedness for any wavenumber in the case involving absorbing media (wavenumber is complex-valued).

C.2 Coercivity of the proposed discrete *Nitsche-type* formulation with high-order X-FEM

The following proof demonstrates that the discrete *Nitsche-type* formulation eq. (4.18) satisfies the Gårding inequality.

Proof[4.2.1] with the definition eq. (4.17), right inequality in eq. (4.21a) follows from:

$$|\lambda^{-1}|^2 = \left|\frac{1}{\beta_h} + \frac{\sigma d}{\mathrm{j}\omega}\right|^2 = \left(\frac{\sigma d}{\omega}\right)^2 + \left(\frac{1}{\beta_h}\right)^2 \geq \frac{1}{\beta_h^2}. \tag{C.6}$$

Then, and left inequality in eq. (4.21a) is bounded as:

$$|\lambda|^{-1} = \left|\frac{1}{\beta_h} + \frac{\sigma d}{\mathrm{j}\omega}\right| \leq \frac{1}{\beta_h} + \frac{\sigma d}{\omega}. \tag{C.7}$$

Identity eq. (4.21b) is obtained directly from the definition of λ. Then, the left-hand side in eq. (4.21c) is expressed as:

$$\frac{\sigma d}{\mathrm{j}\omega}\left(1 - \lambda\frac{\sigma d}{\mathrm{j}\omega}\right) = \frac{\sigma d}{\mathrm{j}\omega}\frac{1}{\beta_h}\lambda = \frac{1}{\beta_h}\left(\frac{1}{\beta_h} + \frac{\sigma d}{\mathrm{j}\omega} - \frac{1}{\beta_h}\right)\lambda = \frac{1}{\beta_h}\left(\lambda^{-1} - \frac{1}{\beta_h}\right)\lambda = \frac{1}{\beta_h} - \left(\frac{1}{\beta_h}\right)^2\lambda, \tag{C.8}$$

and by the triangle inequality and proved inequality eq. (4.21a), leads to the bound eq. (4.21c), that:

$$\left|\frac{\sigma d}{\mathrm{j}\omega}\left(1 - \lambda\frac{\sigma d}{\mathrm{j}\omega}\right)\right| \leq \frac{1}{\beta_h} + \left(\frac{1}{\beta_h}\right)^2 |\lambda| \leq \frac{2}{\beta_h}. \tag{C.9}$$

The last inequality is given by the fact that σd is a real number ($\mathrm{Re}\,(\lambda) > 0$ and $\mathrm{Im}\,(\lambda) > 0$) and $|\mathrm{Re}\,(z)| + |\mathrm{Im}\,(z)| \geq |z|$,

$$\mathrm{Re}\,(\lambda) + \mathrm{Im}\,(\lambda) - \frac{1}{2}|\lambda| = |\mathrm{Re}\,(\lambda)| + |\mathrm{Im}\,(\lambda)| - \frac{1}{2}|\lambda| \geq \frac{1}{2}|\lambda|. \tag{C.10}$$

□

Proof[theorem 4.2.4] choosing $q_h = \bar{p}_h$ as the conjugation in formulation eq. (4.18) yields:

$$\begin{aligned} a_\lambda(\bar{p}_h, p_h) &= a_B(\bar{p}_h, p_h) \\ -\int_{\Gamma^*} \left(1 - \lambda\frac{\sigma d}{\mathrm{j}\omega}\right) [\![\bar{p}_h]\!] \left\langle \frac{1}{\rho}\frac{\partial p_h}{\partial n}\right\rangle_\gamma \mathrm{d}S &- \int_{\Gamma^*} \left(1 - \lambda\frac{\sigma d}{\mathrm{j}\omega}\right) [\![p_h]\!] \left\langle \frac{1}{\rho}\frac{\partial \bar{p}_h}{\partial n}\right\rangle_\gamma \mathrm{d}S \\ -\int_{\Gamma^*} \frac{\sigma d}{\mathrm{j}\omega}\left(1 - \lambda\frac{\sigma d}{\mathrm{j}\omega}\right) \left\langle \frac{1}{\rho}\frac{\partial \bar{p}_h}{\partial n}\right\rangle_\gamma \left\langle \frac{1}{\rho}\frac{\partial p_h}{\partial n}\right\rangle_\gamma \mathrm{d}S &+ \int_{\Gamma^*} \lambda |[\![p_h]\!]|^2 \mathrm{d}S. \end{aligned} \tag{C.11}$$

Let us combine real and imaginary part of all the expression. And applying inequality $\mathrm{Re}\,(z) + \mathrm{Im}\,(z) \leq \sqrt{2}|z|$ to the second, third and fourth terms in the above equations, we get an inequality as :

$$\begin{aligned} \mathrm{Re}\,(a_\lambda(\bar{p}_h, p_h)) + \mathrm{Im}\,(a_\lambda(\bar{p}_h, p_h)) &\geq \mathrm{Re}\,(a_B(\bar{p}_h, p_h)) + \mathrm{Im}\,(a_B(\bar{p}_h, p_h)) \\ -\sqrt{2}\int_{\Gamma^*} \left|\left(1 - \lambda\frac{\sigma d}{\mathrm{j}\omega}\right)\right| \left|[\![\bar{p}_h]\!] \left\langle \frac{1}{\rho}\frac{\partial p_h}{\partial n}\right\rangle_\gamma\right| \mathrm{d}S \\ -\sqrt{2}\int_{\Gamma^*} \left|\left(1 - \lambda\frac{\sigma d}{\mathrm{j}\omega}\right)\right| \left|[\![p_h]\!] \left\langle \frac{1}{\rho}\frac{\partial \bar{p}_h}{\partial n}\right\rangle_\gamma\right| \mathrm{d}S \\ -\sqrt{2}\int_{\Gamma^*} \left|\frac{\sigma d}{\mathrm{j}\omega}\left(1 - \lambda\frac{\sigma d}{\mathrm{j}\omega}\right)\right| \left|\left\langle \frac{1}{\rho}\frac{\partial \bar{p}_h}{\partial n}\right\rangle_\gamma \left\langle \frac{1}{\rho}\frac{\partial p_h}{\partial n}\right\rangle_\gamma\right| \mathrm{d}S \\ + \int_{\Gamma^*} (\mathrm{Re}\,(\lambda) + \mathrm{Im}\,(\lambda))\, |[\![p_h]\!]|^2 \mathrm{d}S \\ = \mathrm{Re}\,(a_B(\bar{p}_h, p_h)) + \mathrm{Im}\,(a_B(\bar{p}_h, p_h)) - 2\sqrt{2}\int_{\Gamma^*} \left|\left(1 - \lambda\frac{\sigma d}{\mathrm{j}\omega}\right)\right| \left|[\![p]\!] \left\langle \frac{1}{\rho}\frac{\partial p_h}{\partial n}\right\rangle_\gamma\right| \mathrm{d}S \\ -\sqrt{2}\int_{\Gamma^*} \left|\frac{\sigma d}{\mathrm{j}\omega}\left(1 - \lambda\frac{\sigma d}{\mathrm{j}\omega}\right)\right| \left|\left\langle \frac{1}{\rho}\frac{\partial p_h}{\partial n}\right\rangle_\gamma\right|^2 \mathrm{d}S + \int_{\Gamma^*} (\mathrm{Re}\,(\lambda) + \mathrm{Im}\,(\lambda))\, |[\![p_h]\!]|^2 \mathrm{d}S, \end{aligned} \tag{C.12}$$

and also with the lemma 4.2.2, we have

$$\mathrm{Re}\,(a_0) + \mathrm{Im}\,(a_0) \geq |a_0|, \tag{C.13}$$

which leads to the following inequality:

$$\begin{aligned}
&\mathrm{Re}\left(a_\lambda(\bar{p}_h, p_h)\right) + \mathrm{Im}\left(a_\lambda(\bar{p}_h, p_h)\right) \geq |a_B(\bar{p}_h, p_h)| \\
&-2\sqrt{2}\int_{\Gamma^*} \left|\left(1 - \lambda\frac{\sigma d}{\mathrm{j}\omega}\right)\right| \left|[\![p_h]\!]\left\langle \frac{1}{\rho}\frac{\partial p_h}{\partial n}\right\rangle_\gamma\right| \mathrm{d}S \\
&-\sqrt{2}\int_{\Gamma^*} \left|\frac{\sigma d}{\mathrm{j}\omega}\left(1 - \lambda\frac{\sigma d}{\mathrm{j}\omega}\right)\right| \left|\left\langle \frac{1}{\rho}\frac{\partial p_h}{\partial n}\right\rangle_\gamma\right|^2 \mathrm{d}S \\
&+\int_{\Gamma^*} \left(\mathrm{Re}\left(\lambda\right) + \mathrm{Im}\left(\lambda\right)\right)|[\![p_h]\!]|^2 \mathrm{d}S.
\end{aligned} \tag{C.14}$$

For the second term in the above equation with identity in eq. (4.21b), we get:

$$2\sqrt{2}\int_{\Gamma^*} \left|\left(1 - \lambda\frac{\sigma d}{\mathrm{j}\omega}\right)\right| \left|[\![p_h]\!]\left\langle \frac{1}{\rho}\frac{\partial p_h}{\partial n}\right\rangle_\gamma\right| \mathrm{d}S = 2\sqrt{2}\int_{\Gamma^*} \frac{1}{\beta_h}|\lambda| \left|[\![p_h]\!]\left\langle \frac{1}{\rho}\frac{\partial p_h}{\partial n}\right\rangle_\gamma\right| \mathrm{d}S. \tag{C.15}$$

Then, using inequalities $2ab \leq 2a^2 + b^2/2$, with $a = \sqrt{2}/\beta_h \left|\left\langle \frac{1}{\rho}\frac{\partial p_h}{\partial n}\right\rangle_\gamma\right|$, $b = \left|[\![p_h]\!]\right|$. The second term is written as:

$$\begin{aligned}
&2\sqrt{2}\int_{\Gamma^*} \frac{1}{\beta_h}|\lambda| \left|[\![p_h]\!]\left\langle \frac{1}{\rho}\frac{\partial p_h}{\partial n}\right\rangle_\gamma\right| \mathrm{d}S \\
&\leq 4\int_{\Gamma^*} \frac{1}{\beta_h^2}|\lambda| \left|\left\langle \frac{1}{\rho}\frac{\partial p_h}{\partial n}\right\rangle_\gamma\right|^2 \mathrm{d}S + \frac{1}{2}\int_{\Gamma^*} |\lambda| \left|[\![p_h]\!]\right|^2 \mathrm{d}S,
\end{aligned} \tag{C.16}$$

and with inequality eq. (4.21a):

$$\begin{aligned}
&4\int_{\Gamma^*} \frac{1}{\beta_h^2}|\lambda| \left|\left\langle \frac{1}{\rho}\frac{\partial p_h}{\partial n}\right\rangle_\gamma\right|^2 \mathrm{d}S + \frac{1}{2}\int_{\Gamma^*} |\lambda| \left|[\![p_h]\!]\right|^2 \mathrm{d}S \\
&\leq 4\int_{\Gamma^*} \frac{1}{\beta_h} \left|\left\langle \frac{1}{\rho}\frac{\partial p_h}{\partial n}\right\rangle_\gamma\right|^2 \mathrm{d}S + \frac{1}{2}\int_{\Gamma^*} |\lambda| \left|[\![p_h]\!]\right|^2 \mathrm{d}S.
\end{aligned} \tag{C.17}$$

Let us simplify the third term in eq. (C.14). The inequality eq. (4.21c) is first used, leading third term become as:

$$\begin{aligned}
&\sqrt{2}\int_{\Gamma^*} \left|\frac{\sigma d}{\mathrm{j}\omega}\left(1 - \lambda\frac{\sigma d}{\mathrm{j}\omega}\right)\right| \left|\left\langle \frac{1}{\rho}\frac{\partial p_h}{\partial n}\right\rangle_\gamma\right|^2 \mathrm{d}S \\
&\leq \frac{2\sqrt{2}}{\beta_h}\int_{\Gamma^*} \left|\left\langle \frac{1}{\rho}\frac{\partial p_h}{\partial n}\right\rangle_\gamma\right|^2 \mathrm{d}S \leq \frac{3}{\beta_h}\int_{\Gamma^*} \left|\left\langle \frac{1}{\rho}\frac{\partial p_h}{\partial n}\right\rangle_\gamma\right|^2 \mathrm{d}S.
\end{aligned} \tag{C.18}$$

Substituting inequalities eq. (C.17) and eq. (C.18) into Equation (C.14), we find that:

$$\begin{aligned}
&\mathrm{Re}\left(a_\lambda(\bar{p}_h, p_h)\right) + \mathrm{Im}\left(a_\lambda(\bar{p}_h, p_h)\right) \\
&\geq |a_B(\bar{p}_h, p_h)| - \frac{7}{\beta_h}\int_{\Gamma^*}\left|\left\langle \frac{1}{\rho}\frac{\partial p_h}{\partial n}\right\rangle_\gamma\right|^2 \mathrm{d}S + \int_{\Gamma^*}\left(\mathrm{Re}\left(\lambda\right) + \mathrm{Im}\left(\lambda\right) - \frac{1}{2}|\lambda|\right)|[\![p_h]\!]|^2 \mathrm{d}S \\
&= |a_0(\bar{p}_h, p_h)| \\
&\quad - \frac{8}{\beta_h}\int_{\Gamma^*}\left|\left\langle \frac{1}{\rho}\frac{\partial p_h}{\partial n}\right\rangle_\gamma\right|^2 \mathrm{d}S \\
&\quad + \frac{1}{\beta_h}\int_{\Gamma^*}\left|\left\langle \frac{1}{\rho}\frac{\partial p_h}{\partial n}\right\rangle_\gamma\right|^2 \mathrm{d}S \\
&\quad + \int_{\Gamma^*}\left(\mathrm{Re}\left(\lambda\right) + \mathrm{Im}\left(\lambda\right) - \frac{1}{2}|\lambda|\right)|[\![p_h]\!]|^2 \mathrm{d}S.
\end{aligned} \tag{C.19}$$

By the definition of a_0 with associated inequality for complex number $|w - z| \geq |w| - |z|$ and lemma 4.2.3, we are able to rewrite the eq. (C.14):

$$\begin{aligned}
\mathrm{Re}\left(a_\lambda(\bar{p}_h, p_h)\right) + \mathrm{Im}\left(a_\lambda(\bar{p}_h, p_h)\right) &\geq \frac{1}{2}\sum_i^2 \left|\frac{1}{\rho_i}\right| \int_{\Omega_i} |\boldsymbol{\nabla} p_h|^2 \mathrm{d}\Omega - \sum_i^2 \left|\frac{\omega^2}{K_i}\right| \int_{\Omega_i} |p_h|^2 \mathrm{d}\Omega \\
&\quad + \left(\frac{1}{2} - \frac{8}{\beta_h}C_I\right)\sum_i^2 \int_{\Omega_i} \left|\frac{1}{\rho_i}\right| \left|\boldsymbol{\nabla} p_h\right|^2 \mathrm{d}\Omega \\
&\quad + \frac{1}{\beta_h}\int_{\Omega_i}\left|\left\langle \frac{1}{\rho}\frac{\partial p_h}{\partial n}\right\rangle_\gamma\right|^2 \mathrm{d}\Omega \\
&\quad + \int_{\Gamma^*}\left(\mathrm{Re}\left(\lambda\right) + \mathrm{Im}\left(\lambda\right) - \frac{1}{2}|\lambda|\right)|[\![p_h]\!]|^2 \mathrm{d}S.
\end{aligned} \tag{C.20}$$

In order to make term associated to C_I be positive, the β_h satisfies the condition:

$$\beta_h \geq 16 C_I \quad \left(\text{that } \left(\frac{1}{2} - \frac{8}{\beta_h}C_I\right) \geq 0\right), \tag{C.21}$$

and the last term in above equation is replaced by the eq. (4.21d). We have finally:

$$\begin{aligned}
\mathrm{Re}\left(a_\lambda(\bar{p}_h, p_h)\right) + \mathrm{Im}\left(a_\lambda(\bar{p}_h, p_h)\right) &\geq \frac{1}{2}\sum_i^2 \left|\frac{1}{\rho_i}\right| \int_{\Omega_i} |\boldsymbol{\nabla} p_h|^2 \mathrm{d}\Omega - \sum_i^2 \left|\frac{\omega^2}{K_i}\right| \int_{\Omega_i} |p_h|^2 \mathrm{d}\Omega \\
&\quad + \frac{1}{\beta_h}\int_{\Omega_i}\left|\left\langle \frac{1}{\rho}\frac{\partial p_h}{\partial n}\right\rangle_\gamma\right|^2 \mathrm{d}\Omega + \int_{\Gamma^*} \frac{1}{2}|\lambda||[\![p_h]\!]|^2 \mathrm{d}S.
\end{aligned} \tag{C.22}$$

Using that $2|z| \geq \mathrm{Re}\left(z\right) + \mathrm{Im}\left(z\right)$, and adding a multiple of $\|p\|$ with $C_k = 2$: we finally obtain:

$$\begin{aligned}
2|a_\lambda(\bar{p}_h, p_h)| + 2\left\|p_h\right\| &\geq \frac{1}{2}\sum_i^2 \left|\frac{1}{\rho_i}\right| \int_{\Omega_i} |\boldsymbol{\nabla} p_h|^2 \mathrm{d}\Omega + \sum_i^2 \left|\frac{\omega^2}{K_i}\right| \int_{\Omega_i} |p_h|^2 \mathrm{d}\Omega \\
&\quad + \frac{1}{\beta_h}\int_{\Omega_i}\left|\left\langle \frac{1}{\rho}\frac{\partial p_h}{\partial n}\right\rangle_\gamma\right|^2 \mathrm{d}\Omega + \int_{\Gamma^*} \frac{1}{2}|\lambda||[\![p]\!]|^2 \mathrm{d}S \\
&\geq \frac{1}{2}|||p|||.
\end{aligned} \tag{C.23}$$

from which the Gårding equality holds for any $\beta_h \geq 16C_I$. $\square$

D

Methodology and procedure for obtaining specific matrices

In the chapter 5, the transfer and admittance matrix are the key ingredient to impose the thin porous layers model into generalized variational formulation. For specific interface conditions, these two matrix are not easy to obtain. This appendix presents the methodologies used in the manuscript for obtaining the transfer matrix in the fluid-Biot-fluid coupling and admittance matrix in the fluid-Biot-Biot coupling.

D.1 Obtention of matrix $[\mathbf{T}^{\mathbf{f-P-f}}]$

In this section, we would find a matrix of 2×2 that connects the pressure and total displacement for faces Γ_1^+ and Γ_2^+ in the coupling `f-P-f`.

Under the continuity condition at the interfaces Γ_i^- and Γ_i^+, a transfer matrix relationship based on the Biot film layer can be obtained with arbitrary coefficients as following:

$$\begin{Bmatrix} \hat{\sigma}_{yx1}^- = 0 \\ u_{x1}^{s\,-} \\ u_{n1}^{t\,+} \\ \hat{\sigma}_{xx1}^- = 0 \\ p^{f\,+}_1 \\ u_{y1}^{s\,-} \end{Bmatrix} = \begin{bmatrix} T_{11}^P & T_{12}^P & T_{13}^P & T_{14}^P & T_{15}^P & T_{16}^P \\ \cancel{T_{21}^P} & \cancel{T_{22}^P} & \cancel{T_{23}^P} & \cancel{T_{24}^P} & \cancel{T_{25}^P} & \cancel{T_{16}^P} \\ T_{31}^P & T_{32}^P & T_{33}^P & T_{34}^P & T_{35}^P & T_{36}^P \\ T_{41}^P & T_{42}^P & T_{43}^P & T_{44}^P & T_{45}^P & T_{46}^P \\ T_{51}^P & T_{52}^P & T_{53}^P & T_{54}^P & T_{55}^P & T_{56}^P \\ \cancel{T_{61}^P} & \cancel{T_{62}^P} & \cancel{T_{63}^P} & \cancel{T_{64}^P} & \cancel{T_{65}^P} & \cancel{T_{66}^P} \end{bmatrix} \begin{Bmatrix} \hat{\sigma}_{yx2}^- = 0 \\ u_{x2}^{s\,-} \\ u_{n2}^{t\,+} \\ \hat{\sigma}_{xx2}^- = 0 \\ p^{f\,+}_2 \\ u_{y2}^{s\,-} \end{Bmatrix}, \tag{D.1}$$

where T_{ij}^P are the coefficients for the PEM layer that could be the matrix 2.22. Since displacements do not exist in the fluid bulk parts, two lines associated with the u_x^s and u_y^s at the interface Γ_1^- of PEM layer need first to be eliminated, then u_x^s and u_y^s at the interface Γ_2^- should be re-expressed by the p^f and u_n^t.

And, based on the relationship in eq. (D.1), we obtain four linear equations, respectively as:

$$0 = T^P_{12} u^{s\,-}_{x2} + T^P_{13} u^{t\,+}_{n2} + T^P_{15} {p^f}^{+}_{2} + T^P_{16} u^{s\,-}_{y2}, \tag{D.2a}$$

$$u^{t\,+}_{n1} = T^P_{32} u^{s\,-}_{x2} + T^P_{33} u^{t\,+}_{n2} + T^P_{35} {p^f}^{+}_{2} + T^P_{36} u^{s\,-}_{y2}, \tag{D.2b}$$

$$0 = T^P_{42} u^{s\,-}_{x2} + T^P_{43} u^{t\,+}_{n2} + T^P_{45} {p^f}^{+}_{2} + T^P_{46} u^{s\,-}_{y2}, \tag{D.2c}$$

$${p^f}^{+}_{1} = T^P_{52} u^{s\,-}_{x2} + T^P_{53} u^{t\,+}_{n2} + T^P_{55} {p^f}^{+}_{2} + T^P_{56} u^{s\,-}_{y2}, \tag{D.2d}$$

in which the two equations associated with u^s_x and u^s_y at the interface Γ^-_2 eqs. (D.2a) and (D.2c) are re-written in matrix form as:

$$\underbrace{\begin{bmatrix} -T^P_{12} & -T^P_{16} \\ -T^P_{42} & -T^P_{46} \end{bmatrix}}_{T_1} \begin{Bmatrix} u^{s\,-}_{x2} \\ u^{s\,-}_{y2} \end{Bmatrix} = \underbrace{\begin{bmatrix} T^P_{15} & T^P_{13} \\ T^P_{45} & T^P_{43} \end{bmatrix}}_{T_2} \begin{Bmatrix} {p^f}^{+}_{2} \\ u^{t\,+}_{n2} \end{Bmatrix}. \tag{D.3}$$

Thus, we have:

$$\begin{Bmatrix} u^{s\,-}_{x2} \\ u^{s\,-}_{y2} \end{Bmatrix} = \underbrace{[\mathbf{T_1}]^{-1}[\mathbf{T_2}]}_{[\mathbf{T^u}]} \begin{Bmatrix} {p^f}^{+}_{2} \\ u^{t\,+}_{n2} \end{Bmatrix}, \tag{D.4}$$

the $u^{s\,-}_{x2}$ and $u^{s\,-}_{y2}$ are expressed by the ${p^f}^{-}_{2}$ and $u^{t\,-}_{n2}$ with the matrices T^u. Then, replacing terms $u^{s\,-}_{x2}$ and $u^{s\,-}_{y2}$ in the left two equations eqs. (D.2b) and (D.2d), we get:

$$u^{t\,+}_{n1} = T^P_{32}(T^u_{11} {p^f}^{+}_{2} + T^u_{12} u^{t\,+}_{n2}) + T^P_{33} u^{t\,+}_{n2} + T^P_{35} {p^f}^{+}_{2} + T^P_{36}(T^u_{21} {p^f}^{+}_{2} + T^u_{22} u^{t\,+}_{n2}), \tag{D.5a}$$

$${p^f}^{+}_{1} = T^P_{52}(T^u_{11} {p^f}^{+}_{2} + T^u_{12} u^{t\,+}_{n2}) + T^P_{53} u^{t\,+}_{n2} + T^P_{55} {p^f}^{+}_{2} + T^P_{56}(T^u_{21} {p^f}^{+}_{2} + T^u_{22} u^{t\,+}_{n2}). \tag{D.5b}$$

Finally, only the variables p^f and u^t_n at the faces Γ^+_i are remained in above equation, we write it in a matrix form as:

$$\begin{Bmatrix} {p^f}^{+}_{1} \\ u^{t\,+}_{n1} \end{Bmatrix} = \underbrace{\begin{bmatrix} T^P_{32}T^u_{11} + T^P_{35} + T^P_{36}T^u_{21} & T^P_{32}T^u_{12} + T^P_{33} + T^P_{36}T^u_{22} \\ T^P_{52}T^u_{11} + T^P_{55} + T^P_{56}T^u_{21} & T^P_{52}T^u_{12} + T^P_{53} + T^P_{56}T^u_{22} \end{bmatrix}}_{[\mathbf{T^{f\text{-}P\text{-}f}}]} \begin{Bmatrix} {p^f}^{+}_{2} \\ u^{t\,+}_{n2} \end{Bmatrix}. \tag{D.6}$$

the matrix $[\mathbf{T^{f\text{-}P\text{-}f}}]$ is obtained, whose coefficients are all original from $[\mathbf{T^P}]$.

D.2 From transfer matrix to Admittance matrix for Biot's model

Let us consider a generalized interface condition for the case `f-P-P` as presented eq. (5.14), which can be re-expressed by a transfer matrix with arbitrary coefficients:

$$\begin{Bmatrix} \hat{\sigma}^{-}_{yx1} = 0 \\ \hat{\sigma}^{-}_{xx1} = 0 \\ {p^f}^{+}_{1} \\ {u^t_{n1}}^{+} \end{Bmatrix} = \begin{bmatrix} T^P_{11} & T^P_{12} & T^P_{13} & T^P_{14} & T^P_{15} & T^P_{16} \\ \cancel{T^P_{21}} & \cancel{T^P_{22}} & \cancel{T^P_{23}} & \cancel{T^P_{24}} & \cancel{T^P_{25}} & \cancel{T^P_{16}} \\ T^P_{31} & T^P_{32} & T^P_{33} & T^P_{34} & T^P_{35} & T^P_{36} \\ T^P_{41} & T^P_{42} & T^P_{43} & T^P_{44} & T^P_{45} & T^P_{46} \\ T^P_{51} & T^P_{52} & T^P_{53} & T^P_{54} & T^P_{55} & T^P_{56} \\ \cancel{T^P_{61}} & \cancel{T^P_{62}} & \cancel{T^P_{63}} & \cancel{T^P_{64}} & \cancel{T^P_{65}} & \cancel{T^P_{66}} \end{bmatrix} \begin{Bmatrix} \hat{\sigma}^{+}_{yx2} \\ u^{s+}_{x2} \\ {u^t_{n2}}^{+} \\ \hat{\sigma}^{+}_{xx2} \\ {p^f}^{+}_{2} \\ u^{s+}_{y2} \end{Bmatrix}, \tag{D.7}$$

as explained in section 2 chapter 5, this matrix is a subset of the original Biot's matrix $[\mathbf{T^P}]$ where two lines (index 2 and 6) related to the solid displacement in the fluid media are eliminated. We are able to reproduce four linear equations from this relationship as:

$$0 = T^P_{11}\hat{\sigma}^{+}_{yx2} + T^P_{12}u^{s+}_{x2} + T^P_{13}{u^t_{n2}}^{+} + T^P_{14}\hat{\sigma}^{+}_{xx2} + T^P_{15}{p^f}^{+}_{2} + T^P_{16}u^{s+}_{y2}, \tag{D.8a}$$

$$0 = T^P_{31}\hat{\sigma}^{+}_{yx2} + T^P_{32}u^{s+}_{x2} + T^P_{33}{u^t_{n2}}^{+} + T^P_{34}\hat{\sigma}^{+}_{xx2} + T^P_{35}{p^f}^{+}_{2} + T^P_{36}u^{s+}_{y2}, \tag{D.8b}$$

$${p^f}^{+}_{1} = T^P_{41}\hat{\sigma}^{+}_{yx2} + T^P_{42}u^{s+}_{x2} + T^P_{43}{u^t_{n2}}^{+} + T^P_{44}\hat{\sigma}^{+}_{xx2} + T^P_{45}{p^f}^{+}_{2} + T^P_{46}u^{s+}_{y2}, \tag{D.8c}$$

$${u^t_{n1}}^{+} = T^P_{51}\hat{\sigma}^{+}_{yx2} + T^P_{52}u^{s+}_{x2} + T^P_{53}{u^t_{n2}}^{+} + T^P_{54}\hat{\sigma}^{+}_{xx2} + T^P_{55}{p^f}^{+}_{2} + T^P_{56}u^{s+}_{y2}. \tag{D.8d}$$

To obtain the admittance matrix which expresses the relationship between dual variables and primal variables, these linear equations need to be rearranged. We put dual variables on the left-hand side and the primal variable in the right-hand sides, leading to the following equations:

$$[\mathbf{B}]_{4\times4} \begin{Bmatrix} {u^t_{n1}}^{+} \\ {u^t_{n2}}^{+} \\ \hat{\sigma}^{+}_{xx2} \\ \hat{\sigma}^{+}_{yx2} \end{Bmatrix} = [\mathbf{C}]_{4\times4} \begin{Bmatrix} {p^f}^{+}_{1} \\ {p^f}^{+}_{2} \\ u^{s+}_{x2} \\ u^{s+}_{y2} \end{Bmatrix}, \tag{D.9}$$

where matrix $[\mathbf{B}]$ and $[\mathbf{C}]$ are:

$$\mathbf{B} = \begin{bmatrix} 0 & -T^P_{13} & -T^P_{14} & -T^P_{11} \\ 0 & -T^P_{33} & -T^P_{34} & -T^P_{31} \\ 0 & -T^P_{43} & -T^P_{44} & -T^P_{41} \\ 1 & -T^P_{53} & -T^P_{54} & -T^P_{51} \end{bmatrix}, \quad \mathbf{C} = \begin{bmatrix} 0 & T^P_{15} & T^P_{12} & T^P_{16} \\ 0 & T^P_{35} & T^P_{32} & T^P_{36} \\ -1 & T^P_{45} & T^P_{42} & T^P_{46} \\ 0 & T^P_{55} & T^P_{52} & T^P_{56} \end{bmatrix}. \tag{D.10}$$

Thus, the final equation for the dual variables expressed by primal variables on the positive side of Γ_2 is written as following:

$$\begin{Bmatrix} u_{n1}^t \\ u_{n2}^t \\ \hat{\sigma}_{xx2} \\ \hat{\sigma}_{yx2} \end{Bmatrix} = [\mathbf{B}]_{4\times4}^{-1}[\mathbf{C}]_{4\times4} \begin{Bmatrix} p_1^f \\ p_2^f \\ u_{x2}^s \\ u_{y2}^s \end{Bmatrix}, \tag{D.11}$$

where all the superscript $(\bullet)^+$ are removed to be consistent to eq. (5.21). The generalized admittance matrix $[\mathbf{A^P}]$ in eq. (5.21) is obtained as:

$$[\mathbf{A^P}] = [\mathbf{B}]^{-1}[\mathbf{C}]. \tag{D.12}$$

The methodology presented here to obtain the generalized admittance matrix is also suitable for other case, for instance the fluid-fluid coupling. Even though, derivation of admittance matrix for fluid-fluid coupling is quite direct.

E

Completed discretized terms in linear systems for TMM enhanced interface

We offer all related discretized terms in the linear system (5.33) and (5.34) in this appendix.

The bulk contribution K^b_{pi} and the enriched one K^b_{pja} are written as:

$$K^b_{pi} = \frac{1}{\omega^2 \rho_i} \int_{\Omega_{e,i}} \boldsymbol{\nabla}\mathbf{N}^T \boldsymbol{\nabla}\mathbf{N} \mathrm{d}\Omega - \frac{1}{\tilde{K}} \int_{\Omega_{e,i}} \mathbf{N}^T \mathbf{N} \mathrm{d}\Omega, \tag{E.1a}$$

$$K^b_{pja} = K^b_{apj} = (-1)^{j-1} \frac{1}{\omega^2 \rho_i} \int_{\Omega_{e,I}} \boldsymbol{\nabla}\mathbf{N}^T \boldsymbol{\nabla}\mathbf{N} \mathrm{d}\Omega - \frac{1}{\tilde{K}} \int_{\Omega_{e,I}} \mathbf{N}^T \mathbf{N} \mathrm{d}\Omega, \tag{E.1b}$$

and the other matrices arise from the interface terms as:

$$K^I_{pi} = (-1)^i A_{ii} \int_\Gamma \mathbf{N}^T \mathbf{N} \mathrm{d}S, \tag{E.2a}$$

$$K^I_{p12} = -A_{12} \int_\Gamma \mathbf{N}^T \mathbf{N} \mathrm{d}S, \quad K^I_{p21} = A_{21} \int_\Gamma \mathbf{N}^T \mathbf{N} \mathrm{d}S, \tag{E.2b}$$

$$K^I_{p1a} = (-A_{11} + A_{12}) \int_\Gamma \mathbf{N}^T \mathbf{N} \mathrm{d}S, \quad K^I_{ap1} = (-A_{11} - A_{21}) \int_\Gamma \mathbf{N}^T \mathbf{N} \mathrm{d}S, \tag{E.2c}$$

$$K^I_{p2a} = (A_{21} + A_{22}) \int_\Gamma \mathbf{N}^T \mathbf{N} \mathrm{d}S, \quad K^I_{ap1} = (-A_{12} + A_{22}) \int_\Gamma \mathbf{N}^T \mathbf{N} \mathrm{d}S, \tag{E.2d}$$

$$K^I_{aa} = \left(\sum_j (-1)^j A_{ij} \right) \int_\Gamma \mathbf{N}^T \mathbf{N} \mathrm{d}S, \tag{E.2e}$$

where $\mathbf{N}$ represents the vector of the shape function as defined in eq. (3.9), $\boldsymbol{\nabla}\mathbf{N}$ is its gradient.

Compared to the previous system, all the terms in (5.34) involving only pressure p_i remain the same, new terms including displacement of solid phase u_i are given here. The bulk contribution including displacement are written as:

$$K^b_{piu} = K^b_{uip} = -\tilde{\gamma} \int_{\Omega_{e,i}} \boldsymbol{\nabla}\mathbf{N}^T \mathbf{N} \mathrm{d}\Omega, \tag{E.3a}$$

$$K^b_{ui} = \hat{P} \int_{\Omega_{e,i}} \boldsymbol{\nabla}\mathbf{N}^T \boldsymbol{\nabla}\mathbf{N} \mathrm{d}\Omega - \omega^2 \tilde{\rho} \int_{\Omega_{e,i}} \mathbf{N}^T \mathbf{N} \mathrm{d}\Omega, \tag{E.3b}$$

where $\hat{P}$ that has been explained in appendix B is the material's modulus for solid phase. The interface terms involving displacement are written as:

$$K^I_{piuj} = -K^I_{pjui} = (-1)^i A_{ij} \int_\Gamma \mathbf{N}^T \mathbf{N} \mathrm{d}S \quad i = 1, \tag{E.4a}$$

$$K^I_{uxa} = (A_{31} - A_{32}) \int_\Gamma \mathbf{N}^T \mathbf{N} \mathrm{d}S, \quad K^I_{aux} = (-A_{13} - A_{23}) \int_\Gamma \mathbf{N}^T \mathbf{N} \mathrm{d}S, \tag{E.4b}$$

$$K^I_{uya} = (A_{41} - A_{42}) \int_\Gamma \mathbf{N}^T \mathbf{N} \mathrm{d}S, \quad K^I_{auy} = (-A_{14} - A_{24}) \int_\Gamma \mathbf{N}^T \mathbf{N} \mathrm{d}S. \tag{E.4c}$$

The symmetry of discrete linear system can be recognized with this discretized expressions. From the interface terms in eq. (E.2), the conclusion in eq. (5.23) is obtained. The same conditions for the system of "f-P-P" are obtained under the expressions provided above eq. (E.4).

Bibliography

[1]Anna Lene Seidler, Janice Hegewald, Melanie Schubert, et al. “The Effect of Aircraft, Road, and Railway Traffic Noise on Stroke - Results of a Case–Control Study Based on Secondary Data”. In: *Noise and Health* 20.95 (Jan. 2018), p. 152 (cit. on p. 1).

[2]*Health Risks Caused by Environmental Noise in Europe — European Environment Agency*. `https://www.eea.europa.eu/publications/health-risks-caused-by-environmental`. Briefing (cit. on p. 1).

[3]European Environment Agency. *Environmental Noise in Europe, 2020*. LU: Publications Office, 2020 (cit. on p. 1).

[4]*Health Implication of Road, Railway and Aircraft Noise in the European Union*, p. 62 (cit. on p. 1).

[5]*Over One Billion People at Risk of Hearing Loss: WHO*. `https://news.un.org/en/story/2022/03/1113182`. Mar. 2022 (cit. on p. 1).

[6]*‘Once Lost, Hearing Doesn’t Come Back,’ World Health Organization Warns on World Hearing Day*. https://news.un.org/en/story/2019/03/1033992. Mar. 2019 (cit. on p. 1).

[7]*How Noise Pollution May Harm the Heart*. https://www.health.harvard.edu/heart-health/how-noise-pollution-may-harm-the-heart. Mar. 2020 (cit. on p. 1).

[8]Manfred E. Beutel, Claus Jünger, Eva M. Klein, et al. “Noise Annoyance Is Associated with Depression and Anxiety in the General Population- The Contribution of Aircraft Noise”. In: *PLOS ONE* 11.5 (May 2016), e0155357 (cit. on p. 1).

[9]Kenneth I. Hume, Mark Brink, and Mathias Basner. “Effects of Environmental Noise on Sleep”. In: *Noise and Health* 14.61 (Jan. 2012), p. 297 (cit. on p. 1).

[10]Brett Day, Ian Bateman, and Iain Lake. “Estimating the Demand for Peace and Quiet Using Property Market Data”. In: *Working Paper - Centre for Social and Economic Research on the Global Environment* (Jan. 2006) (cit. on p. 1).

[11]WHO Reginal Office for Europe. *Environmental Noise Guidelines for the European Region*. 2018 (cit. on p. 1).

[12]Min-Chie Chiu. “Shape Optimization of Multi-Chamber Mufflers with Plug-Inlet Tube on a Venting Process by Genetic Algorithms”. In: *Applied Acoustics* 71.6 (June 2010), pp. 495–505 (cit. on p. 2).

[13]Aleksandar Milosevi and Urs Schaufelberger. “Active Noise Control”. PhD thesis. University of Applied Sciences Rapperswil HSR, Dec. 2005 (cit. on p. 2).

[14]T. Kitagawa, K. Nagakura, S. Tanaka, and K. Murata. “Study on Effective Sound Barriers for High Speed Trains”. In: *Noise and Vibration Mitigation for Rail Transportation Systems*. Ed. by Jens C.O. Nielsen, David Anderson, Pierre-Etienne Gautier, et al. Notes on Numerical Fluid Mechanics and Multidisciplinary Design. Berlin, Heidelberg: Springer, 2015, pp. 683–690 (cit. on p. 2).

[15]N. I. Ivanov, I. S. Boiko, and A. E. Shashurin. “The Problem of High-Speed Railway Noise Prediction and Reduction”. In: *Procedia Engineering*. Roceedings of the International Scientific Conference Transportation Geotechnics and Geoecology (TGG-2017). 189 (Jan. 2017), pp. 539–546 (cit. on p. 2).

[16]Herbert Fellner, Irena Hauer, Hans H. Priebsch, Gernot Polt, and Franz K. Brandl. “Numerical Simulation of Trim in the Vehicle Interior”. In: *ATZ worldwide* 104.7 (July 2002), pp. 17–20 (cit. on p. 2).

[17]C. Silva, Márcio Calçada, and Luiz Cesar Massarelli. “Vehicle Interior Noise Reduction Using Innovative Roof Trim Structure”. In: 2014 (cit. on p. 2).

[18]Laura Labia, Louena Shtrepi, and Arianna Astolfi. “Improved Room Acoustics Quality in Meeting Rooms: Investigation on the Optimal Configurations of Sound-Absorptive and Sound-Diffusive Panels”. In: *Acoustics* 2.3 (Sept. 2020), pp. 451–473 (cit. on p. 2).

[19]F. -C. Lee and W. -H. Chen. “ACOUSTIC TRANSMISSION ANALYSIS OF MULTI-LAYER ABSORBERS”. In: *Journal of Sound and Vibration* 248.4 (Dec. 2001), pp. 621–634 (cit. on p. 2).

[20]I.P. Dunn and W.A. Davern. “Calculation of Acoustic Impedance of Multi-Layer Absorbers”. In: *Applied Acoustics* 19.5 (Jan. 1986), pp. 321–334 (cit. on pp. 2, 3).

[21]Mohammad Hosseini Fouladi, Mohd Jailani Mohd Nor, Md. Ayub, and Zulkarnain Ali Leman. “Utilization of Coir Fiber in Multilayer Acoustic Absorption Panel”. In: *Applied Acoustics* 71.3 (Mar. 2010), pp. 241–249 (cit. on p. 2).

[22]*Automotive Interior Trim: Materials, Types, and Processes*. `https://maycointernational.com/blog/automotive-interior-trim-materials-types-and-processes/`. Mar. 2021 (cit. on p. 2).

[23]F. Chevillotte. “Controlling Sound Absorption by an Upstream Resistive Layer”. In: *Applied Acoustics* 73.1 (Jan. 2012), pp. 56–60 (cit. on p. 2).

[24]Mathieu Gaborit, Olivier Dazel, and Peter Göransson. “A Simplified Model for Thin Acoustic Screens”. In: *The Journal of the Acoustical Society of America* 144.1 (July 2018), EL76–EL81 (cit. on pp. 2, 7, 8, 99).

[25]Mathieu Gaborit, Olivier Dazel, Peter Göransson, and Luc Jaouen. “Generation of Uncertainty Envelopes for Thin Acoustic Screens with Uncertain Parameters”. In: *Acta Acustica* 4.3 (2020), p. 8 (cit. on p. 2).

[26]Mathieu Gaborit. “KTH School of Engineering Sciences SE-100 44 Stockholm Sweden”. In: (), p. 162 (cit. on pp. 2, 13).

[27]Won Uk Yoon, Jun Hyeong Park, Joong Seok Lee, and Yoon Young Kim. “Topology Optimization Design for Total Sound Absorption in Porous Media”. In: *Computer Methods in Applied Mechanics and Engineering* 360 (Mar. 2020), p. 112723 (cit. on p. 2).

[28]Yang Yu, Guozhong Zhao, Shanhong Ren, and Boping Wang. “Layout Optimization of Porous Sound-Absorbing Material in Mid-Frequency Vibro-Acoustic Systems”. In: *Journal of Fluids and Structures* 100 (Jan. 2021), p. 103197 (cit. on p. 2).

[29]J.-F. Allard and Noureddine Atalla. *Propagation of Sound in Porous Media: Modelling Sound Absorbing Materials*. 2nd ed. Hoboken, N.J: Wiley, 2009 (cit. on pp. 4, 19, 20, 22, 48, 58, 113).

[30]Michel Bruneau and Catherine Potel. *Matériaux et Acoustique 1 : Propagation Des Ondes Acoustiques 1*. http://www.lavoisier.eu/books/physics/materiaux-et-acoustique-1-propagation-des-ondes-acoustiques-1/bruneau/description-9782746213623 (cit. on p. 5).

[31]C Zwikker and Cornelis Willem Kosten. *Sound Absorbing Materials,* New York: Elsevier Pub. Co., 1949 (cit. on p. 5).

[32]M.E. Delany and E.N. Bazley. "Acoustical Properties of Fibrous Absorbent Materials". In: *Applied Acoustics* 3.2 (Apr. 1970), pp. 105–116 (cit. on p. 5).

[33]David Linton Johnson, Joel Koplik, and Roger Dashen. "Theory of Dynamic Permeability and Tortuosity in Fluid-Saturated Porous Media". In: *Journal of Fluid Mechanics* 176 (Mar. 1987), pp. 379–402 (cit. on pp. 5, 18, 69).

[34]Steven R. Pride, Anthony F. Gangi, and F. Dale Morgan. "Deriving the Equations of Motion for Porous Isotropic Media". In: *The Journal of the Acoustical Society of America* 92.6 (Dec. 1992), pp. 3278–3290 (cit. on p. 5).

[35]Denis Lafarge, Pavel Lemarinier, Jean F. Allard, and Viggo Tarnow. "Dynamic Compressibility of Air in Porous Structures at Audible Frequencies". In: *The Journal of the Acoustical Society of America* 102.4 (Oct. 1997), pp. 1995–2006 (cit. on p. 5).

[36]D. Keith Wilson. "Relaxation-matched Modeling of Propagation through Porous Media, Including Fractal Pore Structure". In: *The Journal of the Acoustical Society of America* 94.2 (Aug. 1993), pp. 1136–1145 (cit. on p. 5).

[37]Raymond Panneton. "Comments on the Limp Frame Equivalent Fluid Model for Porous Media". In: *The Journal of the Acoustical Society of America* 122.6 (Dec. 2007), EL217–EL222 (cit. on pp. 5, 21).

[38]Olivier Doutres, Nicolas Dauchez, Jean-Michel Génevaux, and Olivier Dazel. "Validity of the Limp Model for Porous Materials: A Criterion Based on the Biot Theory". In: *The Journal of the Acoustical Society of America* 122.4 (Oct. 2007), pp. 2038–2048 (cit. on p. 5).

[39]M. A. Biot. "Theory of Propagation of Elastic Waves in a Fluid-Saturated Porous Solid. I. Low-Frequency Range". In: *The Journal of the Acoustical Society of America* 28.2 (Mar. 1956), pp. 168–178 (cit. on p. 5).

[40]Maurice A Biot. "Mechanics of Deformation and Acoustic Propagation in Porous Media". In: (1962), p. 19 (cit. on p. 5).

[41]V. Easwaran, W. Lauriks, and J. Coyette. "Displacement-Based Finite Element Method for Guided Wave Propagation Problems: Application to Poroelastic Media". In: (1996) (cit. on p. 5).

[42]Noureddine Atalla, Raymond Panneton, and Patricia Debergue. "A Mixed Displacement-Pressure Formulation for Poroelastic Materials". In: *The Journal of the Acoustical Society of America* 104.3 (Sept. 1998), pp. 1444–1452 (cit. on pp. 5, 20, 22).

[43]Peter Göransson. "A 3-D, Symmetric, Finite Element Formulation of the Biot Equations with Application to Acoustic Wave Propagation through an Elastic Porous Medium". In: *International Journal for Numerical Methods in Engineering* 41.1 (1998), pp. 167–192 (cit. on p. 5).

[44]Olivier Dazel, Bruno Brouard, Claude Depollier, and Stéphane Griffiths. "An Alternative Biot's Displacement Formulation for Porous Materials". In: *J. Acoust. Soc. Am.* 121.6 (2007), p. 8 (cit. on p. 5).

[45] D. Bigoni, S. K. Serkov, M. Valentini, and A. B. Movchan. “Asymptotic Models of Dilute Composites with Imperfectly Bonded Inclusions”. In: *International Journal of Solids and Structures* 35.24 (Aug. 1998), pp. 3239–3258 (cit. on p. 6).

[46] M. B. Rubin and Y. Benveniste. “A Cosserat Shell Model for Interphases in Elastic Media”. In: *Journal of the Mechanics and Physics of Solids* 52.5 (May 2004), pp. 1023–1052 (cit. on p. 7).

[47] Ingo Mey, Milena Stephan, Eva K. Schmitt, et al. “Local Membrane Mechanics of Pore-Spanning Bilayers”. In: *Journal of the American Chemical Society* 131.20 (May 2009), pp. 7031–7039 (cit. on p. 7).

[48] V.M. Aleksandrov. “Asymptotic solution of a contact problem for a thin elastic layer”. In: *Prikl. Mat. Mekh.* 33.1 (1969), pp. 61–73 (cit. on p. 7).

[49] P. Meijers. “The Contact Problem of a Rigid Cylinder on an Elastic Layer”. In: *Applied Scientific Research* 18.1 (1968), pp. 353–383 (cit. on p. 7).

[50] J.B. Alblas and M. Kuipers. “On the Two Dimensional Problem of a Cylindrical Stamp Pressed into a Thin Elastic Layer”. In: *Acta Mechanica* 9.3-4 (1970), pp. 292–311 (cit. on p. 7).

[51] I. Argatov and G. Mishuris. “Frictionless Elliptical Contact of Thin Viscoelastic Layers Bonded to Rigid Substrates”. In: *Applied Mathematical Modelling* 35.7 (July 2011), pp. 3201–3212 (cit. on p. 7).

[52] Z. Hashin. “Thermoelastic Properties of Fiber Composites with Imperfect Interface”. In: *Mechanics of Materials* 8.4 (Feb. 1990), pp. 333–348 (cit. on p. 7).

[53] Z. Hashin. “The Spherical Inclusion With Imperfect Interface”. In: *Journal of Applied Mechanics* 58.2 (June 1991), pp. 444–449 (cit. on p. 7).

[54] Zvi Hashin. “Thin Interphase/Imperfect Interface in Elasticity with Application to Coated Fiber Composites”. In: *Journal of the Mechanics and Physics of Solids* 50.12 (Dec. 2002), pp. 2509–2537 (cit. on p. 7).

[55] Y. Benveniste. “The Effective Mechanical Behaviour of Composite Materials with Imperfect Contact between the Constituents”. In: *Mechanics of Materials* 4.2 (July 1985), pp. 197–208 (cit. on p. 7).

[56] Morton E. Gurtin and A. Ian Murdoch. “Surface Stress in Solids”. In: *International Journal of Solids and Structures* 14.6 (Jan. 1978), pp. 431–440 (cit. on p. 7).

[57] D. J. Steigmann and R. W. Ogden. “Plane Deformations of Elastic Solids with Intrinsic Boundary Elasticity”. In: *Proceedings of the Royal Society of London. Series A: Mathematical, Physical and Engineering Sciences* 453.1959 (Apr. 1997), pp. 853–877 (cit. on p. 7).

[58] S. T. Gu and Q. C. He. “Interfacial Discontinuity Relations for Coupled Multifield Phenomena and Their Application to the Modeling of Thin Interphases as Imperfect Interfaces”. In: *Journal of the Mechanics and Physics of Solids* 59.7 (July 2011), pp. 1413–1426 (cit. on p. 7).

[59] Allan Pierce. *Acoustics: An Introduction to Its Physical Principles and Applications*. Vol. 34. June 1989 (cit. on pp. 7, 15, 24, 58).

[60] Peter Bövik. “On the modelling of thin interface layers in elastic and acoustic scattering problems”. In: *The Quarterly Journal of Mechanics and Applied Mathematics* 47.1 (Feb. 1994), pp. 17–42 (cit. on pp. 7, 24).

[61]E. Becker. “L. M. Brekhovskikh, Waves in Layered Media (Applied Mathematics and Mechanics, Vol. 6). Translated from the Russian. New York/London 1960. Academic Press. Preis Geb. $ 16.00”. In: *ZAMM - Journal of Applied Mathematics and Mechanics / Zeitschrift für Angewandte Mathematik und Mechanik* 42.3 (1962), pp. 129–129 (cit. on p. 7).

[62]Kurt P. Scharnhorst. “Properties of Acoustic and Electromagnetic Transmission Coefficients and Transfer Matrices of Multilayered Plates”. In: *The Journal of the Acoustical Society of America* 74.6 (Dec. 1983), pp. 1883–1886 (cit. on p. 7).

[63]B. Brouard, D. Lafarge, and J. -F. Allard. “A General Method of Modelling Sound Propagation in Layered Media”. In: *Journal of Sound and Vibration* 183.1 (May 1995), pp. 129–142 (cit. on p. 7).

[64]Q. S. Li, Ke Yang, Lixiang Zhang, and N. Zhang. “Frequency Domain Analysis of Fluid–Structure Interaction in Liquid-Filled Pipe Systems by Transfer Matrix Method”. In: *International Journal of Mechanical Sciences* 44.10 (Oct. 2002), pp. 2067–2087 (cit. on p. 7).

[65]C. -M. Lee and Y. Xu. “A Modified Transfer Matrix Method for Prediction of Transmission Loss of Multilayer Acoustic Materials”. In: *Journal of Sound and Vibration* 326.1 (Sept. 2009), pp. 290–301 (cit. on p. 7).

[66]Th. Pastureaud, V. Laude, and S. Ballandras. “Stable Scattering-Matrix Method for Surface Acoustic Waves in Piezoelectric Multilayers”. In: *Applied Physics Letters* 80.14 (Apr. 2002), pp. 2544–2546 (cit. on p. 8).

[67]S. N.Y. Gerges, R. Jordan, F. A. Thieme, J. L. Bento Coelho, and J. P. Arenas. “Muffler Modeling by Transfer Matrix Method and Experimental Verification”. In: *Journal of the Brazilian Society of Mechanical Sciences and Engineering* 27.2 (June 2005) (cit. on p. 8).

[68]Bryan H. Song and J. Stuart Bolton. “A Transfer-Matrix Approach for Estimating the Characteristic Impedance and Wave Numbers of Limp and Rigid Porous Materials”. In: *The Journal of the Acoustical Society of America* 107.3 (Mar. 2000), pp. 1131–1152 (cit. on p. 8).

[69]P. Khurana, L. Boeckx, W. Lauriks, et al. “A Description of Transversely Isotropic Sound Absorbing Porous Materials by Transfer Matrices”. In: *The Journal of the Acoustical Society of America* 125.2 (Feb. 2009), pp. 915–921 (cit. on p. 8).

[70]O. Dazel, J.-P. Groby, B. Brouard, and C. Potel. “A Stable Method to Model the Acoustic Response of Multilayered Structures”. In: *Journal of Applied Physics* 113.8 (Feb. 2013), p. 083506 (cit. on pp. 8, 26, 45, 114).

[71]Yijun Liu. “On the BEM for Acoustic Wave Problems”. In: *Engineering Analysis with Boundary Elements* 107 (Oct. 2019), pp. 53–62 (cit. on p. 8).

[72]F. Ihlenburg and I. Babuška. “Finite Element Solution of the Helmholtz Equation with High Wave Number Part I: The h-Version of the FEM”. In: *Computers & Mathematics with Applications* 30.9 (Nov. 1995), pp. 9–37 (cit. on p. 8).

[73]Frank Ihlenburg and Ivo Babška. “Finite Element Solution of the Helmholtz Equation with High Wave Number Part II: The h-p Version of the FEM”. In: *SIAM Journal on Numerical Analysis* 34.1 (Feb. 1997), pp. 315–358 (cit. on pp. 8, 9).

[74]Arnaud Deraemaeker, Ivo Babuška, and Philippe Bouillard. “Dispersion and Pollution of the FEM Solution for the Helmholtz Equation in One, Two and Three Dimensions”. In: (1999), p. 29 (cit. on p. 9).

[75] Hadrien Bériot, Gwénaël Gabard, and Emmanuel Perrey-Debain. “Analysis of High-Order Finite Elements for Convected Wave Propagation: High-order finite elements for convected acoustics”. In: *International Journal for Numerical Methods in Engineering* 96.11 (Dec. 2013), pp. 665–688 (cit. on pp. 9, 71).

[76] Albert Gerrard Prinn. “Efficient Finite Element Methods for Aircraft Engine Noise Prediction”. PhD thesis, p. 223 (cit. on pp. 9, 23).

[77] Rida T. Farouki. “The Bernstein Polynomial Basis: A Centennial Retrospective”. In: *Computer Aided Geometric Design* 29.6 (Aug. 2012), pp. 379–419 (cit. on p. 9).

[78] S. Petersen, Daniel Dreyer, and O. Estorff. “Assessment of Finite and Spectral Element Shape Functions for Efficient Iterative Simulations of Interior Acoustics”. In: (2006) (cit. on p. 9).

[79] A. El Kacimi, O. Laghrouche, M. S. Mohamed, and J. Trevelyan. “Bernstein–Bézier Based Finite Elements for Efficient Solution of Short Wave Problems”. In: *Computer Methods in Applied Mechanics and Engineering* 343 (Jan. 2019), pp. 166–185 (cit. on p. 9).

[80] Hadrien Bériot, Albert Prinn, and Gwénaël Gabard. “Efficient Implementation of High-order Finite Elements for Helmholtz Problems”. In: *International Journal for Numerical Methods in Engineering* 106.3 (Apr. 2016), pp. 213–240 (cit. on pp. 9, 113).

[81] Nicolas Dauchez, Sohbi Sahraoui, and Noureddine Atalla. “Convergence of Poroelastic Finite Elements Based on Biot Displacement Formulation”. In: *The Journal of the Acoustical Society of America* 109.1 (Jan. 2001), pp. 33–40 (cit. on pp. 9, 49, 51).

[82] N.-E. Hörlin, M. Nordström, and P. Göransson. “A 3-D hierarchical FE formulation of Biot’s equations for elasto-acoustic modelling of porous mediaA”. In: *Journal of Sound and Vibration* 245.4 (Aug. 2001), pp. 633–652 (cit. on pp. 9, 47, 50, 54).

[83] Nils-Erik Hörlin. “3D Hierarchical -FEM Applied to Elasto-Acoustic Modelling of Layered Porous Media”. In: *Journal of Sound and Vibration* 285.1-2 (July 2005), pp. 341–363 (cit. on pp. 9, 47, 50, 54).

[84] S. Rigobert, N. Atalla, and F. C. Sgard. “Investigation of the Convergence of the Mixed Displacement-Pressure Formulation for Three-Dimensional Poroelastic Materials Using Hierarchical Elements”. In: *The Journal of the Acoustical Society of America* 114.5 (2003), p. 2607 (cit. on pp. 9, 107).

[85] Stijn Jonckheere, Hadrien Bériot, Olivier Dazel, and Wim Desmet. “An Adaptive Order Finite Element Method for Poroelastic Materials Described through the Biot Equations”. In: *International Journal for Numerical Methods in Engineering* 123.5 (2022), pp. 1329–1359 (cit. on p. 9).

[86] Ivo M. Babuška and Stefan A. Sauter. “Is the Pollution Effect of the FEM Avoidable for the Helmholtz Equation Considering High Wave Numbers?” In: *SIAM Journal on Numerical Analysis* 34.6 (Dec. 1997), pp. 2392–2423 (cit. on p. 9).

[87] Olivier Cessenat and Bruno Després. “Using Plane Waves as Base Functions for Solving Time Harmonic Equations with the Ultra Weak Variational Formulation”. In: *Journal of Computational Acoustics* 11.02 (June 2003), pp. 227–238 (cit. on pp. 9, 10).

[88] Tomi Huttunen, Peter Monk, and Jari P. Kaipio. “Computational Aspects of the Ultra-Weak Variational Formulation”. In: *Journal of Computational Physics* 182.1 (Oct. 2002), pp. 27–46 (cit. on p. 10).

[89] J.M. Melenk and I. Babuška. “The Partition of Unity Finite Element Method: Basic Theory and Applications”. In: *Computer Methods in Applied Mechanics and Engineering* 139.1-4 (Dec. 1996), pp. 289–314 (cit. on pp. 10, 11, 29).

[90] M.S. Mohamed, O. Laghrouche, and A. El-Kacimi. “Some Numerical Aspects of the PUFEM for Efficient Solution of 2D Helmholtz Problems”. In: *Computers & Structures* 88.23-24 (Dec. 2010), pp. 1484–1491 (cit. on p. 10).

[91] O. Laghrouche, P. Bettess, E. Perrey-Debain, and J. Trevelyan. “Plane Wave Basis Finite-Elements for Wave Scattering in Three Dimensions”. In: *Communications in Numerical Methods in Engineering* 19.9 (2003), pp. 715–723 (cit. on p. 10).

[92] O. Laghrouche, P. Bettess, E. Perrey-Debain, and J. Trevelyan. “Wave Interpolation Finite Elements for Helmholtz Problems with Jumps in the Wave Speed”. In: *Computer Methods in Applied Mechanics and Engineering*. Selected Papers from the 11th Conference on The Mathematics of Finite Elements and Applications 194.2 (Feb. 2005), pp. 367–381 (cit. on p. 10).

[93] Subhajit Banerjee and N. Sukumar. “Exact Integration Scheme for Planewave-Enriched Partition of Unity Finite Element Method to Solve the Helmholtz Problem”. In: *Computer Methods in Applied Mechanics and Engineering* 317 (Apr. 2017), pp. 619–648 (cit. on p. 10).

[94] J.-D. Chazot, B. Nennig, and E. Perrey-Debain. “Performances of the Partition of Unity Finite Element Method for the Analysis of Two-Dimensional Interior Sound Fields with Absorbing Materials”. In: *Journal of Sound and Vibration* 332.8 (Apr. 2013), pp. 1918–1929 (cit. on pp. 10, 47).

[95] Jean-Daniel Chazot, Emmanuel Perrey-Debain, and Benoit Nennig. “The Partition of Unity Finite Element Method for the Simulation of Waves in Air and Poroelastic Media”. In: *The Journal of the Acoustical Society of America* 135.2 (Feb. 2014), pp. 724–733 (cit. on p. 10).

[96] G. Gabard and O. Dazel. “A Discontinuous Galerkin Method with Plane Waves for Sound-Absorbing Materials: Plane-wave DGM for poro-elastic materials”. In: *International Journal for Numerical Methods in Engineering* 104.12 (Dec. 2015), pp. 1115–1138 (cit. on pp. 10, 52).

[97] Lucas C. Wilcox, Georg Stadler, Carsten Burstedde, and Omar Ghattas. “A High-Order Discontinuous Galerkin Method for Wave Propagation through Coupled Elastic–Acoustic Media”. In: *Journal of Computational Physics* 229.24 (Dec. 2010), pp. 9373–9396 (cit. on p. 10).

[98] B. Nennig, E. Perrey-Debain, and J.-D. Chazot. “The Method of Fundamental Solutions for Acoustic Wave Scattering by a Single and a Periodic Array of Poroelastic Scatterers”. In: *Engineering Analysis with Boundary Elements* 35.8 (Aug. 2011), pp. 1019–1028 (cit. on p. 10).

[99] Eisuke Kita and Norio Kamiya. “Trefftz Method: An Overview”. In: *Advances in Engineering Software* 24.1 (Jan. 1995), pp. 3–12 (cit. on p. 10).

[100] W. Desmet, B. van Hal, P. Sas, and D. Vandepitte. “A Computationally Efficient Prediction Technique for the Steady-State Dynamic Analysis of Coupled Vibro-Acoustic Systems”. In: *Advances in Engineering Software*. Engineering Computational Technology & Computational Structures Technology 33.7 (July 2002), pp. 527–540 (cit. on p. 10).

[101] B. Pluymers, W. Desmet, D. Vandepitte, and P. Sas. “Application of an Efficient Wave-Based Prediction Technique for the Analysis of Vibro-Acoustic Radiation Problems”. In: *Journal of Computational and Applied Mathematics*. Selected Papers from the Second International Conference on Advanced Computational Methods in Engineering (ACOMEN 2002) 168.1 (July 2004), pp. 353–364 (cit. on p. 10).

[102]B. Pluymers, B. van Hal, D. Vandepitte, and W. Desmet. “Trefftz-Based Methods for Time-Harmonic Acoustics”. In: *Archives of Computational Methods in Engineering* 14.4 (Dec. 2007), pp. 343–381 (cit. on p. 10).

[103]Elke Deckers, Bert Van Genechten, Dirk Vandepitte, and Wim Desmet. “Efficient Treatment of Stress Singularities in Poroelastic Wave Based Models Using Special Purpose Enrichment Functions”. In: *Computers & Structures*. Computational Fluid and Solid Mechanics 2011 89.11 (June 2011), pp. 1117–1130 (cit. on p. 10).

[104]Elke Deckers, Nils-Erik Hörlin, Dirk Vandepitte, and Wim Desmet. “A Wave Based Method for the Efficient Solution of the 2D Poroelastic Biot Equations”. In: *Computer Methods in Applied Mechanics and Engineering* 201–204 (Jan. 2012), pp. 245–262 (cit. on p. 10).

[105]Elke Deckers, Bart Bergen, Bert Van Genechten, Dirk Vandepitte, and Wim Desmet. “An Efficient Wave Based Method for 2D Acoustic Problems Containing Corner Singularities”. In: *Computer Methods in Applied Mechanics and Engineering* 241–244 (Oct. 2012), pp. 286–301 (cit. on p. 10).

[106]Elke Deckers, Dirk Vandepitte, and Wim Desmet. “A Wave Based Method for the Axisymmetric Dynamic Analysis of Acoustic and Poroelastic Problems”. In: *Computer Methods in Applied Mechanics and Engineering* 257 (Apr. 2013), pp. 1–16 (cit. on p. 10).

[107]Bert Van Genechten, Karel Vergote, Dirk Vandepitte, and Wim Desmet. “A Multi-Level Wave Based Numerical Modelling Framework for the Steady-State Dynamic Analysis of Bounded Helmholtz Problems with Multiple Inclusions”. In: *Computer Methods in Applied Mechanics and Engineering* 199.29-32 (June 2010), pp. 1881–1905 (cit. on p. 11).

[108]Natalia Climent, Ionut Dragos Moldovan, and João António Freitas. “Three-Dimensional Hybrid-Trefftz Displacement Elements for Poroelastodynamic Problems in Saturated Media”. In: *International Journal for Numerical Methods in Engineering* 123.12 (2022), pp. 2919–2958 (cit. on p. 11).

[109]Nicolas Moës, John Dolbow, and Ted Belytschko. “A Finite Element Method for Crack Growth without Remeshing”. In: *International Journal for Numerical Methods in Engineering* 46.1 (1999), pp. 131–150 (cit. on pp. 11, 31).

[110]N Sukumar, D L Chopp, and N Mo. “Modeling Holes and Inclusions by Level Sets in the Extended ®nite-Element Method”. In: *Comput. Methods Appl. Mech. Engrg.* (2001), p. 18 (cit. on pp. 11, 12, 29, 31).

[111]N. Moës, M. Cloirec, P. Cartraud, and J.-F. Remacle. “A Computational Approach to Handle Complex Microstructure Geometries”. In: *Computer Methods in Applied Mechanics and Engineering* 192.28-30 (July 2003), pp. 3163–3177 (cit. on pp. 11, 12, 27, 31).

[112]F. L. Stazi, E. Budyn, J. Chessa, and T. Belytschko. “An Extended Finite Element Method with Higher-Order Elements for Curved Cracks”. In: *Computational Mechanics* 31.1-2 (May 2003), pp. 38–48 (cit. on pp. 11, 30).

[113]Axel Gerstenberger and Wolfgang A Wall. “An eXtended Finite Element Method/Lagrange Multiplier Based Approach for Fluid–Structure Interaction”. In: *Comput. Methods Appl. Mech. Engrg.* (2008), p. 16 (cit. on pp. 11, 12).

[114]Thomas-Peter Fries and Ted Belytschko. “The Extended/Generalized Finite Element Method: An Overview of the Method and Its Applications”. In: *International Journal for Numerical Methods in Engineering* 84.3 (Oct. 2010), pp. 253–304 (cit. on p. 11).

[115]Guizhong Xiao, Longfei Wen, and Rong Tian. “Arbitrary 3D Crack Propagation with Improved XFEM: Accurate and Efficient Crack Geometries”. In: *Computer Methods in Applied Mechanics and Engineering* 377 (Apr. 2021), p. 113659 (cit. on p. 11).

[116]Anita Hansbo and Peter Hansbo. “An Unfitted Finite Element Method, Based on Nitsche’s Method, for Elliptic Interface Problems”. In: *Computer Methods in Applied Mechanics and Engineering* 191.47-48 (Nov. 2002), pp. 5537–5552 (cit. on p. 12).

[117]Anita Hansbo and Peter Hansbo. “A Finite Element Method for the Simulation of Strong and Weak Discontinuities in Solid Mechanics”. In: *Computer Methods in Applied Mechanics and Engineering* 193.33-35 (Aug. 2004), pp. 3523–3540 (cit. on pp. 12, 36, 59, 60, 62).

[118]Jeong-Hoon Song, Pedro M. A. Areias, and Ted Belytschko. “A Method for Dynamic Crack and Shear Band Propagation with Phantom Nodes”. In: *International Journal for Numerical Methods in Engineering* 67.6 (2006), pp. 868–893 (cit. on p. 12).

[119]Zilong Zou, Wilkins Aquino, and Isaac Harari. “Nitsche’s Method for Helmholtz Problems with Embedded Interfaces: Nitsche’s method for Helmholtz problems”. In: *International Journal for Numerical Methods in Engineering* 110.7 (May 2017), pp. 618–636 (cit. on pp. 12, 13, 61).

[120]Anita Hansbo, Peter Hansbo, and Mats G. Larson. “A Finite Element Method on Composite Grids Based on Nitsche’s Method”. In: *ESAIM: Mathematical Modelling and Numerical Analysis* 37.3 (May 2003), pp. 495–514 (cit. on p. 12).

[121]Peter Hansbo, Mats G. Larson, and Sara Zahedi. “A Cut Finite Element Method for a Stokes Interface Problem”. In: *Applied Numerical Mathematics* 85 (Nov. 2014), pp. 90–114 (cit. on p. 12).

[122]Wen Jiang, Benjamin W. Spencer, and John E. Dolbow. “Ceramic Nuclear Fuel Fracture Modeling with the Extended Finite Element Method”. In: *Engineering Fracture Mechanics* 223 (Jan. 2020), p. 106713 (cit. on p. 12).

[123]Anders Bernland, Eddie Wadbro, and Martin Berggren. “Acoustic Shape Optimization Using Cut Finite Elements”. In: *International Journal for Numerical Methods in Engineering* 113.3 (2018), pp. 432–449 (cit. on p. 12).

[124]Erik Burman, Susanne Claus, Peter Hansbo, Mats G. Larson, and André Massing. “CutFEM: Discretizing Geometry and Partial Differential Equations”. In: *International Journal for Numerical Methods in Engineering* 104.7 (2015), pp. 472–501 (cit. on pp. 12, 13, 32, 60).

[125]Ted Belytschko, Chandu Parimi, Nicolas Moës, N. Sukumar, and Shuji Usui. “Structured Extended Finite Element Methods for Solids Defined by Implicit Surfaces”. In: *International Journal for Numerical Methods in Engineering* 56.4 (Jan. 2003), pp. 609–635 (cit. on p. 12).

[126]I. Babuška. “The Finite Element Method with Penalty”. In: (1973) (cit. on pp. 12, 32, 59).

[127]Ivo Babuška. “The Finite Element Method with Lagrangian Multipliers”. In: *Numerische Mathematik* 20.3 (June 1973), pp. 179–192 (cit. on pp. 12, 32).

[128]H. Ji and J.E. Dolbow. “On Strategies for Enforcing Interfacial Constraints and Evaluating Jump Conditions with the Extended Finite Element Method”. In: *International Journal for Numerical Methods in Engineering* 61.14 (2004), pp. 2508–2535 (cit. on p. 12).

[129]Éric Béchet, Nicolas Moës, and Barbara Wohlmuth. “A Stable Lagrange Multiplier Space for Stiff Interface Conditions within the Extended Finite Element Method”. In: *International Journal for Numerical Methods in Engineering* 78.8 (2009), pp. 931–954 (cit. on p. 12).

[130] D. S. Malkus. “Incompressible Finite Elements: The LBB Condition and the Discrete Eigenstructure”. In: *Nonlinear Finite Element Analysis in Structural Mechanics*. Ed. by W. Wunderlich, E. Stein, and K.-J. Bathe. Berlin, Heidelberg: Springer, 1981, pp. 696–711 (cit. on pp. 12, 35).

[131] Martin Hautefeuille, Chandrasekhar Annavarapu, and John E. Dolbow. “Robust Imposition of Dirichlet Boundary Conditions on Embedded Surfaces”. In: *International Journal for Numerical Methods in Engineering* 90.1 (2012), pp. 40–64 (cit. on p. 12).

[132] J. Nitsche. “Über Ein Variationsprinzip Zur Lösung von Dirichlet-Problemen Bei Verwendung von Teilräumen, Die Keinen Randbedingungen Unterworfen Sind”. In: (1971) (cit. on pp. 12, 32).

[133] John Dolbow and Isaac Harari. “An Efficient Finite Element Method for Embedded Interface Problems”. In: *International Journal for Numerical Methods in Engineering* 78.2 (Apr. 2009), pp. 229–252 (cit. on pp. 12, 65).

[134] Anand Embar, John Dolbow, and Isaac Harari. “Imposing Dirichlet Boundary Conditions with Nitsche’s Method and Spline-Based Finite Elements”. In: *International Journal for Numerical Methods in Engineering* (2010), n/a–n/a (cit. on pp. 13, 71).

[135] Wen Jiang, Chandrasekhar Annavarapu, John E. Dolbow, and Isaac Harari. “A Robust Nitsche’s Formulation for Interface Problems with Spline-Based Finite Elements: A Robust Nitsche’s Formulation for Interface Problems with Spline-Based Finite Elements”. In: *International Journal for Numerical Methods in Engineering* 104.7 (Nov. 2015), pp. 676–696 (cit. on pp. 13, 65, 66, 74, 78).

[136] Wen Jiang, Yingjie Liu, and Chandrasekhar Annavarapu. “A Weighted Nitsche’s Method for Interface Problems with Higher-Order Simplex Elements”. In: *Computational Mechanics* (Jan. 2022) (cit. on pp. 13, 68, 87).

[137] Esubalewe Lakie Yedeg, Eddie Wadbro, Peter Hansbo, Mats G. Larson, and Martin Berggren. “A Nitsche-type Method for Helmholtz Equation with an Embedded Acoustically Permeable Interface”. In: *Computer Methods in Applied Mechanics and Engineering* 304 (June 2016), pp. 479–500 (cit. on pp. 13, 36, 60, 62).

[138] John A. Nairn. “Numerical Implementation of Imperfect Interfaces”. In: *Computational Materials Science* 40.4 (Oct. 2007), pp. 525–536 (cit. on p. 13).

[139] Zhilin Han, Stein K. F. Stoter, Chien-Ting Wu, et al. “Consistent Discretization of Higher-Order Interface Models for Thin Layers and Elastic Material Surfaces, Enabled by Isogeometric Cut-Cell Methods”. In: *Computer Methods in Applied Mechanics and Engineering* 350 (June 2019), pp. 245–267 (cit. on p. 13).

[140] J. Yvonnet, H. Le. Quang, and Q. -C. He. “An XFEM/Level Set Approach to Modelling Surface/Interface Effects and to Computing the Size-Dependent Effective Properties of Nanocomposites”. In: *Computational Mechanics* 42.1 (Apr. 2008), pp. 119–131 (cit. on p. 13).

[141] Q.-Z. Zhu, S.-T. Gu, J. Yvonnet, J.-F. Shao, and Q.-C. He. “Three-Dimensional Numerical Modelling by XFEM of Spring-Layer Imperfect Curved Interfaces with Applications to Linearly Elastic Composite Materials”. In: *International Journal for Numerical Methods in Engineering* 88.4 (Oct. 2011), pp. 307–328 (cit. on pp. 13, 60).

[142] Elena Benvenuti, Giulio Ventura, Nicola Ponara, and Antonio Tralli. “Variationally Consistent eXtended FE Model for 3D Planar and Curved Imperfect Interfaces”. In: *Computer Methods in Applied Mechanics and Engineering* 267 (Dec. 2013), pp. 434–457 (cit. on p. 13).

[143]Antoine Legay. “The Extended Finite Element Method Combined with a Modal Synthesis Approach for Vibro-Acoustic Problems: X-FEM combined with a modal synthesis approach for vibro-acoustics”. In: *International Journal for Numerical Methods in Engineering* 101.5 (Feb. 2015), pp. 329–350 (cit. on p. 13).

[144]Yvan Champoux and Jean-F. Allard. “Dynamic Tortuosity and Bulk Modulus in Air-saturated Porous Media”. In: *Journal of Applied Physics* 70.4 (Aug. 1991), pp. 1975–1979 (cit. on pp. 18, 69).

[145]Frank Ihlenburg. *Finite Element Analysis of Acoustic Scattering*. 1998 (cit. on pp. 20, 64, 159, 160).

[146]Patricia Debergue, Raymond Panneton, and Noureddine Atalla. “Boundary Conditions for the Weak Formulation of the Mixed (u,p) Poroelasticity Problem”. In: *The Journal of the Acoustical Society of America* 106.5 (Nov. 1999), pp. 2383–2390 (cit. on p. 21).

[147]J. M. Melenk. “On Condition Numbers in Hp-FEM with Gauss–Lobatto-based Shape Functions”. In: *Journal of Computational and Applied Mathematics* 139.1 (Feb. 2002), pp. 21–48 (cit. on p. 23).

[148]Stanley Osher and James A Sethian. “Fronts Propagating with Curvature-Dependent Speed: Algorithms Based on Hamilton-Jacobi Formulations”. In: *Journal of Computational Physics* 79.1 (Nov. 1988), pp. 12–49 (cit. on p. 27).

[149]G. Legrain, P. Cartraud, I. Perreard, and N. Moës. “An X-FEM and Level Set Computational Approach for Image-Based Modelling: Application to Homogenization”. In: *International Journal for Numerical Methods in Engineering* 86.7 (2011), pp. 915–934 (cit. on p. 28).

[150]Kristell Dréau, Nicolas Chevaugeon, and Nicolas Moës. “Studied X-FEM Enrichment to Handle Material Interfaces with Higher Order Finite Element”. In: (), p. 16 (cit. on p. 30).

[151]G. Legrain, N. Chevaugeon, and K. Dréau. “High Order X-FEM and Levelsets for Complex Microstructures: Uncoupling Geometry and Approximation”. In: *Computer Methods in Applied Mechanics and Engineering* 241–244 (Oct. 2012), pp. 172–189 (cit. on pp. 30, 78).

[152]M. Komijani and R. Gracie. “Enriched Mixed Finite Element Models for Dynamic Analysis of Continuous and Fractured Porous Media”. In: *Computer Methods in Applied Mechanics and Engineering* 343 (Jan. 2019), pp. 74–99 (cit. on p. 30).

[153]A. Legay, H. W. Wang, and T. Belytschko. “Strong and Weak Arbitrary Discontinuities in Spectral Finite Elements”. In: *International Journal for Numerical Methods in Engineering* 64.8 (Oct. 2005), pp. 991–1008 (cit. on p. 30).

[154]Christoph Lehrenfeld. “High Order Unfitted Finite Element Methods on Level Set Domains Using Isoparametric Mappings”. In: *Computer Methods in Applied Mechanics and Engineering* 300 (Mar. 2016), pp. 716–733 (cit. on pp. 30, 148).

[155]Grégory Legrain. “A NURBS Enhanced Extended Finite Element Approach for Unfitted CAD Analysis”. In: *Computational Mechanics* 52.4 (Oct. 2013), pp. 913–929 (cit. on pp. 30, 53).

[156]J. Chessa and T. Belytschko. “An Extended Finite Element Method for Two-Phase Fluids”. In: *Journal of Applied Mechanics* 70.1 (Jan. 2003), pp. 10–17 (cit. on p. 31).

[157]Pedro M.A. Areias and Ted Belytschko. “A Comment on the Article “A Finite Element Method for Simulation of Strong and Weak Discontinuities in Solid Mechanics” by A. Hansbo and P. Hansbo [Comput. Methods Appl. Mech. Engrg. 193 (2004) 3523–3540]”. In: *Computer Methods in Applied Mechanics and Engineering* 195.9-12 (Feb. 2006), pp. 1275–1276 (cit. on pp. 32, 33).

[158] T. Menouillard, J. Réthoré, N. Moës, A. Combescure, and H. Bung. "Mass Lumping Strategies for X-FEM Explicit Dynamics: Application to Crack Propagation". In: *International Journal for Numerical Methods in Engineering* 74.3 (Apr. 2008), pp. 447–474 (cit. on p. 33).

[159] J.-H. Heegaard and A. Curnier. "An Augmented Lagrangian Method for Discrete Large-Slip Contact Problems". In: *International Journal for Numerical Methods in Engineering* 36.4 (1993), pp. 569–593 (cit. on p. 36).

[160] Dominik Schillinger, Isaac Harari, Ming-Chen Hsu, et al. "The Non-Symmetric Nitsche Method for the Parameter-Free Imposition of Weak Boundary and Coupling Conditions in Immersed Finite Elements". In: *Computer Methods in Applied Mechanics and Engineering* 309 (Sept. 2016), pp. 625–652 (cit. on p. 36).

[161] Olivier Dazel. "Numerical Methods for the Biot Theory in Acoustics". In: (), p. 106 (cit. on p. 44).

[162] Patrick R. Amestoy, Alfredo Buttari, Jean-Yves L'Excellent, and Theo Mary. "Performance and Scalability of the Block Low-Rank Multifrontal Factorization on Multicore Architectures". In: *ACM Transactions on Mathematical Software* 45.1 (Mar. 2019), pp. 1–26 (cit. on p. 46).

[163] Alice Lieu, Gwénaël Gabard, and Hadrien Bériot. "A Comparison of High-Order Polynomial and Wave-Based Methods for Helmholtz Problems". In: *Journal of Computational Physics* 321 (Sept. 2016), pp. 105–125 (cit. on pp. 46, 52).

[164] Owe Axelsson, János Karátson, and Fréderic Magoulès. "Superlinear Convergence Using Block Preconditioners for the Real System Formulation of Complex Helmholtz Equations". In: *Journal of Computational and Applied Mathematics* (2018), p. 8 (cit. on pp. 52, 110).

[165] C. Ager, B. Schott, M. Winter, and W.A. Wall. "A Nitsche-based Cut Finite Element Method for the Coupling of Incompressible Fluid Flow with Poroelasticity". In: *Computer Methods in Applied Mechanics and Engineering* 351 (July 2019), pp. 253–280 (cit. on pp. 59, 72).

[166] Chandrasekhar Annavarapu, Martin Hautefeuille, and John E. Dolbow. "A Robust Nitsche's Formulation for Interface Problems". In: *Computer Methods in Applied Mechanics and Engineering* 225–228 (June 2012), pp. 44–54 (cit. on pp. 64, 66).

[167] M. Griebel and M. A. Schweitzer. "A Particle-Partition of Unity Method Part V: Boundary Conditions". In: *Geometric Analysis and Nonlinear Partial Differential Equations*. Ed. by Stefan Hildebrandt and Hermann Karcher. Berlin, Heidelberg: Springer Berlin Heidelberg, 2003, pp. 519–542 (cit. on p. 65).

[168] S Jonckheere, D Vandepitte, and W Desmet. "A Wave Based Transfer Matrix Method for Accurate Simulation of Acoustic Problems with Multilayered Damping Treatment". In: (2015), p. 6 (cit. on p. 101).

[169] Hadrien Bériot and Gwénaël Gabard. "Anisotropic Adaptivity of the P-FEM for Time-Harmonic Acoustic Wave Propagation". In: *Journal of Computational Physics* 378 (Feb. 2019), pp. 234–256 (cit. on pp. 113, 114).

[170] Mathieu Gaborit and Dazel Olivier. *Pymls-Multilayer Solver in Python*. 2021 (cit. on p. 114).

[171] Christophe Geuzaine and Jean-François Remacle. "Gmsh: A 3-D Finite Element Mesh Generator with Built-in Pre- and Post-Processing Facilities". In: *International Journal for Numerical Methods in Engineering* 79.11 (2009), pp. 1309–1331 (cit. on p. 118).

[172] Elias J. G. Arcondoulis, Thomas F. Geyer, and Yu Liu. “An Investigation of Wake Flows Produced by Asymmetrically Structured Porous Coated Cylinders”. In: *Physics of Fluids* 33.3 (Mar. 2021), p. 037124 (cit. on p. 132).

[173] George Stefanou. “The Stochastic Finite Element Method: Past, Present and Future”. In: *Computer Methods in Applied Mechanics and Engineering* 198.9-12 (Feb. 2009), pp. 1031–1051 (cit. on p. 137).

[174] Keith Stein, Tayfun E. Tezduyar, and Richard Benney. “Automatic Mesh Update with the Solid-Extension Mesh Moving Technique”. In: *Computer Methods in Applied Mechanics and Engineering* 193.21-22 (May 2004), pp. 2019–2032 (cit. on p. 139).

[175] Benoit Van den Nieuwenhof and Jean-Pierre Coyette. “Modal Approaches for the Stochastic Finite Element Analysis of Structures with Material and Geometric Uncertainties”. In: *Computer Methods in Applied Mechanics and Engineering* 192.33-34 (Aug. 2003), pp. 3705–3729 (cit. on p. 141).

[176] Alfio Quarteroni, Andrea Manzoni, and Federico Negri. *Reduced Basis Methods for Partial Differential Equations*. Vol. 92. UNITEXT. Cham: Springer International Publishing, 2016 (cit. on p. 142).

Titre : Eléments finis étendus pour la modélisation des interfaces en vibro-acoustique dissipative

Mots clés : Vibro-acoustique, Matériaux poreux, Interfaces, X-FEM haut ordre

Résumé : Le bruit est aujourd'hui omniprésent dans notre société, ce qui incite à en diminuer les impacts sur la santé. Grâce à leur légèreté et à leur flexibilité en termes de conception, les ensembles d'absorption acoustique constitués de matériaux poreux pourraient occuper une position centrale parmi les approches visant à réduire le bruit. Notre intérêt se porte sur les systèmes d'absorption comportant de multiples couches avec de grandes disparités d'épaisseur (de quelques millimètres à plusieurs mètres), et de géométries potentiellement complexes. Notre objectif est d'élaborer des méthodes numériques plus efficaces que la méthode des éléments finis (FEM) pour prédire le comportement vibro-acoustique de ces systèmes.

Sur la base de la méthode des éléments finis étendus (X-FEM), des stratégies d'enrichissement et de discrétisation sont proposées pour le couplages de milieux poreux impliquant des équations de Biot. Des formulations variationnelles stables et robustes sont proposées pour prendre en compte l'effet des couches poreuses minces. Il est démontré que nos approches sont capables de réduire considérablement le temps de pré-traitement et de résolution tout en maintenant le niveau de précision par rapport aux éléments finis classiques.

Title : Interface modeling within eXtended Finite Element Method for dissipative vibro-acoustic problems

Keywords : Vibro-acoustic, Porous materials, Interfaces, high-order X-FEM

Abstract : Noise is nowadays omnipresent in our society, which encourages us to reduce its impact on health. Thanks to their design flexibility and lightness, sound absorbing packages made of porous materials might hold a pivotal position among noise reduction approaches. Our prime interest is in sound packages which have multiple layers with significant thickness disparity ranging from several meters to millimeters and potentially complex geometries. We aim at elaborating on more efficient numerical methods to identify and predict the vibroacoustic behaviour of such packages compared to the classical Finite Element Method (FEM).

Based on the eXtended Finite Element Method (X-FEM), enrichment and discretization strategies are developed to couple porous media involving mixed Biot's equations. Stable and robust variational formulations are proposed to represent the acoustic effects of thin porous layers. Our approaches are demonstrated to be capable of reducing considerably the pre-processing and resolution times while maintaining the accuracy level in comparison with classical FEM.